STRUCTURE AND REACTIVITY OF SELECTED INCLUSION COMPOUNDS

by

ANITA COETZEE
M.Sc. (Rhodes University)

Thesis presented to the

UNIVERSITY OF CAPE TOWN

for the degree of

DOCTOR OF PHILOSOPHY

Department of Chemistry
University of Cape Town
Rondebosch
7700
South Africa

July 1996

IAMQVE OPVS EXEGI, QVOD NEC IOVIS IRA, NEC IGNIS, NEC POTERIT FERRVM, NEC EDAX ABOLERE VETVSTAS.

And now I have finished the work, which neither the wrath of Jove, nor fire, nor the sword, nor devouring age shall be able to destroy.

Ovid (43 B.C.-A.D. 18), Metamorphoses

ACKNOWLEDGEMENTS

I would like to extend a special word of thanks to:

my supervisors Professor Luigi R. Nassimbeni and Associate Professor Mino R. Caira for their enthusiasm and excellent guidance,

Mr Klaus Achleitner who shared some of his electronic knowledge with me

Dr Len Barbour for the all his useful computer programmes

the members of the Crystallography Research Group, for their friendship, support and proof-reading

my family and especially my husband, Charles Herbaut, for their loving support and encouragement.

PUBLICATIONS AND CONFERENCES

Parts of this thesis have been published in the following journals:

1. M.R. Caira, A. Coetzee, L.R. Nassimbeni, E. Weber, A. Wierig, *J. Chem. Soc., Perkin Trans 2*, 1995, 281.

2. L.J. Barbour, M.R. Caira, A. Coetzee, L.R. Nassimbeni, *J. Chem. Soc., Perkin Trans 2*, 1995, 1345.

3. M.R. Caira, A. Coetzee, Klaus R. Koch, L.R. Nassimbeni, Fumio Toda, *J. Chem. Soc., Perkin Trans 2*, 1996, 569.

4. M.R. Caira, A. Coetzee, L.R. Nassimbeni, Fumio Toda, *J. Chem. Res. (S)*, 1996, 280.

5. M.R. Caira, A. Coetzee, L.R. Nassimbeni, E. Weber, A. Wierig, *J. Chem. Soc., Perkin Trans 2*, submitted.

Parts of this thesis have been presented at the following conferences:

1. Paper entitled: Kinetics of Desolvation of Inclusion Compounds delivered at Conference on Molecular Recognition and Synthetic Design, UCT, 9 - 11 February 1994.

2. Paper entitled: Kinetics of Desolvation of Tricyclic Inclusion Compounds delivered at a one-day symposium on Molecular Recognition and Synthetic Design, UCT, 3 February 1995.

3. Poster entitled: Kinetics of Desolvation of Inclusion Compounds presented at the International School of Crystallography, Erice, Sicily, 1-11 June 1995.

4. Poster entitled: A Quartz Microbalance for Measuring Guest Uptake from the Vapour presented at the SACI Conference, Cape Town, 29 January-3 February 1996.

5. I have been invited to deliver a paper entitled: Structure and Reactivity of Host-Guest Inclusion Compounds at the XVII Congress of the International Union of Crystallography in Seattle, USA, 8-17 August 1996.

ABSTRACT

Selected inclusion compounds of hydroxy hosts from three different classes were investigated. The host compounds in class **A** are 2,7-substituted 2,2'-bis(9-hydroxy-9-fluorenyl)biphenyls, with the substituents being Cl, Br or *tert*-butyl. They readily form inclusion compounds with a wide variety of solvents. Their inclusion compounds with 1,4-dioxane, 1,3-dioxane, 1,3-dioxolane and acetone were investigated. The crystal structure of an unsolvated, α-phase, of the host compound 2,2'-bis(2,7-dichloro-9-hydroxy-9-fluorenyl)biphenyl was elucidated. The host compounds in class **B** are modified dihydroanthracenes. The inclusion compounds of *trans*-9,10-dihydroxy-9,10-diphenyl-9,10-dihydroanthracene with 1,3-dioxolane, *trans*-9,10-dihydroxy-9,10-di-α-naphtyl-9,10-dihydroanthracene with 1,3-dioxolane and with benzene, as well as trans-9,10-dihydroxy-9,10-di-*p*-*tert*-butylphenyl-9,10-dihydroanthracene with methanol and with benzene, were studied. The host in class **C**, 2,2'-bis(diphenylhydroxymethyl)-1,1'-biphenyl (**H**), is similar to the host compounds in class **A**, but is rendered conformationally more flexible. It forms two structurally similar inclusion compounds, $\mathbf{H}\cdot H_2O\cdot 1/6\ C_6H_6$ and $\mathbf{H}\cdot 21/6H_2O$. The crystal structure of a *p*-xylene inclusion compound was also elucidated.

The crystal structures of all these inclusion compounds were elucidated. All the compounds were characterised using thermal analysis and X-ray powder diffraction. The kinetics of desolvation of all the inclusion compounds in class **A** and **B** were studied, using isothermal or programmed temperature thermogravimetry. Attempts were made to describe the kinetic behaviour in terms of the crystal structures of these compounds. The Arrhenius parameters for the desolvation of all the inclusion compounds under investigation were found to show the compensation effect. The kinetics of solvation of *trans*-9,10-dihydroxy-9,10-diphenyl-9,10-dihydroanthracene and 1,3-dioxolane was studied, using a quartz microbalance designed especially for this purpose.

ABBREVIATIONS USED IN THIS THESIS

Most of the abbreviations and symbols used in this thesis are widely used in the chemical literature. The inclusion compounds are described by mnemonics which are detailed on the inserted bookmark and in the fold-out table at the end of the document.

A	Arrhenius pre-exponential factor
α	extent of reaction
	unsolvated, non-porous phase of the host compound
	the angle between *b* and *c* unit cell axes
β	the angle between *a* and *c* unit cell axes
γ	the angle between *a* and *b* unit cell axes
CSD	Cambridge Structural Database
DSC	differential scanning calorimetry
DTG	differential thermogravimetry
E	normalised structure factor
E_a	activation energy
F	structure factor
$f(\alpha)$	kinetic rate expression
G	guest
H	host
k	rate constant
M_r	molecular mass
NMR	nuclear magnetic resonance
TG	thermogravimetry
τ	torsion angle
V	cell volume
XRD	X-ray powder diffraction
Z	number of structural units in the unit cell

TABLE OF CONTENTS

CHAPTER 1 INTRODUCTION

Inclusion Compounds

It would be presumptuous even to attempt to cover all topics included in the wide field of inclusion compounds. Since Davy[1] reported the observation of the first chlorine clathrate hydrate in 1811, a new field of chemistry has developed - that of "chemistry beyond the molecule"[2]. In this condensed historical overview an attempt has been made to highlight some of the milestones in the development of the field of inclusion chemistry. This is by no means a comprehensive review, since volumes can be, and have been[3,4], written on this subject. The aim of this concise chronology is merely to place the current study in the context of the broad development of inclusion chemistry. A short historical overview has been drawn up from 1811 until the early 1990's. Since the more recent entries would be totally subjective, only a few interesting concepts are discussed.

Historical Overview

	1811	H. Davy prepares a chlorine hydrate[1]
	1823	M. Faraday confirms Davy's observation and determines the composition of the chlorine hydrate[5]
	1840	A. Damour observes the reversible dehydration of zeolite crystals[6]
	1841	C. Schafthäult prepares the graphite intercalates[7]
	1849	F. Wohler prepares a β-quinol·H_2S molecular complex[8]
	1891	A. Villiers prepares the first cyclodextrin inclusion compounds[9]
	1893	S.U. Pickering publishes a study of alkylamine hydrates[10]
	1894	E. Fischer introduces the "lock and key" principle[11]
Discovery of X-rays by Röntgen[12]	**1895**	
	1897	preparation of Hofmann's benzene inclusion compound: $Ni(CN)_2 \cdot NH_3 \cdot C_6H_6$[13]

	1903	preparation of Hofmann's compound with aniline and phenol[14]
	1906	preparation of inclusion compounds of triphenylmethane[15]
	1909	preparation of tri-*o*-thymotide (TOT) benzene inclusion compound[16]
Nobel prize for Physics: M.T.F. von Laue	**1914**	synthesis of Dianin's compound: 4-(4-hydroxyphenyl)-2,2,4-trimethylchroman[17]
Nobel prize for Physics: W.H. Bragg and W.L. Bragg	**1915**	
World War I	**1916**	H. Wieland and H. Sorge prepare the first choleic acid inclusion compounds[18]
	1918	
	1930	gas hydrates block natural gas pipelines in USA and USSR at temperatures higher than for normal ice formation - this results in a renewed interest in gas hydrates[19]
	1932	the term **"molecular sieve"** is coined to describe the behaviour of some microporous charcoals and zeolites[20]
	1935	E. Terres and W. Vollmer publish the preparation of phenol molecular complexes[21]
	1936	O. Kratky and G. Giacomello elucidate the crystal structure of choleic acid[22]
	1939	
World War II	**1940**	M.F. Bengen patents the preparation of urea inclusion compounds[23]
	1945	
	1946	F.F. Mikus, R.M. Hixon and R.E. Rundle publish the preparation of amylose inclusion compounds[24]
	1947	D.E. Palin and H.M. Powell publish the crystal structures of the β-quinol·H_2S inclusion compound[25]
	1948	H.M. Powell coins the word **"clathrate"**[26]

	1951	D.J. Cram and H. Steinberg publish the synthesis of [2.2]paracyclophane[27]
	1951	M. Von Stackelberg and H.R. Müller[28];W.F. Claussen[29]; L. Pauling and R.E. Marsh[30] all propose crystal structures for the two types of gas hydrate and recognise them as clathrates[10]
Launch of Sputnik I	**1957**	W.D. Schaeffer *et al.* publish an article entitled: "Separation of xylenes, cymenes, methylnaphthenes and other isomers by clathration of inorganic complexes", using Werner clathrates[31]
	1964	publication of "Non Stoichiometric Compounds", L. Mandelcorn[32]
	1967	C.J.Pederson publishes the preparation of crown ethers[33]
Man lands on the moon	**1969**	J.L. Atwood "accidentally" prepares first liquid clathrates[34]
	1969	J.-M. Lehn and co-workers publish the preparation of cryptands[35]
	1972	R.J. Argauer and G.R. Landolt describe zeolite ZSM5[36]
	1974	D.J. Cram and J.M. Cram introduce the terms **"host", "guest"** and **"host-guest complexation"**[37]
	1976	D.D. MacNicol synthesises first hexa-hosts[38]
	1978	J.-M. Lehn introduces the concept and term **"supramolecular chemistry"**[39]
	1979	G.D. Andreetti, R. Ungaro and A. Pochini report the crystal structure of *p-tert*-butyl-calix[4]arene with toluene included in the cavity[40]
	1980	J. Lipkowski describes the physical chemistry of Werner clathrates[41]
	1980	Institute of Physical chemistry of the Polish Academy of Sciences hosts the First International Symposium on "Clathrate Compounds and Molecular inclusion phenomena" in Jachranka, near Warsaw.
	1983	first issue of *J. of Inclusion Phenomena* is published, editors J.L Atwood and J.E.D. Davies

	1983	E. Weber and H.-P. Josel propose nomenclature and classification of host-guest type compounds[42]
	1984	First volume of *Inclusion Compounds* is published by Academic Press, London
Nobel prize for Chemistry: J. Karle and H.A. Hauptman for developing direct phasing methods to determine X-ray crystal structures	**1985**	
	1987	J.F. Stoddart and co-workers publish the synthesis of the first catenanes and rotaxanes[43]
	1987	Nobel prize for Chemistry: D.J. Cram[44] J.-M. Lehn[45] C.J. Pederson[46] for their respective work in the field of supramolecular chemistry
	1992	first issue of *Supramolecular Chemistry* is published, editors J.L. Atwood and G.W. Gokel[47]
	1993	F.H. Herbstein proposes principles for classification of crystalline binary adducts[48]
	1994	first issue of *Supramolecular Science* is published, editor-in-chief W. Knoll[49]
	1996	publication of *Comprehensive Supramolecular Chemistry*, Vol. 1-11, Executive editors: J.L. Atwood, J.E.D. Davies, D.D. MacNicol and F. Vögtle, Pergamon Press, to appear in 1996[4].

Inclusion Phenomena and Supramolecular Chemistry in the 1990's

The collective physicochemical features of supramolecular assemblies are determined by both the properties of the individual components and the interactions between them[2]. Supramolecular engineering gives rise to the controlled generation of polymolecular patterns in molecular layers, films, membranes, micelles, gels, mesophases and solids. In Nature, structures and superstructures at the sub-cellular and cellular levels are created by self-assembly processes. Hence it is not surprising that chemists are looking at supramolecular assemblies as possible models of biological systems[50]. Reichert *et al.*[51] have attempted to mimic biomembrane processes using supramolecular assemblies. Recently Anderson *et al.*[52] reported the construction of model enzymes, based on porphyrins and steroids that are capable of binding, recognition and catalysis.

Inorganic supramolecular materials and composites are becoming accessible through controlled synthesis, employing recognition features and mild reactions. With nanosize structures novel properties may be obtained . Solid-state inorganic materials present tunnels, cages and micropores, whose size and shape may be tailored by the choice of the components. Tetraphenyl porphyrins and their metal complexes act as "sponges", forming programmable lattice clathrates that include selected guest molecules. Recently Burrel *et al.*[53] reported the assembly of an aldehyde-appended tetraphenyl porphyrin which may act as a light harvesting device.

Molecular recognition-directed processes present a powerful entry into supramolecular solid state chemistry and crystal engineering. Crystallisation itself is a good example of molecular recognition. Crystal engineering is defined by Desiraju[54] as the understanding of intermolecular interactions in the context of crystal packing and its utilisation in the design of new solids with desired physical and chemical properties. Recently Toda[55] reviewed solid-to-solid reactions and showed that many traditional reactions, e.g. Baeyer-Villiger oxidation, Grignard, Reformatsky and Wittig-Horner reactions can be successfully carried out in the absence of a solvent.

Classification of Inclusion Compounds

Inclusion compounds, comprising a host and guest component, may be classified into two main groups: (a) Molecular Complexes, where the guest fits into the cavity of a host molecule, and (b) Lattice Clathrates, where the guest fits into the intermolecular spaces created by the packing of the host molecules (shown in Fig 1.1)[56]. Calixarenes[57], cyclodextrins, cyclophanes[58], cryptands and crown ethers[59] are all examples of hosts which form molecular complexes. Lattice clathrates comprise a wide variety of host compounds. In the design of this type of clathrate it has been shown that host molecules should be rigid and bulky, in order to provide suitable cavities in the crystal structure which will accommodate a guest molecule[60].

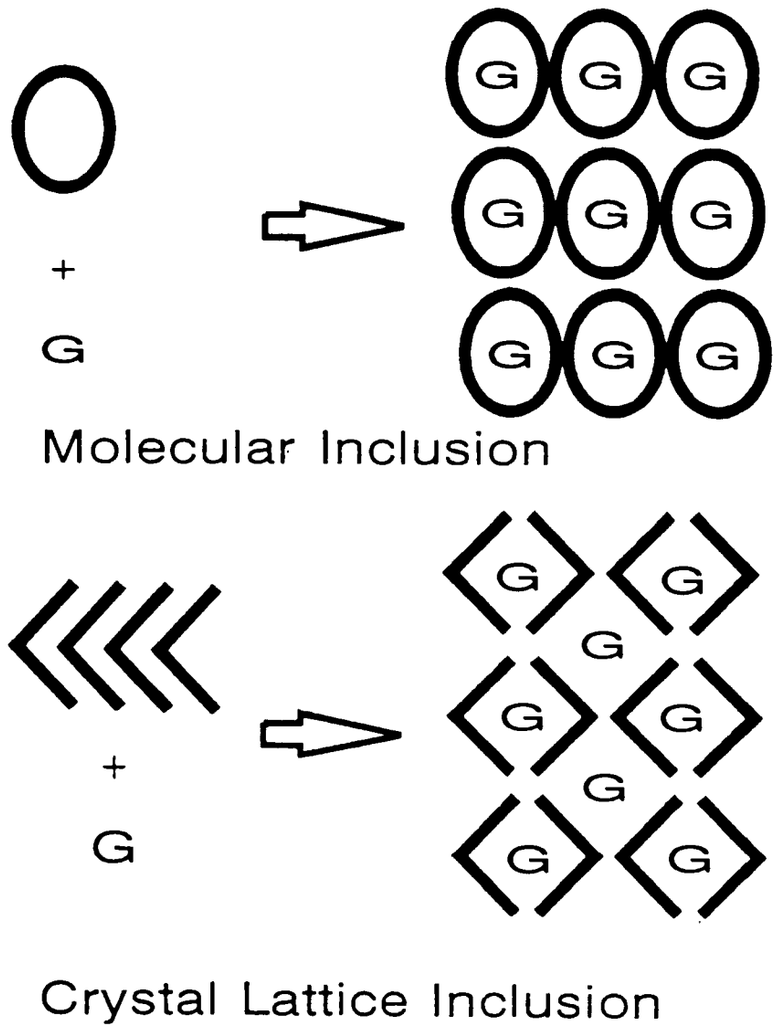

Fig 1.1. The difference between molecular and lattice inclusion.

Weber and Josel[42] suggested a broad classification of inclusion compounds based on (a) the host-guest type and host-guest interaction, (b) the topology of the host-guest aggregate and (c) the number of the various components forming the aggregate. The host-guest interactions and topologies are summarised in Figs 1.2 and 1.3 respectively.

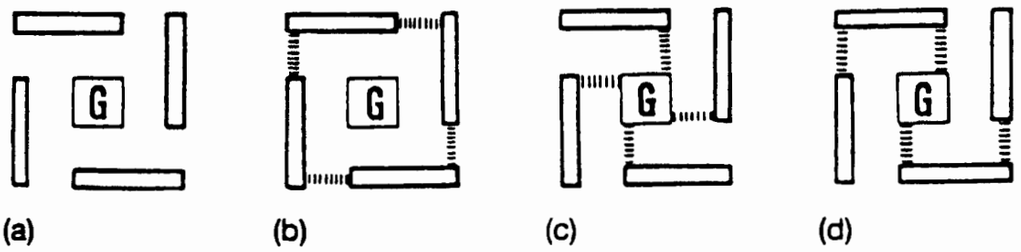

Fig 1.2. Diagrammatic representation of different lattice inclusions. Taken from reference 42.

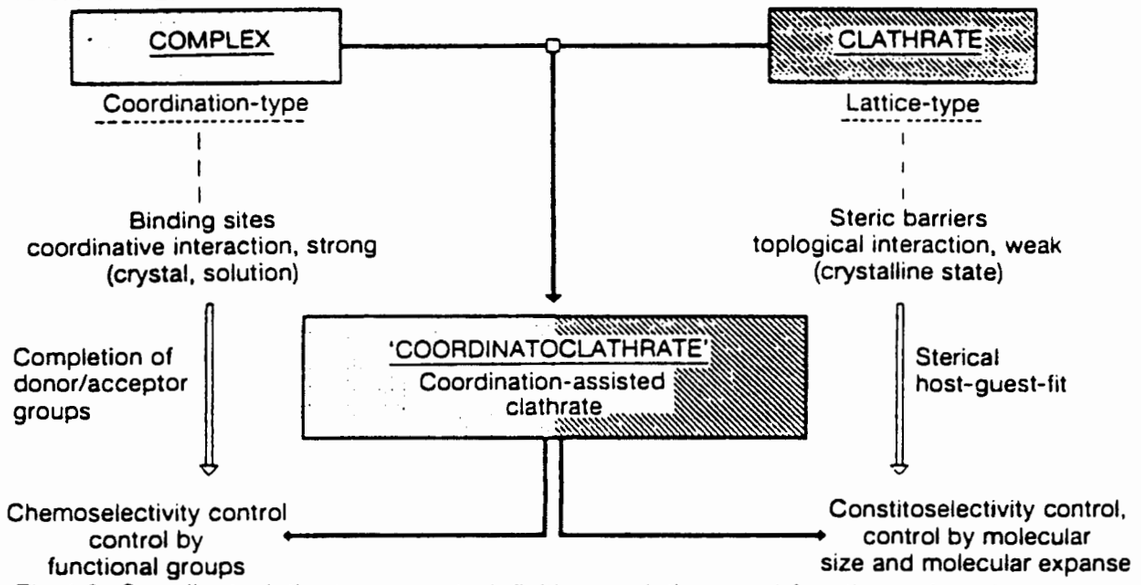

Fig 1.3. Coordinatoclathrate concept: definitions, relations and functions of control. Taken from reference 42.

Herbstein[48] suggested the classification of two component (A and B) systems, based upon the interactions between components. According to this classification A···A interactions would dominate in inclusion compounds. In segregated stack charge transfer complexes A···A and B···B interactions are equally important. All interactions are of equal importance in packing complexes and A···B interactions would dominate in molecular compounds.

Hydroxy Host Compounds

In lattice clathrates the host itself does not possess a central void. These host molecules form crystalline lattices which include guest compounds. It is often useful to incorporate a coordinating moiety in the host molecule, such as a hydrogen bonding donor or acceptor, which will enhance the process of molecular recognition between host and guest, and thus lead to the formation of the desired inclusion compound. In contrast to the classical hydroquinone and Dianin clathrates these new host molecules do not rely on host-host hydrogen bonding interactions only, but coordinative host-guest interactions are often found[56]. This design strategy has recently been reviewed by Desiraju, who has coined the term "supramolecular synthon", and has discussed its use in the process of crystal engineering[61].

Weber[60] summarised the characteristics of a good host compound as follows:
It should:

1. be bulky in constitution to provide low-density packing in the crystal.
2. have a rigid conformation to maintain the cavity structure.
3. have appropriately placed functional groups to achieve specific and strong host-guest interaction.
4. have a balanced shape to help in stabilisation of the crystal packing.

A diagrammatic representation of such a host-guest system is illustrated in Fig 1.4.

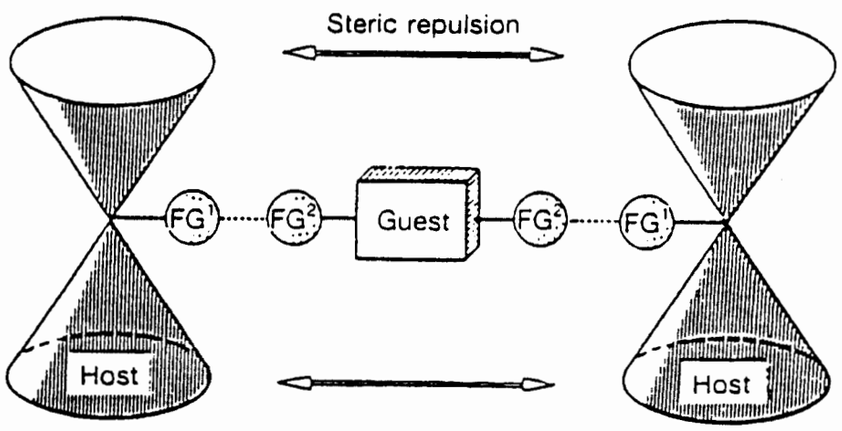

Fig 1.4. Coordinatoclathrate formation. FG=Functional group.
Taken from reference 57.

This strategy has given rise to the design of numerous host compounds which have hydroxy or amide groups, capable of forming hydrogen bonds. Weber *et al.*[60] synthesised a class of host compounds, based on the geometry of a common pair of scissors. These scissor-type host compounds are polar, bulky and have two-fold symmetry (C_2).

Toda *et al.*[62] synthesised the "wheel-and-axle" type hosts in 1968:

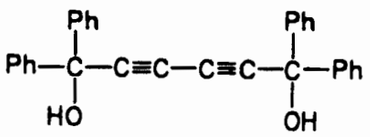

Scheme 1

These acetylenic alcohols form stoichiometric host-guest compounds with a wide variety of guests, capable of hydrogen bonding. Toda[63] found that inclusion is mediated by the formation of hydrogen bonds, and by the surrounding of the guest molecules with phenyl groups, which could allow van der Waals interactions between the host and guest molecules. He also found that the introduction of larger substituents increased the inclusion capability of these hosts.

The concept of molecular recognition is very important in the practical application of inclusion chemistry. If the molecular recognition is specific and the host includes one isomer selectively from a mixture, complexation can be used in the separation of isomers and the isolation of one compound in a pure state. If a chiral host compound recognises the chirality of the guest and includes one enantiomer selectively, inclusion can be used for the optical resolution of the racemic guest compound. Highly selective host compounds can separate different fractions from solution. The separation of ethanol from aqueous solution, obtained from the fermentation of biomass, has important industrial and ecological implications. Host compounds which possess either hydroxy or amide functionalities were found to include a large variety of alcohols and form crystalline inclusion compounds[64].

Physical Chemistry of Inclusion Compounds

Since Powell elucidated the crystal structure of the β-quinol·H_2S clathrate nearly half a century ago, single crystal X-ray analysis has been used extensively in the study of inclusion compounds. X-ray studies provide information on both the host-guest interactions and topologies. Non-bonded host-guest distances and geometries are easily obtained from X-ray analysis. These include weak interactions (e.g. π(arene)···H and C-H···O interactions) as well as strong hydrogen bonding (e.g. N-H···O and O-H···O)[65]. Weak interactions play an important role in molecular assembly in solids and currently a lot of attention is focused on these types of interactions[66]. For example, in complexes of crown ethers containing guests with weakly acidic C-H bonds, e.g. 18-crown-6·$2CH_3CN$, weak C-H···O interactions are the only source of host-guest binding[67]. The extent of host-guest interactions can often be related to the stability of the inclusion compound. The topology of the host framework can be investigated and the crystal structure reveals whether the guests are located in cavities or channels.

The stability of crystalline inclusion compounds can be measured by means of thermal analysis[68]. The guest loss process is often accompanied by a loss in mass, and the host:guest stoichiometry can be measured to a precision of 1% by thermal gravimetry (TG). The guest loss reaction is usually accompanied by an absorption of heat, and this can be detected using differential scanning calorimetry (DSC). The onset temperature (T_{on}) of the desolvation step, measured from DSC, is a reliable measure of the stability of a given inclusion compound. Often the guest release temperature is higher than the normal boiling point (T_b) of the guest. Caira and Nassimbeni[69] have suggested that the ratio of T_{on}/T_b or their difference $T_{on}-T_b$ is a useful parameter for the measurement of the stabilities of inclusion compounds. For example, *trans*-9,10-dihydroxy-9,10-diphenyl-9,10-dihydroanthracene forms an inclusion compound with diethyl ether with T_{on}= 64.2°C, which is 29.8°C above the normal boiling point of diethyl ether[70].

The thermal events measured using TG and DSC can often be related to physical changes in the crystal, observed using optical microscopy. Hot stage microscopy (HSM) is a favoured complementary technique used in the study of the thermal degradation of inclusion compounds. Richardson *et al.*[71] recently described a

system which permits the recording of hot stage observations on videotape with simultaneous DSC measurements. The authors confirmed that visual observations are often more sensitive indicators of phase changes than DSC measurements. Upon guest loss the host often undergoes a phase change from the β-phase of the inclusion compound, to the non-porous α-phase of the pure host compound. Clear crystals become opaque upon guest loss. The loss of guest can also easily be detected by submerging the crystal in an inert liquid (e.g. silicone oil) and observing the evolution of gas bubbles.

Desolvation products can be identified using various qualitative analytical techniques, e.g. evolved gas analysis (EGA) involving mass spectroscopy (MS) has been used successfully to identify the volatile components released by cyclodextrin inclusion compounds[72]. The remaining host decomposition products can be identified using X-ray powder diffraction or infrared spectroscopy (IR or FTIR). Inclusion compounds which release mixed guests can be analysed using gas liquid chromatography (GLC)[73] or MS[74] in order to determine the relative concentrations of the released gases.

Solid State Reaction Kinetics

"If the development of thermal analysis kinetics in the past thirty or so years could be summarised by a single statement it would be that it was the era in which hundreds of cute and clever mathematical manipulations were performed on variations of three (highly stylised) equations:

The rate equation: $d\alpha/dt = f(\alpha)k(T)$ *(1)*

The Arrhenius equation: $k(T) = A\ exp(-E_a/RT)$ *(2)*

The temperature integral: $p(x) = \int_x^\infty (\exp - x)x^{-2}dx$ *(3)*

where $x = E_a/RT$.

...Equations (1) and (2) can be applied to some, but certainly not all, solid state systems. Equation (3) cannot be integrated in closed form and unfortunately, gross and inaccurate approximations for it are used in many of the more popular techniques of kinetic analysis."

J.H. Flynn (1992)[75].

In spite of the various controversies surrounding the validity of solid state kinetics[75,76,77], it has developed tremendously over the past 30 years. This is not intended to be an extensive survey of solid state kinetics. The application of solid state kinetics to the study of inclusion compounds and the validity of the interpretation of reaction mechanisms and the Arrhenius parameters will be dealt with.

Solid State Reactions - Decomposition

The decomposition of a solid is signified by the breakdown of one or more constituents of reactant into simpler atomic groupings[78]. During the generalised decomposition reaction:

$$A_{(s)} \rightarrow B_{(s)} + C_{(g)}$$

gas, and therefore mass, is lost and heat is absorbed.

When an inclusion compound is heated, the guest is often released, and the general decomposition reaction, above, can be rewritten in the form:

$$H{\cdot}G_{n(\beta,s)} \rightarrow H_{(\alpha,s)} + nG_{(g)}$$

The guest loss reaction (desolvation) is generally accompanied by the rearrangement of the crystal structure from the β-phase of the inclusion compound to the non-porous α-phase of the host compound. Alternatively, partial guest loss can occur, and a new, metastable intermediate compound can be formed:

$$H.G_{n(\beta,s)} \rightarrow H.G_{m(\gamma,s)} + (n\text{-}m)G_{(g)}$$

The intermediate compound (γ-phase) could in turn desolvate upon heating to form the non-porous α-phase of the host:

$$H.G_{m(\gamma,s)} \rightarrow H_{(\alpha,s)} + mG_{(g)}$$

Often different polymorphic forms of a host compound exist and the same host compound would not necessarily return to the same α-phase upon desolvation from different inclusion compounds. The different crystalline phases occurring upon guest loss are summarised in Fig 1.5.

The reactivity and chemical properties of solids are influenced by the relative immobility of the constituent ions or molecules. The main distinguishing features of solids are that the chemical transformation takes place in a restricted zone of the solid and in cases where there is more than one reactant, the solid products may constitute a barrier layer which tends to oppose further reaction. Kinetic characteristics are determined by the velocity of advance of the reaction interface[78]. Solid state reactions occur predominantly at reaction interfaces which advance into the unchanged reactant[79]. Grain size plays an important role in the rate of solid state reactions. Often the reaction rate increases with decreasing grain size of the solid[80].

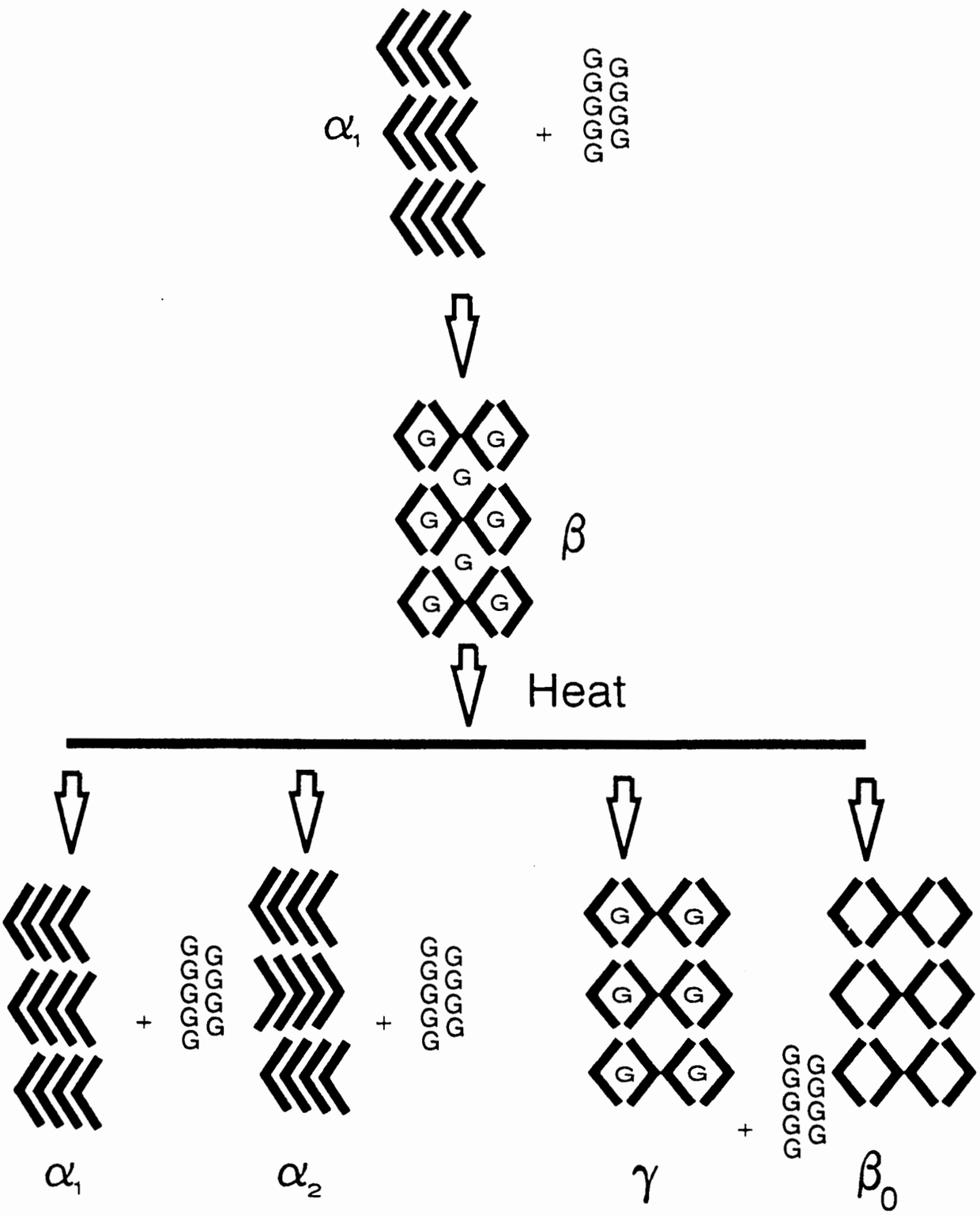

Fig 1.5. Desolvation possibilities of inclusion compounds upon heating.

Homogeneous Kinetics

The reaction rate of a homogeneous reaction of the type:

$$A \rightarrow B + C$$

can be measured by following the change in concentration of either the reactants or products. The rate of reaction is a function of these changing concentrations and a rate equation of the form:

$$Rate = k\,f(conc.\ of\ reactants\ or\ products)$$

can be determined experimentally, at a constant temperature. The rate coefficient k is a function of temperature. By repeating the experiment at various temperatures, the Arrhenius equation:

$$\ln k = -E_a/RT + \ln A \qquad (or\ k = A\exp(-E_a/RT))$$

can be used to determine the activation energy (E_a) and the pre-exponential or frequency factor (A) for the reaction.

Heterogeneous Kinetics

The assumption is made that solid state reactions are activated processes and consequently the kinetics are usually described using the Arrhenius equation, developed for homogeneous reactions[90]. In the case of heterogeneous reactions the concept of concentration no longer has the same significance and the progress of the reaction has to be measured in a different way[81]. Depending on the changes taking place upon decomposition, the extent of reaction (α) can be measured using a variety of techniques, such as TG, DSC, X-ray powder diffraction or infrared spectroscopy[82]. Thermogravimetry is often favoured[78], since the decomposition of solids regularly involves the loss of a gaseous product, resulting in a reduction in sample mass.

The classical method of measuring reaction kinetics as a function of mass loss is the use of isothermal thermogravimetry (TG)[83]. The discussion of kinetic measurements will be limited to that of isothermal TG. This was chosen as the preferred method of analysis, since it does not involve the "infamous" temperature integral[75]. Various methods have been derived to analyse the kinetics of rising temperature experiments. This includes differential[84] as well as integral[81] methods.

The fraction decomposed (α) can be calculated from the mass loss:

$$\alpha = \frac{m_0 - m_t}{m_0 - m_f}$$

where m_0 is the initial mass of the sample, m_t is the mass at any time t and m_f is the final mass, after decomposition. Often the reverse reaction:

$H_{(s)} + nG_{(g)} \rightarrow H{\cdot}G_{n(s)}$

can be studied. The same principles can be used to study the kinetics of the sorption reaction, but α is now defined as:

$$\alpha = \frac{m_t - m_0}{m_f - m_0}$$

The extent of reaction (α) is plotted against time for a variety of different temperatures. From the α *vs.* time curves the reaction mechanism can be evaluated and the specific rate constant k can be determined for each temperature. Fig 1.6. contains a generalised α *vs.* time curve summarising characteristic behaviour observed for isothermal decompositions of solids. The α *vs.* time curve can be divided into the following sections:

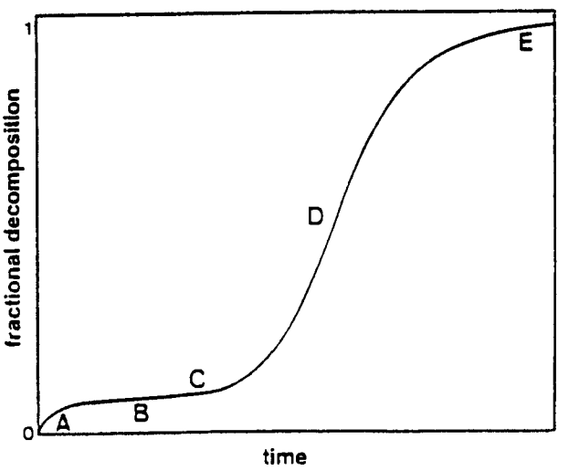

A: initial reaction, often decomposition of impurities or unstable superficial material

B: induction period (due to nucleation)

C: acceleratory period of growth

D: maximum rate of reaction

E: decay period

F: completion

Fig. 1.6. Generalised α-time plot summarising characteristic behaviour for the isothermal decomposition of solids. Taken from reference 78.

In practice, different types of kinetic behaviour are observed, and some of these features may be absent.

Kinetic Models and Interpretations

It is important to note that kinetic features are pathway dependent, and hence the pre-history of the sample has to be known[85]. Kinetic models and hence mathematical relationships have been established between α and the time of heat treatment. Most of the kinetic models for decomposition are based on the appearance of nuclei and the result of their subsequent growth via a reaction interface. Nucleation is the process by which the reaction interface is initially established[86]. Usually the nucleation takes place at the particle surface or at an imperfection. Initially a few "germ nuclei" are established. These are very unstable due to the high ratio of surface strain to volume. Some of these may develop into "growth nuclei" which increase in size through advance of the reactant-product interface into the bulk of the crystallite so reducing the relative importance of the surface strain term[78]. Subsequent growth then reflects the geometry of the contracting area of interface often imposed by the original shape and surface of the decomposing particles. This is illustrated in Fig 1.7.

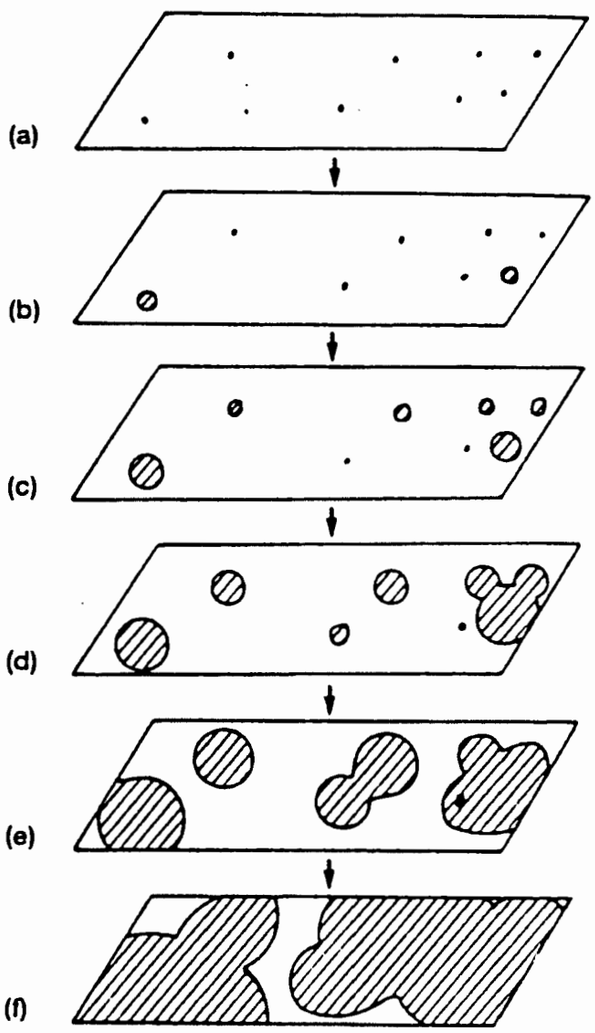

Fig 1.7. Formation and growth of nuclei of product in the decomposition of solids. a) nucleation sites; b) first nuclei formed; c) growth and further nucleation; d) overlap of nuclei; e) ingestion of nucleation sites; f) continued growth. Taken from reference 81.

The shapes of α-time curves are sensitive to the relative ease with which nucleation takes place. Where many product particles are formed rapidly at the onset of a reaction, the rate process is deceleratory throughout, whereas the slow development of a restricted number of nuclei results in a sigmoidal α-time relationship.

The α-time curves can be broadly divided into three groups: acceleratory (α-time curves consisting mainly of section C in Fig 1.6.), deceleratory (corresponding to α-time curves consisting mainly of section E and F in Fig 1.6.) and sigmoidal (sections B through F exist in the α-time curves). The solid state rate expressions are summarised in Table 1.1. The kinetic models based upon nucleation and growth describe the sigmoidal α-time curves. The Avrami-Erofe'ev equations were developed to describe the sigmoidal curves, according to one-, two- and three-dimensional growth of the reaction interface (A1, A2 and A3 respectively)[87,88]. The Prout-Tompkins (B1) model was developed for symmetrically shaped sigmoidal curves, and has found application to many systems[89]. Later studies explored the effect of the additional process of diffusion of species away from or toward the reaction interface, and gave rise to a set of rate expressions based on diffusion mechanisms (D1-D4)[81]. In a diffusion limited reaction the overall rate is determined by the movement of product away from or reactant towards a reaction interface. These kinetic models were largely developed for gas-solid interactions. Other rate expressions are based on simpler geometrical models (R2 and R3)[92]. These models consider the two- or three dimensional growth of the product interface on cylindrical or spherical particles, respectively. Another group of rate equations describing deceleratory α-time curves is based on the apparent "order" of reaction, being analogous to the homogeneous rate laws. The "order" of these reactions does not have the same significance as in homogeneous reactions. The first order reaction is based on the mechanism of random nucleation, followed by unimolecular decay[90].

Table 1.1. Broad classification of solid state rate expressions

	$f(\alpha)=kt$	$g(\alpha)=\frac{1}{k}\frac{d\alpha}{dt}$
1. Acceleratory		
P1 power law	$\alpha^{1/n}$	$n(\alpha)^{(n-1)/n}$
E1 exponential law	$\ln \alpha$	α
2. Sigmoidal		
A2 Avrami-Erofe'ev	$[-\ln(1-\alpha)]^{1/2}$	$2(1-\alpha)[-\ln(1-\alpha)]^{1/2}$
A3 Avrami-Erofe'ev	$[-\ln(1-\alpha)]^{1/3}$	$3(1-\alpha)[-\ln(1-\alpha)]^{2/3}$
A4 Avrami-Erofe'ev	$[-\ln(1-\alpha)]^{1/4}$	$4(1-\alpha)[-\ln(1-\alpha)]^{3/4}$
B1 Prout-Tompkins	$\ln[\alpha/(1-\alpha)]$	$\alpha(1-\alpha)$
3. Deceleratory		
Geometrical models		
R2 contracting area	$1-(1-\alpha)^{1/2}$	$2(1-\alpha)^{1/2}$
R3 contracting sphere	$1-(1-\alpha)^{1/3}$	$3(1-\alpha)^{2/3}$
Diffusion controlled models		
D1 one-dimensional	α^2	$1/2\alpha$
D2 two-dimensional	$(1-\alpha)\ln(1-\alpha)+\alpha$	$[-\ln(1-\alpha)]^{-1}$
D3 three-dimensional	$[1-(1-\alpha)^{1/3}]^2$	$3(1-\alpha)^{2/3}/2[(1-\alpha)^{1/3}]$
D4 Ginstling-Brounshtein	$(1-2\alpha/3)-(1-\alpha)^{2/3}$	$3/2[(1-\alpha)^{-1/3}-1]$
"order" of reaction		
F1 first order	$-\ln(1-\alpha)$	$1-\alpha$
F2 second order	$1/(1-\alpha)$	$(1-\alpha)^2$
F3 third order	$[1/(1-\alpha)]^2$	$(1-\alpha)^3$
Fn n-th order	$[1/(1-\alpha)]^n$	$(1-\alpha)^n$

All the above rate expressions can be summarised into the combined equation[104]:

$$\frac{d\alpha}{dt} = k \bullet \alpha^m \bullet (1-\alpha)^n \bullet (-\ln(1-\alpha))^p$$

Specific mathematical relationships have been associated with particular models, but one should be cautious when giving physical interpretations to kinetic models, since the same model can give rise to various mathematical relationships[83]. For example, if we have cylindrically shaped particles, of which the area contracts during decomposition the reaction rate can be expressed by:

$$kt=1-(1-\alpha)^{1/2}$$

but if the particles are large, a first order relationship develops

$$\frac{d\alpha}{dt} = k(1-\alpha)$$

The same is true for the contracting sphere model. As the particle size diminishes, the model depicts initially a zero order, then a first order relationship and finally a contracting area or contracting volume equation[83]. Here we have the same model giving rise to two or three mathematical expressions. The converse is also true. A zero order reaction (i.e. constant rate of decomposition) can give rise to a variety of reaction models[78], for example: Zero-order kinetic behaviour can be accounted for by any of the following reaction models.

1. The rate-controlling step is desorption at existing (immobile) crystal surfaces[91], e.g. dehydration of $UO_2(NO_3).6H_2O$.
2. The rapid formation of a small number of nuclei on a lath-shaped reactant, followed by one-dimensional growth, e.g. the reaction of hexammine nickel per-chlorate with water vapour (see Fig 1.8.a)[78].
3. Rapid and complete nucleation of all surfaces of the reactant, in the form of thin plates (see Fig 1.8.b)[78].
4. Rapid formation of product, simultaneously along the axis and over the curved surface of a cylindrical reactant particle, e.g. decomposition of cobalt oxalate[92] (see Fig 1.8.c).
5. Rapid and dense nucleation at equidistant planes perpendicular to longer axes of plate-like crystals, e.g. decomposition of nickel malonate (see Fig 1.8.d)[78].

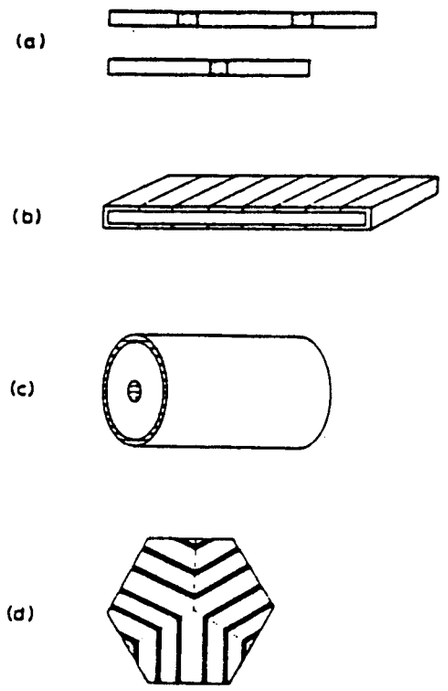

Fig 1.8. Various dispositions of reaction interface which result in obedience to the zero-order kinetic equation. Taken from reference 78.

The demonstration that a given set of α-time data obeys a particular kinetic expression does not constitute absolute proof of the operation of the reaction mechanism from which that rate equation was derived. Geometric interpretations should always be supported by independent evidence[83]. Often it is difficult to distinguish between two or more kinetic models when attempting to fit a rate law to an experimental α-time curve. Dollimore *et al.*[93] suggested that an investigation of the shape of the differential thermal gravimetric curve (DTG) may be useful in distinguishing between similar rate equations.

Meaning of the Arrhenius Parameters

The kinetic models developed for solid state reactions only reflect physical processes, e.g. nucleation, crystallisation, diffusion or changes in surface area, and do not take the chemical nature of these processes into account[94]. The activation energy (E_a) is defined as the energy barrier which must be surmounted to transform reactants into products during the rate limiting step[78]. This definition implies the existence of an activated complex, analogous to that observed in homogenous

reactions. Large variations in values of E_a obtained by different workers led Garn[95] to conclude that there can be no "uniquely describable activated state". Laidler[96] stated that the activation energy of a solid state reaction does not have the same significance as in homogeneous reaction kinetics. This is still a highly controversial subject, with Mulokozi[97] stating that these variations are often consequences of experimental, physical conditions that can be accounted for, and that the concept of the energy barrier is therefore still applicable in heterogeneous kinetics. Most authors[78-85] are cautious in assigning physical meaning to the Arrhenius parameters, and refer to them as "apparent kinetic parameters", preferring to treat them as having empirical rather than theoretical meaning.

The pre-exponential, or frequency factor (A) is associated with frequency of occurrence of reaction configuration. This was initially identified as a molecular encounter (collision) and later as a specific vibration in the reaction coordinate. Since no collisions occur in solids, there is a need to provide an alternative theoretical basis for A. It is usually quoted as an empirical, rather than theoretical value[78].

The meaning of kinetic parameters is determined by the logic of model derivation[98]. Measured magnitudes of A and E_a will depend on the form of rate expression used to determine the reaction rate coefficient (k)[78]. The magnitude of the measured value of E_a, is relatively insensitive to the particular rate expression used to determine k, as long as k values are expressed in the same units.

Galwey[99] surveyed over 400 kinetic studies on solid compounds and concluded that there is no characteristic magnitude for *A* for solid state reactions. This emphasises the difficulties inherent in the meaningful determination of the significance of *A*. He suggests that values of E_a are usually accurate to better than 10%. Pre-exponential factors are inevitably less reliable. Uncertainties in *ln A* arising from those inherent in E_a are estimated to be 0.7-1.0 unit in *ln A*. It is more difficult to assess contributions arising from the calculation method used, but it is estimated that *ln A* is generally accurate to 1.5 units.

The Compensation Effect

The compensation effect occurs in a group of related reactions, for which the influence of changes in A on reaction rate is accompanied by a change in E_a:

$$\ln A = B E_a + C$$

where B and C are constants. The compensation effect has been observed in both homogeneous and heterogeneous rate processes. Attempts have been made to give physical meaning to the parameters B and C in the compensation equation. Zsako *et al.*[100] suggest that B characterises the strength of the bond being broken when gaseous products are formed. They suggest that a decrease in the value of B, would imply an increase in the strength of the bond to be broken. Parameter C is proposed to be related to the structure of, and defects in, the starting material or to the mobility of the constituents of the crystal[101].

In spite of the fact that several theoretical explanations have been presented for the occurrence of the compensation effect, many researchers consider it as an empirical observation, while others are sceptical as to its existence[102]. In a review, Galwey[103] concluded that no simple theoretical explanation for the compensation effect has been recognised as having general application.

Aims and Objectives of this Thesis

The literature contains relatively few quantitative correlations between the detailed crystal structure and the solid phase reactivities of compounds[78]. This study will attempt to relate the crystal structures and reactivities of a few selected host-guest inclusion compounds. The study of reactions can be divided into three steps[104]:

1. Stages, intermediates and products of reaction
2. Energetics of reaction stages
3. Reaction mechanism and reaction kinetics.

This study is mainly concerned with the first and third points, relating to reactions of inclusion compounds. The crystal structures of the inclusion compounds under investigation were elucidated and their physico-chemical properties have been studied. The stages, intermediates and products of their decomposition have been isolated and identified. The kinetics of the decomposition and formation of inclusion compounds have been investigated.

Diol host compounds were chosen, in this study, to enhance the possibility of host-guest interactions. The host compounds under investigation, belong to 3 different classes (see Scheme 2). The host compounds in Class **A** (hosts **A1**, **A2** and **A3**) are scissor-shaped. The host compounds in this class are 2,2'-bis (2,7-dichloro-9-hydroxy-9-fluorenyl) biphenyl (host **A1**), 2,2'-bis (2,7-dibromo-9-hydroxy-9-fluorenyl) biphenyl (host **A2**) and 2,2'-bis (2,7-di-*tert*-butyl-9-hydroxy-9-fluorenyl) biphenyl (host **A3**). The hosts in Class **B** are structurally modified dihydroanthracenes. These compounds are *trans*-9,10-dihydroxy-9,10-diphenyl-9,10-dihydroanthracene (host **B1**), *trans*-9,10-dihydroxy-9,10-di-α-naphthyl-9,10-dihydroanthracene (host **B2**) and *trans*-9,10-dihydroxy-9,10-di-*p*-*tert*-butylphenyl-9,10-dihydroanthracene (host **B3**). The host compound in Class **C**, 2,2'-bis(diphenylhydroxymethyl)-1,1'-biphenyl, is similar to the host compounds in Class **A**, but is rendered conformationally more flexible. The guest compounds are all relatively volatile common organic solvents. Some of the guest compounds possess hydrogen bond receptors, while others are purely hydrophobic. The inclusion compounds have been designed with similar guests, in order to compare their kinetic behaviour.

Scheme 2

CLASS A

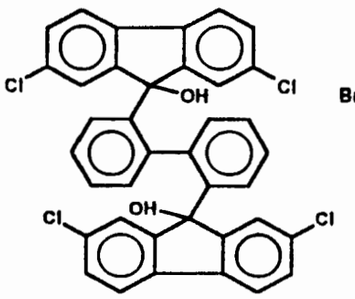

Host **A1**

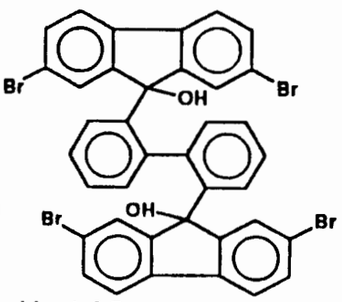

Host **A2**

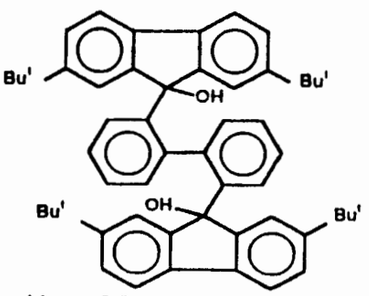

Host **A3**

CLASS B

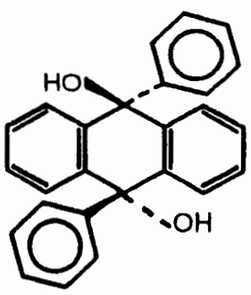

Host **B1**

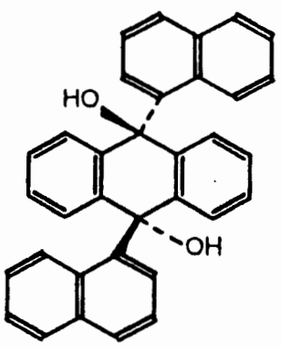

Host **B2**

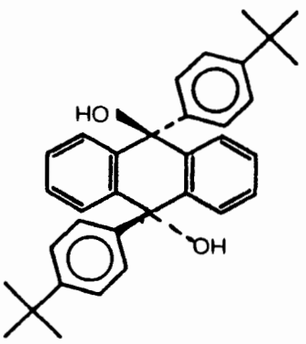

Host **B3**

CLASS C

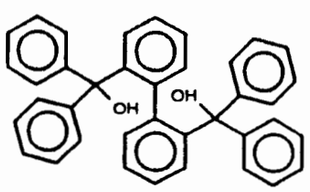

1 H. Davy, *Trans. R. Soc. London.*, **101**, 1811, 1.

2 J.-M. Lehn, *Supramolecular Chemistry - Concepts and Perspectives*, VCH, Weinheim, 1995, 4.

3 J.L. Atwood, J.E.D. Davies and D.D. MacNicol (eds.), *Inclusion Compounds*, Vol. 1-5, Academic Press, London, 1984.

4 J.L. Atwood, J.E.D. Davies, D.D. MacNicol and F. Vögtle (exec. eds.), *Comprehensive Supramolecular Chemistry*, Vol. 1-11, Pergamon Press, to be published, 1996.

5 M. Faraday, *Quart. J. Sci.*, **15**, 1823, 71.

6 A. Damour, *Ann. Mines.*, **17**, 1840, 191.

7 C. Schafthäult, *J. Pract. Chem.*, **21**, 1841, 129.

8 F. Wohler, *Ann. Chem. Liebigs*, **69**, 1849, 297.

9 A. Villiers, *C. R. Hebd. Sceances Acad. Sci.*, **112**, 1891, 536.

10 S.U. Pickering, *J. Chem. Soc. London Trans.*, **63**, 1893, 141.

11 E. Fischer, *Ber. Deutsch. Chem. Ges.*, **27**, 1894, 2985.

12 J. Lima de Faria (ed.), *Historical Atlas of Crystallography*, Kluwer Academic Publishers, Dordrecht, 1990, 8.

13 K.A. Hofman and F. Küspert, *Z. Anorg. Allg. Chem.*, **15**, 1897, 204.

14 K.A. Hofman and F. Höchtlen, *Chem. Ber.*, **36**, 1903, 1149.

15 H. Hartley and N.G. Thomas, *J. Chem. Soc.*, 1906, 1013.

16 R. Spallino and G. Provenzal, *Gazz. Chim. Ital.*, **39**, 1909, 325.

17 A.P. Dianin, *J. Soc. Phys. Chem. Russe*, **46**, 1914, 1310.

18 H. Wieland and H. Sorge, *Z. Physical Chem. Hoppe-Seyler's*, **97**, 1916, 1.

19 E.G. Hammerschmidt, *Ind. Eng. Chem.*, **26**, 1934, 851.

20 J.W. McBain, *The Sorption of Gases and Vapours by Solids*, Routledge and Sons, 1932, Chapter 5.

21 E. Terres and W. Vollmer, *Z. Petroleum*, **31**, 1935, 1.

22 O. Kratky and G. Giacomello, *Monatsh. Chem.*, **69**, 1936, 427.

23 M.F. Bengen, *German Patent Application*, OZ123438, March 18, 1940.

24 F.F. Mikus, R.M. Hixon and R.E. Rundle, *J. Am. Chem. Soc.*, **63**, 1946, 1115.

25 D.E. Palin and H.M. Powell, *J. Chem. Soc.*, 1947, 208.

26 H.M. Powell, *J. Chem. Soc.*, 1948, 61.

27 D.J. Cram and H. Steinberg, *J. Am. Chem. Soc.*, **73**, 1951, 5691.

28 M. Von Stackelberg and H.R. Müller, *J. Chem. Phys.*, **19**, 1951, 1319.

29 W.F. Claussen, *J. Chem. Phys.*, **19**, 1951, 259.

30 L. Pauling and R.E. Marsh, *Proc. Natl. Acad. Sci. USA*, **38**, 1952, 112.

31 W.D. Schaeffer, W.S. Dorsey, D.A. Skinner and C.G. Christian, *J. Am. Chem. Soc.* **79**, 1957, 5870.

32 *Non Stoichiometric Compounds* ed. L. Mandelcorn, Academic Press, New York, 1964.

33 C.J. Pederson, *J. Am. Chem. Soc.*, **89**, 1967, 7071.

34 J.L. Atwood, P.A. Milton and S.K. Seale, *J. Organomet. Chem.*, **28**, 1971, C29.

35 B. Dietrich, J.-M. Lehn and J.-P. Sauvage, *Tetrahedron Lett.*, 1969, 2885.

36 R.J. Argauer and G.R. Landolt, US Patent, 3, 702, 886 1972.

37 D.J. Cram and J.M. Cram, *Science*, 1974, **183**, 803.

38 D.D. MacNicol and D.R. Wilson, *J. Chem. Soc. Chem. Comm.*, 1976, 494.

39 J.-M. Lehn, *Pure Appl. Chem.*, **50**, 1978, 871.

40 G.D. Andreetti, R. Ungaro and A. Pochini, *J. Chem. Soc. Chem. Comm.*, 1979, 1005.

41 J. Lipkowski, *Accademia Polacca delle Scienze, Biblioteca e centro di studi a Roma, Conferenze,* **81**, 1980.

42 E. Weber and H.-P. Josel, *J. Incl. Phenom.*, **1**, 1983, 79.

43 B.L. Allwood, N. Spencer, H. Shairiari-Zavarech, J.F. Stoddart and D.J. Williams, *J. Chem. Soc. Chem. Commun.*, 1987, 1064.

44 D.J. Cram, *Angew. Chem. Int. Ed. Engl.*, **27**, 1988, 1009.

45 J.-M. Lehn, *Angew. Chem. Int. Ed. Engl.*, **27**, 1988, 90.

46 C.J. Pederson, *Angew. Chem. Int. Ed. Engl.*, **27**, 1988, 1021.

47 *Supramolecular Chemistry*, Vol **1**, No 1, 1992.

48 F.H. Herbstein, *Acta Chim. Hung.*, **130**(3-4), 1993, 377.

49 *Supramolecular Science*, **1**, 1994.

50 V. Balzani and L. de Cola, *Supramolecular Chemistry*, Kluwer Academic Publishers, Dordrecht, 1992, 1.

51 A. Reichert, H. Ringsdorf and A. Wagenknecht, in *Supramolecular Chemistry*, V. Balzani and L. de Cola (eds.) Kluwer Academic Publishers, Dordrecht, 1992, 325.

52 H.L. Anderson, R.P. Bonar-Law, L.G. Mackay, S. Nicholson and J.K.M. Sanders, in *Supramolecular Chemistry*, V. Balzani and L de Cola (eds.) Kluwer Academic Publishers, Dordrecht, 1992, 359.

53 A.K Burrel, D.L. Officer and D.C.W. Reid, *Angew. Chem. Int. Ed. Engl.*, **34**(8), 1995, 900.

54 G.R. Desiraju, *Crystal Engineering: The Design Of Organic Solids*, Elsevier, Amsterdam, 1989, 2.

55 F. Toda, in *Reactivity in Molecular Crystals*, ed. Y. Ohashi, VHC, Weinheim, 1993, 177.

56 F. Vögtle, *Supramolecular Chemistry*, Wiley, 1991, 172.

57 C.D. Gutsche, *Calixarenes*, The Royal Society of Chemistry, Cambridge, 1989.

58 F. Diederich, *Cyclophanes*, The Royal Society of Chemistry, Cambridge, 1991.

59 G. Gokel, *Crown Ethers and Cryptands*, The Royal Society of Chemistry, Cambridge, 1991.

60 E. Weber, in *Inclusion Compounds*, vol. 4, eds J.L. Atwood, J.E.D. Davies and D.D. MacNicol, Oxford University Press, 1991, 188.

61 G.R. Desiraju, *Angew. Chem. Int. Ed. Engl.*, **34**, 1995, 2311.

62 F. Toda and K. Akagi, *Tetrahedron Lett.*, 1968, 3695.

63 F. Toda, in *Inclusion Compounds*, J.L. Atwood, J.E.D. Davies and D.D. MacNicol (eds.), Vol. 4, Oxford University Press, London (1991), 126.

64 F. Toda, K. Tanaka and T.C.W. Mak, *Chem. Lett.*, 1983, 1699.

65 R. Taylor, O. Kennard and W. Versichel, *Acta Crystallogr.*, **B40**, 1984, 280.

66 J. Bernstein, M.C. Etter and L. Leiserowitz, in *Structure Correlation*, Chapt. 11, Vol. 2, eds H.-B. Bürgi and J.D. Dunitz, VCH, Weinheim, 1994.

67 R.D. Rogers, P.D. Richards and E.J. Voss, *J. Incl. Phenom.*, **6**, 1988, 65.

68 A. Sopková, P. Mondok and M. Reháková, *ICTAC News*, Dec. 1995, 112.

69 M.R. Caira , L.R. Nassimbeni, M.L. Niven, W.-D. Schubert and E. Weber, *J. Chem. Soc. Perkin Trans 2*, 1990, 2129.

70 L.J. Barbour, M.R. Caira and L.R. Nassimbeni, *J. Chem. Soc. Perkin Trans. 2*, 1993, 1413.

71 M.F. Richardson, Q.-C. Yang, E. Novotny-Bregger and J.D. Dunitz, *Acta Crystallogr.*, **B46**, 1990, 653.

72 J. Szejtli, "Cyclodextrin Technology", *Topics in Inclusion Science*, ed. J.E.D. Davies, Kluwer Academic publishers, Dordrecht, 1988, 94.

73 M.R. Caira, A. Horne, L.R. Nassimbeni, K. Okuda and F. Toda, *J. Chem. Soc. Perkin Trans. 2*, 1995, 1063.

74 J. Chiu and A.J. Beattie, *Thermochim. Acta*, **50**, 1981, 49.

75 J.H. Flynn, *Thermochim. Acta*, **203**, 1992, 519.

76 W. Gomes, *Nature*, **192**, 1961, 865.

77 H. Anderson, *Thermochim. Acta*, **203**, 1992, 515.

78 C.H. Bamford and C.F.H. Tipper (eds), *Comprehensive Chemical Kinetics* (Vol 22), Elsevier, Amsterdam, 1980.

79 A.K. Galwey, *J. Therm. Anal.*, **41**, 1994, 267.

80 J. Pysiak, *J. Therm. Anal.*, **43**, 1995, 9.

81 M.E. Brown, *Introduction To Thermal Analysis - Techniques And Applications*, Chapmann and Hall, London, 1988.

82 G. Pannetier and P. Souchay, *Chemical Kinetics*, Elsevier, Amsterdam, 1964.

83 D.Dollimore in *Thermal Analysis-Techniques and Applications*, eds. E.L. Charsley and S.B. Warrington.

84 W.W.M. Wendlandt, *Thermal Analysis*, John Wiley and Sons, New York, 1964.

85 D. Dollimore, *Thermochim. Acta*, **203**, 1992, 7.

86 H. Eyring, S.H. Lin and S.M. Lin, *Basic Chemical Kinetics*, Wiley & son, New York, 1980, 435.

87 M. Avrami, *J. Chem. Phys.*, **7**, 1939, 1103.

88 B.V. Erofe'ev, *C.R. Dokl. Acad. Sci. URSS*, **52**, 1946, 511.

89 E.G. Prout and F.C. Tompkins, *Trans. Faraday Soc.*, **40**, 1944, 488.

90 J.M. Craido and A. Ortega, *Thermochim. Acta*, **239**,1994,1.

91 M.L. Franklin and T.B. Flanagan, *J. Chem. Soc. Dalton Trans.*, 1972, 192.

92 D. Broadbent, D. Dollimore and J. Dollimore, *J. Chem. Soc. A*, 1966, 1491.

93 D. Dollimore, T.A. Evans, Y.F. Lee and F.W. Wilburn, *Thermochim. Acta*, **198**, 1992, 249.

94 J. Blazejowski, J. Rak and M. Gutowski, *J. Therm. Anal.*, **43**, 1995, 45.

95 P.D. Garn, *J. Therm. Anal.*, **13**, 1978, 581.

96 K.J. Laidler, *Chemical Kinetics 2nd ed.*, McGraw-Hill, New York, 1965.

97 A. M. Mulokizi, *Thermochim. Acta*, **197**, 1992, 363.

98 A. Korobov, *J. Therm. Anal.*, **44**, 1995, 187.

99 A.K. Galwey, *Thermochim. Acta*, **242**, 1994, 259.

100 J. Zsako, Cs. Varhelyi and K. Szilagyi, *J. Therm. Anal.*, **7**, 1975, 41.

101 A.I. Lesnikovich and V.A. Levchik, *J. Therm. Anal.*, **30**, 1985, 677.

102 M.P. Suáres, A. Palermo and C.M. Aldao, *J. Therm. Anal.*, **41**, 1994, 807.

103 A.K. Galwey, *Catal. Rev.*, **26**, 1977, 247.

104 P.J. Haines, *Thermal Methods of Analysis*, Chapman and Hall, 1995, London, 31.

CHAPTER 2 EXPERIMENTAL

Host Compounds

Class A

The host compounds 2,2'-bis (2,7-dichloro-9-hydroxy-9-fluorenyl) biphenyl (host **A1**), 2,2'-bis (2,7-dibromo-9-hydroxy-9-fluorenyl) biphenyl (host **A2**) and 2,2'-bis (2,7-di-*tert*-butyl-9-hydroxy-9-fluorenyl) biphenyl (host **A3**) were synthesised[14] and supplied by Prof. Edwin Weber of the Technische Universität Bergakademie Freiberg, Germany. Host **A1** (R=Cl) was recrystallised from 1,4-dioxane, host **A2** (R=Br) was recrystallised from chloroform and host **A3** (R=*tert*-butyl) was recrystallised from acetone. All three hosts formed inclusion compounds with the respective solvents and had to be dried under vacuum until all the solvent was lost, and the host structure had returned to the non-porous α-phase.

Class B

The compound *trans*-9,10-dihydroxy-9,10-diphenyl-9,10-dihydroanthracene was first synthesised in 1904, by Haller and Guyot[15]. Since then the syntheses of various other 9,10-substituted anthracenediols have been reported[16,17,18]. The host compounds in class **B** were synthesised using the Grignard method with anthraquinone as starting material[19]. The Grignard reagents were prepared from the appropriate aryl bromide (ArBr) compounds where Ar= phenyl (**B1**), α-naphthyl (**B2**) or 4-*tert*-butylphenyl (**B3**).

Methodology: A solution of 100 mmol ArBr was prepared in 30 ml dry diethyl ether. An initial volume of 5 ml of this solution was added to a hot mixture of 2.4 g (98.7 mmol) of magnesium in 10 ml diethyl ether. Once the reaction had commenced, the remainder of the solution was added dropwise. The reaction mixture was refluxed for two hours. The resulting Grignard reagent was then added dropwise to a stirred and heated suspension of 4 g (19.2 mmol) of anthraquinone (recrystallised from acial acetic acid) in 100 ml diethyl ether. The reaction was allowed to continue under reflux for approximately 20 hours. The reaction mixture was cooled on ice

and acidified to a pH of approximately 2, using 2.5 M HCl. The resulting grey-green precipitate was heated in 500 ml acetone, and filtered. The filtrate was reduced to approximately 400 ml, and cooled on ice in order to facilitate the precipitation of the product. The product was repeatedly recrystallised from acetone until pure.

Inclusion compounds with acetone were formed by all the related hosts, and the compounds had to be dried under vacuum at 60°C until all the solvent was lost, and the host structure had collapsed to the non-porous α-phase.

Class C

Host compound **C**, 2,2'bis(diphenylhydroxymethyl)-1,1'-biphenyl, was synthesised[7] and supplied by Prof. Fumio Toda of Ehime University in Matsuyama, Japan. The host compound was of sufficient purity when obtained and was not recrystallised.

Inclusion Compounds

All solvents were bought from Aldrich and dried over molecular sieves. The inclusion compounds were obtained by dissolving the appropriate host compound in an excess of the solvent to be included. In the case of **TODBEN1** and **TODOXLT** water was included from the atmosphere. A polymorph of the non-porous α-phase of host **A1** (**WCL**) was crystallised from 1,3,6-trimethylbenzene. The inclusion compounds formed, and the host:guest ratios obtained from thermogravimetry (TG) are summarised in Table 2.1. The TG mass losses were measured with an accuracy of 1%.

Table 2.1. Inclusion compounds.

Host	Guest	H:G	Code name
Class A			
A1	1,4-dioxane	2:7	**W17DIA**
R=Cl	1,3-dioxane	1:2	**W13DT**
	1,3-dioxolane	1:2	**W17**
	acetone	1:2	**WC17AC**
	-	-	**WCL**
A2	1,4-dioxane	2:7	**W17DB**
R=Br	1,3-dioxolane	1:2	**WB3DA**
	acetone	1:2	**WB17AC**
A3	1,4-dioxane	1:1	**WTB14D**
R=*tert*-butyl	acetone	1:1	**WTBAC**
Class B			
B1	1,3-dioxolane	1:1	**DP13D**
R= phenyl			
B2	1,3-dioxolane	1:2	**DN13D**
R= α-naphthyl	benzene	1:1	**DNBz**
B3	methanol	1:2	**DTBDM**
R= p-*tert*-butylphenyl	benzene	1:3	**DBBz**
Class C			
	water/benzene	1:1:⅙	**TODBEN1**
	p-xylene	1:½	**TODPXLT**
	water	1:2⅙	**TODOXLT**

Crystal Growth

In each case a hot solution of the host compound, in the solvent to be included, was forced through a 0.5 μm Teflon Millex-LCR filter, via a syringe, to remove excessive nucleation sites. Single crystals of diffraction quality were obtained by slow evaporation or cooling of these solutions in glass vials covered with perforated parafilm.

Density Measurement

When crystals of inclusion compounds were sufficiently stable, densities were measured by the flotation method. A few crystals were blotted dry on filter paper and submerged in a mixture of saturated KI solution and water. Further additions of KI and water were made until the crystal was suspended in a homogeneous solution. The density of the solution was measured using a Paar Digital Densitymeter DMA35. This method is fairly slow and could only be used on relatively stable inclusion compounds.

Powdered Samples

Powdered samples of the inclusion compounds were obtained by slow evaporation of a continuously stirred solution of the host compound in the solvent, at room temperature. These samples were used for thermal analysis, X-ray powder diffraction and guest absorption studies.

Particle Sizing

The particle size distributions of the powdered samples were measured using a Malvern Series 2600 laser particle sizer. It was found that the method discussed above yielded samples with particle diameters in the range of 10 to 100μm, having a mean particle size of approximately 35μm.

X-Ray Powder Diffraction

X-ray powder diffraction (XRD) patterns were obtained using Ni-filtered CuKα radiation (λ=1.5418Å). If enough sample was available the patterns were recorded on a Philips PW1050/80 vertical goniometer with a PW1394 motor control unit and a PW11390 channel control unit, linked to a personal computer, and stored on disk for subsequent analysis, using a spread-sheet package. The powder patterns were collected over a 2θ range of 6-40°. The powdered samples were packed in an aluminium holder and step scans were recorded at 0.1° 2θ intervals and 1s counts,

unless otherwise specified in the text. Automatic receiving and divergence slits were used.

Powder photography was carried out, in cases where not enough sample was obtained to collect powder diffraction spectra on the Philips PW1050/80 vertical goniometer, using a Debye-Scherrer powder camera with a radius of 57.31 mm. The powdered samples were packed into 0.5 mm Lindemann glass capillaries. The spectra were recorded photographically and traces of relative intensity *vs.* 2θ were produced by scanning the powder patterns photometrically.

NMR

In the analysis of **TODBEN1** ^{1}H NMR spectra were recorded using a Varian Unity FT-NMR spectrometer operating at 400 MHz. The samples were dissolved in dry $CDCl_3$ and ^{1}H spectra were recorded at 25°C. Spectra were recorded with a sufficient pulse delay time to ensure quantitative resonance integrals to estimate host:guest ratios accurately. All other ^{1}H NMR spectra were recorded at 200 MHz on a Varian VXR200 spectrometer.

Thermal Analysis

Differential scanning calorimetry (DSC) and thermogravimetry (TG) were performed on a Perkin Elmer PC7 series system. The TG thermocouple and balance were calibrated using built-in procedures for furnace and weight calibration. Two-point standard temperature calibration was performed by measuring the Curie-points of Alumel (163°C) and Nickel (354°C).

The DSC analyser was calibrated by measuring the melting points of Indium (156.6°C) and Zinc (419.5°C). The heat flow was calibrated using the enthalpy of melting of Indium (28.62 Jg^{-1}).

Powdered specimens were blotted dry on filter paper and placed in open platinum pans for TG experiments and in crimped, but vented aluminium sample pans for DSC experiments. The sample weight in each case was 2 to 5 mg. The

programmed temperature runs typically started at 30°C, and ended at temperatures chosen depending on the melting point of the compound. The programmed temperature runs were recorded at a heating rate of 20°C min^{-1}. The samples were purged by a stream of nitrogen flowing at 40 ml min^{-1}. Data for the kinetics of desolvation were obtained from isothermal TG experiments done at selected temperatures in appropriate ranges, depending on the onset temperature of desolvation of a specific compound.

Hot Stage Microscopy

Hot stage microscopy (HSM) was carried out in an attempt to correlate the physical appearance of samples with the thermal events observed in the thermal analysis experiments. A Linkam TH600 hot stage mounted on a Nikon microscope equipped with polarising and overhead light was used. The temperature was controlled manually with a Linkam CO600 temperature controller. The hot stage was calibrated using the melting points of azobenzene (68°C), benzil (95°C), benzanilide (163°C) and dicyandiamide (210°C).

Scanning Electron Microscopy

Scanning electron microscopy (SEM) was carried out on a Lica S440*I* scanning electron microscope. An accelerating potential of 5 kV and a probe current of 21 pA were used. The working distance varied between 12-14 mm, depending on the sample.

Levitation Balance

A levitation balance, designed by Barbour *et al.*[8] was used to confirm guest sorption studies, carried out on the quartz microbalance (QMB), discussed in Chapter 3. The principal features of the levitation balance are indicated in Fig 2.1. The reaction vessel was evacuated and thermostatted at 25°C. Sample masses of *ca.* 300 mg of host were measured accurately on a three place balance. The levitation balance was tared with the host in the sample pan, so that the mass difference, due to guest

absorption could be measured. The mass readings were accurate to ±1mg. Reactant liquid was slowly admitted into the reaction vessel via a tap. The partial pressure of the guest vapour was measured using a stainless steel diaphragm pressure transducer. Mass gain *vs.* time data were captured, using a PC, and displayed in real time on the computer screen.

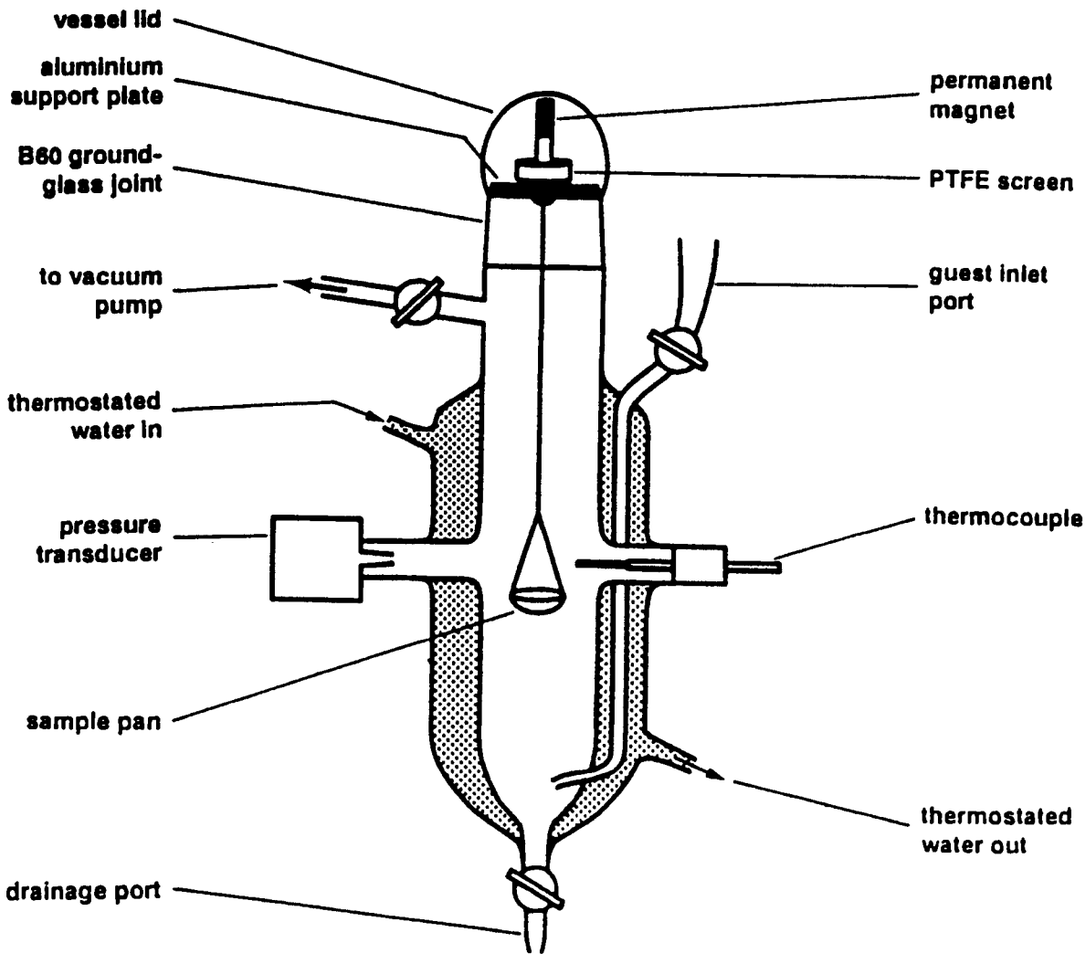

Fig 2.1. Schematic diagram showing the principal features of the levitation balance system, taken from reference 8.

Crystal Structure Analysis

Single crystals of suitable size (typically between 0.2 and 0.5 mm in all dimensions) were flame sealed in Lindemann capillary tubes (with either 0.3 mm or 0.5 mm diameter) together with mother liquor in order to prevent desorption of the guest. In cases where the inclusion compound was stable in the atmosphere (**TODBEN1**, **TODOXLT** and **TODPX**) the crystals were mounted in Lindemann capillaries, without any mother liquor, to protect the crystals from the atmosphere. The sealed Lindemann tube was then mounted on a brass pin and placed on a goniometer head.

Preliminary unit cell parameters and space group symmetry were determined from oscillation and Weissenberg photographs taken on a Stoë goniometer using Ni-filtered CuKα radiation (λ=1.5418Å).

X-ray diffraction data were measured on an Enraf-Nonius CAD4 diffractometer, using graphite-monochromated MoKα radiation, (λ=0.7107Å). Cell parameters were determined from 24 reflections at θ 10 - 12°. The unit cell was refined by least-squares analysis of the setting angles of 24 reflections collected in the θ range 16 - 17° and centred on the diffractometer. Data were collected in the ω-2θ scan mode with a final acceptance limit of 20 σ at 20°min^{-1} and a maximum scan time of 40s. The vertical aperture length was fixed at 4mm, the aperture width at
(1.12 + 1.05 tan θ)mm and the scan width at ω = (x + 0.35 tanθ)°, with x = 0.80 or 0.85. During data collection three reference reflections were monitored periodically to check crystal stability. Data collections were done at room temperature, except for **TODPXLT** and **TODOXLT**, which were repeated at -50°C, in order to obtain better quality diffraction data. The data reduction included correction for Lorentz and polarisation effects. In the cases where heavy atoms (Cl, Br) were present in the host, empirical absorption corrections were applied[9].

Structure Solution And Refinement

Structure solution and refinement computations were performed on a remote DEC 3000 model 400. Structures were solved by direct methods, using the program

SHELX-86[10], which is based on a random start multisolution philosophy[11]. Equivalent reflections were merged and those with $I < 2\sigma(I)$ suppressed. Mean $|E^2-1|$ (E is the normalised structure factor) were investigated to confirm the choice of space group - *i.e.* if $|E^2-1|$ is close to 0.968, the structure is centrosymmetric, and if $|E^2-1|$ is close to 0.736, the structure is acentric. Subsequent refinement was done using SHELXL-93[12].

SHELXL-93 employs full-matrix least-squares refinement against F^2. Agreement between observed and calculated structure factors is expressed by the residual index, R. The residual index for refinement against F^2, R_2, is much larger than (often nearly double) that for refinement against F, R_1. For comparison with structures refined in SHELX-76[13], the R-index based on F values (R_1) as well as that based on F^2 (R_2) will be quoted.

The residual index (R) is defined as:

$$R_1 = \frac{\sum ||F_o|-|F_c||}{\sum |F_o|} \qquad wR_2 = \left(\frac{\sum w\left(F_o^2 - F_c^2\right)^2}{\sum w\left(F_o^2\right)^2} \right)^{1/2}$$

A weighting scheme (w) was refined for each structure, where:

$w = 1/[\sigma^2(F_o^2) + (aP)^2 + bP]$

$P = [max(0,F_o^2) + 2F_c^2] / 3$

and a and b were refined for each structure. The Goodness of Fit (S) is based on F^2 (which causes the deviation from unity to be magnified in comparison with SHELX-76):

$S = [\sum [w(F_o^2-F_c^2)^2]/(n-p)]^{1/2}$

where n is the number of reflections and p is the total number of parameters refined. The program examines the analysis of variance and prints a warning that an extinction parameter, x, should be refined if S is significantly higher than unity. When necessary an extinction parameter, x, was refined by least-squares, where F_c is multiplied by:

$[(1 + 0.001 \times x \times F_c^2 \times \lambda^3) / \sin(2\theta)]^{-1/4}$. The expression is empirical and covers both primary and secondary extinction.

Computation

X-ray powder diffraction (XRD) patterns were calculated using a modified version of the computer program LAZYPULVERIX[14] on a personal computer in a DOS environment. The input includes cell parameters, space group symmetry, atomic coordinates and Debye-Waller factors. The output was taken into a spread sheet program and presented with experimentally obtained patterns for comparison.

The shapes and sizes of voids, resulting from the removal of the guest from an inclusion compound crystal structure were investigated using the program MOLMAP[15]. Guest molecules are removed from the structure solution and the host atoms are represented with spherical radii equal to their van der Waals radii[16]. The program allows one to cut the unit cell at selected intervals and plots the intersection of the cell (lines) and atoms (circles) with a chosen plane perpendicular to any chosen unit cell direction. This enables one to investigate the shape of channels or cavities formed by the host molecules.

The Cambridge Structural Database (CSD)[17] was used to investigate published crystal data, for comparison with structures reported in this thesis. Molecular and packing diagrams were produced using the PC versions of PLUTO[18] and ZORTEP[19].

1 S.A. Bourne, L.R. Nassimbeni, M.L. Niven, E. Weber and A. Wierig, *J. Chem. Soc. Perkin Trans. 2*, 1994, 1215.

2 A. Haller and A. Guyot, *Compt. Rend.*, **138**, 1904, 327.

3 A. Mustafa, *J. Chem. Soc.*, 1952, 2435.

4 A. Mustafa, *J. Chem. Soc.*, 1949, 1662.

5 A. Willermart, *Bull. Soc. Chim.*, **4**, 1937, 357.

6 C. K. Ingold and P.G. Marshall, *J. Chem. Soc.*, 1926, 3080.

7 F. Toda, A. Kai, R. Toyotaka, W.-H. Yip and T.C.W. Mak, *Chem. Lett.*, 1989, 1921.

8 L.J. Barbour, K. Achleitner and J.R. Greene, *Thermochim. Acta*, **205**, 1992, 171.

9 A.C.T. North, D.C. Phillips, F.S. Mathews, *Acta Crystallogr.*, **A24**, 1968, 351.

10 G.M. Sheldrick, SHELX-86, *Crystallographic Computing 3*, eds. G.M. Sheldrick, C. Kruger and R. Goddard, Oxford University Press, 1985.

11 *International Tables for Crystallography*, Vol C, ed. A.J.C. Wilson, Kluwer Academic publishers, Dordrecht, 1992, 523.

12 G.M. Sheldrick, SHELXL-93: Programme for Crystal Structure Determination, unpublished work.

13 G.M. Sheldrick, *Computing in Crystallography*, eds. H. Schenk, Olthof-Hasenkamp, J. von Koningsveld and G.C. Bassi, Delft University Press, 1978, 34.

14 K. Yvon, W. Jeitschko and E. Parthé, *J. Appl. Cryst.*, 1977, **10**, 73.

15 L.J. Barbour, *Clathration by Diol Hosts: Thermodynamics and Structure*, PhD Thesis, University of Cape Town, 1994.

16 A. Bondi, *J. Phys. Chem.*, **68**, 1964, 441.

17 Cambridge Structural Database and Cambridge Structural Database System, Version 5.11 (April 1996), Cambridge Crystallographic Data Centre, University Chemical Laboratory, Cambridge, England.

18 W.D.S. Motherwell in "PLUTO and PLUTOX - Programmes for plotting molecular and crystal structures", Cambridge University, England, unpublished.
Modified by E.J. Dodson and G.D. Smith, further modified by M. Webster and E.J. Gabe, NRC, Canada, 1985.

19 L. Zolnai, Zortep: Programme for plotting molecular structures with thermal elipsoids, University of Heidelberg, Heidelberg, Germany, unpublished.

CHAPTER 3 A QUARTZ MICROBALANCE FOR MEASURING GUEST UPTAKE FROM THE VAPOUR

Introduction

In recent years there has been great interest in developing chemical sensors based on oscillating quartz crystals[1,2]. These sensors have possible applications in measuring concentrations for medical purposes, as well as industrial process control. They are often employed as "chemical noses" to detect very small amounts of odorant[3]. The method is based on the mass-frequency dependence of an oscillating quartz crystal according to the formula:

$\Delta f = -kf_0^2 \Delta m$

where f_0 is the frequency of the unloaded crystal, and k is a constant specific to each crystal. The frequency of the oscillation decreases with increasing mass of the crystal, and this can be exploited to weigh very small quantities of the organic compound coating the surface. A detection limit of 1 ng, using 9 MHz quartz crystals, has been reported[1].

An oscillating quartz crystal can be made into a Quartz Microbalance (QMB) by coating it with a suitable host compound (**H**) which in turn reacts with the targeted guest compound (**G**) according to the following equation:

$$H_{(s,\alpha)} + nG_{(g)} \rightarrow HG_{n(s,\beta)}$$

When the host compound, in the non-porous α-phase, is exposed to a guest vapour a phase change takes place and the inclusion compound in the β-phase is formed. This change in phase can be monitored using X-ray powder diffraction. The gain in mass of the quartz crystal results in a decrease in oscillation frequency which can be monitored as a function of time, thus enabling the kinetics of reaction to be measured. A multiple probe QMB was designed for the study of the response of related host compounds to various vapours.

Saunders *et al.* [4] have obtained "kinetic signatures" of six different surface coatings when exposed to one of 18 different odorants. This method has recently been extended to chiral molecular recognition from a solution, where the quartz crystal was coated with a dipeptide host compound[5]. Jane and Shih[6] developed a quartz crystal electrode, coated with a crown ether, as a detector of either cations or anions in ion chromatography.

Most of the references to the use of QMBs in the literature refer to their use as chemical sensors. A QMB was designed in order to investigate the kinetics of guest sorption of very small samples. The hosts investigated in this study are specialised compounds which are not commercially available. The limited availability of the host compounds dictated the types of experiments which could be carried out. The kinetics of desorption of inclusion compounds could be studied on a TG using sample sizes ranging between 2-5 mg. In order to study the formation of inclusion compounds, the host has to be placed in a saturated guest atmosphere. Siedel *et al.*[7] recently reported guest uptake studies carried out on a conventional simultaneous TG-DSC. Due to the corrosive nature of the guest vapours, the Perkin Elmer Series 7 TG at the author's disposal could not be used for this purpose. A levitation balance[9], previously designed for this purpose, could not be used, since it requires sample masses of 300-500 mg of host compound. The QMB was hence developed to study very small samples (100-500 μg).

Description Of Apparatus

The QMB apparatus, shown in Fig. 3.1, consists of a glass cell which can be evacuated and whose internal pressure can be monitored, using a pressure transducer with a stainless steel diaphragm. There is an inlet for the guest vapour which is injected via a rubber septum. The cell was placed in a thermostatted cupboard, and the temperature was controlled within 0.1°C using a PID controller. The cell contains three quartz crystal probes. Each probe, shown in Fig. 3.2, comprises a 10 MHz quartz crystal which has been mounted in a socket on a glass cone, with a crystal oscillator circuit secured inside the cone. Each cone was sealed with a silicone sealant.

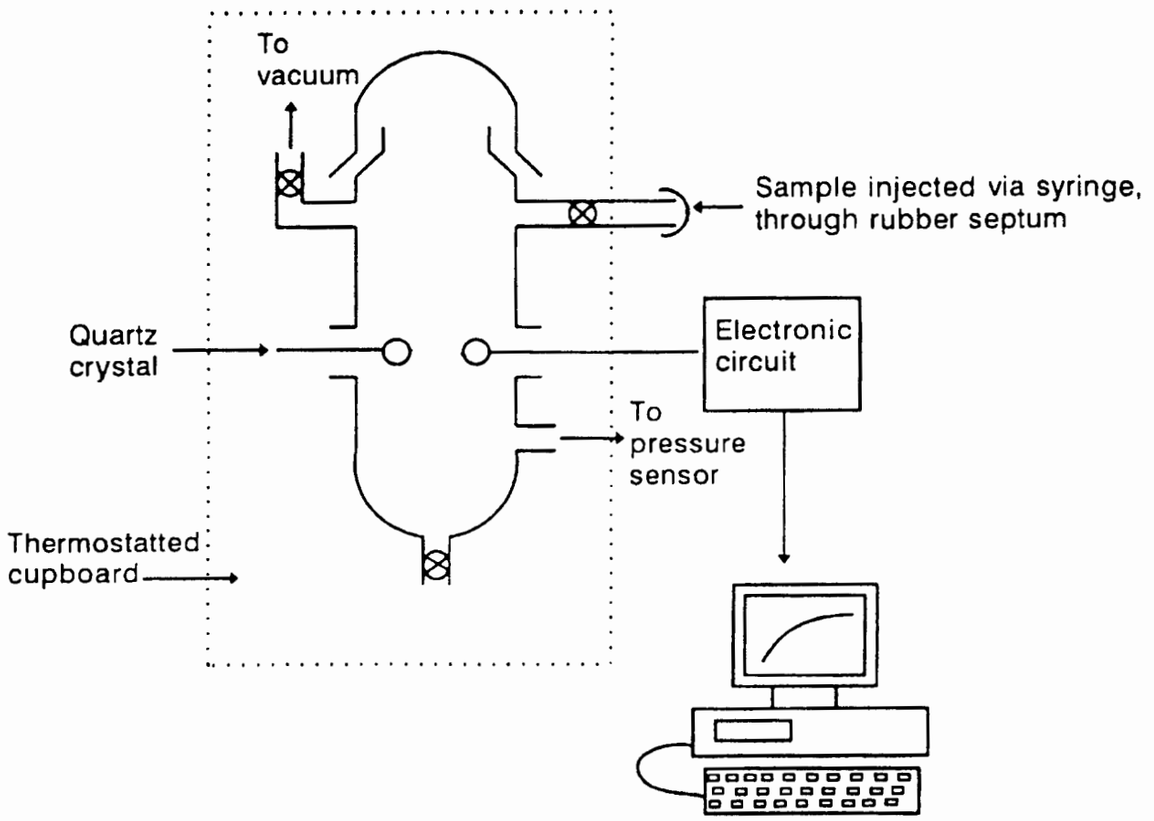

Fig 3.1. Schematic diagram showing the principal features of the QMB system.

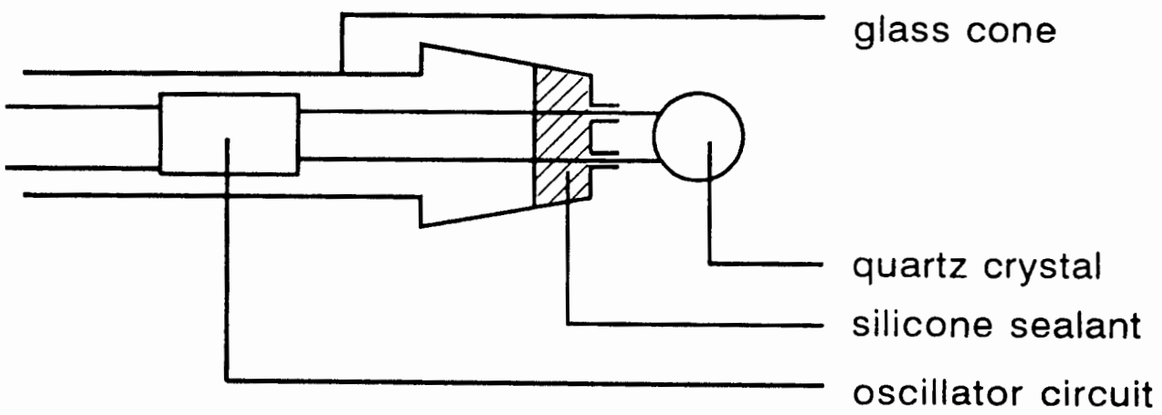

Fig 3.2. Schematic diagram of the quartz crystal probe.

An electronic circuit, shown in Fig. 3.3, monitors the change in frequency of a given crystal and the signal is fed to a microcomputer which displays the change in frequency against time. The QMB circuit consists of a 6 MHz reference quartz oscillator located inside the main instrument case and the three probes in the reaction cell. The quartz crystal oscillator is very compact and consists of a commercially available 8 pin integrated circuit. The circuit requires a five volt power supply, a 0.01 μF supply decoupling capacitor and the appropriate pin connections as shown in Fig 3.4. The quartz crystal determines the frequency of oscillation and the circuit can be configured to oscillate between 10 kHz and 10 MHz.

The software controls the Channel Selector which sequentially scans the frequencies of the probe oscillators in the reaction cell and feeds the frequency F_s into a subtractive mixer, which subtracts the frequency of the reference oscillator F_r from each incoming probe oscillator frequency. It feeds the difference (F_s - F_r) to a frequency to voltage converter (F/V). The F/V produces an output of one volt for every kHz of difference frequency, with a maximum output voltage of 10 volts (10 kHz).

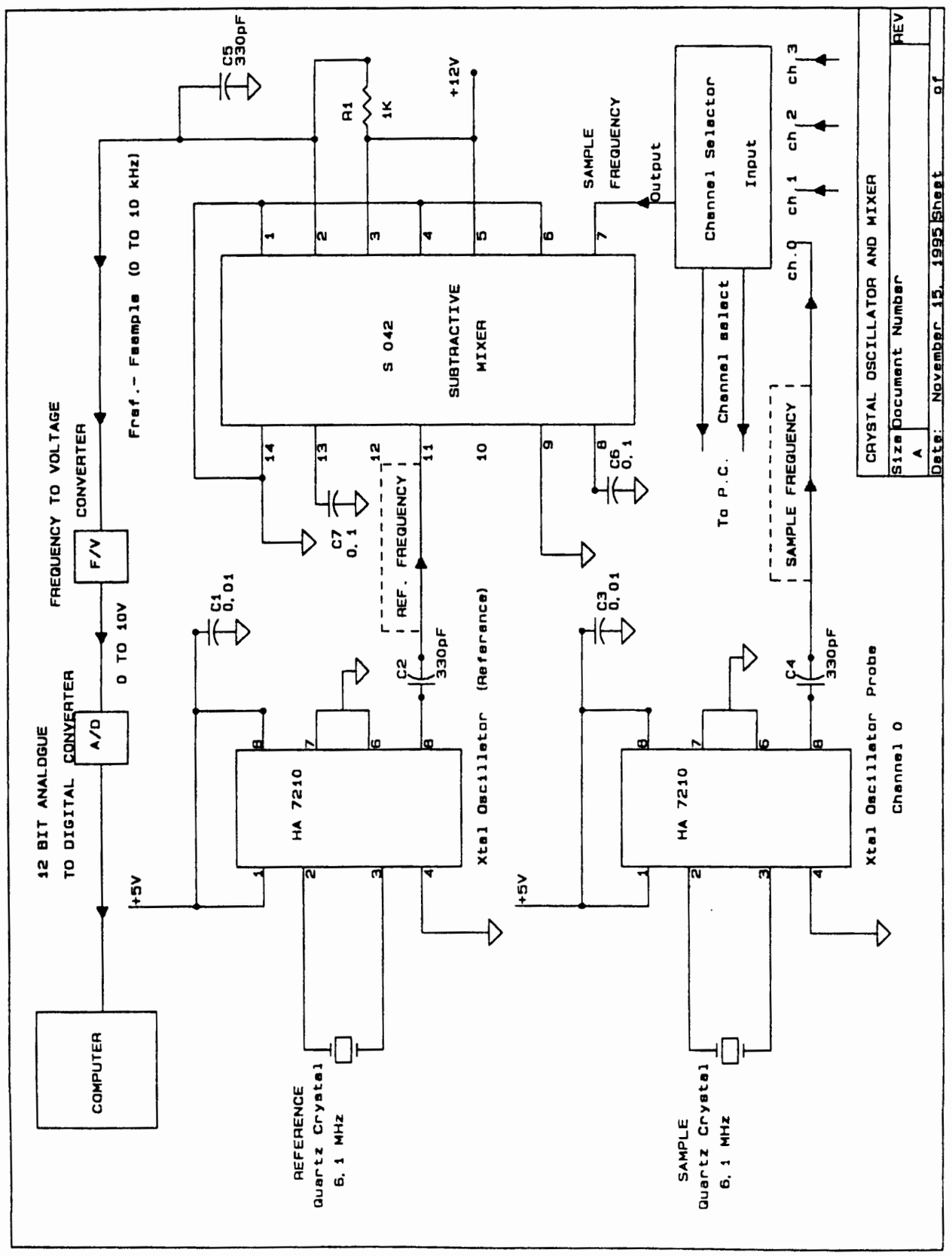

Fig 3.3. Crystal oscillator and mixer circuit.

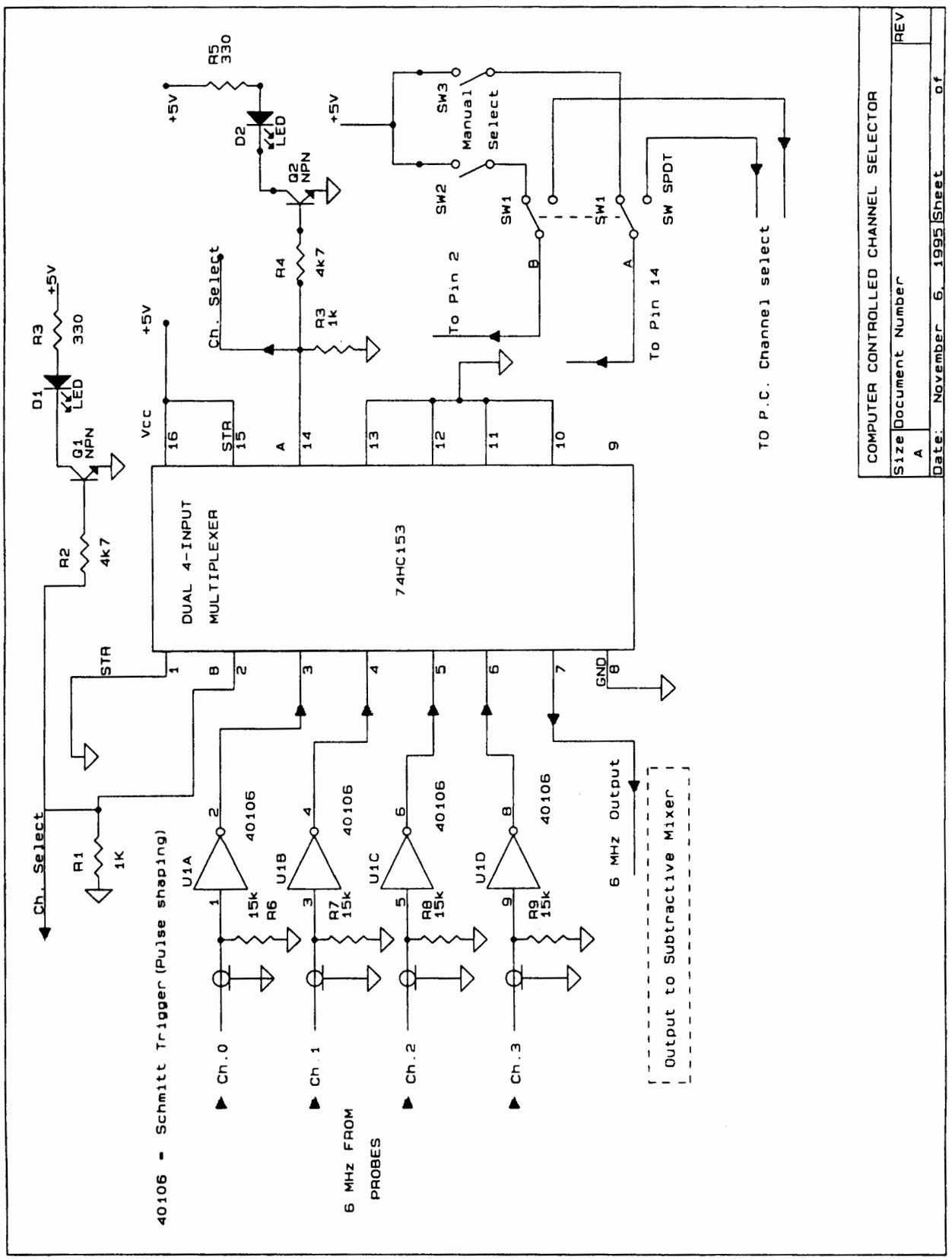

Fig 3.4. Channel selector circuit.

Experimental

Coating

The quartz crystals were coated with the α-phase of the appropriate host compounds. An even coating was obtained by dipping the quartz crystal into a concentrated solution of the host compound in diethyl ether. Upon evaporation of the solvent a coating of the unstable diethyl ether inclusion compound remained on the surface of the quartz crystal. This coating procedure was repeated until a sufficient coating (100-500μg) was obtained. The quartz crystal was left at atmospheric pressure overnight, so that the diethyl ether could desorb, yielding the non-porous α-phase of the host. It is imperative to allow the evaporation and desorption to take place slowly, at room temperature and atmospheric pressure, in order to obtain a uniformly coated crystal. As can be seen from a SEM photograph taken of the surface of a quartz crystal coated with host compound **B1** (see Scheme 1), an even distribution of host was obtained using this method (see Fig. 3.5.) . The host particles are evenly sized, lath shaped, uniformly spread over the surface and possess random orientations.

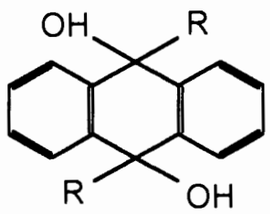

B1: R=phenyl

B2: R=*p-tert*-butylphenyl

B3: R=α-naphthyl

Scheme 1

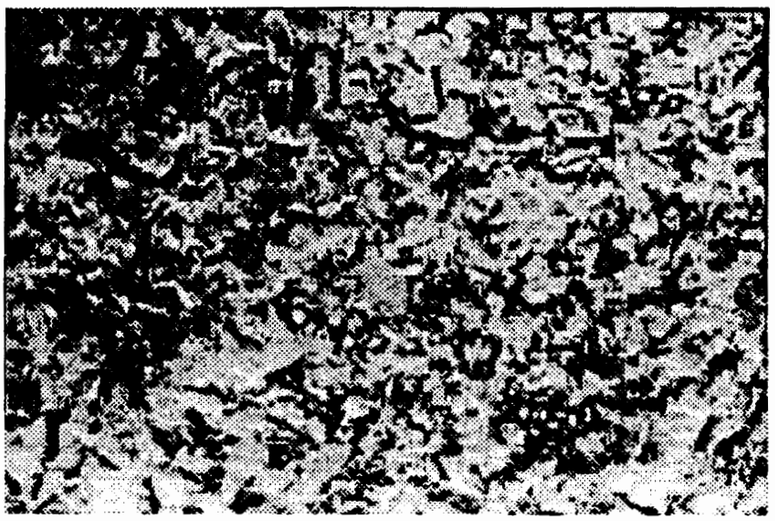

Fig 3.5. SEM photograph of the surface of a quartz crystal coated with host **B1**.

Calibration

One probe was left uncoated in the reaction cell to monitor the response of the quartz crystal due to changes in temperature and pressure, while the other two quartz crystals were incrementally coated with host compound **B1**. A series of Δf *vs.* Δm data were obtained at room temperature. From Fig 3.6. it is clear that a linear relationship exists between mass and frequency. The mass-frequency dependence was also confirmed at other temperatures.

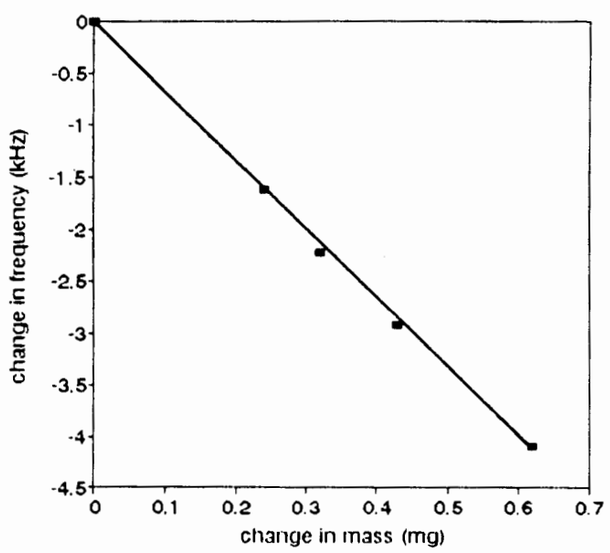

Fig 3.6. Calibration curve of QMB at 25°C.

Guest Sorption

The formation of an inclusion compound between host **B1** and acetone vapour, with a host:guest ratio of 1:2, has been studied by Barbour *et al.*[8] Since this system had been very well characterised it was chosen as a trial system to be investigated on the QMB. The quartz crystal in channel 0 was left uncoated, the one in channel 1 was coated with host **B1** and the crystal in channel 2 was coated with host **B2**, which does not include acetone from the vapour phase. The reaction vessel was evacuated to a pressure of 1 mmHg and then isolated. A volume of 0.5 ml acetone was injected with a microsyringe via the rubber septum. It vaporised completely and yielded a pressure of 126 mmHg. The guest uptake reaction reached completion within a few minutes. The reaction vessel was again pumped down to 1 mmHg, and the acetone was released from the inclusion compound, with the frequency reading of channel 1 returning to that corresponding to the desolvated host compound. The sorption reaction, followed by desorption was repeated six times. It was found that the rate of the sorption reaction increased, with each cycle, but stabilised after the fourth repetition. A SEM photograph of the quartz crystal, coated with host B1 having undergone seven sorption and desorption cycles is compared with a sample which has undergone only one sorption-desorption cycle, in Fig 3.7. The host particles showed severe surface damage, due to the repeated sorption-desorption cycles. This resulted in an increased host surface area which would explain the observed increase in the rate of sorption. Based on this result, host compounds were conditioned prior to kinetic studies, by repeating sorption-desorption cycles until the rate of reaction remained constant.

Fig 3.7. a) Quartz crystal coating (host **B1**) after one sorption-desorption cycle with acetone.

Fig 3.7. b) Quartz crystal coating (host **B1**) after seven sorption-desorption cycles with acetone.

Discussion

The advantages of this system are:

- Each crystal requires very small quantities of host compound (approximately 100-500 μg)
- With multiple crystals, one can simultaneously test the selectivity of several host compounds for a given guest.
- In many cases it will be possible to study the reverse reaction, by raising the temperature and pumping out the cell.
- Real-time graphical display of the change in frequency and pressure.

The major disadvantage of this apparatus is that the QMB uses such small samples that it is not possible to monitor the X-ray diffraction patterns of the material. In the case where bulk analyses of the samples are required the levitation balance designed for the study of guest uptake in controlled atmospheres[9] still has to be used. Another disadvantage of using such small samples, is that the signal to noise ratio is fairly high. In cases where volatile host compounds are used, there is a danger that the reference oscillator can be coated by condensation of the host. The system is still under development and it is hoped that it can be improved.

This system is ideal for preliminary investigations. One can easily establish whether a given host includes the guest under investigation, without using much sample. The instrument could be extended to measuring analytes in solutions. This will require special coating techniques of the host on the quartz crystal to ensure durability. In Chapter 8 the application of this instrument for the study of the kinetics of the formation of a 1:1 inclusion compound between host **B1** and 1,3-dioxolane is discussed in detail.

1 A. Ehlen, C. Wimmer, E. Weber and J. Bargon, *Angew. Chem. Int. Ed. Engl.*, **32**, 1993, 110.

2 Y. Okahata and H. Ebato, *Anal. Chem.*, **61**, 1989, 2185.

3 J. Emsley, *New Scientist*, 11 March 1995, 21.

4 B.W. Saunders, D.V. Thiel and A. Mackay-Sim, *Analyst*, **120**, 1995, 1013.

5 Y. Okahata, K. Yasunaga and K. Ogura, *J. Chem. Soc. Chem. Commun.*, 1994, 469.

6 Y-S. Jane and J-S. Shih, *Analyst*, **120**, 1995, 517.

7 J. Siedel, G. Wolf and E. Weber, *Thermochim. Acta*, **271**, 1996, 141.

8 L.J. Barbour, M.R. Caira and L.R. Nassimbeni, *J. Chem. Soc. Perkin Trans. 2*, 1993, 2321.

9 L.J. Barbour, K. Achleitner and J. Greene, *Thermochim. Acta*, **205**, 1992, 171.

CHAPTER 4 INCLUSION COMPOUNDS OF HOSTS IN CLASS A WITH 1,4-DIOXANE.

The inclusion compounds, formed by hosts in Class **A**, will be discussed in the following chapters. These host compounds have the general structure:

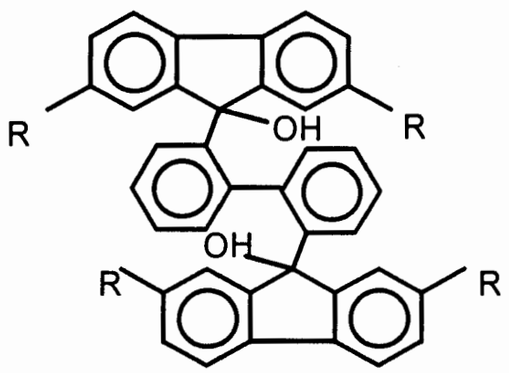

where R= Br, Cl, p-*tert*-butyl. The inclusion compounds have been divided into three chapters, according to the guests which were included, and are discussed in terms of thermal analysis, crystal structure and kinetics of desorption. In an additional chapter the host conformations are compared with structures found in the literature for these hosts as well as the host compound with R=H. The space group, cell parameters, host:guest ratio and other crystallographic information are summarised at the beginning of the discussion of each inclusion compound. Each structure is discussed in terms of refinement, host and guest location and molecular structure. In this chapter the 1,4-dioxane inclusion compounds of the host with R=Cl, Br and p-*tert*-butyl are discussed (hosts **A1**, **A2** and **A3** respectively).

W17DIA

$C_{38}H_{22}O_2Cl_4 \cdot 3.5(C_4H_8O_2)$

Guest:1,4-dioxane

Space group: $P\bar{1}$

a=12.878(4) Å α=102.95(4)°

b=13.221(3) Å β=100.53(4)°

c=15.78(1) Å γ=108.83(2)°

Volume=2382(2) $Å^3$

Z=2

Tables containing complete crystal and refinement data appear at the end of this chapter.

Thermal Analysis

A host:guest ratio of 2:7 was confirmed by TG (calc. 32.1%, obs. 31.2%). The TG, DTG and DSC traces for the desolvation of **W17DIA**, carried out on powdered samples (with particle diameters in the range 10-100μm), are shown in Fig 4.1. The DTG curve shows that the guest loss reaction took place in three steps. The three mass loss steps, with onset temperatures of 66°C, 114°C and 145°C, corresponding to the loss of 2, ½ and 1 guest molecules respectively, were sharply differentiated by doing the experiment on small crystallites (with particle diameters of approximately 0.05 mm), shown in Fig 4.2. Only two diffuse endotherms, corresponding to overlapping desolvation processes, were observed in the DSC experiments. As can be seen from the DSC trace obtained from small crystallites (Fig 4.2.), the change in particle size did not differentiate a third desolvation endotherm in the DSC experiments, but only affected the relative peak heights of the two endothermic processes. It is well documented that the areas of DSC peaks decrease as the degree of crystallinity of the sample is decreased[1]. A sharp endotherm at 355°C corresponds to the melting point of the host. This peak is not shown in Fig 4.1., since the sample decomposes and sublimes upon melting and attempts were made to recycle the host, whenever possible.

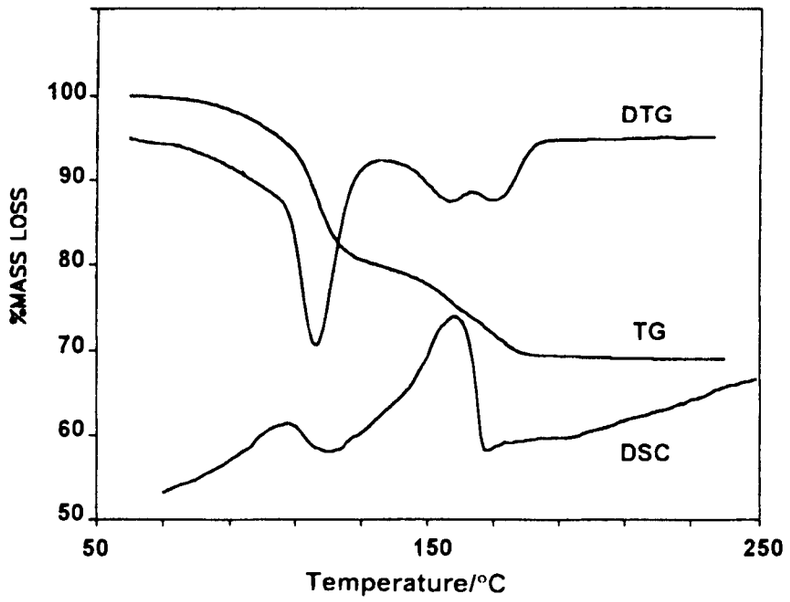

Fig 4.1.TG, DTG and DSC traces for a powdered sample of **W17DIA**.

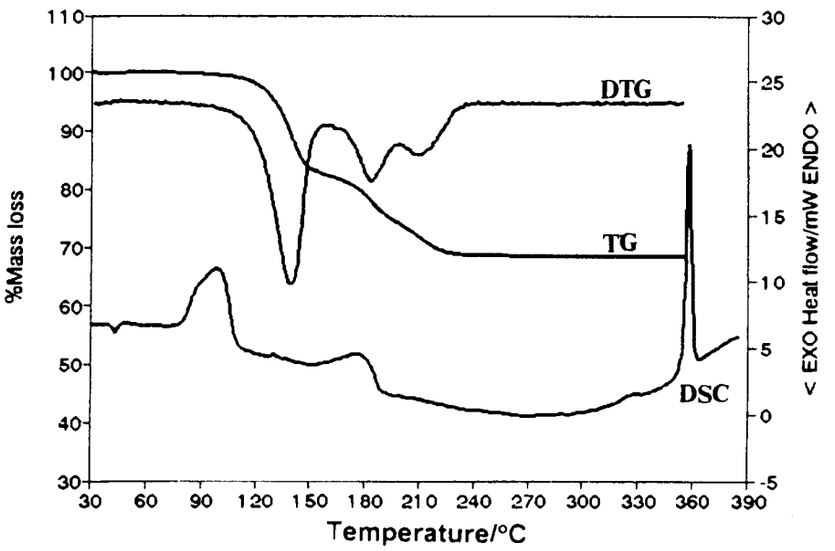

Fig 4.2.TG, DTG and DSC traces for a sample of small crystallites of **W17DIA**.

Hot Stage Microscopy

Two single crystals of **W17DIA** were placed on a glass slide and covered in silicone oil. The crystals were heated on the hot stage microscope and photographs were taken whenever physical changes occurred in the crystals. The photographs depicting the changes observed upon heating of the crystals of **W17DIA** are shown and described in Colour Plate 4.1. The temperatures at which the changes were observed were often slightly higher than that observed in the thermal analysis of the powdered samples, mainly due to particle size differences and the fact that the hot stage possesses an entirely different geometry from the DSC. Fairly large crystals were used (with diameters of 0.5 mm) as opposed to the powdered samples (10-100μm).

Colour Plate 4.1.

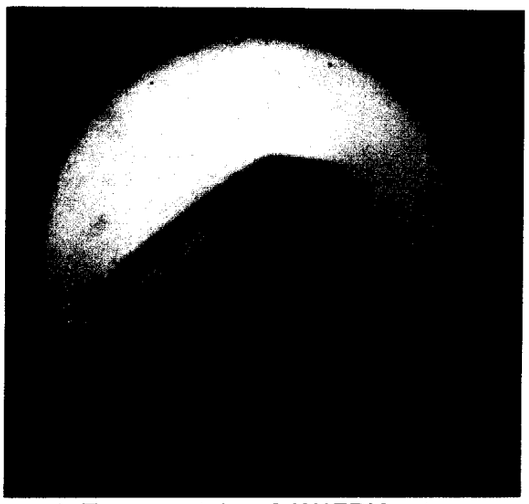

a) Two crystals of **W17DIA** at room temperature. 28 X enlarged.

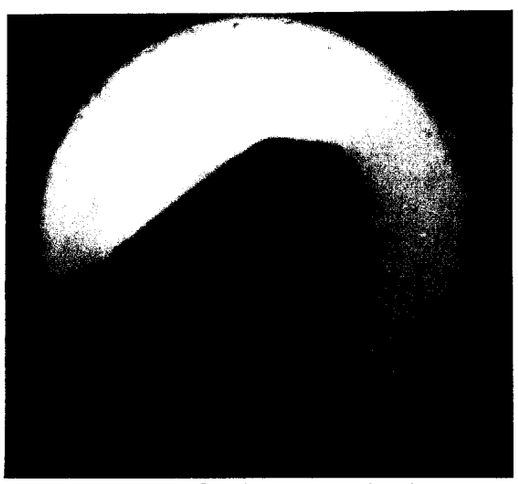

b) At 104°C the crystals became opaque. 28 X enlarged.

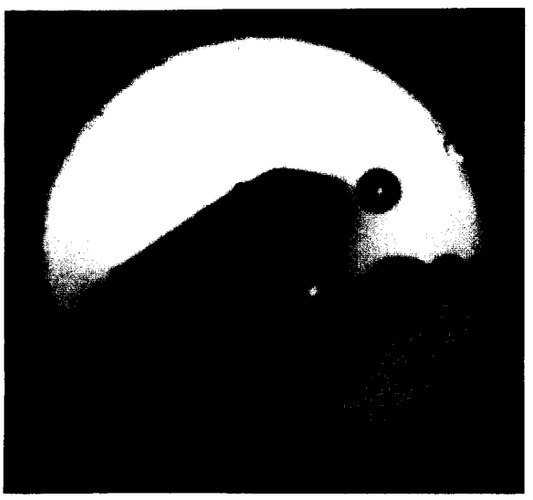

c) At 124°C the loss of guest was observed. Limited guest loss occurred. 28 X enlarged.

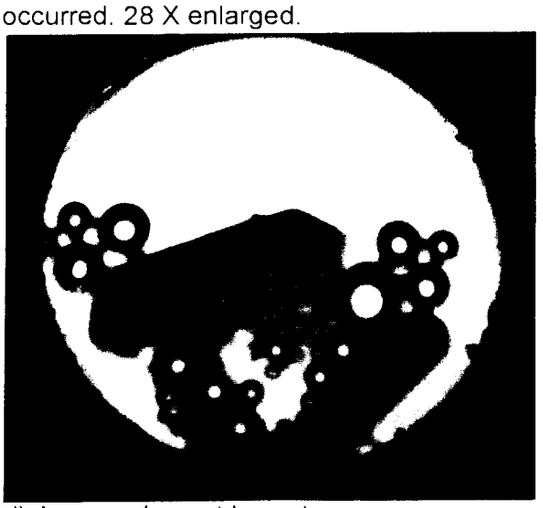

d) A second guest loss step was observed at 154°C and was completed at 190°C. 28 X enlarged.

Crystal Structure

Preliminary X-ray photography was employed to determine the unit cell parameters and crystal system. Compounds **W17DIA** and **W17DB** were found to belong to the triclinic crystal system; therefore the possible space groups are P1 and P $\bar{1}$. The centrosymmetric space group P $\bar{1}$ was chosen, in each case, based on the mean $|E^2-1|$ values for the zonal reflections, *i.e. 0kl, h0l, hk0*, and the remainder of the reflections. We are aware that intensity statistics are not completely reliable for the differentiation of centrosymmetric versus non-centrosymmetric space groups. This is particularly true for structures containing heavy atoms. However, whenever the choice of space group was ambiguous the final choice was always justified by the successful subsequent refinement of the structure.

Solution and Refinement

Direct methods yielded the positions of all the host non-hydrogen atoms in the asymmetric unit. There are two host molecules in the unit cell (Z=2). The host molecule was located in a general position. The non-hydrogen atoms in the guest molecules were located in the difference electron density maps upon subsequent refinement. The O atoms on the guest molecules were placed at the location of the highest peaks in the difference electron density map for each dioxane molecule. Refinement was carried out with the non-hydrogen atoms of the host treated anisotropically. The non-hydrogen atoms on one of the dioxane guest molecules (G1) were also treated anisotropically. The remaining guests were refined isotropically, due to relatively high thermal motion (U_{eq} > 0.11Å^2). The host hydrogen atoms were placed in geometrically constrained positions and refined with a common temperature factor for atoms of the same type. The hydroxyl hydrogens, which were located in a difference map, were refined with a simple bond length constraint according to a function of O-H *versus* O···O distances[2]. The hydrogen atoms on guest (G1) were placed in geometrically constrained positions and refined with a common temperature factor. The remaining guest hydrogen atoms were omitted from the final model. A residual electron density of 0.824 eÅ^{-3} was observed in the region of the guest molecule (G4), but could not be modelled

sensibly. An extinction coefficient (x= 0.009(2)) was refined for the structure. The structure refined successfully to R_1=0.0954.

Fig 4.3. shows an Ortep diagram of the host molecule, indicating host conformation and the numbering scheme used. The bond lengths and angles were all in the acceptable range for structures of this kind[3].

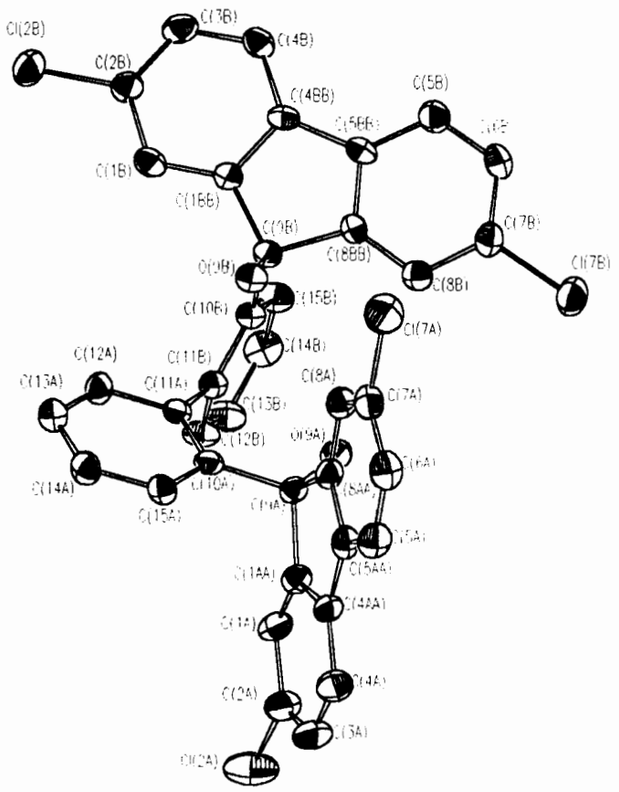

Fig 4.3. Host conformation of **W17DIA**.

Three dioxane molecules are located in general positions ((G1), (G2) and (G4)), while one guest dioxane (G3) lies on a centre of inversion, at Wyckoff position *h*, thus yielding a host:guest ratio of 1:3.5. This was confirmed by the TG analysis (discussed above). Careful analysis of difference electron density maps showed that two of the guests were partially disordered. Thus the final model employed two positions for C(32) of guest (G3) [C(32) and C(32A) with a fractional site occupancy factor of 0.5 each] as shown in Fig 4.4. The site occupancy factors for these two atoms were linked and allowed to refine.

The resultant bond lengths were:

O(31)-C(32) 1.48(2)Å
O(31)-C(32A) 1.35(3)Å
C(36)-C(32) 1.51(2)Å
C(36)-C(32A) 1.53(3)Å.

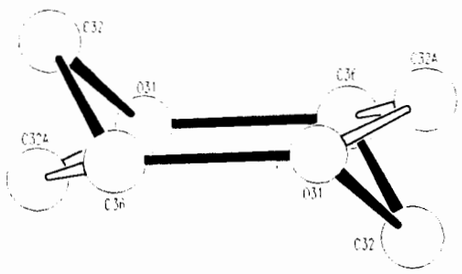

Fig 4.4. Disorder modelled in guest molecule (G3), **W17DIA**. C(32) and C(32A) were placed with a s.o.f. 0.5 each.

The disorder in C(43) and C(46) for (G4) was modelled with C(43) and C(46) with fractional site occupancies of 0.65 each, and C(43A) and C(46A) at 0.35 each (see Fig 4.5.). The site occupancy factors were determined from the relative peak heights in the difference electron density map. The following bond lengths were obtained:

O(41)-C(46) 1.52(2)Å
O(41)-C(46A) 1.44(3)Å
C(45)-C(46) 1.23(2)Å
C(45)-C(46A) 1.44(3)Å
C(42)-C(43) 1.35(2)Å
C(42)-C(43A) 1.45(3)Å
O(44)-C(43) 1.51(2)Å
O(44)-C(43A) 1.65(3)Å.

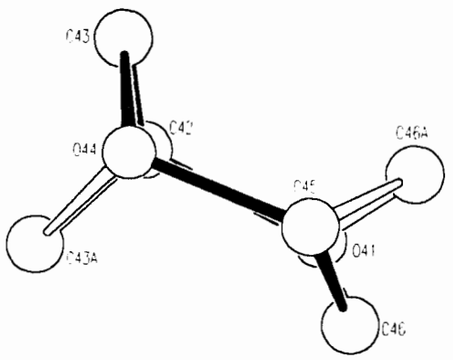

Fig 4.5. Disorder modelled in guest molecule (G4), **W17DIA**. C(43) and C(46) were placed with a s.o.f. of 0.65, while C(43A) and C(46A) were placed with a s.o.f. of 0.35 each.

Only two of the dioxane molecules are hydrogen bonded to the host. One dioxane molecule, (G1), is bonded via one oxygen [O(9B)-H9B···O(14), with d(O···O) = 2.766(5)Å]. Molecule (G3), the dioxane molecule located on the centre of inversion, has two hydrogen bonds, related by the centre of symmetry, [O(9A)-H(9A)···O(31), with d(O···O) = 2.846(7)Å].

Molecular Structure

The host-guest arrangement, consisting of a host molecule and four crystallographically independent guest molecules is shown in Fig 4.6.

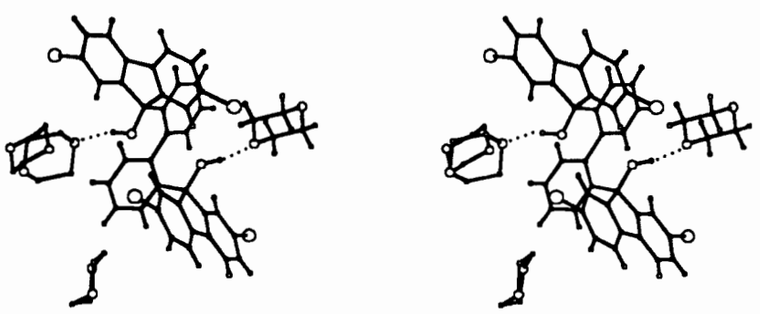

Fig 4.6. Molecular structure of **W17DIA**.

The molecular structure of **W17DIA** is similar to that of **W17DB** which will be discussed subsequently. The crystal packing, viewed down [001] and [010], for **W17DIA** are shown in Fig 4.7. and Fig 4.8. respectively.

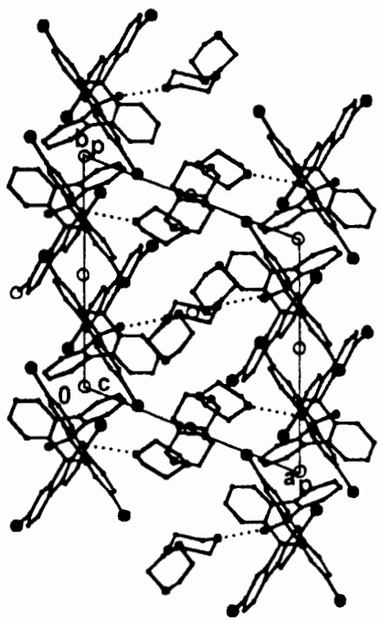

Fig 4.7. A projection down [001] showing the crystal packing in **W17DIA**.

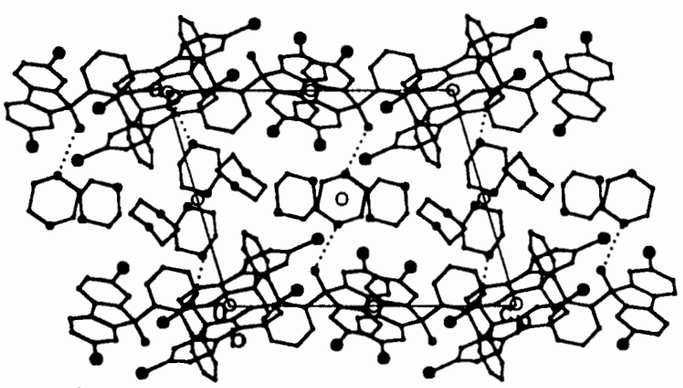

Fig 4.8. A projection down [010] showing the crystal packing in **W17DIA**.

Kinetics

In the programmed temperature TG experiments, discussed above, three overlapping desolvation steps were observed. Isothermal TG was employed in an attempt to separate these steps, in order to investigate the kinetics of desolvation. Two distinct desolvation steps were separated by appropriate selection of temperatures for isothermal TG runs. A typical example is shown in Fig 4.9., in which we exhibit the mass loss *vs.* time curve plotted with the temperature programme used. The first desolvation step, occurring in a temperature range of 50-70°C, corresponds to the loss of 2.5 moles of dioxane. This represents the first two desolvation steps, observed in the programmed temperature TG traces.

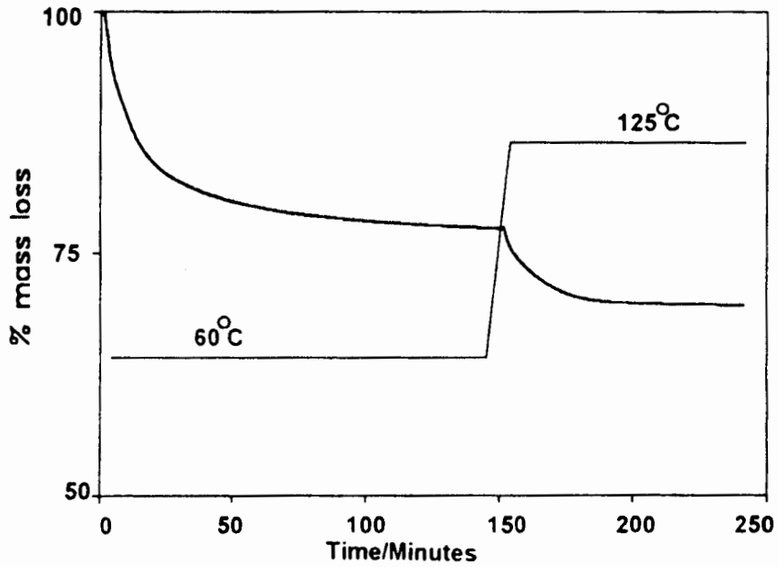

Fig 4.9. Temperature programme used to separate the two guest loss processes.

This resultant 1:1 inclusion compound is stable up to 100°C. The second desolvation step was analysed by isothermal TG over a temperature range of 100-125°C. The data, for each step, were reduced to curves of fractional reaction (α) *vs.* time. The first desolvation step was deceleratory, with an initial linear portion, corresponding to surface evaporation. Various kinetic models[4] were fitted to the data. The first desolvation step was best fitted by the equation representing the first order (F1) reaction mechanism: $kt = ln[1/(1-\alpha)]$ over an α-range of 0.10 to 0.95. The first portion of the curves (α-range 0 to 0.10) were linear, corresponding to surface evaporation. The second desolvation step, corresponding to the loss of one dioxane molecule, also fitted the F1 mechanism (α-range 0 to 0.9). The plots of *ln k*

vs. $1/T$ are shown in Fig 4.10. and 4.11., which yield activation energies of 34 (3) kJ mol^{-1} and 111 (9) kJ mol^{-1} for the first and second desolvation steps respectively.

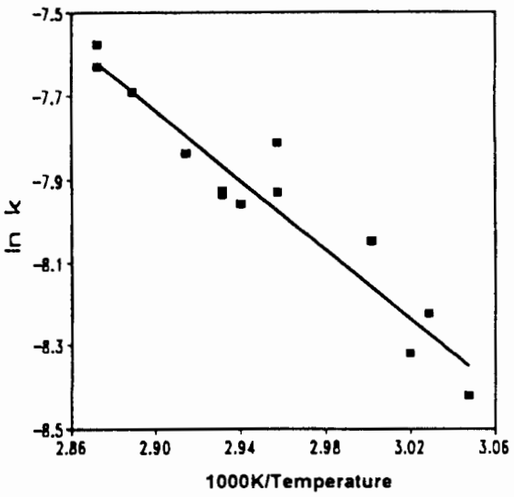

Fig 4.10. Arrhenius plot for the first desolvation process observed for **W17DIA**.

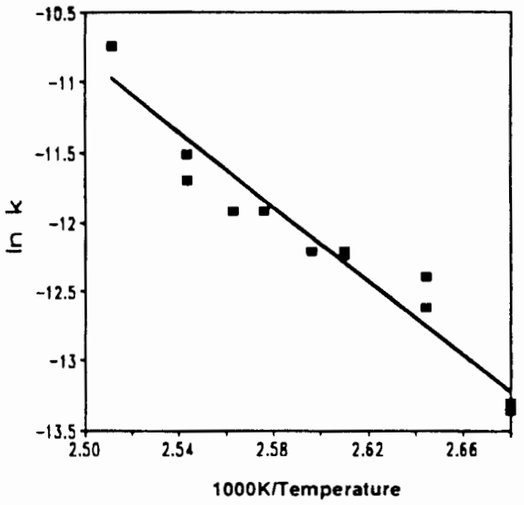

Fig 4.11. Arrhenius plot for the second desolvation process observed for W17DIA.

X-Ray Powder Diffraction

We have monitored the phase changes which occur upon desolvation of **W17DIA** by X-ray powder diffraction. Fig. 4.12. shows the photometric traces of the powder photographs we obtained for the inclusion compound **W17DIA**, trace a), while trace b) was obtained after the first desolvation step, i.e. a new, intermediate 1:1 inclusion compound. The final trace c) is that achieved after complete desolvation and corresponds to the α_1-phase of the pure host. It is clear that trace b is different from the other two and thus corresponds to a new crystalline phase, γ. Similar results have been reported for the desolvation of other inclusion compounds, which yielded intermediate phases upon partial guest loss.[5,6]

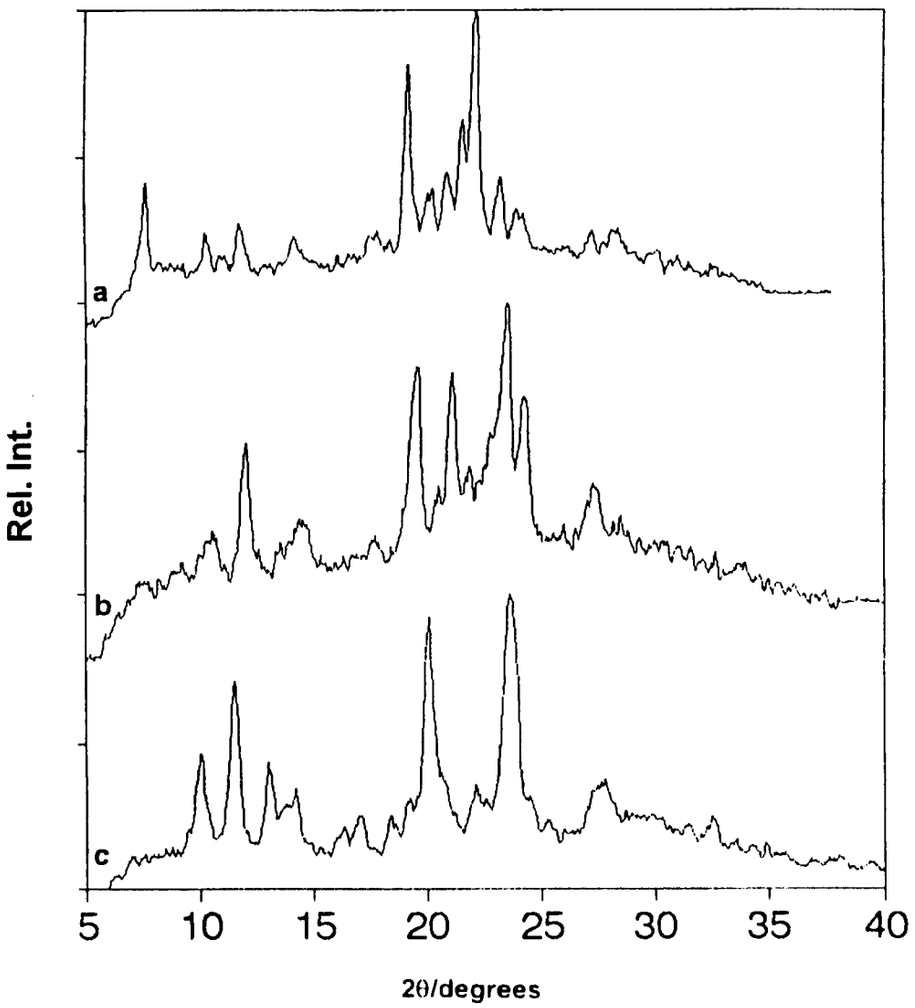

Fig 4.12. X-ray powder diffraction traces of a) **W17DIA**, b) after partial desolvation, c) after complete desolvation, corresponding to the host α-phase.

W17DB

$C_{38}H_{22}O_2Br_4 \cdot 3.5(C_4H_8O_2)$

Guest:1,4-dioxane

Space group: P $\bar{1}$

a=12.854(3) Å α=102.58(5)°

b=13.286(6) Å β=100.65(4)°

c=15.78(1) Å γ=108.66(3)°

Volume=2395(2) $Å^3$

Z=2

Tables containing complete crystal and refinement data appear at the end of this chapter.

Thermal Analysis

The TG trace for the desorption of **W17DB** indicates two overlapping mass loss steps. The two steps can be clearly distinguished in the DTG trace (Fig 4.13.). The total mass loss of 26.2% corresponds to the loss of 3.5 moles of 1,4-dioxane (calc. 27.1%). The two steps correspond to the loss of 2 moles of dioxane (calc. 15.5%, obs. 15.1%), followed by 1.5 moles (calc. 11.6%, obs. 11.1%). It was not possible to distinguish a third mass loss step as in the case of **W17DIA**. The DSC experiment yielded three endotherms corresponding to the guest loss. The first two endotherms, with onset temperatures of 94°C and 154°C correspond to the mass loss steps observed in the TG experiment. A third diffuse endotherm was observed at an onset temperature of 177°C. A sharp endotherm at 380°C corresponds to the melt of the host, which is accompanied by sublimation.

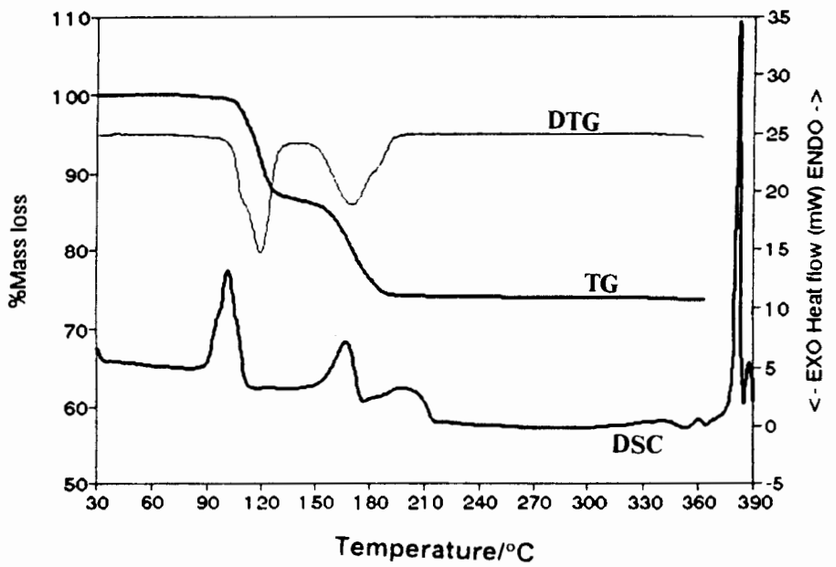

Fig 4.13. TG/DTG and DSC trace for **W17DB**.

Crystal Structure

Solution and Refinement

Direct methods yielded all the host non-hydrogen atoms in the asymmetric unit. The host molecule was located in a general position, and a whole molecule was placed in the asymmetric unit (Z=2). The non-hydrogen atoms in the guest molecules were located in the difference electron density maps upon subsequent refinement. The O atoms on the guest molecules were placed at the location of the highest peaks in the electron density map for each dioxane molecule. Refinement was carried out with the non-hydrogen atoms of the host treated anisotropically. The non-hydrogen atoms on one of the dioxane guest molecules (G1), as well as O(21) and O(31) on guest (G2) and (G3) respectively were also treated anisotropically. The non-hydrogen atoms of the remaining guest molecules were refined isotropically, since they exhibited relatively high thermal motion (U_{eq} > 0.09Å^2). Hydrogen atoms on the host were placed in geometrically constrained positions and refined with a common temperature factor for atoms of the same type. The hydroxyl hydrogens could not be located in a difference electron density map, and were placed in idealised positions, with tetrahedral C-O-H angles. The refinement of the hydroxyl hydrogen atoms was carried out using an established subroutine in SHELXL-93[7]. The H atoms were allowed to ride on the preceding O atom, and were rotated along the C-O bond, and placed in the region of maximum electron density. The isotropic

temperature factors were constrained at 120% that of the preceding O atom. The hydrogen atoms on guest (G1) and (G2) were placed in geometrically constrained positions and refined with a common temperature factor. The remaining guest hydrogen atoms were omitted from the final model. A residual electron density of 0.864eÅ^{-3} was observed. Most of the residual electron density peaks were observed in the region of the Br atoms, but could not be sensibly modelled. The structure refined successfully to R_1=0.0706.

The host conformation and the numbering scheme used are shown in Fig 4.14. The bond lengths and angles were all in the acceptable range for structures of this kind.

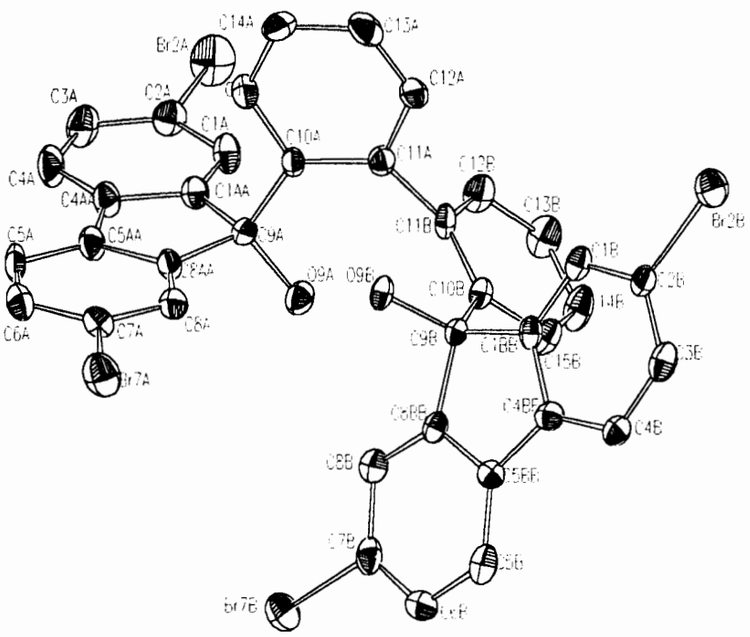

Fig 4.14. Host conformation of **W17DB**.

Three dioxane molecules are located in general positions ((G1), (G2) and (G4)), while one guest dioxane (G3) lies on a centre of inversion, at Wyckoff position *h*, thus yielding a host:guest ratio of 1:3.5, as for **W17DIA**. Analysis of the difference electron density maps showed that guest molecules (G3) and (G4) were again partially disordered. The final model therefore employed two positions for C(32) of guest (G3) [C(32) and C(32A) with a fractional site occupancy factor of 0.5 each] as shown in Fig 4.15. The site occupancy factors for these two atoms were linked and allowed to refine.

O(31)-C(32) 1.35(3)Å
O(31)-C(32A) 1.55(3)Å
C(36)-C(32) 1.47(3)Å
C(36)-C(32A) 1.43(3)Å.

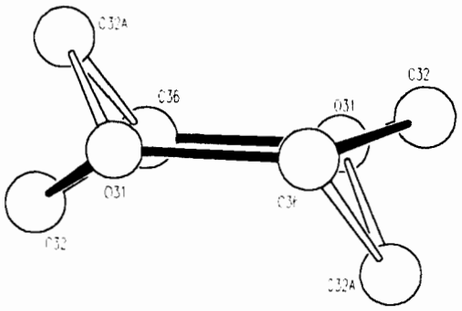

Fig 4.15. Disorder modelled in guest molecule (G3), **W17DB**. C(32) and C(32A) were placed with a s.o.f. 0.5 each.

In guest (G4), O(44), C(43) and C(46) were found to be disordered. The site occupancy factors for each atom and its disordered counterpart were linked and allowed to refine. The disorder in C(43) and C(46) was modelled with C(43) and C(46) with fractional site occupancy factors of 0.60 each, and subsequently C(43A) and C(46A) at 0.40 each. The site occupancy of O(44) refined to 0.68 and O(44A) to 0.32. The model of disorder in guest (G4) is shown in Fig 4.16.

O(41)-C(46)	1.53(2)Å
O(41)-C(46A)	1.47(4)Å
C(45)-C(46)	1.29(3)Å
C(45)-C(46A)	1.46(4)Å
C(42)-C(43)	1.32(3)Å
C(42)-C(43A)	1.39(4)Å
O(44)-C(43)	1.36(3)Å
O(44A)-C(43A)	1.34(4)Å
O(44)-C(45)	1.46(2)Å
O(44A)-C(45)	1.58(3)Å

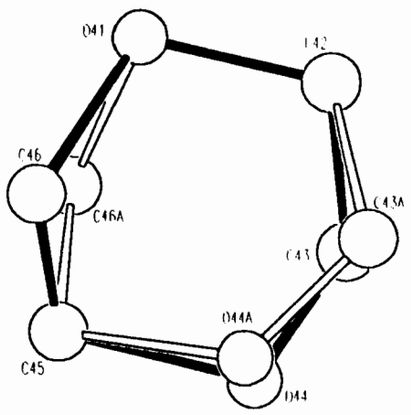

Fig 4.16. Disorder modelled in guest molecule (G4), **W17DB**. C(43) and C(46) were placed with a s.o.f. of 0.65, while C(43A) and C(46A) were placed with a s.o.f. of 0.35 each. O(44) and O(44A) were placed with s.o.f. of 0.68 and 0.32 respectively.

The same hydrogen bonding motif is observed as in the case of **W17DIA** , with two of the dioxane molecules hydrogen bonded to the host. One dioxane molecule, (G1), is bonded via one oxygen [O(9B)-H9B···O(11), with d(O···O) = 2.770(7)Å]. Molecule (G3), the dioxane molecule located on the centre of inversion, has two hydrogen bonds, related by the centre of inversion, [O(9A)-H(9A)···O(31), with d(O···O) = 2.840(9)Å].

Molecular Structure

The crystal structures of **W17DIA** and **W17DB** are isomorphous. Kálmán *et al.*[8] suggested the use of the synonym "isometric" above "isomorphous" since isomorphism is a morphological property which exists independently of the crystalline state. The host conformations of the two compounds are compared in Chapter 7. The host-guest arrangements, consisting each time of a host molecule and four crystallographically independent guest molecules, differ only in so far as the guest conformations are concerned.

The crystal packing, viewed down [001] and [010], for **W17DB** are shown in Fig 4.17. and Fig 4.18. respectively.

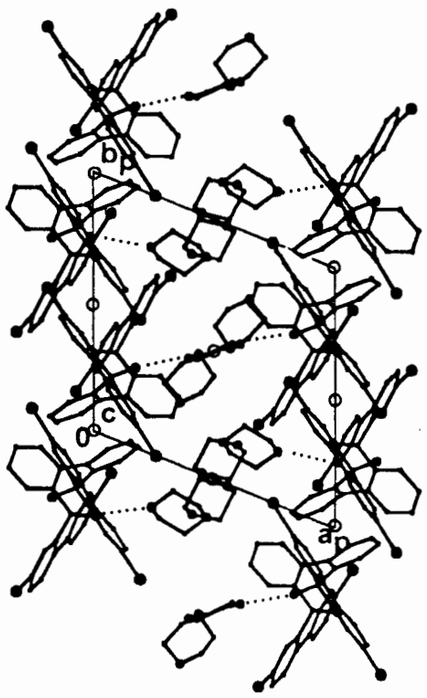

Fig 4.17. A projection down [001] showing the crystal packing in **W17DB**.

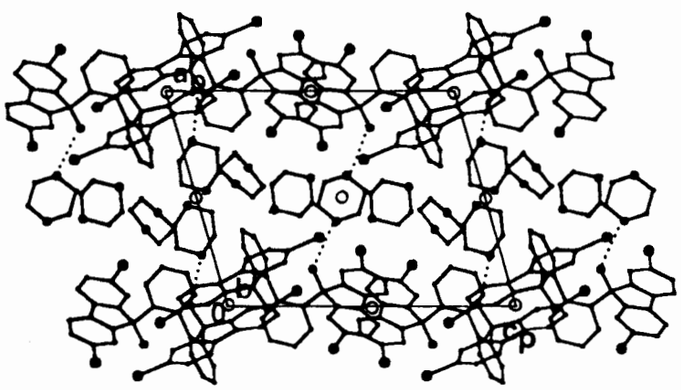

Fig 4.18. A projection down [010] showing the crystal packing in **W17DB**.

The guest molecules lie in distinct channels running parallel to [001]. This can be seen in Fig 4.19. where the hatched area represents the host, and the guest atoms are presented with van der Waals radii.

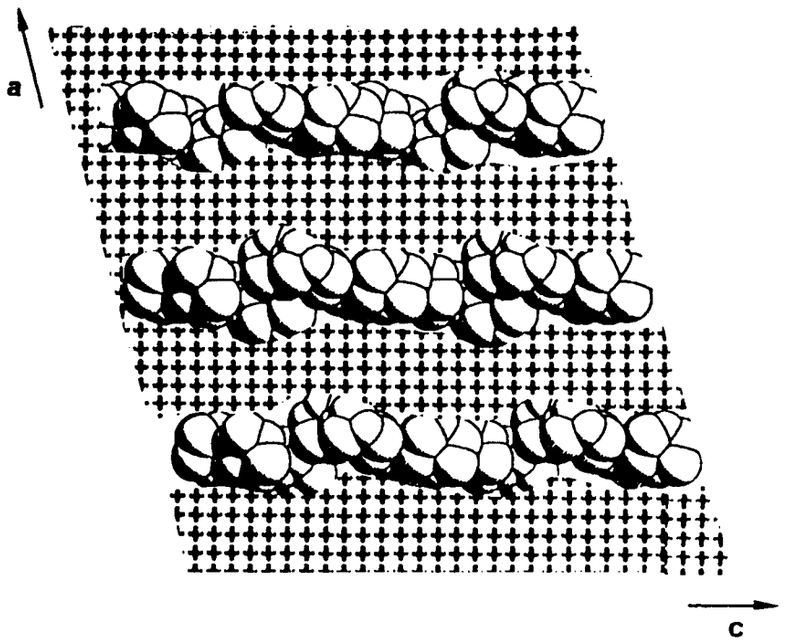

Fig 4.19. A projection of the crystal structure of **W17DB**, viewed down [010]. The hatched area represents a cross section of the host framework, cut at y=½, , while the guest is presented with van der Waals radii.

Kinetics

Attempts have been made to isolate the different desolvation steps of **W17DB**, in order to evaluate their kinetics. Although the ramped TG traces for **W17DIA** and **W17DB** showed similar features it was not possible to isolate two distinct desolvation steps for **W17DB** using isothermal TG. Various temperature programmes were implemented, but the resulting steps could not be separated into sensible stoichiometric mass losses.

WTB14D

$C_{54}H_{58}O_2 \cdot (C_4H_8O_2)$

Guest:1,4-dioxane

Space group: *C2/c*

a=17.217(5)Å

b=17.895(3)Å β=113.18(2)°

c=17.219(3)Å

V=4877(2)Å^3

Z=4

Tables containing complete crystal and refinement data appear at the end of this chapter.

Thermal Analysis

The thermal analytical results for **WTB14D** are shown in Fig 4.20. A single mass loss step of 10.8% was observed and corresponds to the loss of one mole of 1,4-dioxane (calc. 10.7%), confirming a host:guest ratio of 1:1. The guest loss corresponds to a single endotherm in the DSC trace, with an onset temperature of 179°C. A sharp endotherm, corresponding to the melt of the host compound was observed at 334°C.

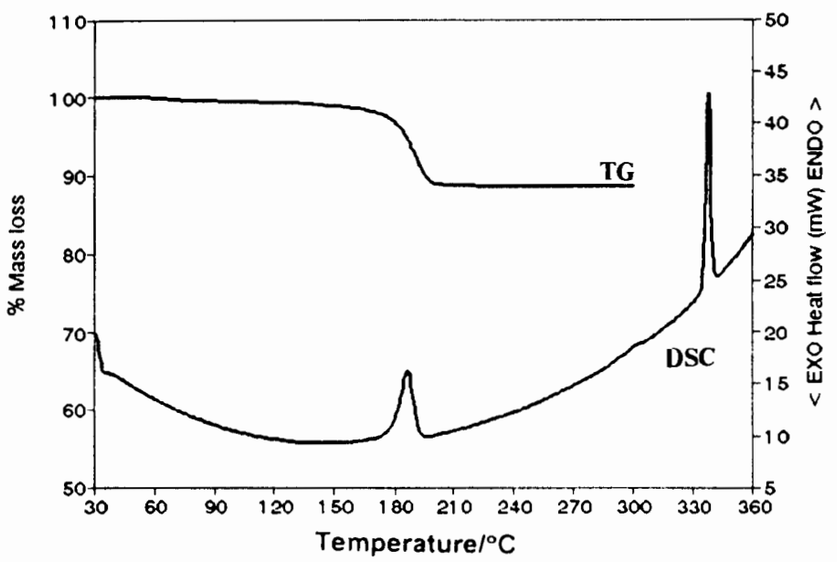

Fig 4.20. TG and DSC traces for **WTB14D**.

Hot Stage Microscopy

A series of photographs, depicting the changes occurring to **WTB14D** upon heating are shown in Colour Plate 5.2. Discrepancies between the temperatures at which the changes were observed on the hot stage and the thermal events observed for the powdered samples on the TG and DSC were mainly due to differences in the geometries of the instruments and particle sizes. Fairly large crystals were used on the hot stage (with diameters of 0.5 mm) as opposed to the powdered samples (10-100μm) used for the other thermal analysis experiments. At 98°C droplets of solvent appeared on the surface of the crystal of **WTB14D**. At 178°C the start of desolvation was observed, which was completed by 200°C. The crystal melted at 345°C.

Crystal Structure

Preliminary X-ray photography indicated that **WTB14D** belongs to the monoclinic crystal system (2/m Laue symmetry). The conditions limiting possible reflections

hkl h+k=2n

h0l l=2n; (h=2n)

0k0 (k=2n)

were observed, implying that the space group was either *Cc* or *C2/c*. The centrosymmetric space group *C2/c* was chosen, based on the intensity statistics obtained from the direct methods run. The choice of the centrosymmetric space group was vindicated by the successful final refinement of the structure in this space group.

Colour Plate 4.2.

a) A crystal of **WTB14D** at room temperature. 28X enlarged.

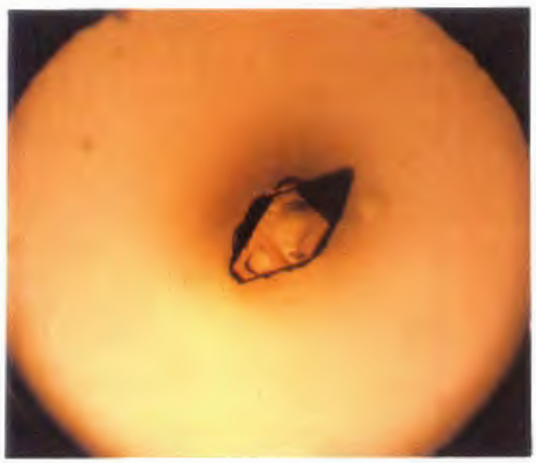

b) At 98°C droplets of guest (1,4-dioxane) appeared on the surface of the crystal of **WTB14D**. 28X enlarged.

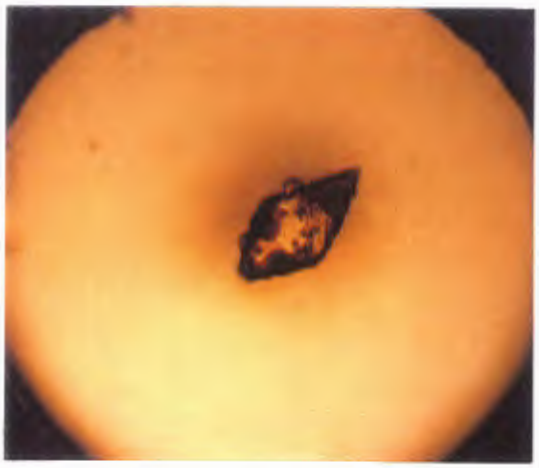

c) At 178°C the appearance of defects in the crystal was observed. 28X enlarged.

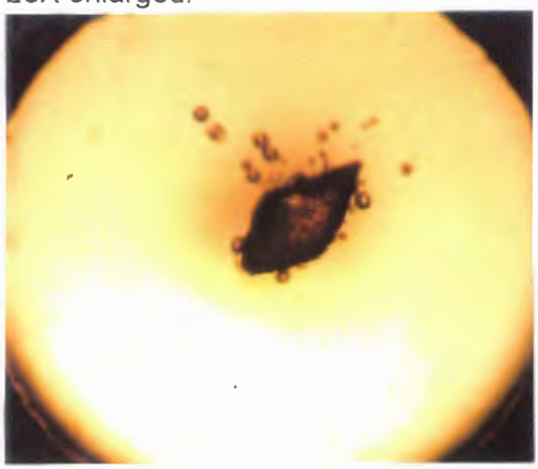

d) Guest loss was observed at 190°C, as bubbles in the silicone oil, and was completed by 200°C. 28X enlarged.

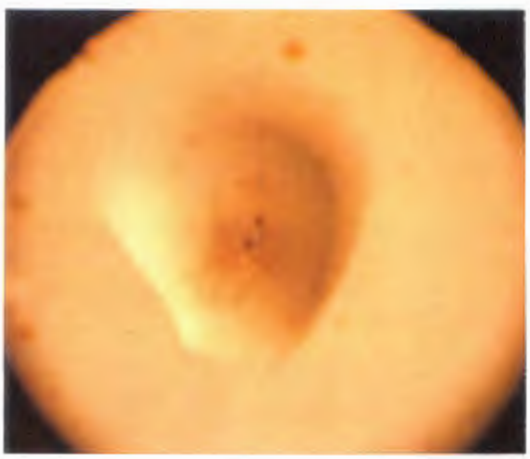

e) The crystal finally melted at 345°C. 28X enlarged.

Solution and Refinement

Direct methods yielded the positions of all the host non-hydrogen atoms in the asymmetric unit, except for the C atoms on the *tert*-butyl groups, which were located in the difference electron density map upon subsequent refinement. **WTB14D** crystallises in the space group *C2/c* with Z=4. The host molecule exhibits two-fold symmetry and was placed with the central biphenyl bond on a special position, located on a diad at Wyckoff position *e*. The non-hydrogen atoms in the guest molecule were located in the difference electron density maps upon subsequent refinement. Most of the host non-hydrogen atoms were refined anisotropically. High thermal motion was observed in the *tert*-butyl groups and only the pivotal C atoms [C(16A) and C(20A)] were refined anisotropically. The temperature factors of the remaining carbon atoms on the *tert*-butyl groups were typically high, with U_{eq} = 0.11Å^2. The guest showed high thermal motion and was refined isotropically. A residual electron density of 0.508eÅ^{-3} was observed in the region of the guest and could not be modelled. The hydroxyl hydrogen atoms were located in the difference electron density maps and refined with bond length constraints and individual temperature factors. The rest of the hydrogen atoms were placed with geometric constraints and refined with a common isotropic temperature factor for similar groups. The structure refined successfully to R_1= 0.0867.

The conformation of the host molecule, with atomic numbering scheme, is shown in Fig. 4.21. The host molecule is locked into conformation [with C(10A)-C(11A)-C(11A')-C(10A') = 90(1)°] via an intramolecular hydrogen bond [O(9A) ···O(9A')=2.744(7)Å].

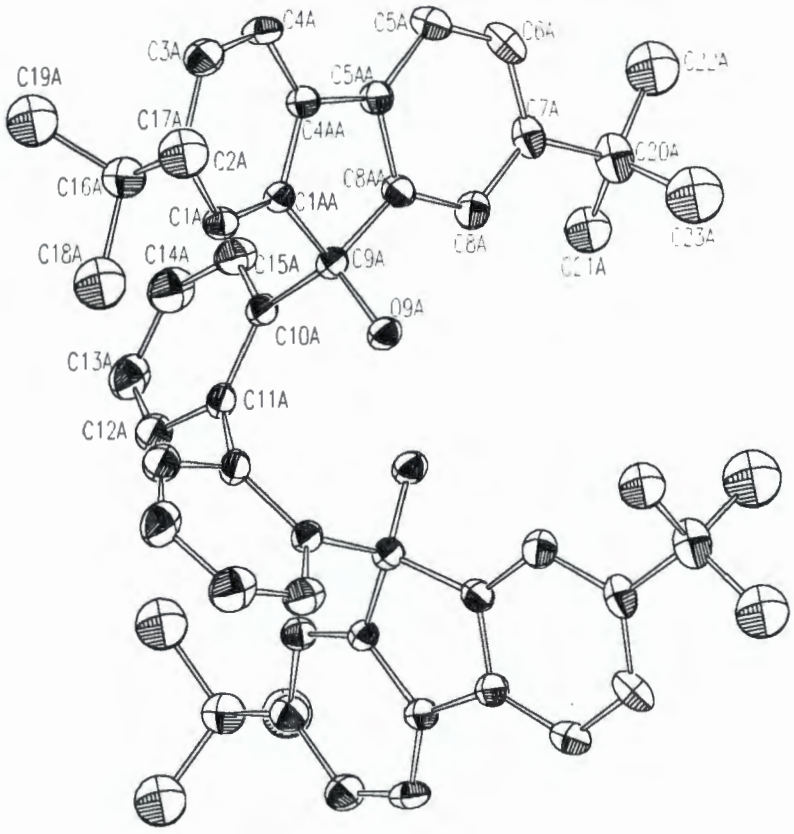

Fig 4.21. Host conformation of **WTB14D**.

The host:guest ratio of 1:1 requires half a 1,4-dioxane molecule to be located in the asymmetric unit. The dioxane molecule was located on a centre of inversion, at Wyckoff position *a*. Careful analysis of the difference electron density map revealed that the guest molecule is in fact disordered. The dioxane molecule was modelled with two possible positions for the oxygen atom [O(2G) with a site occupancy of 0.70 and O(2GA), with a site occupancy of 0.30]. The site occupancy factors were based on the relative peak heights in the electron density map. Fig 4.22. depicts the disorder in the guest molecule. An intermolecular hydrogen bond exists between the guest molecule and host with O(9A)-H(9A)···O(2G) = 2.81(1)Å. O(2GA) does not take part in any hydrogen bonding.

C(1G)-O(2G)	1.34(1)Å
C(1G)-O(2GA)	1.57(2)Å
C(3G)-O(2GA)	1.30(2)Å
C(3G)-O(2G)	1.50(1)Å

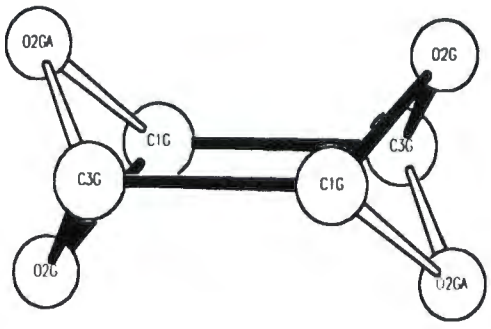

Fig 4.22. Disorder modelled in guest molecule. O(2G) and O(2GA) were placed with s.o.f. of 0.70 and 0.30 respectively.

Molecular Structure

The molecular structure of **WTB14D** is shown in Fig 4.23. The crystal packing, viewed down [001] and [010], are shown in Fig 4.24. and Fig 4.25. respectively. The guests lie in constricted channels running parallel to [001]. This can be seen in Fig 4.26. where the host is represented with van der Waals radii and the guest has been omitted.

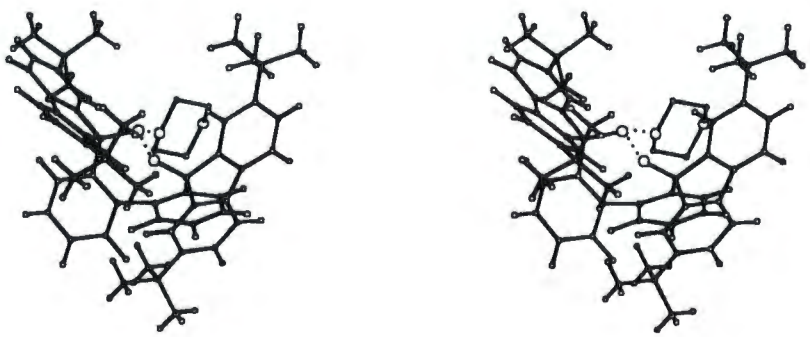

Fig 4.23. Molecular structure of **WTB14D**.

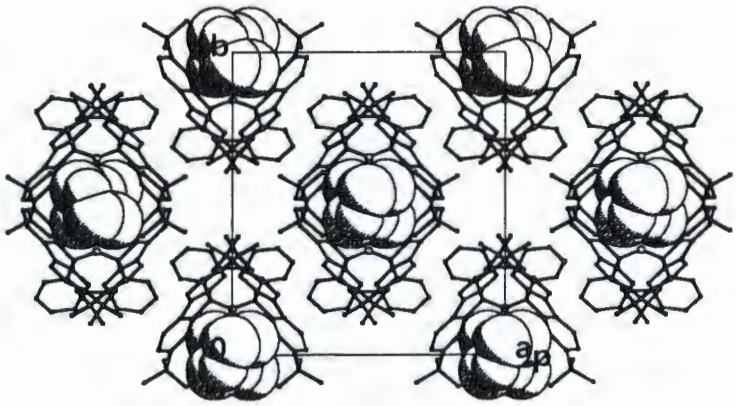

Fig 4.24. A projection down [001] showing the crystal packing in **WTB14D**.

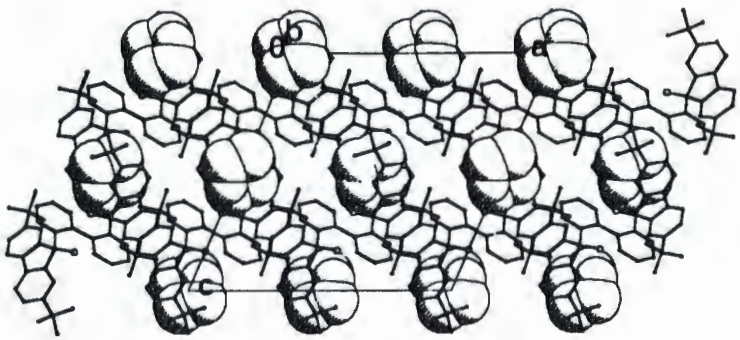

Fig 4.25. A projection down [010] showing the crystal packing in **WTB14D**.

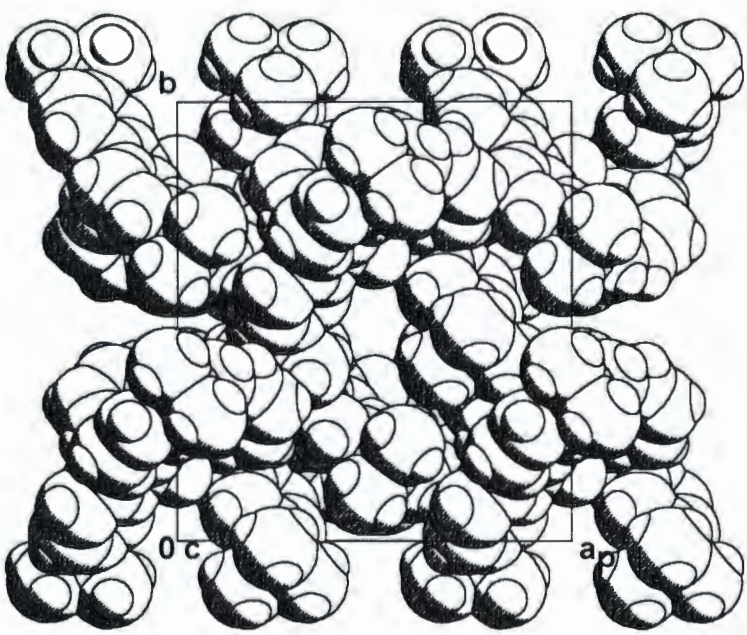

Fig 4.26. A space filled diagram of the host in **WTB14D** viewed down [001].

Kinetics

A series of isothermal TG experiments were carried out on **WTB14D**, at 2-3°C intervals over a temperature range of 148-160°C. The resultant mass loss *vs.* time curves were reduced to extent of reaction (α) *vs.* time curves. These curves were deceleratory and the data were best fitted over an α range of 0.05-0.95 by the first order (F1) reaction mechanism. A plot of *ln k vs. 1/T* is shown in Fig 4.27., which yielded an activation energy of 150(6)kJ/mol.

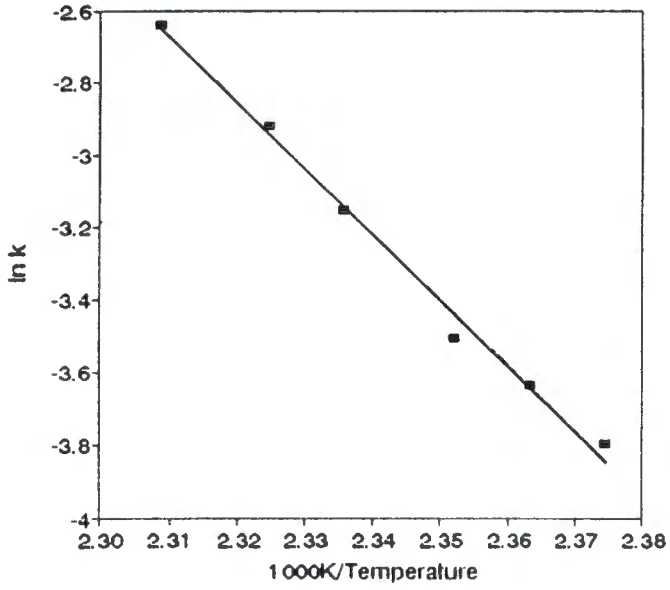

Fig 4.27. Arrhenius plot for the desolvation reaction of **WTB14D**.

X-Ray Powder Diffraction

The host crystal structure changes upon desolvation to the non-porous α-phase. This is clearly seen in Fig. 4.28. in which the calculated powder pattern for the inclusion compound (**WTB14D**) is compared with the powder diffraction trace obtained experimentally for the desolvated host compound.

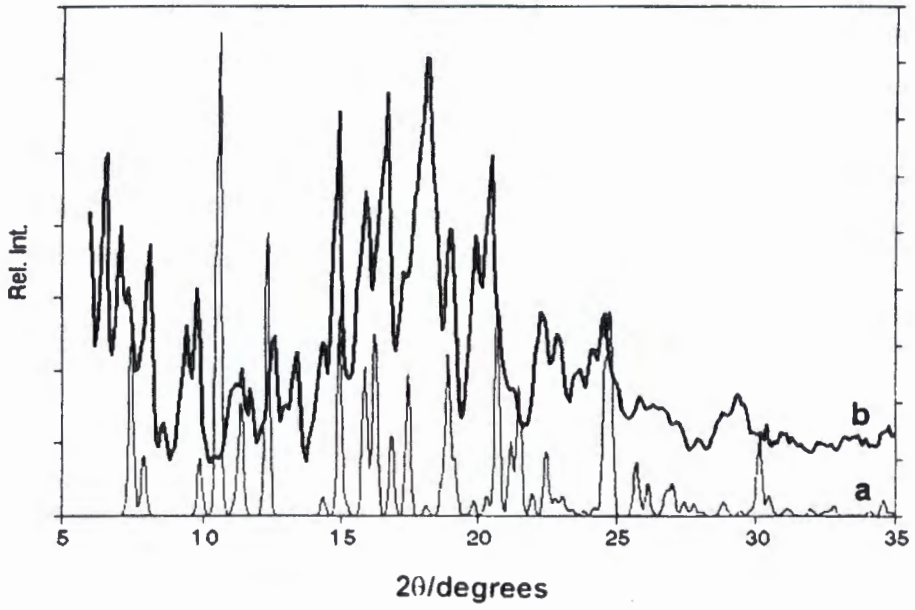

Fig 4.28. X-ray powder diffraction patterns for a) **WTB14D**, b) the desolvated, α-phase of the host compound.

Discussion

Both $C_{38}H_{22}O_2Cl_4$ (host **A1**) and $C_{38}H_{22}O_2Br_4$ (host **A2**) form 2:7 inclusion compounds with 1,4-dioxane (**W17DIA** and **W17DB** respectively), and crystallise in the triclinic space group, P $\bar{1}$. In each case four crystallographically independent guest molecules were observed. The interactions of these guest molecules with the host vary widely. One guest molecule (G3) is linked via two hydrogen bonds to two separate host molecules, while another (G1) is linked to the host via one hydrogen bond. The remaining two guest molecules are not hydrogen bonded and one (G4) shows high thermal motion in both structures. From the crystal structure we know that the guest molecules are located in channels, running parallel to [001]. There seems to be no physical barrier to guest loss, except for hydrogen bonding which stabilises the structure. Multiple desolvation steps are clearly visible in the thermal analytical results of both compounds. It was possible to separate two distinct steps for the desolvation of **W17DIA** and the kinetics of these steps could be successfully analysed. A stable intermediate, γ-phase (with host:guest ratio of 1:1) was isolated

and characterised by X-ray powder diffraction. It is clearly different from both the α- and β- phases. Attempts to obtain single crystals of the γ-phase failed. It is tempting to postulate that the two guest molecules which are not hydrogen bonded, i.e. (G2) and (G4), are the first to be lost upon desolvation (this would correspond to the first mass loss step observed in the programmed temperature TG trace). This step could not be separated from the loss of another half a guest molecule (again observed in the programmed temperature TG run), in the isothermal TG experiments. It is important to note that the guest loss process is accompanied by a change in the structure of the inclusion compound. The structure is rearranging to form the stable intermediate 1:1 inclusion compound (the γ-phase). This intermediate compound is stable up to 100°C. The activation energy for the first desolvation step of 34(3) kJ mol^{-1} is remarkably lower than that for the second step, 111(9) kJ mol^{-1}. Both desolvation steps observed for **W17DIA** follow the apparent first order mechanism. There is no physical explanation for reactions based on order with respect to α, since concentration is not usually a meaningful term in solid state reactions[4].

$C_{54}H_{58}O_2$ (host **A3**) forms a 1:1 inclusion compound with 1,4-dioxane (**WTB14D**), which is remarkably stable. The isothermal desolvation reached completion only above 148°C and an activation energy of 150(6)kJ.mol^{-1} was obtained. The constricted channel structure would imply that the gaseous decomposition product can escape only by severely disrupting the host framework. A further possible explanation of the stability and higher activation energy observed for **WTB14D** lies in the fact that the host molecules are rendered rigid by an intramolecular hydrogen bond. This may also impede the phase transformation to the α-phase, which occurs upon desolvation. It is important to note that the change in phase cannot be accounted for in the kinetic models obtained, since the extent of reaction was measured as a function of the guest loss.

Code	W17DIA	W17DB	WTB14D
Guest	1,4-dioxane	1,4-dioxane	1,4-dioxane
Molecular formula	$C_{38}H_{22}O_2Cl_4 \cdot 3.5(C_4H_8O_2)$	$C_{38}H_{22}O_2Br_4 \cdot 3.5(C_4H_8O_2)$	$C_{54}H_{58}O_2 \cdot C_4H_8O_2$
M_r/g mol^{-1}	960.77	1138.58	827.16
Temperature/K	294(2)	294(2)	294(2)
Crystal data			
Crystal system	Triclinic	Triclinic	Monoclinic
Space group	$P\bar{1}$	$P\bar{1}$	*C2/c*
a/Å	12.878(4)	12.854(3)	17.217(5)
b/Å	13.221(3)	13.286(6)	17.895(3)
c/Å	15.78(1)	15.78(1)	17.219(3)
α/°	102.95(4)	102.58(5)	90.0
β/°	100.53(4)	100.65(4)	113.18(2)
γ/°	108.83(2)	108.66(3)	90.0
Z	2	2	4
V/Å^3	2382(2)	2395(2)	4877(2)
D_C/g cm^{-3}	1.340	1.579	1.127
μ(MoK_α) /cm^{-1}	3.05	34.17	0.78
F(000)	1004	1148	1880
Data collection			
Crystal dimensions /mm	0.34 x 0.31 x 0.31	0.34 x 0.38 x 0.34	0.28 x 0.28 x 0.28
Range scanned θ/°	1.38 to 24.97	1.38 to 25.09	1.72 to 24.98
Range of indices *h,k,l*	-15,15; -15,15; -18,18	-15,15; -15,15; -18,18	-20,18; 0,21; 0,20
No. of reflections collected	8684	8745	4457
No. of unique reflections	8350	8412	4300
No. of reflections observed with $I_{rel}>2\sigma(I_{rel})$	4133	4191	2025
Final refinement			
No. of restraints	4	0	2
No. of parameters	535	545	288

Code	W17DIA	W17DB	WTB14D
Guest	1,4-dioxane	1,4-dioxane	1,4-dioxane
Molecular formula	$C_{38}H_{22}O_2Cl_4 \cdot 3.5(C_4H_8O_2)$	$C_{38}H_{22}O_2Br_4 \cdot 3.5(C_4H_8O_2)$	$C_{54}H_{58}O_2 \cdot C_4H_8O_2$
M_r/g mol^{-1}	960.77	1138.58	827.16
Temperature/K	294(2)	294(2)	294(2)
Crystal data			
Crystal system	Triclinic	Triclinic	Monoclinic
Space group	$P\bar{1}$	$P\bar{1}$	$C2/c$
a/Å	12.878(4)	12.854(3)	17.217(5)
b/Å	13.221(3)	13.286(6)	17.895(3)
c/Å	15.78(1)	15.78(1)	17.219(3)
α/°	102.95(4)	102.58(5)	90.0
β/°	100.53(4)	100.65(4)	113.18(2)
γ/°	108.83(2)	108.66(3)	90.0
Z	2	2	4
V/Å^3	2382(2)	2395(2)	4877(2)
D_c/g cm^{-3}	1.340	1.579	1.127
$\mu(MoK_\alpha)$ /cm^{-1}	3.05	34.17	0.78
F(000)	1004	1148	1880
Data collection			
Crystal dimensions /mm	0.34 x 0.31 x 0.31	0.34 x 0.38 x 0.34	0.28 x 0.28 x 0.28
Range scanned θ/°	1.38 to 24.97	1.38 to 25.09	1.72 to 24.98
Range of indices *h,k,l*	-15,15; -15,15; -18,18	-15,15; -15,15; -18,18	-20,18; 0,21; 0,20
No. of reflections collected	8684	8745	4457
No. of unique reflections	8350	8412	4300
No. of reflections observed with $I_{rel}>2\sigma(I_{rel})$	4133	4191	2025
Final refinement			
No. of restraints	4	0	2
No. of parameters	535	545	288
R1 ($I_{rel}>2\sigma(I_{rel})$)	0.0954	0.0685	0.0894
wR2 ($I_{rel}>2\sigma(I_{rel})$)	0.2991	0.1779	0.2596
Extinction coefficient	0.008(2)	-	-
Max. height in electron density map /eÅ^{-3}	0.896	0.869	0.632
Min. height in electron density map /eÅ^{-3}	-0.736	-0.921	-0.455
Absorption Correction factor range	0.9860-0.9914	0.8015-0.9994	-

1 W.W.M. Wendtlandt, *Thermal Analysis*, John Wiley and Sons, New York, 1964.

2 P. Schuster, G. Zundel and C. Sanderfy, *The Hydrogen Bond II, Structure and Spectroscopy*, North Holland Publishing Co., Amsterdam, 1976, 411.

3 F.H. Allen, O. Kennard, D.G. Watson, L. Brammer, A.G. Orpen, R. Taylor, *J. Chem Soc. Perkin Trans. 2*, 1987, S1-S19.

4 M.E. Brown, D. Dollimore and A.K. Galwey, *Comprehensive Chemical Kinetics*, ed. C.H. Bamford and C.J. Tipper, Elsevier, Amsterdam, 1980, vol.22, 220.

5 D.R. Bond, M.R. Caira, G.A. Harvey, L.R. Nassimbeni and F. Toda, *Acta Crystallogr.*, **B46**, 1990, 771.

6 S.A. Bourne, L.R. Nassimbeni, K. Skobridis and E. Weber, *J. Chem. Soc., Chem. Commun.*, 1991, 282.

7 G.M. Sheldrick, SHELXL-93: Programme for Crystal Structure Determination, unpublished work.

8 A. Kálmán, L. Parkanyi and G Argay, *Acta Crystallogr.*, **B49**, 1993, 1039.

CHAPTER 5 INCLUSION COMPOUNDS OF HOSTS IN CLASS A WITH 1,3-DIOXOLANE AND 1,3-DIOXANE.

In this chapter the thermal analysis, crystal structures and kinetics of desolvation of the host compounds $C_{38}H_{22}O_2Cl_4$ (host **A1**) and $C_{38}H_{22}O_2Br_4$ (host **A2**) with 1,3-dioxolane (**W17** and **WB3DA**) and $C_{38}H_{22}O_2Cl_4$ with 1,3-dioxane (**W13DT**) are discussed. **W17**, **WB3DA** and **W13DT** are isostructural. Kálmán *et al.*[1] pointed out that molecular associates, such as clathrates, are often isostructural, possessing similar host skeletons with different guest molecules in their voids. Depending on the relationship between the different guest molecules, the crystal pairs may exhibit varying degrees of isostructurality.

W17

$C_{38}H_{22}O_2Cl_4 \cdot 2(C_3H_6O_2)$
Guest:1,3-dioxolane
Space group: *C2/c*
a=21.954(3)Å
b=11.423(2)Å β=123.63(2)°
c=18.157(3) Å
V=3791 (1) Å^3
Z=4

Tables containing complete crystal and refinement data appear at the end of this chapter.

Thermal Analysis

The TG, DTG and DSC traces for the desolvation of **W17** are shown in Fig 5.1. Desolvation takes place in a single step, seen in the TG trace, which corresponds to an endotherm, with an onset temperature of 133°C in the DSC trace. Note that the mass loss step in the TG experiment starts at a lower temperature, *ca* 110°C. This difference in onset temperature between the TG and DSC is due to the different geometries of the instruments[2]. The DSC sample pan is covered with a vented

aluminium lid, whereas the TG sample pan is open. Hence a better defined and reliable onset temperature is obtained from the DSC experiment . The host:guest ratio of 1:2 was established by the TG experiment, showing a mass loss of 18.8% (calc. 18.5%). The host melts at 340°C.

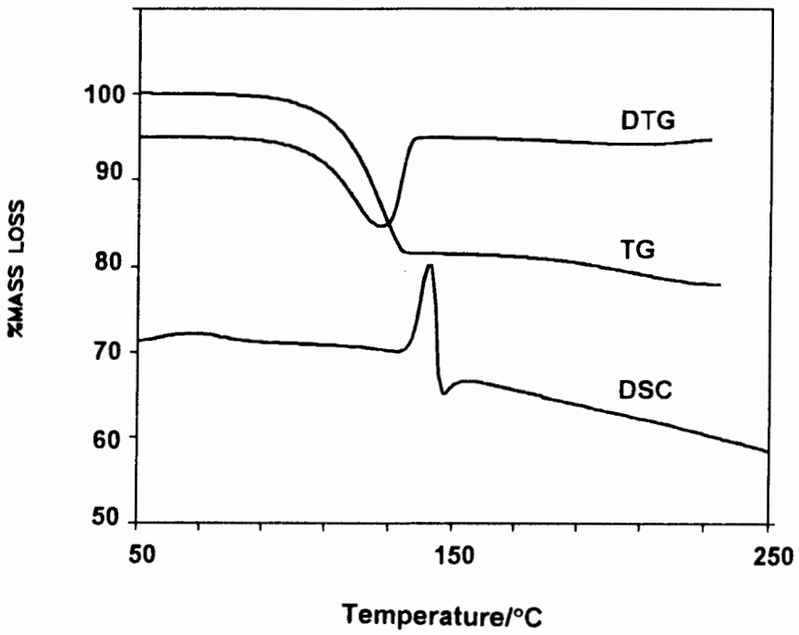

Fig 5.1. TG/DTG and DSC of **W17**

Hot Stage Microscopy

A single crystal of **W17** was placed on the hot stage microscope, under a drop of silicone oil and heated. A series of photographs depicting the changes occurring upon heating are shown in Colour Plate 5.1. They show the crystal starting to crack at 89°C, perpendicular to the direction of *c*. These cracks spread through the crystal, without desorption taking place. At 162°C the crystal turns opaque and the guest is lost. Upon desorption the crystal breaks up. The melt was observed at 350°C.

Colour Plate 5.1.

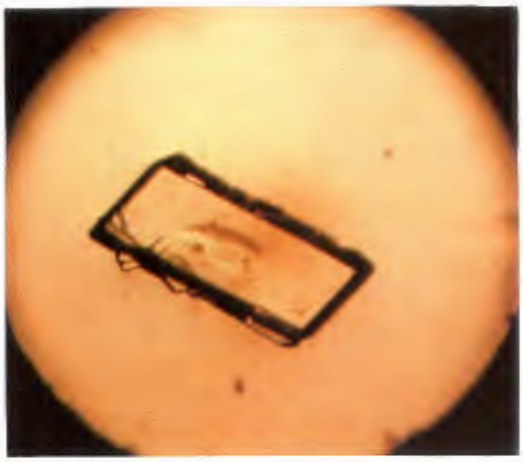

a) A single crystal of **W17** was placed in silicone oil, at room temperature. 28X enlarged.

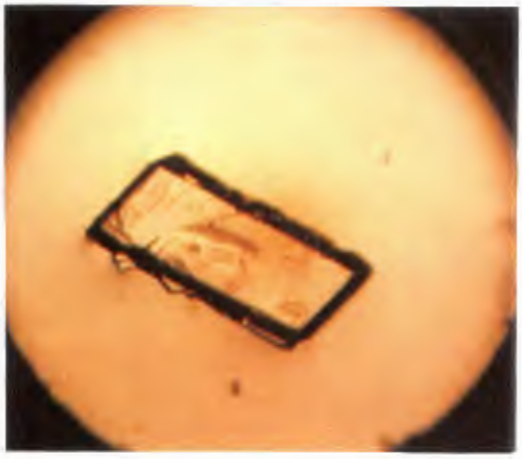

b) At 89°C small cracks appeared, perpendicular to the long axis of the crystal. 28X enlarged.

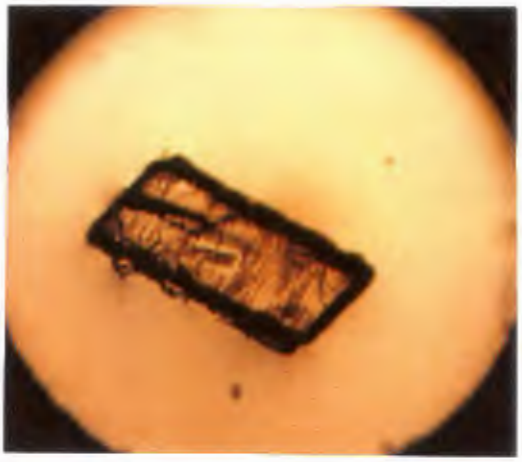

c) At 95°C more cracks appeared in the crystal. 28X enlarged.

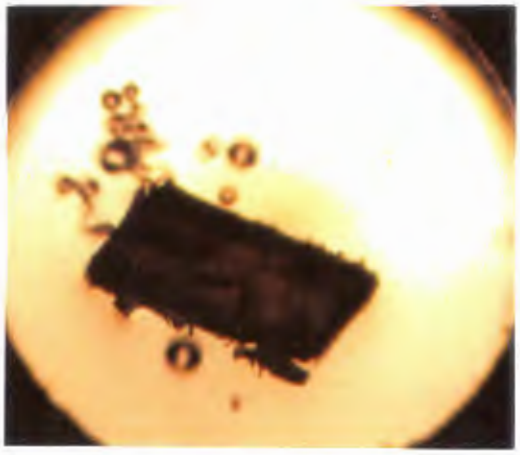

d) At 160°C the guest was first lost from the major cracks in the crystal. 28X enlarged.

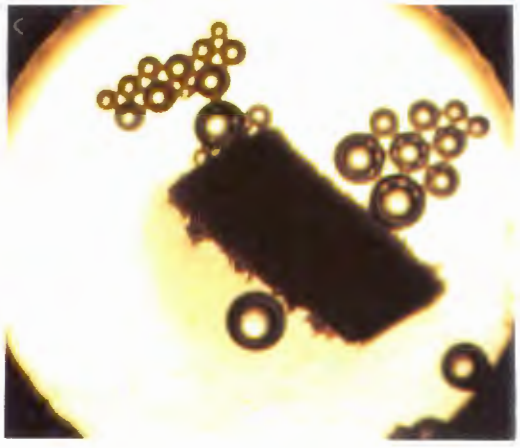

e) After completion of the guest loss step (1 min at 160°C). 28X enlarged.

Crystal Structure

Preliminary photography indicated that **W17**, as well as **WB3DA** and **W13DT** belong to the monoclinic crystal system (2/m Laue symmetry). The reflection conditions

hkl	h+k=2n
h0l	l=2n; (h=2n)
0k0	(k=2n)

were observed, implying that the space group was either *Cc* or *C2/c*. In each case the centrosymmetric space group *C2/c* was chosen, based on the mean $|E^2-1|$ values obtained from the direct methods run. This choice was vindicated in each case by the successful refinement of the structures.

Solution and Refinement

Direct methods yielded all host non-hydrogen atoms. There are four host molecules in the unit cell, and these were located at Wyckoff position *e*, on the diads, thus fulfilling the symmetry requirements for the space group *C2/c*. The dioxolane guest molecule was located upon subsequent refinement. The O atoms on the guest molecule were placed as follows: O(1G) was located as a very strong peak in the electron density map. It was also located within hydrogen bonding distance from the hydroxyl O on the host molecule, and could therefore confidently be placed as an O atom. There was not much difference in electron density between the peaks representing O(3G) and C(4G). Both peaks were originally placed as C atoms and allowed to refine. The temperature factor for peak C(3G) was much higher than those of the other C atoms in the guest, and it was changed to an O atom. This resulted in the satisfactory refinement of the thermal motion parameter. All the host non-hydrogen atoms were treated anisotropically. The guest non-hydrogen atoms were treated isotropically, since they showed comparatively high thermal motion (U_{eq} *ca* 0.10Å^2). The hydroxyl hydrogen atoms were located in the difference electron density maps and refined with bond length constraints[3] and individual temperature factors. The rest of the hydrogen atoms were placed with geometric constraints and refined with common isotropic temperature factors for similar hydrogens. A

residual electron density of 0.669 eÅ^{-3} was observed in the region of the guest, but could not be modelled. The structure refined successfully to R_1=0.0680.

Half a host molecule was placed in the asymmetric unit, and Fig 5.2. shows the conformation of the host, as well as the numbering scheme used.

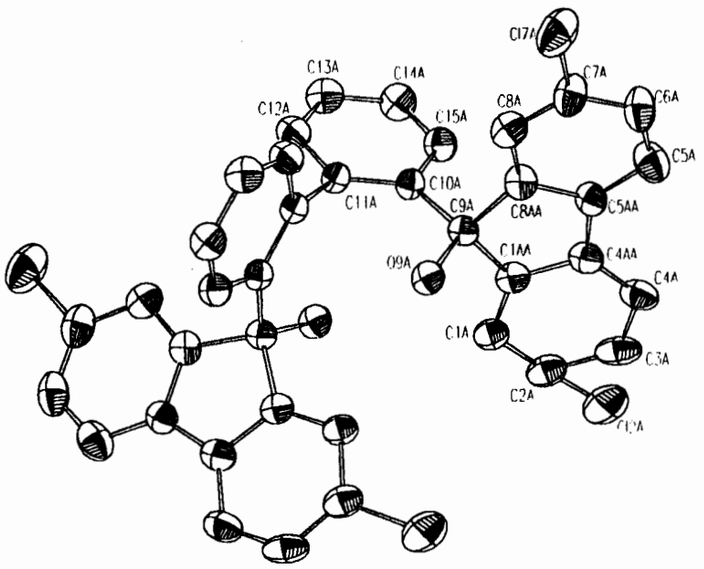

Fig 5.2. Host conformation of **W17**.

The host:guest ratio of 1:2 required one dioxolane molecule in the asymmetric unit, located in a general position. No disorder was found in the positions of the dioxolane guests. Each guest exhibits one hydrogen bond to the host [O(9A)-H(9A)···O(3G), with d(O···O) = 2.868(6)Å].

Molecular Structure

A stereo view of the molecular structure of **W17** is shown in Fig 5.3.

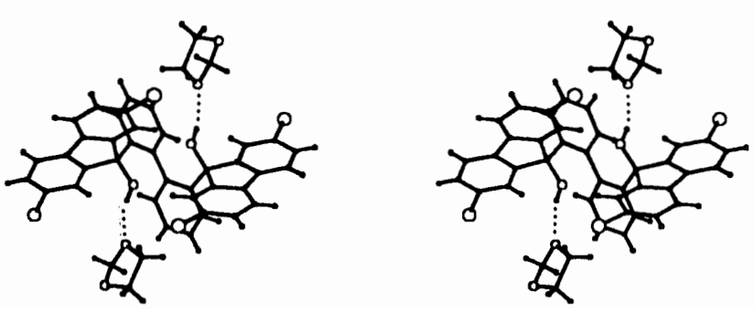

Fig 5.3. Molecular structure of **W17.**

The crystal packing, as viewed down [010] and [001], is shown in Figs 5.4. and 5.5., respectively. The 1,3-dioxolane molecules, propagated by a two-fold screw axis, are located in channels running parallel to [010]. The guest molecules are located in the channel with one O atom pointing towards the host hydroxyl group, resulting in an intermolecular H-bond which stabilises the structure.

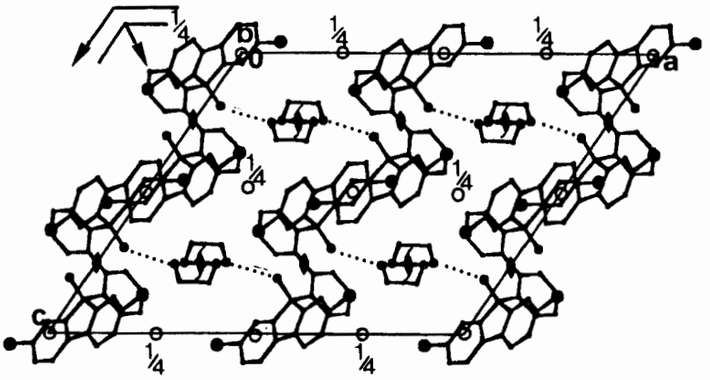

Fig 5.4. Projection of crystal packing in **W17** viewed down [010].

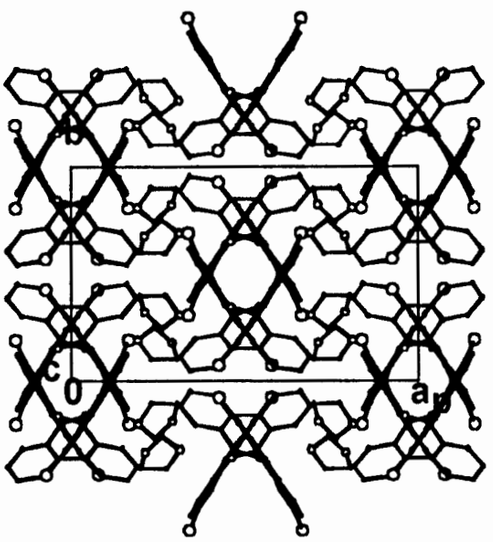

Fig 5.5. Projection of crystal packing in **W17** viewed down [001].

Kinetics

A series of isothermal TG experiments were carried out over a temperature range of 60-72°C. The resultant α *vs.* time curves were deceleratory. Appropriate kinetic models were tested for linearity and the data were best described by the contracting area (R2) kinetic model: $kt=1-(1-\alpha)^{1/2}$.

An activation energy of 129 (16) kJ mol^{-1} was obtained for this reaction over an α-range of 0 to 0.95. A curve of *ln k vs. 1/T* is shown in Fig. 5.6.

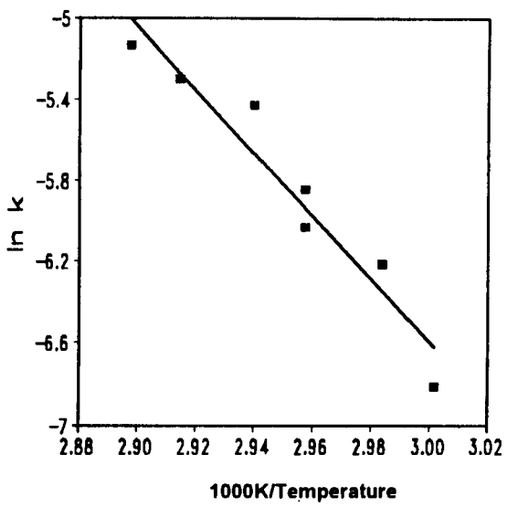

Fig 5.6. Arrhenius plot for the desolvation of **W17**.

X-Ray Powder Diffraction

In Fig 5.7. the calculated X-ray powder diffraction pattern of the inclusion compound is compared with that obtained experimentally upon desolvation. It is clear that the guest loss reaction is accompanied by a phase change of the structure of the host compound. The solvated β-form is transformed to the non-porous α-phase.

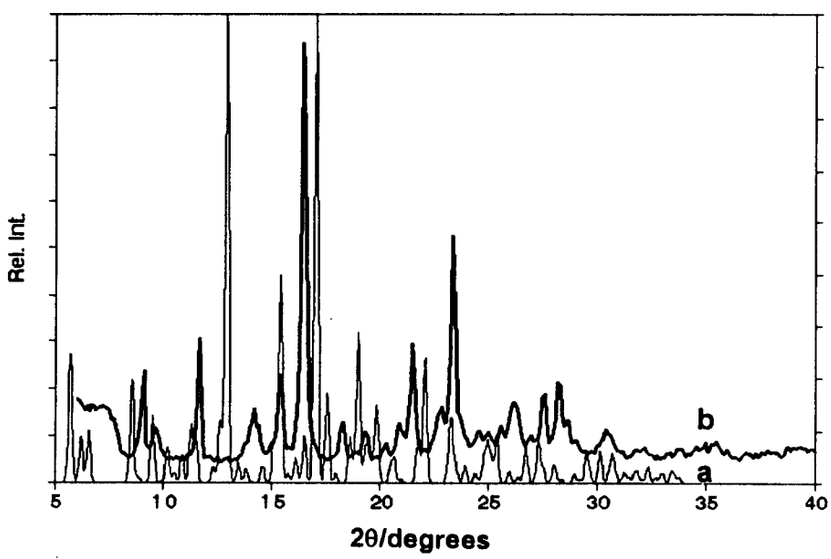

Fig 5.7. X-ray powder diffraction patterns of a) **W17**, b) the desolvated α-phase of the host compound.

WB3DA

$C_{38}H_{22}O_2Br_4 \cdot 2(C_3H_6O_2)$

Guest: 1,3-dioxolane

Space group: *C2/c*

a=21.570(8)Å

b=11.717(3)Å β=124.22(4)°

c=18.37(1)Å

V= 3840(4)Å^3

Z= 4

Tables containing complete crystal and refinement data appear at the end of this chapter.

Thermal Analysis

The guest loss reaction corresponds to a single mass loss step in the TG trace (see Fig 5.8.). The DSC trace shows three endotherms at onset temperatures of 103°C, 166°C and 357°C respectively. The first endotherm corresponds to the guest loss process. Based on the results obtained from hot stage microscopy carried out on a single crystal of **WB3DA** (discussed below), the second endotherm was attributed to the partial decomposition of the host compound. The third endotherm corresponds to the host melt.

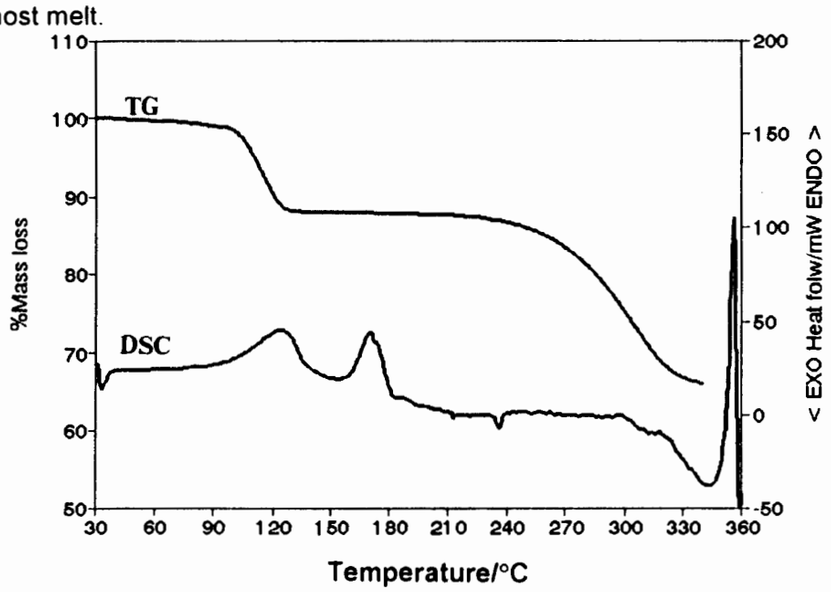

Fig 5.8. TG and DSC traces for **WB3DA**.

Hot Stage Microscopy

Two photographs depicting crystals of **W17DB** (discussed in Chapter 4), the first at room temperature and the second when it melts at 380°C are shown in Colour Plate 5.2. in order to compare the melting of the pure host (**A2**), with that of the partially decomposed host. A single crystal of **WB3DA** was placed on the hot stage and heated. A series of photographs depicting the changes occurring upon heating are shown in colour Plate 5.2. At 136°C guest loss commences and the crystal becomes opaque. As guest loss continues the crystal decomposes and discoloration takes place. When the crystal melts at 360°C, a brown decomposition product is visible.

Crystal Structure

Solution and Refinement

Direct methods yielded the positions of all the host non-hydrogen atoms. There are four host molecules in the unit cell, and these were located on the diads, as in **W17** above. The dioxolane guest molecule was located upon subsequent refinement. The O atoms on the guest molecule were placed in the location of the two highest peaks in the difference electron density map. O(1G) was also located within hydrogen bonding distance from the hydroxyl O on the host molecule, and could therefore confidently be placed as an O atom. O(3G) corresponded to the next highest peak in the difference map, and was placed as an O since it was in the 3-position relative to O(1G). All the host non-hydrogen atoms were treated anisotropically. The guest non-hydrogen atoms were treated isotropically, since they showed comparatively high thermal motion (U_{eq} > 0.09Å^2). The hydroxyl hydrogen atoms were located in the difference electron density maps and refined with bond length constraints[3] and individual temperature factors. The rest of the hydrogen atoms were placed with geometric constraints and refined with common isotropic temperature factors for similar hydrogens. A residual electron density of 0.669 eÅ^{-3} was observed in the region of the guest, but could not be modelled. The structure refined successfully to R_1=0.0462.

Colour Plate 5.2.

a) Single crystals of **W17DB** at room temperature. 60X.

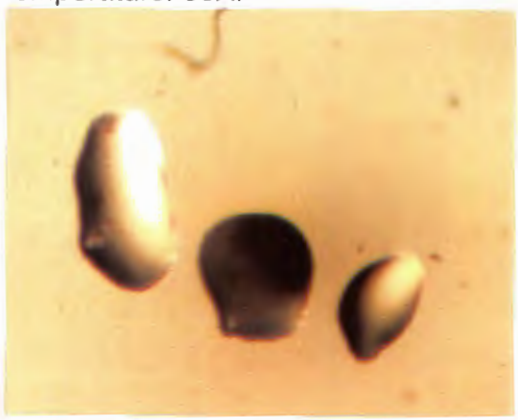

b) The melting point of the α_1-phase of pure host **A2** at 380°C. 60X.

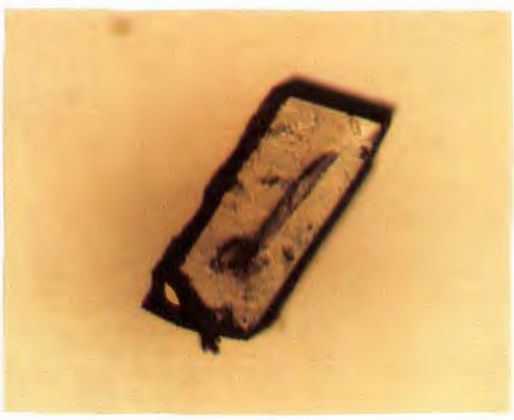

c) A single crystal of **WB3DA** at room temperature. 60X.

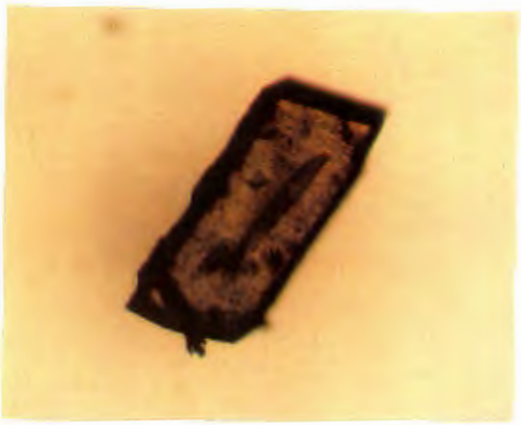

d) At 136°C guest loss commenced and the crystal became opaque. 60X.

e) By 200°C the crystal had decomposed and discoloration had taken place. 60X.

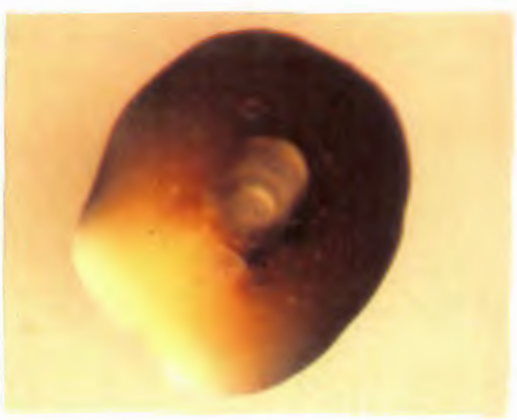

d) The crystal melted at 360°C and a brown decomposition product was visible.

Half a host molecule was placed in the asymmetric unit, and the same numbering scheme as in **W17** was used. The host:guest ratio of 1:2 required one dioxolane molecule in the asymmetric unit, located in a general position. No disorder was found in the positions of the dioxolane guests. The dioxolane molecules were located in channels running along the screw diads. Each guest exhibits one hydrogen bond to the host [O(9A)-H(9A)···O(1G), with d(O···O) = 2.756(6)Å].

Molecular Structure

According to the classification suggested by Kalman *et al.*[1] **W17** and **WB3DA** are isometric. The two structures exhibit similar host conformations (compared in Chapter 7) as well as similar packing with respect to both the host and guest molecules. The molecular structure of **WB3DA** is shown in Fig 5.9.

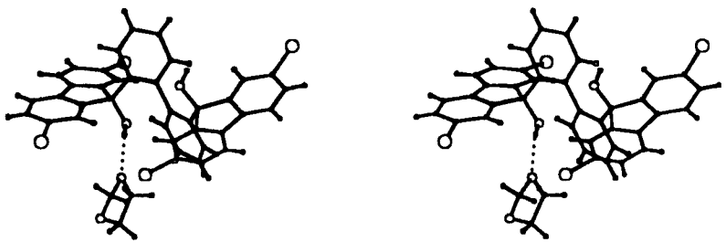

Fig 5.9. Molecular structure of **WB3DA**.

The crystal packing, as viewed down [010] and [001], is shown in Figs 5.10. and 5.11., respectively. The 1,3-dioxolane molecules are located in channels running parallel to [010], as in the case of **W17**. The crystal structure is stabilised by an intermolecular hydrogen bond from one of the O atoms on the 1,3-dioxolane guest molecule to the host hydroxyl group.

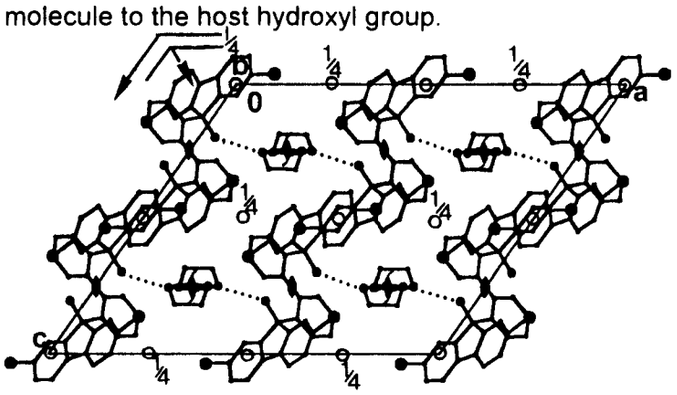

Fig 5.10. Projection of crystal packing in **WB3DA** viewed down [010].

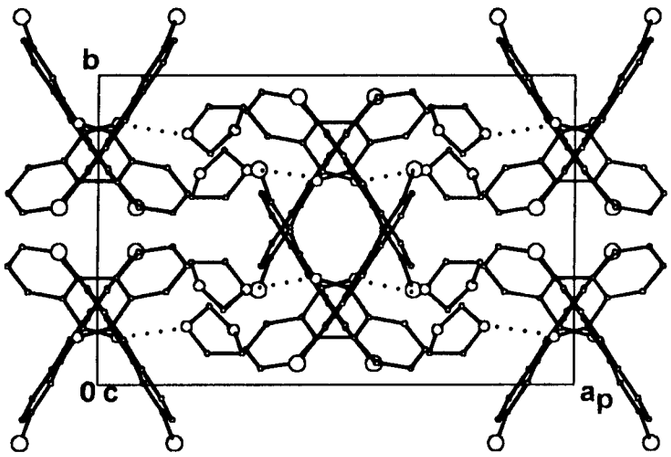

Fig 5.11. Projection of crystal packing in **WB3DA** viewed down [001].

Kinetics

Although no signs of mass loss were observed for the decomposition of the host compound in the programmed TG curves, the host degradation was more strongly observed in the isothermal TG experiments. The kinetics of desolvation could therefore not be studied using this method. In an attempt to obtain Arrhenius parameters for this reaction, the programmed temperature TG run was analysed according to a method described by Borchardt and Daniels[4] . The mass loss *vs.* temperature curve was converted to an α *vs.* time curve, shown in Fig 5.12., since $\alpha = \frac{mass_t}{mass_{Total}}$, where $mass_t$ is the mass loss at a given time t, $mass_{Total}$ is the total mass loss and $t = T/\varphi$, where t is time in seconds, T is temperature in °C and φ is the heating rate in °C/second. An Arrhenius plot can be acquired, if the kinetic model is known, since $g(\alpha) = \frac{1}{k}\frac{d\alpha}{dt}$. A variety of kinetic models[5] were tested for linearity, and the first order reaction mechanism (F1) gave the best fit of the data (see Fig 5.13.). It yielded an activation energy of 136(5)kJ.mol^{-1} for the desolvation reaction, over an α-range of 0.25-0.90.

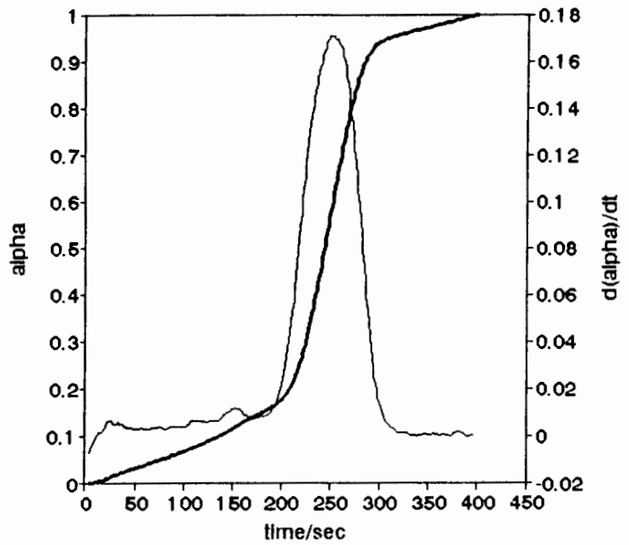

Fig 5.12. α *vs.* time curve for the desolvation of WB3DA

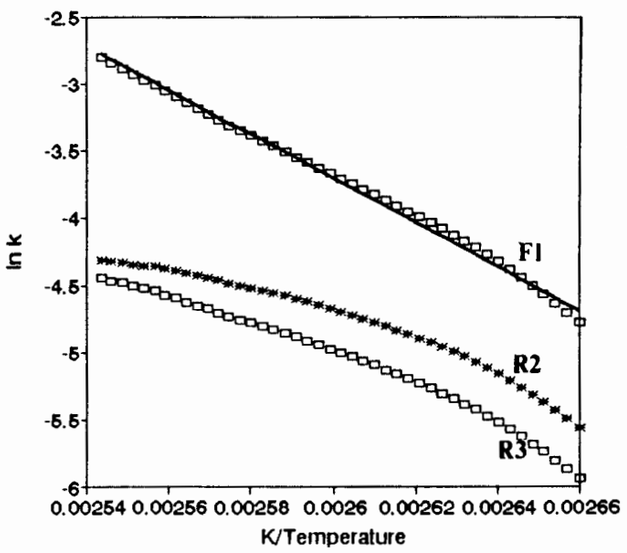

Fig 5.13. Arrhenius plot for the desolvation of WB3DA.

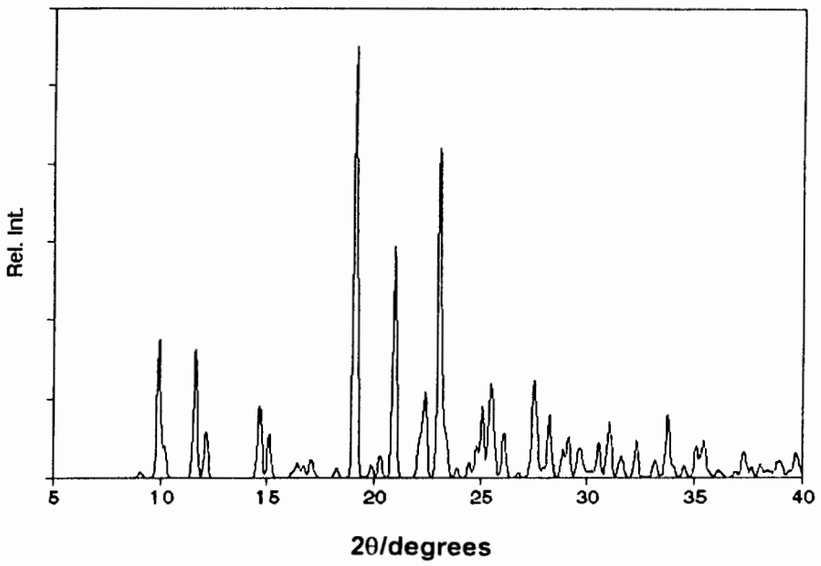

Fig 5.14. X-ray powder diffraction pattern of **WB3DA**.

X-Ray Powder Diffraction

The calculated X-ray powder diffraction pattern for the inclusion compound, **WB3DA** is shown in Fig 5.14. The X-ray powder diffraction pattern of the host compound after desolvation of **WB3DA** could not be obtained, since host A2 decomposed upon heating.

W13DT

$C_{38}H_{22}O_2Cl_4 \cdot 2(C_4H_8O_2)$

Guest: 1,3-dioxane

Space group: *C2/c*

a=22.08(1)Å

b=11.414(7)Å β=124.06(5)°

c=18.60(1)Å

V=3883(4)Å^3

Z=4

Tables containing complete crystal and refinement data appear at the end of this chapter.

Thermal Analysis

The thermal gravimetric traces for the desolvation of **W13DT** are shown in Fig 5.15. A single desolvation step of 20.8% mass loss confirmed the host:guest ratio of 1:1 (calc. 21.3%). This corresponded to an endotherm with an onset temperature of 130°C in the DSC curve.

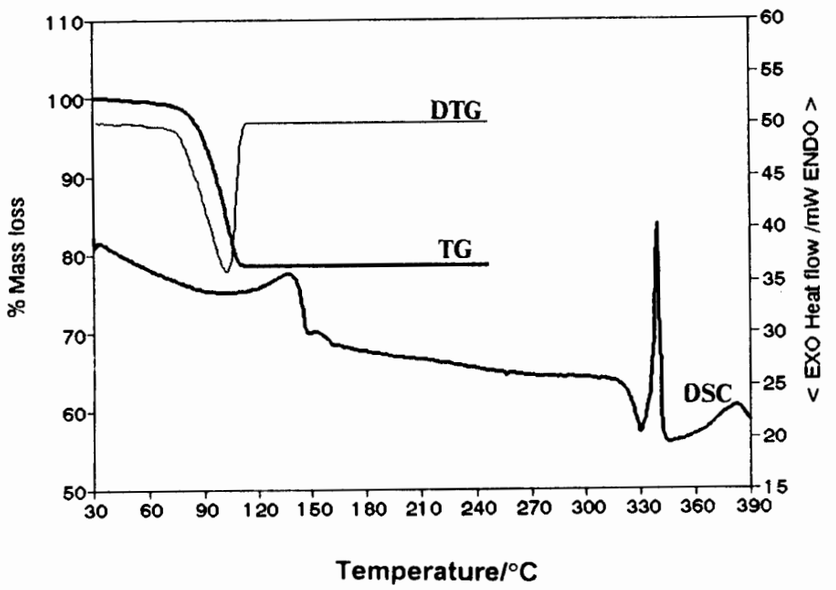

Fig 5.15. TG/DTG/DSC traces of **W13DT**.

Hot Stage Microscopy

A crystal of **W13DT** was placed in silicone oil on a hot stage microscope. A series of photographs, depicting the changes occurring upon heating of the inclusion compound are shown in Colour Plate 5.3. Fine cracks appeared upon heating at 160°C. At 169°C the guest loss process started and the crystal turned opaque.

Colour Plate 5.3.

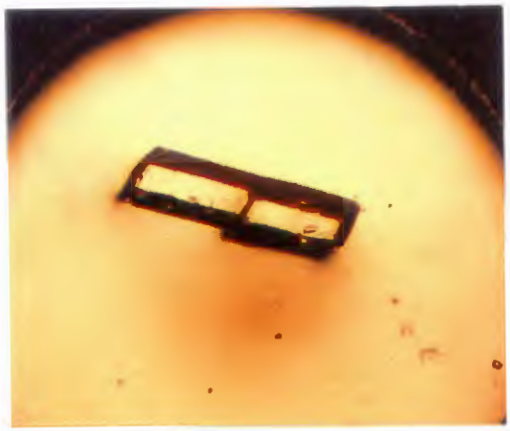

a) A crystal of **W13DT** in silicone oil, at room temperature.

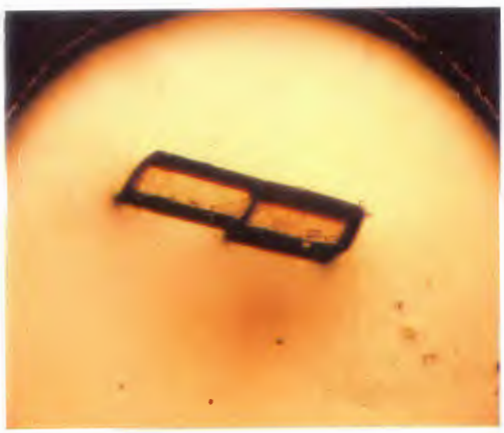

b) Fine cracks appeared at 160°C.

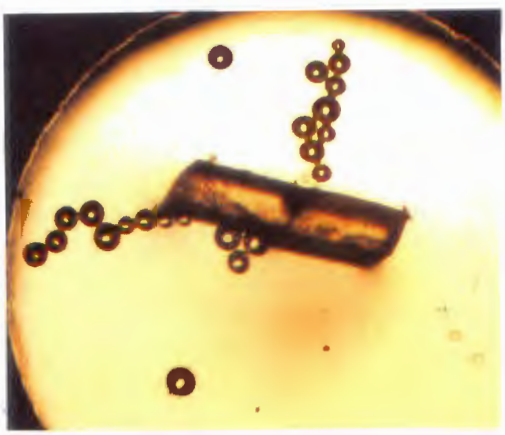

c) At 169°C the guest loss process started and the crystal became opaque.

Crystal Structure

Solution and Refinement

Direct methods yielded the positions of all the host non-hydrogen atoms in the asymmetric unit. There are four host molecules in the unit cell (Z=4). The host molecule is thus located in a special position. It was placed at Wyckoff position *e*, fulfilling the symmetry requirements for the space group *C2/c*. The non-hydrogen atoms in the guest molecule were located in the difference electron density maps upon subsequent refinement. The O atoms on the guest molecule were placed at the location of the highest peaks in the difference electron density map; these peaks were observed in the 1,3-position relative to each other. O(1G) was located within hydrogen bonding distance from the hydroxyl O on the host molecule, and could therefore confidently be placed as an O atom. There was sufficient difference in electron density between the peaks to distinguish between O(3G) and C(5G). All non-hydrogen atoms were refined anisotropically. The hydroxyl hydrogen atoms were located in the difference electron density maps and refined with bond length constraints[3] and individual temperature factors. The rest of the hydrogen atoms were placed with geometric constraints and refined with a common isotropic temperature factor. A residual electron density of 0.697 $eÅ^{-3}$ was observed in the region Cl(7A), but could not be modelled. The structure refined successfully to R_1=0.0809.

The host conformation was similar to that observed in **W17**, and the same numbering scheme was used. The central biphenyl residue is twisted at right angles with the torsion angle C(10A)-C(11A)-C(11A')-C(10A') =96.9(7)°.

The guest is located in a general position, similar to **W17**. The structure is stabilised by a host to guest hydrogen bond, O(9A)-H(9A)···O(1G), with d(O···O) = 2.835(6)Å.

Molecular Structure

The molecular structure of **W13DT** (shown in Fig 5.16.) is very similar to that of **W17**and **WB3DA**. **W13DT** is isostructural to **W17** and **WB3DA**. **W13DT** exhibits the same host packing motif as **W17** and **WB3DA** as can be seen from the crystal packing diagrams viewed down [010] and [001] in Figs 5.17. and 5.18. respectively. The host conformations are compared in Chapter 7.

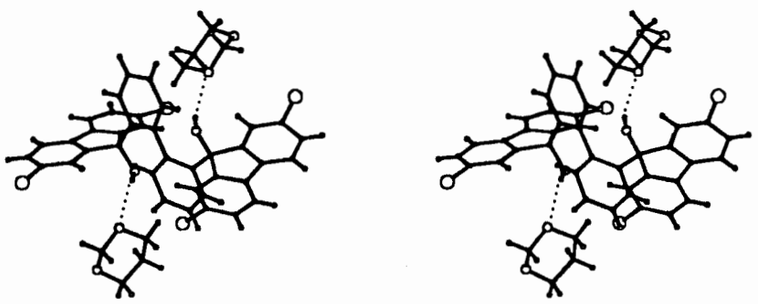

Fig 5.16. Molecular structure of **W13DT**.

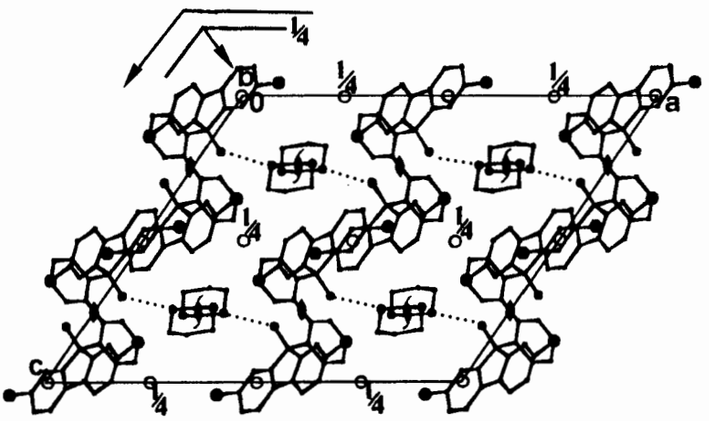

Fig 5.17. Projection of crystal packing in **W13DT** viewed down [010].

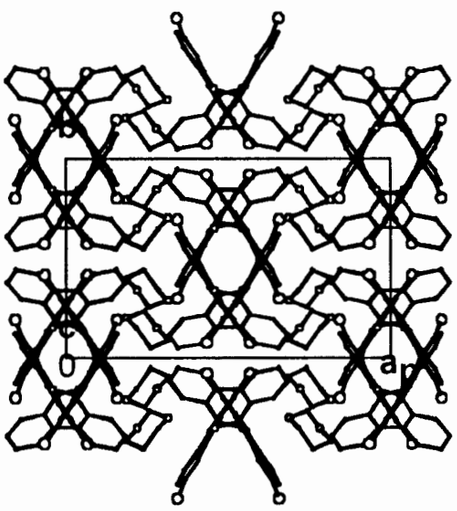

Fig 5.18. Projection of crystal packing in **W13DT** viewed down [001].

In all three structures the host molecules stack along "wavy" layers parallel to [001] which constricts at (¼,y,½) so as to form channels running parallel to [010]. These channels are clearly visible in Fig 5.19. The guest molecules, propagated by a two-fold screw axis, are located in these channels. The channels are illustrated in Fig 5.20., in which the hatched area represents a cut through the host at z=0.5. In each structure the guest molecules are located in the channel with one O atom pointing towards the host hydroxyl group, resulting in an intermolecular H-bond which stabilises the structure.

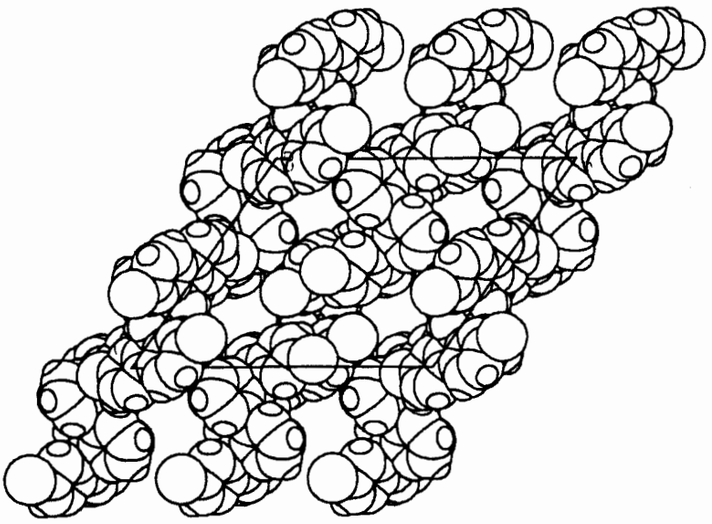

Fig 5.19. Space filled diagram of the host in W13DT viewed down [010].

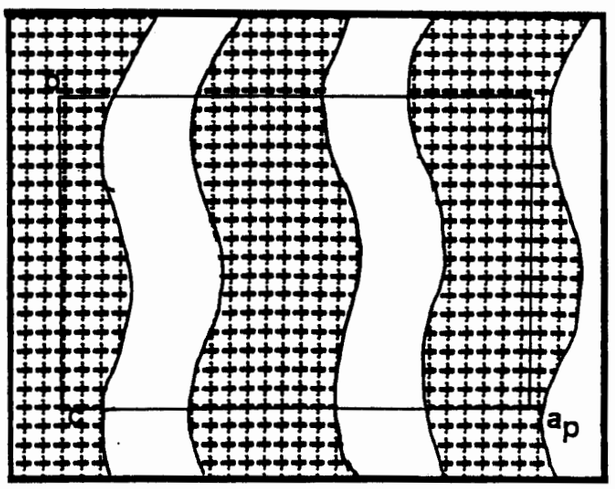

Fig. 5.20. Projection of the general host structure of **W13DT**, viewed down [001], with the hatched area representing the host cut at z=0.5. The guest was omitted for clarity.

Kinetics

A series of isothermal TG traces were collected for the desolvation of **W13DT**, over a temperature range of 55-75°C. These could not be analysed successfully. The reaction did not reach completion below 65°C, but was very rapid at the higher temperatures, exhibiting an almost linear region. The kinetics of desolvation had to be investigated, analysing the programmed temperature TG curve, according to the method of Borchardt and Daniels[4] described above. The two dimensional growth model (R2) fitted the data over an α-range of 0.03-0.99. The semilogarithmic plot (Fig 5.21.) yielded an activation energy of 122(2)kJ.mol^{-1}.

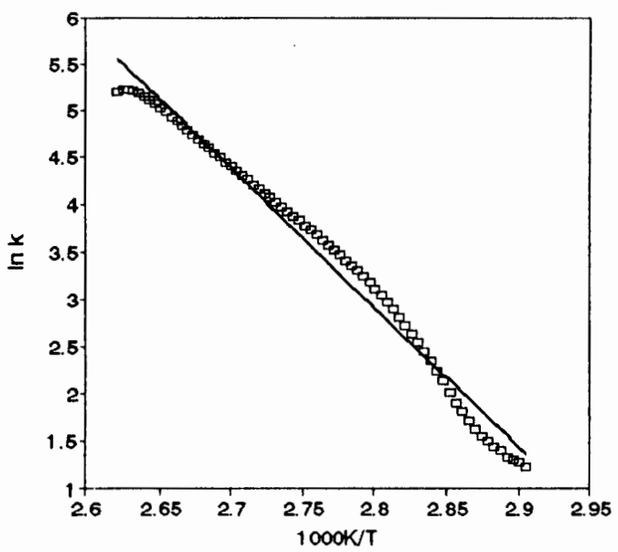

Fig 5.21. Arrhenius plot for the desolvation of **W13DT**.

X-Ray Powder Diffraction

An X-ray powder diffraction trace of the desolvation product is compared with the calculated pattern of the inclusion compound in Fig 5.22. From this it is clear that the guest loss reaction is accompanied by a phase change in the structure of the host compound to form the non-porous α-phase.

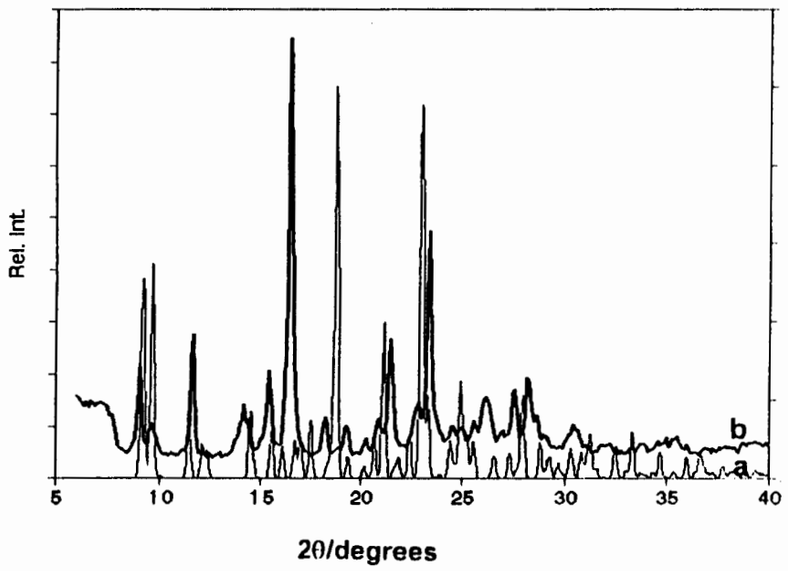

Fig 5.22. X-ray powder diffraction pattern of a) inclusion compound W13DT and b) desolvated α-phase of the host compound.

Discussion

W17, **WB3DA** and **W13DT** exhibit similar crystal packing and hydrogen bonding motifs. In each case the guest molecules are located in channels running parallel to [010] and are hydrogen bonded to the host via one hydrogen bond. The desolvation of all three inclusion compounds followed deceleratory kinetic models. The activation energies obtained for the desolvation of these compounds were similar, with that of **WB3DA** being the highest. The hydrogen bond between the host and 1,3-dioxolane in the structure of **WB3DA** was significantly shorter than that of the other two inclusion compounds, see Table 5.1.

Table 5.1.

Compound	Kinetic model	d(O•••O)/Å	E_a/kJ.mol^{-1}
W17	R2	2.868(6)	129(16)
WB3DA	F1	2.756(6)	136(5)
W13DT	R2	2.836(6)	122(2)

Code	W17	WB3DA	W13DT
Guest	1,3-dioxolane	1,3-dioxolane	1,3-dioxane
Molecular formula	$C_{38}H_{22}O_2Cl_4 \cdot 2(C_3H_6O_2)$	$C_{38}H_{22}O_2Br_4 \cdot 2(C_3H_6O_2)$	$C_{38}H_{22}O_2Cl_4 \cdot 2(C_4H_8O_2)$
M_r/g mol^{-1}	800.51	978.35	828.56
Temperature/K	293(2)	294(2)	294(2)
Crystal data			
Crystal system	Monoclinic	Monoclinic	Monoclinic
Space group	*C2/c*	*C2/c*	*C2/c*
a/Å	21.954(3)	21.570(8)	22.08(1)
b/Å	11.423(2)	11.717(3)	11.414(7)
c/Å	18.157(3)	18.37(1)	18.60(1)
β/°	123.63(2)	124.22(4)	124.06(5)
Z	4	4	4
V/Å^3	3791.3(1)	3840(4)	3883(4)
D_c/g cm^{-3}	1.402	1.692	1.417
μ(MoK$_\alpha$) /cm^{-1}	3.62	42.42	3.56
F(000)	1656	1944	1720
Data collection			
Crystal dimensions /mm	0.50x0.40x0.40	0.34 x 0.21 x 0.21	0.37x0.34x0.34
Range scanned θ/°	2.10 to 25.05	2.08 to 24.97	2.10 to 24.99
Range of indices *h,k,l*	-21,25;-13,0;-21,0	-25,21; 0,13; 0,21	-26,20; -13,0; -22,20
No. of reflections collected	3277	3493	3526
No. of unique reflections	3277	3376	3413
No. of reflections observed with $I_{rel}>2\sigma(I_{rel})$	2034	2084	1822
Final refinement			
No. of restraints	2	2	0
No. of parameters	225	220	256
R1 ($I_{rel}>2\sigma(I_{rel})$)	0.068	0.0462	0.0809
wR2 ($I_{rel}>2\sigma(I_{rel})$)	0.2023	0.1210	0.2020
Max. height in electron density map /eÅ^{-3}	0.67	0.710	0.617
Min. height in electron density map /eÅ^{-3}	-0.62	-0.708	-0.493
Absorption Correction factor range	09507-0.9994	0.8948-0.9990	0.8926-0.9970

1 A. Kálmán, L. Parkanyi and G. Argay, *Acta Crystallogr.*, **B49**, 1993, 1039.

2 P.J. Haines, *Thermal Methods of Analysis*, Chapman and Hall, 1995, London.

3 P. Schuster, G. Zundel and C. Sanderfy, *The Hydrogen Bond II, Structure and Spectroscopy*, North Holland Publishing Co., Amsterdam, 1976, 411.

4 H.J. Borchardt and F. Daniels, *J. Am. Chem. Soc.*, **79**, 1957, 41.

5 M.E. Brown, D. Dollimore and A.K. Galwey, *Comprehensive Chemical Kinetics*, ed. C.H. Bamford and C.J. Tipper, Elsevier, Amsterdam, 1980, vol.22, p 220.

CHAPTER 6 INCLUSION COMPOUNDS OF HOSTS IN CLASS A WITH ACETONE.

In this chapter the thermal analysis, crystal structures and kinetics of desolvation of the inclusion compounds of $C_{38}H_{22}O_2Cl_4$ (host **A1**) and $C_{54}H_{58}O_2$ (host **A3**) with acetone (**WC17AC** and **WTBAC** respectively) are discussed. The crystal structure of an unsolvated α-phase of host **A1**, **WCL**, will also be discussed.

WC17AC

$C_{38}H_{22}O_2Cl_4 \cdot 2(C_3H_6O)$
Guest:Acetone
Space group: *C2/c*
a=20.424(6)Å
b=11.496(3)Å β=122.23(3)°
c=18.885(7)Å
V=3751(2)Å^3
Z=4

Tables containing complete crystal and refinement data appear at the end of this chapter.

Thermal Analysis

The thermal analytical results for **WC17AC** are shown in Fig 6.1. The guest loss reaction takes place in a single step, with a mass loss of 14.0%, corresponding to the loss of 2 acetone molecules per host molecule (calc. 15.1%). The DSC trace shows a diffuse endotherm with an onset temperature of 80°C, corresponding to the desolvation process. A sharp endotherm at 340°C corresponds to the melt.

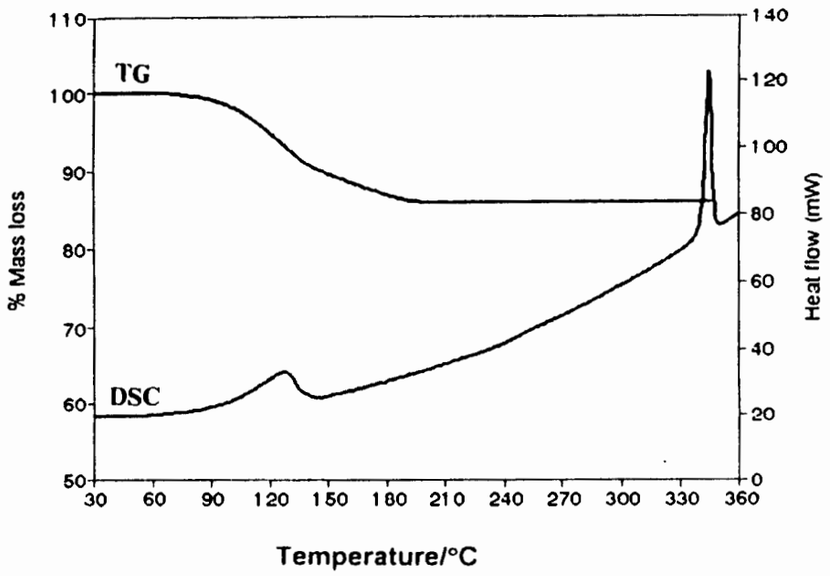

Fig 6.1. TG and DSC for **WC17AC**.

Hot stage microscopy

A single crystal of **WC17AC** was placed on the hot stage microscope, under a drop of silicone oil and heated. A series of photographs, depicting the changes occurring upon heating are shown in Colour Plate 6.1., page 124.

Crystal Structure

Preliminary photography indicated that **WC17AC** and **WTBAC** both belong to the monoclinic crystal system (2/m Laue symmetry). The reflection conditions

hkl h+k=2n

h0l l=2n; (h=2n)

0k0 (k=2n)

were observed, implying that the space groups were either *Cc* or *C2/c*. In each case the centrosymmetric space group *C2/c* was chosen, based on the mean $|E^2-1|$ values for the zonal reflections and the remainder, obtained from the direct methods run. This choice was vindicated in each case by the successful refinement of the structures.

Solution and Refinement

Direct methods yielded the positions of all the host non-hydrogen atoms in the asymmetric unit. The compound crystallises in the space group C2/c with Z=4, which requires the host molecule to be in a special position. The host molecule exhibits two-fold symmetry and was placed with the central biphenyl bond on a special position, located on a diad at Wyckoff position *e*. The non-hydrogen atoms in the guest molecule were located in the difference electron density maps upon subsequent refinement. All host non-hydrogen atoms, and O(1G) and C(1G) on the guest were refined anisotropically. The guest methyl C-atoms were treated isotropically, since they showed comparatively high thermal motion (U_{eq} C(2G)=0.108(2)Å^2). A residual electron density of 0.631 eÅ^{-3} was observed in the region of the guest, but could not be modelled. The hydroxyl hydrogen atoms were located in the difference electron density maps and refined with bond length constraints[1] and individual temperature factors. The rest of the host hydrogen atoms were placed with geometric constraints and refined with a common isotropic temperature factor. The guest hydrogen atoms were omitted from the final model. The structure refined successfully to R_1=0.0643.

The structure of the host molecule with atomic numbering scheme is shown in Fig 6.2. The central biphenyl moiety is twisted at right angles with the torsion angle C(10A)-C(11A)-C(11A')-C(10A') = 92.50(69)°.

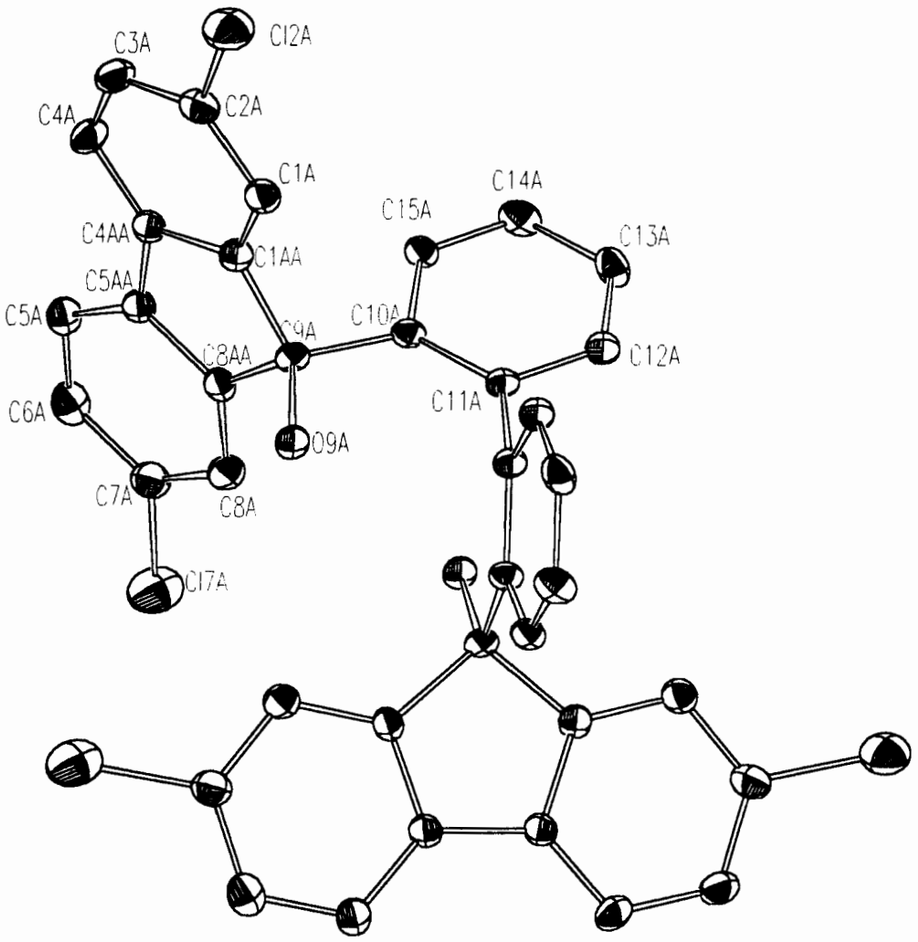

Fig 6.2. Host conformation of **WC17AC**.

The guest is located in a general position. The acetone molecule was modelled with one of the methyl carbon atoms disordered over two positions, C(3GA) and C(3GB), each with a site occupancy of 0.50, as shown in Fig 6.3. The structure is stabilised via a hydrogen-bond O(9A)-H(9A)···O(1G), from the host hydroxyl group to the guest molecule [d(O···O)=2.825(4)Å].

C(1G)-C(3GA)	1.57(1)Å
C(1G)-C(3GB)	1.46(1)Å

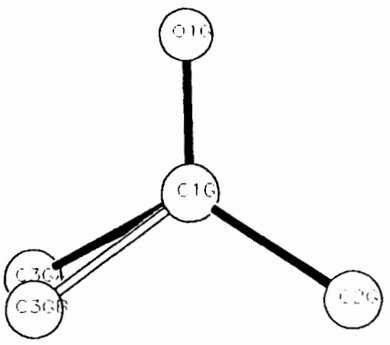

Fig 6.3. Disorder modelled in acetone molecule with C(3GA) and C(3GB) with s.o.f. of 0.50 each.

Molecular Structure

The molecular structure of **WC17AC** is shown in Fig 6.4. Projections of the structure , viewed along [010] and [001] are shown in Fig. 6.5. and 6.6. The guest molecules are situated in channels running parallel to [010], along the two-fold screw axes, similar to the packing observed in **W17**, **WB3DA** and **W13DT**. In Fig 6.7. the host molecules are represented with van der Waals radii, with the guest molecules omitted, looking down these channels.

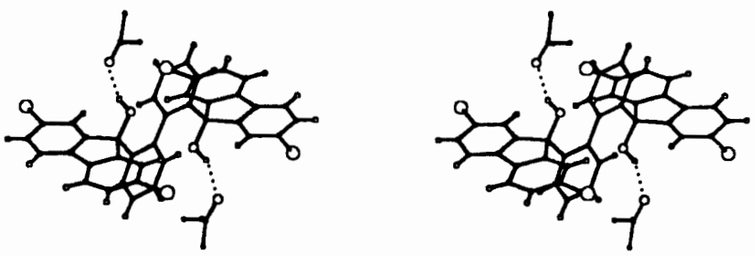

Fig 6.4. Stereoscopic view of the molecular structure of **WC17AC**.

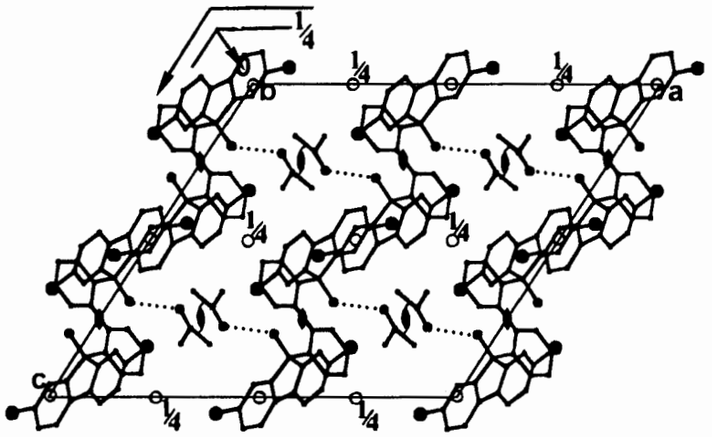

Fig 6.5. Crystal packing in **WC17AC** as viewed down [010].

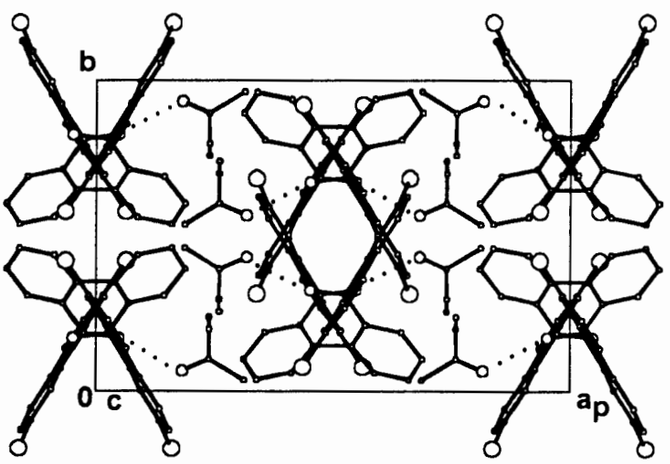

Fig 6.6. Crystal packing in **WC17AC** as viewed down [001].

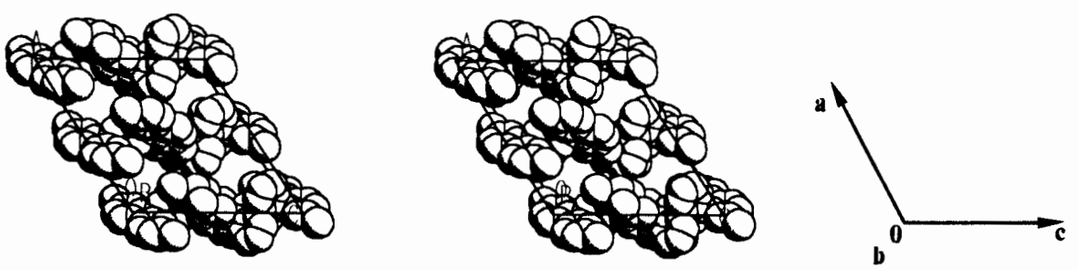

Fig 6.7. Stereoscopic view of the host molecules, depicted with van der Waals radii, looking down the channels running along [010]. The guest molecules were omitted for clarity.

Kinetics

A series of mass loss *vs.* time curves were obtained for the isothermal desolvation of **WC17AC,** over a temperature range of 40-65°C. The data were reduced to fractional reaction (α) *vs.* time curves. All these curves were deceleratory. Various appropriate kinetic models[2] were tested for linearity. The data were best fitted by the three-dimensional diffusion mechanism (D3): $[1-(1-\alpha)^{1/3}]^2 = kt$.

The semilogarithmic plot of *ln k vs. 1/T* is shown in Fig. 6.8., and yields an activation energy of 58(3) kJ mol^{-1} over an α-range of 0.05 to 0.90.

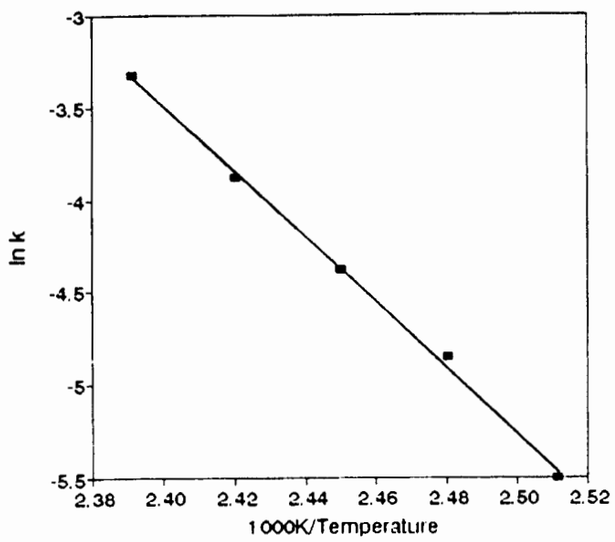

Fig 6.8. Arrhenius plot for the desolvation of **WC17AC**.

X-Ray Powder Diffraction

In Fig 6.9. the calculated X-ray powder diffraction pattern of the inclusion compound is compared with that obtained upon desolvation. It is clear that the guest loss reaction is accompanied by a phase change of the host crystal structure to the non-porous α-phase.

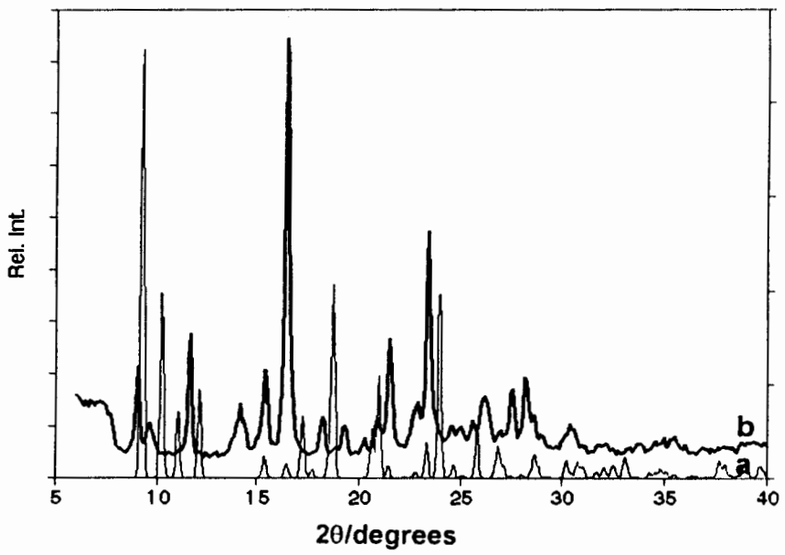

Fig 6.9. X-ray powder diffraction patterns for a) **WC17AC** and b) α-phase of the desolvated host compound.

WTBAC

$C_{54}H_{58}O_2 \cdot (C_3H_6O)$

Guest:Acetone

Space group: *C2/c*

a=17.120(2)Å

b=17.935(2)Å β=114.15(1)°

c=17.232(3)Å

V=4828(1)Å^3

Z=4

Tables containing complete crystal and refinement data appear at the end of this chapter.

Thermal Analysis

The host:guest ratio of 1:1 for **WTBAC**, was confirmed by the TG experiment, showing a single mass loss step of 7.6% (calc. 7.3%). This corresponds to a single sharp endotherm in the DSC trace at an onset temperature of 175°C, followed by the melt at 334°C, as shown in Fig 6.10.

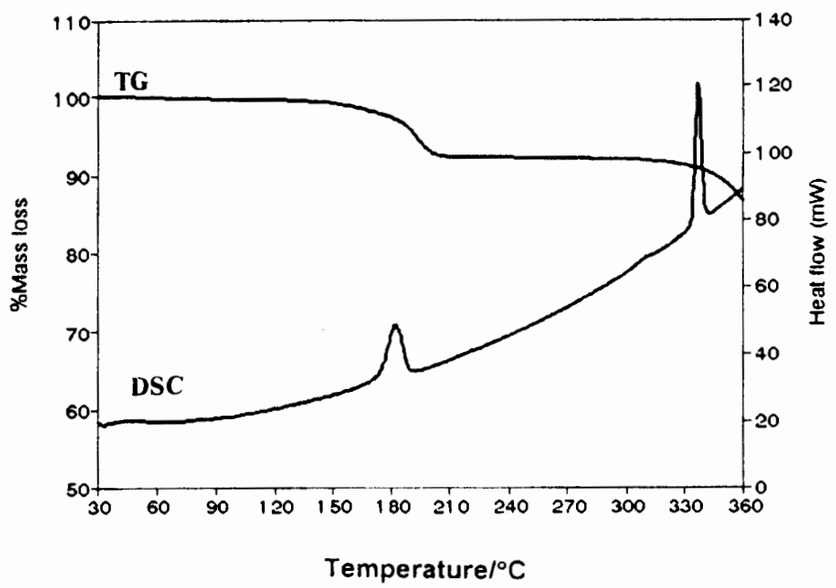

Fig 6.10. TG and DSC for **WTBAC**

Hot stage microscopy

A single crystal of **WTBAC** was placed on the hot stage microscope under a drop of silicone oil and heated. A series of photographs which depict the changes occurring upon heating are shown in Colour Plate 6.1.

Crystal Structure

Solution and Refinement

Direct methods yielded the positions of most of the host non-hydrogen atoms in the asymmetric unit, except for the atoms on the *tert*-butyl groups, which were located in the difference electron density map upon subsequent refinement. The space group C2/c with Z=4, requires the host molecule to be in a special position. The host molecule was located on a diad at Wyckoff position *e*. The non-hydrogen atoms in the guest molecule were subsequently located in the difference electron density maps. All host non-hydrogen atoms were refined anisotropically. High thermal motion was observed in the *tert*-butyl groups [especially C(22A) and C(23A)]. It is clear from Fig 6.11. that the thermal motion is directional. When C(22A) and C(23A) were treated isotropically electron density peaks were observed in their proximity, but disorder in these atoms could not be modelled sensibly. It was therefore decided to treat these atoms anisotropically in the final refinement, although the factors describing thermal motion were high. Atom O(3G) on the guest showed high thermal motion. Strong peaks in the difference electron density map [at less than 1Å away from O(3G)] could not be modelled with sensible geometry. O(3G) was therefore treated anisotropically, although the subsequent anisotropic displacement parameters were fairly high. The remaining guest atoms were treated isotropically, since they showed comparatively high thermal motion (U_{eq} >0.09(2)Å^2). A residual electron density of 0.510eÅ^{-3} was observed in the region of the guest. The hydroxyl hydrogen atoms were located in the difference electron density maps and refined with bond length constraints[1] and individual temperature factors. The rest of the host hydrogen atoms were placed with geometric constraints and refined with a common isotropic temperature factor for similar groups. The guest hydrogen atoms were omitted from the final model. The structure refined successfully to R_1=0.0659.

Colour Plate 6.1.

a) A crystal of **WC17AC** at room temperature. 28X enlarged.

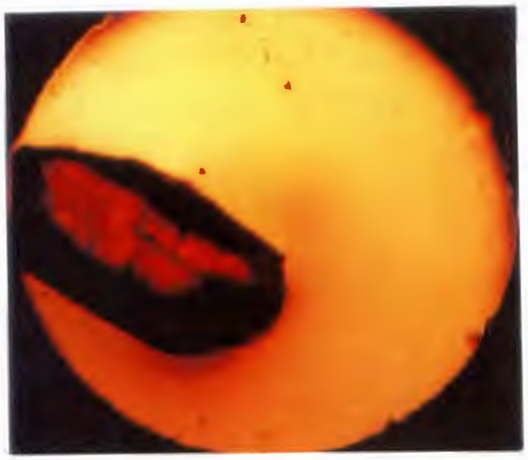

b) At 80°C the crystalof **WC17AC** cracks and becomes opaque. 28X enlarged.

c) At 89°C the guest loss reaction is observed in **WC17AC**. 28X enlarged.

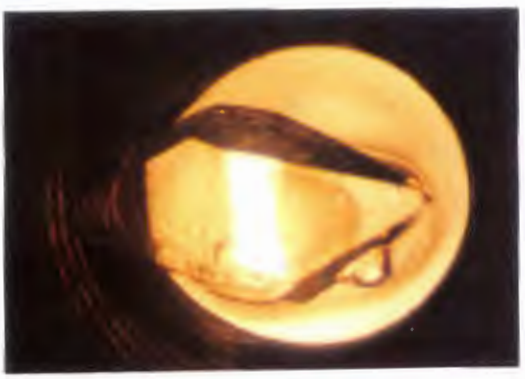

d) A crystal of **WTBAC** at room temperature. 17.5X enlarged.

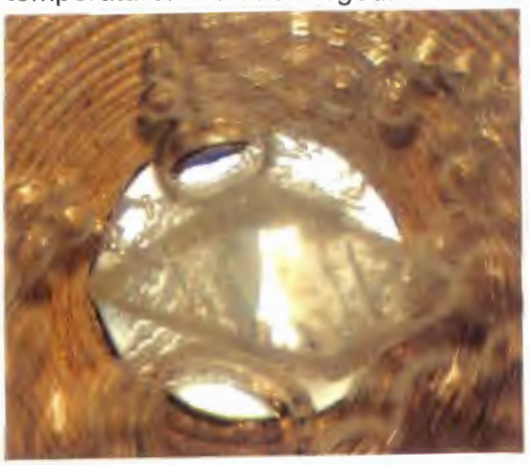

e) At 185°C the crystal of **WTBAC** cracks and guest loss commences. 17.5X enlarged.

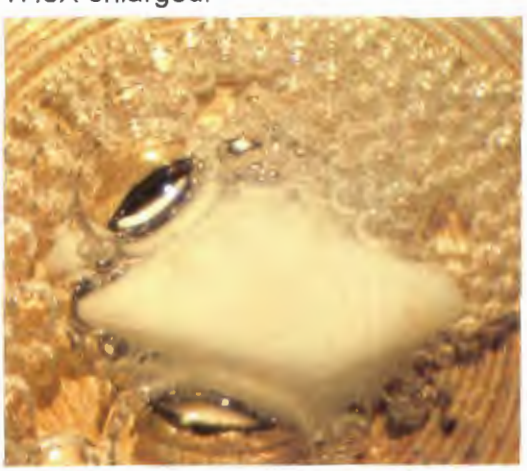

f) After 5 min. at 185°C the crystal of **WTBAC** is opaque and the guest loss reaction reaches completion. 17.5X enlarged.

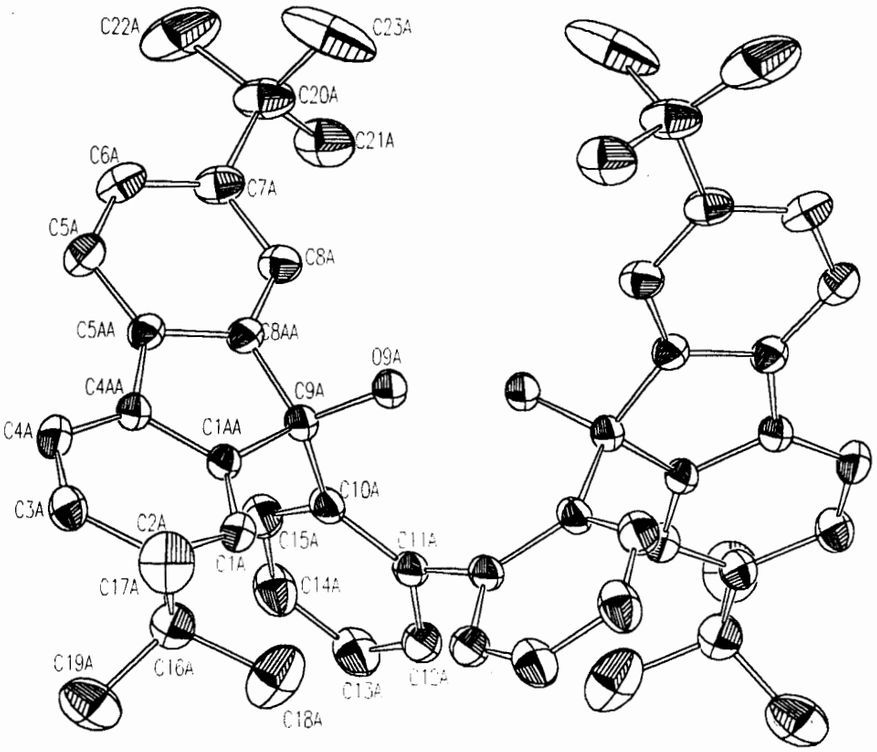

Fig 6.11. Host conformation in **WTBAC**.

The host hydroxyl hydrogen is disordered over two positions (each with 0.50 site occupancy) giving rise to "flip-flop" hydrogen bonding[3]. The host molecule is locked into conformation [with C(10A)-C(11A)-C(11A')-C(10A') = 89.1(6)°] via an intramolecular hydrogen bond [O(9A)-H(9A)···O(9A')=2.752(5)Å]. An intermolecular hydrogen bond exists between the guest molecule and host with O(9A)-H(9B)···O(3G)=2.691(9)Å. Fig 6.12. illustrates the two alternating hydrogen bonding motifs observed in the structure depending on the position of the guest molecule.

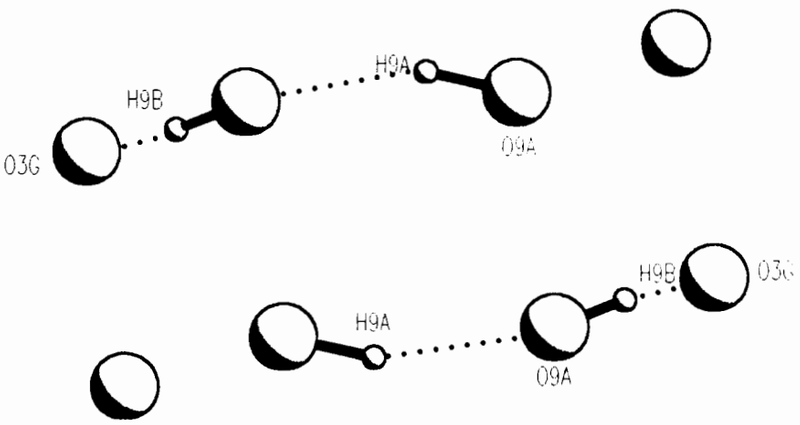

Fig 6.12. Disordered hydrogen bonding, observed in **WTBAC**.

The guest molecule is disordered over two positions, related by a centre of symmetry. The asymmetric unit consists of an acetone molecule with O(3G) and C(1G) at a site occupancy of 0.50, and the methyl carbon C(2G) with full site occupancy, as shown in Fig 6.13.

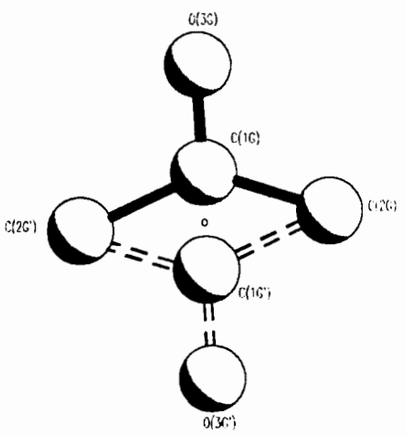

Fig 6.13. Disorder in acetone molecule, **WTBAC**.

Molecular structure

The molecular structure of **WTBAC** is shown in Fig 6.14. A projection of the structure viewed along [001] is shown in Fig 6.15. The acetone guest molecules are indicated with van der Waals radii and are located in constricted channels parallel to [001]. It is clear from a space filled diagram of the host with the guest omitted (Fig 6.16.) that these channels become as narrow as 1.7 Å.

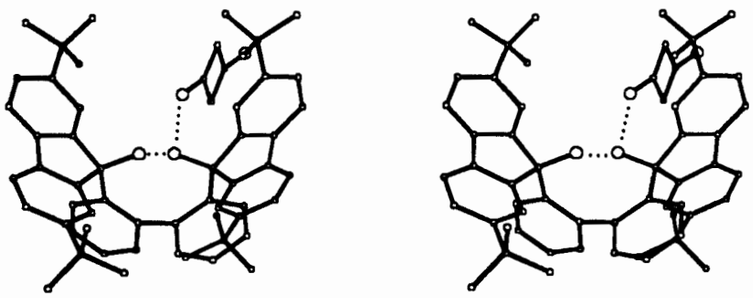

Fig 6.14. Stereoscopic view of the molecular structure of **WTBAC**.

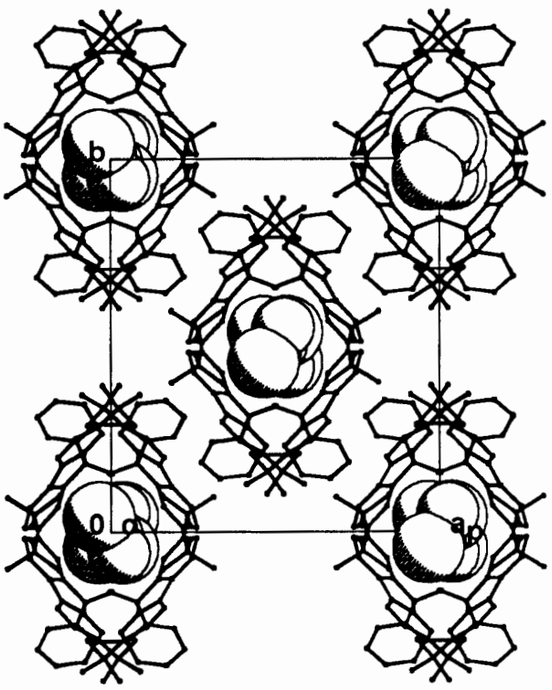

Fig 6.15. Crystal packing in **WTBAC** as viewed down [001].

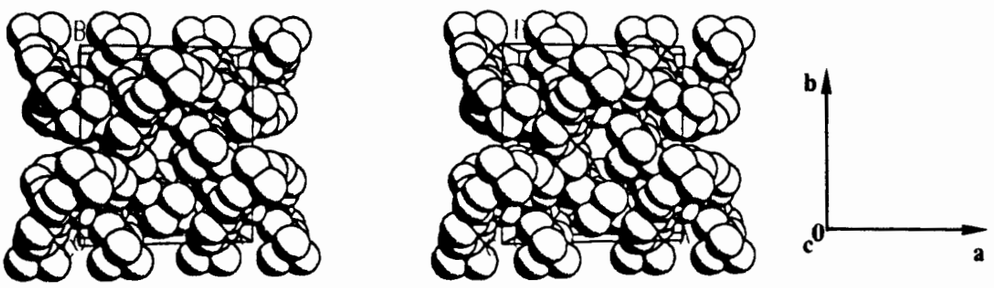

Fig 6.16. Stereoscopic view of the host molecules, depicted with van der Waals radii, looking down the channels running along [001]. The guest molecules were omitted for clarity.

Kinetics

A series of isothermal TG experiments were carried out on **WTBAC** over a temperature range of 125-145°C. Below 125°C the reaction did not reach completion. The α *vs.* time curves were deceleratory and were best described by the first order (F1) kinetic model: $1-(1-\alpha)=kt$. An activation energy of 147(4)kJmol^{-1} was obtained for this reaction over an α-range of 0.05 to 0.95. A curve of *ln k vs.* $1/T$ is shown in Fig 6.17.

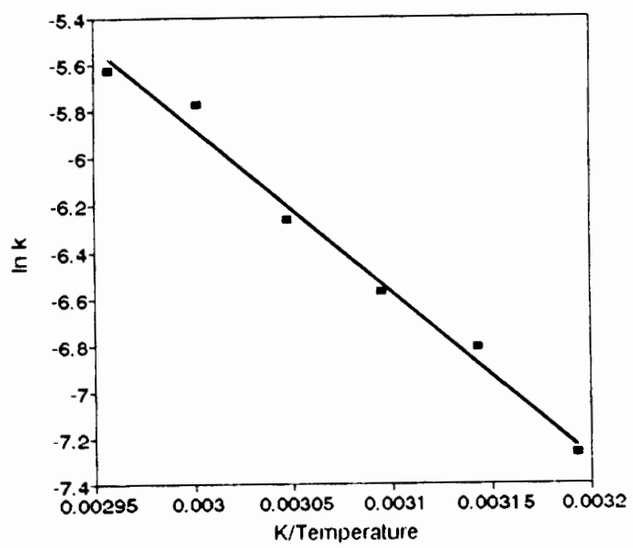

Fig 6.17. Arrhenius plot for the desolvation of **WTBAC**.

X-Ray Powder Diffraction

In Fig 6.18. the calculated X-ray powder diffraction pattern of the inclusion compound is compared with that obtained upon desolvation. It is clear that the guest loss reaction is accompanied by a phase change of the host crystal structure to the non-porous α-phase.

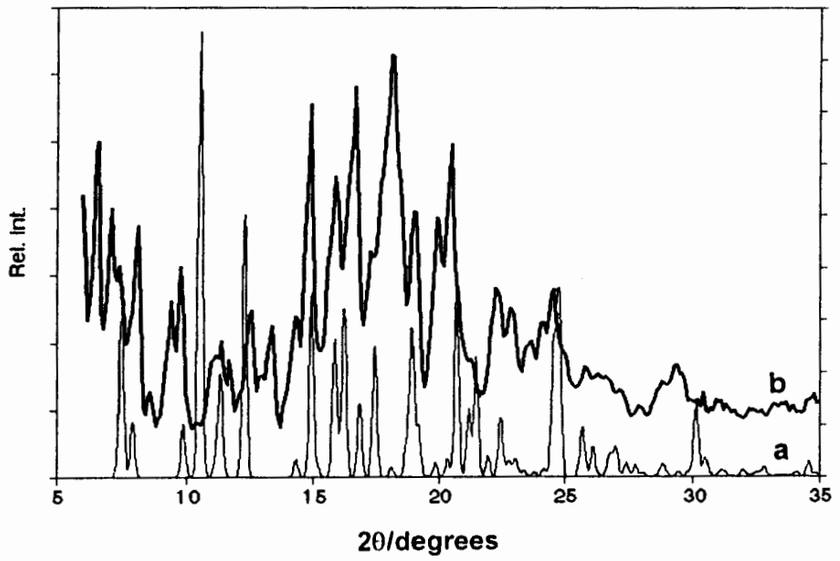

Fig 6.18. X-ray powder diffraction patterns for a) WTBAC and b) α-phase of desolvated host compound.

WCL

$C_{38}H_{22}O_2Cl_4$
Guest:None
Space group: *P2/n*
a=16.938(2) Å
b=11.385(2) Å β=116.64(1)°
c=17.620(3) Å
V=3037.2(7) $Å^3$
Z=4

Tables containing complete crystal and refinement data appear at the end of this chapter.

Thermal Analysis

Crystals of an unsolvated, non-porous, α-phase of host **A1** were obtained from a solution of the host, in hot 1,3,5-trimethylbenzene. The melting point of **WCL** was determined using DSC and hot stage microscopy. The melting point occurs at 336°C and is accompanied by sublimation. Both hot stage microscopy and DSC confirmed that no solvent was included.

Crystal Structure

Preliminary photography indicated that **WCL** belongs to the monoclinic crystal system (2/m Laue symmetry). The only conditions limiting possible reflections were

hkl none
h0l h+l=2n

indicating that the space group was either *Pn* or *P2/n*. The centrosymmetric space group *P2/n* was chosen, based on the mean $|E^2-1|$ values obtained from the direct methods run. This choice was vindicated by the successful refinement of the structure.

Solution and Refinement

Direct methods yielded the positions of all the non-hydrogen atoms in the asymmetric unit. The compound crystallises in the space group *P2/n* with Z=**4**. Two crystallographically independent half molecules were located in the asymmetric unit. The molecules exhibit two-fold symmetry and hence both were placed with their central biphenyl bond on a diad. Molecule A is located at Wyckoff position *f* and molecule B at Wyckoff position *e*. All non-hydrogen atoms were refined anisotropically. The hydroxyl hydrogen atoms were located in the difference electron density maps and refined with individual temperature factors. The rest of the hydrogen atoms were placed with geometric constraints and refined with a common isotropic temperature factor. A residual electron density of 0.22eÅ^{-3} was observed. The structure refined successfully to R_1=0.0429.

The structures of the molecules, with atomic numbering schemes, are shown in Figs 6.19. and 6.20. The central biphenyl moieties are twisted at right angles with the torsion angles C(10A)-C(11A)-C(11A')-C(10A') = 97.9(5)° and C(10B)-C(11B)-C(11B')-C(10B') = 89(1)°. The intramolecular O··O distances observed were 3.502(5) Å for O(9A)··O(9A') and 3.327(5) for O(9B)··O(9B').

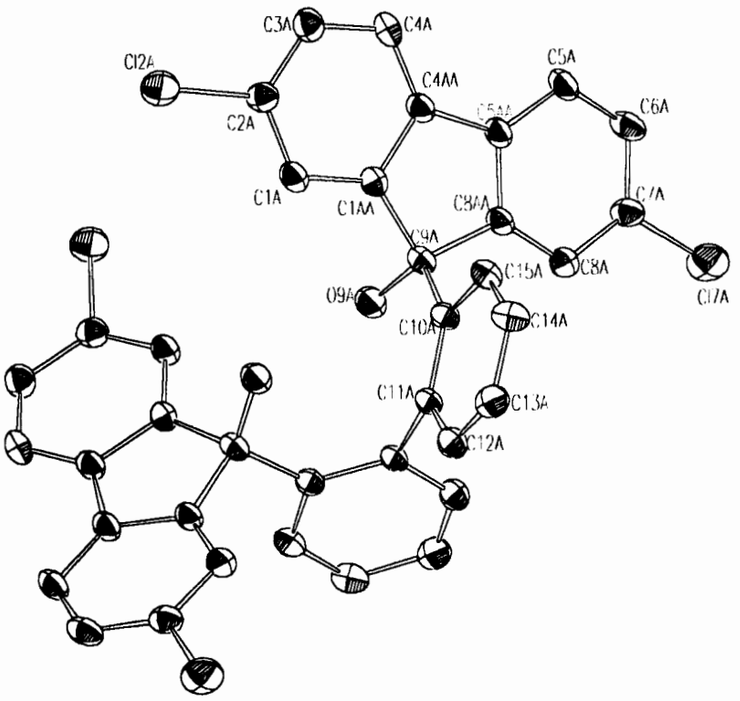

Fig 6.19. Zortep diagram of molecule A in **WCL**.

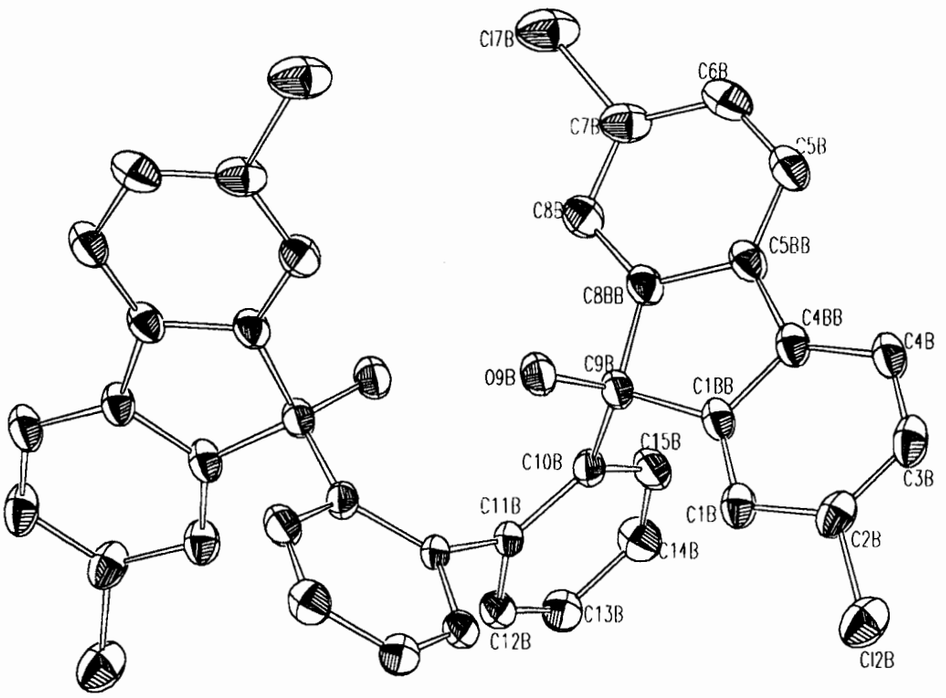

Fig 6.20. Zortep diagram of molecule B in **WCL**.

Molecular Structure

The molecular structure of **WCL** is shown in Fig 6.21.

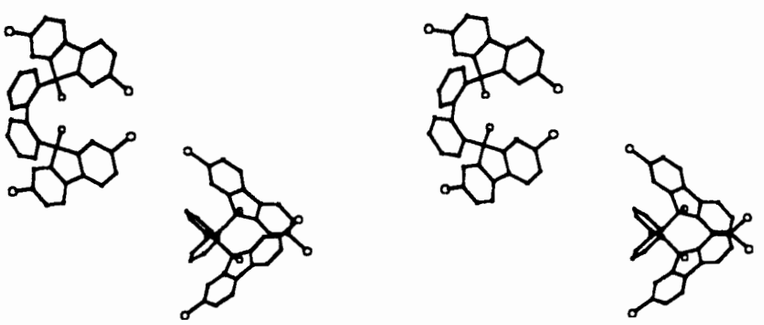

Fig 6.21. A stereo diagram of the molecular structure of **WCL**.

Layers of molecules running parallel to [100] are stacked along [010], as can be seen in Fig 6.22. This gives rise to the formation of "wavy" chains, running along [101], as seen in Fig 6.23. These chains resemble the layers observed in the structures of the inclusion compounds **W17**, **WB3DA**, **W13DT** and **WC17AC**,

running parallel to [001] (see Fig 6.7.). The main difference lies in the fact that in the latter cases these layers gave rise to the formation of channels running parallel to [010], in which the guest molecules are located. There are no voids in the structure of **WCL**, as can be seen from a space filled diagram viewed down [010], shown in Fig 6.24.

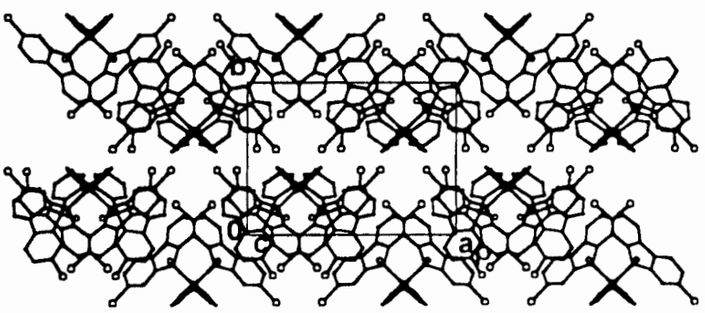

Fig 6.22. Projection of the crystal packing in **WCL**, viewed down [001].

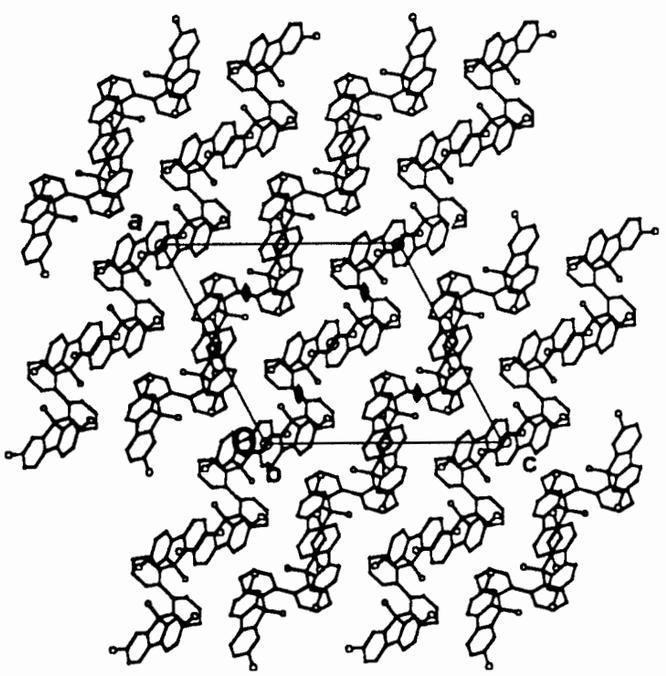

Fig 6.23. Projection of the crystal packing in **WCL**, viewed down [010].

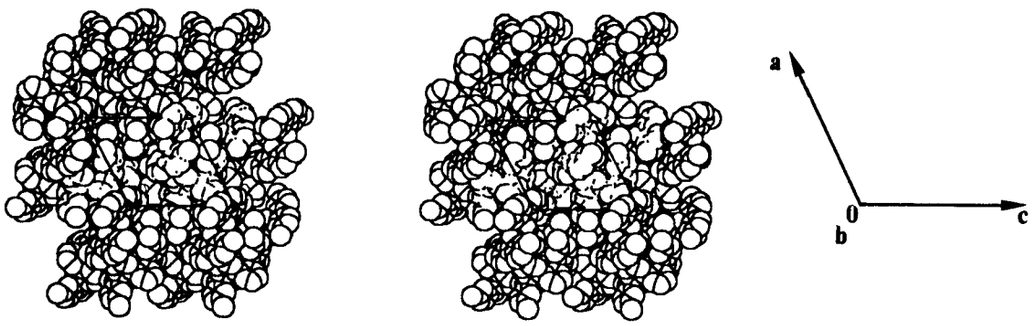

Fig 6.24. Stereoscopic view of the structure of **WCL**, depicted with van der Waals radii, viewed down [010].

X-Ray Powder Diffraction

The X-ray powder diffraction pattern for **WCL** was calculated using the atomic coordinates obtained from the single crystal structure and is shown in Fig 6.25. In Chapter 7 this pattern is compared with the X-ray powder diffraction patterns obtained from the desolvated inclusion compounds of this host.

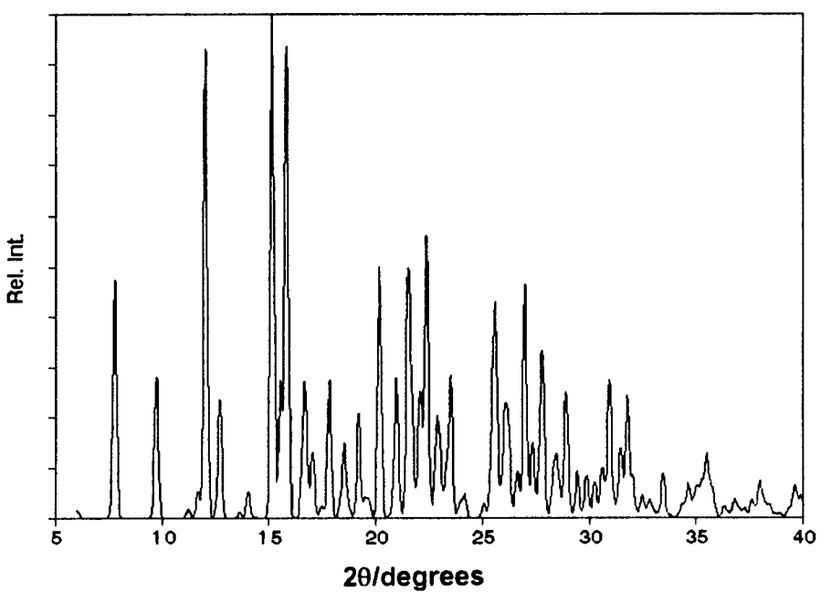

Fig 6.25. Calculated X-ray powder diffraction pattern for **WCL**.

Discussion

The desolvation reaction

$Host{\cdot}(acetone)_{n(s,\beta)} \rightarrow Host_{(s,\alpha)} + n.acetone_{(g)}$

is accompanied by a phase change in the crystal structure. The solvated β-form is transformed to the non-porous α-phase. This was confirmed by X-ray powder diffraction on the compounds, taken before and after desolvation.

The α *vs.* time curves for the desolvation of both compounds are deceleratory. **WC17AC** desolvates according to the three-dimensional diffusion model. The rate of a diffusion-limited reaction is determined by the movement of reactants, or products, to or from, a reaction interface[2]. From the crystal structure it is clear that the guest molecules are located in channels running parallel to [010]. The reaction mechanism observed suggests that the diffusion of the guest is the rate-determining step in the desolvation of **WC17AC**. The model of unrestricted guest diffusion along the channels could explain the relatively low activation energy required for this reaction, and the low temperature at which it takes place.

WTBAC is much more stable than **WC17AC** and desolvates at a much higher temperature (significantly higher than the normal boiling point of acetone). This step is observed as a sharp endotherm in the DSC curve. The desolvation of **WTBAC** follows the F1 mechanism. There is no physical explanation for reactions based on order with respect to α, since concentration is not usually a meaningful term in solid state reactions[2]. The constricted channel structure however would imply that the gaseous decomposition product can escape only by severely disrupting the host framework. In addition we note that the host to guest hydrogen bonding is stronger in **WTBAC** than in **WC17AC**. A further possible explanation of the stability and higher activation energy observed for **WTBAC** lies in the fact that the host molecules are rendered rigid by an intramolecular hydrogen bond. This may also impede the phase transformation to the α-form, which occurs upon desolvation.

The crystal structure of an unsolvated α-phase of the host compound **A1**, was obtained, by crystallising the host from 1,3,5-trimethylbenzene. It is interesting to note that this α-phase differs in structure from that obtained from the desolvation of

WC17AC (compare X-ray powder diffraction patterns Fig 6.9. and 6.25). This implies that the host can crystallise in different polymorphic modifications. There seems to be a similarity, though between the packing of the host in the structure of **WCL** and in the solvated structures, **W17**, **W13DT** and **WC17AC**, with the structure of **WCL** being packed more densely. The two structures can be compared by looking at the two projections, Fig 6.5. for **WC17AC** and Fig 6.23. for **WCL**. In both cases the host packs in ribbons which run along [001] in **WC17AC** and along [101] in **WCL**. In the former structure, however, the ribbons of host molecules are prized apart by the guest molecules, yielding the inclusion compound.

Code	WC17AC	WTBAC	WCL
Guest	Acetone	Acetone	-
Molecular formula	$C_{38}H_{22}O_2Cl_4 \cdot 2(C_3H_6O)$	$C_{54}H_{58}O_2 \cdot C_3H_6O$	$C_{38}H_{22}O_2Cl_4$
M_r/g mol^{-1}	768.56	797.08	652.36
Temperature/K	293(2)	294(2)	293(2)
Crystal data			
Crystal system	Monoclinic	Monoclinic	Monoclinic
Space group	*C2/c*	*C2/c*	*P2/n*
a/Å	20.424(6)	17.120(2)	16.938(2)
b/Å	11.496(3)	17.935(2)	11.385(2)
c/Å	18.885(7)	17.232(3)	17.620(3)
β/°	122.23(3)	114.145(10)	116.64(1)
Z	4	4	4
V/Å^3	3751(2)	4828(1)	3037.2(7)
D_c/g cm^{-3}	1.322	1.097	1.427
μ(MoK_α) /cm^{-1}	3.59	0.66	4.25
F(000)	1592	1720	1336
Data collection			
Crystal dimensions /mm	0.40x0.50x0.40	0.45x0.45x0.50	0.40x0.35x0.35
Range scanned θ/°	2.13 to 24.97	1.73 to 24.97	1.79 to 22.54
Range of indices *h,k,l*	-24,20; 0,13; 0,22	-20,18; 0,21; 0,20	-18,16; 0,12; 0,18
No. of reflections collected	3397	4407	3867
No. of unique reflections	3295	4252	3867
No. of reflections observed with $I_{rel}>2\sigma(I_{rel})$	1967	2200	2593
Final refinement			
No. of restraints	2	4	0
No. of parameters	234	287	406
R1 ($I_{rel}>2\sigma(I_{rel})$)	0.0643	0.0659	0.0429
wR2 ($I_{rel}>2\sigma(I_{rel})$)	0.1777	0.1802	0.1107
Extinction coefficient	-	0.0034(5)	-
Max. height in electron density map /eÅ^{-3}	0.631	0.510	0.222
Min. height in electron density map /eÅ^{-3}	-0.462	-0.226	-0.345
Absorption Correction factor	0.9512-0.9980	-	0.8950-0.9972

1 P. Schuster, G. Zundel and C. Sanderfy, *The Hydrogen Bond II, Structure and Spectroscopy*, North Holland Publishing Co., Amsterdam, 1976, 411.

2 M.E. Brown, D. Dollimore and A.K. Galwey, *Comprehensive Chemical Kinetics*, ed. C.H. Bamford and C.J. Tipper, Elsevier, Amsterdam, 1980, vol.22, p 220.

3 B. Hingerty, B. Klar, G.L.Hardgrove, Ch. Betzel and W. Saenger, *J. Biomol. Struct. Dyn.*, **2**, 1984, 249.

CHAPTER 7 HOST COMPOUNDS - CLASS A

In this chapter the host conformations of the inclusion compounds of the three related hosts in Class **A** are discussed.

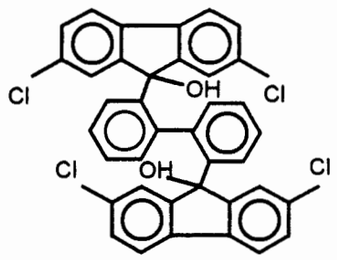

Host A1

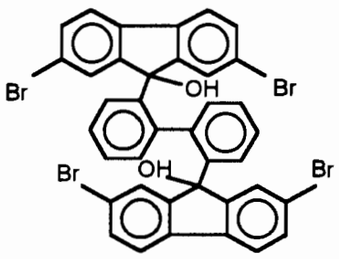

Host A2

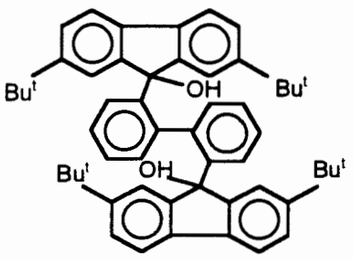

Host A3

Scheme 1

The host conformations are compared with those of related host compounds found in the Cambridge Structural Database[1]. The existence of different polymorphic forms of the host compounds upon desolvation was observed and that will be discussed at the end of this chapter.

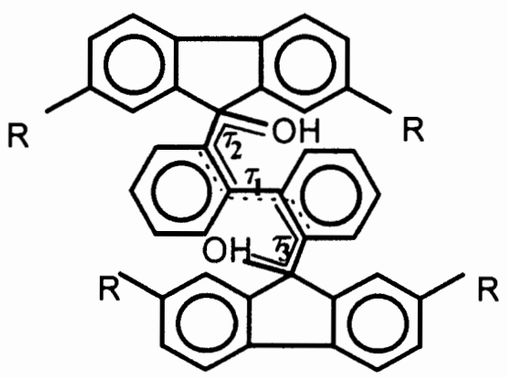

Scheme 2

The torsion angles describing the host conformation.

Host Conformation

The host conformation is governed by three torsion angles, τ_1, τ_2 and τ_3 , shown in Scheme 2. The two benzene rings in the central biphenyl moiety are at approximate right angles, and Table 7.1. compares the torsion angle around this bond, τ_1, and the other torsion angles for host molecules derived from similar structures[2,3,4,5]. Torsion angle τ_1 varies from 88.4 to 101.4°, while τ_2 and τ_3 range considerably from -30 to -1°.

In the case where compounds crystallised in centrosymmetric space groups, we chose to quote the torsion angle τ_1 as positive, i.e. for the (S)-molecule. This allowed us to make direct comparisons with the structures of the enantiomerically pure (S)-isomer of the host which crystallised in the space group $P2_12_12_1$.

Compounds **WTB14D** and **WTBAC** exhibited intramolecular hydrogen bonding stabilising the crystal structure. Only one other inclusion compound of $C_{54}H_{58}O_2$ (host **A3**) has been published[3], and it is also stabilised by an intramolecular hydrogen bond. From the information obtained for other crystal structures, this intramolecular hydrogen bonding seems very common in the structures involving $C_{38}H_{26}O_2$. In fact, the only crystal structure[5] to date of this host, which does not exhibit intramolecular hydrogen bonding is that of the α-phase of (S)-$C_{38}H_{26}O_2$. Previous studies[3] showed the existence of intramolecular hydrogen bonding in inclusion compounds of $C_{38}H_{22}O_2Cl_4$ (host **A1**). This was not observed in the structures elucidated in the current study. In the structures involving the halogenated host compounds, the distance between the O atoms on the hydroxyl groups varied from 3.242(4) to 3.528(6)Å.

Table 7.1. Torsion angles describing host conformation, as well as intramolecular O···O distances.

Compound‡	R	Guest (H:G)	τ_1/°	τ_2/°	τ_3/°	O···O/Å
W17DIA	Cl	1,4-dioxane (2:7)	101.4(6)	-2.0(7)	-8.5(7)	3.528(6)
W17DB	Br	1,4-dioxane (2:7)	100.9(9)	-1(1)	-8.3(9)	3.519(5)
W17	Cl	1,3-dioxolane (1:2)	94.2(7)	-10.9(5)	-10.9(5)	3.277(5)
WB3DA	Br	1,3-dioxolane (1:2)	93.5(8)	-10.6(6)	-10.6(6)	3.242(4)
W13DT	Cl	1,3-dioxane (1:2)	96.9(7)	-7.2(6)	-7.2(6)	3.408(4)
WC17AC	Cl	acetone (1:2)	92.5(7)	-1.6(5)	-1.6(5)	3.398(5)
WTB14D	Bu^t	1,4-dioxane (1:1)	89.7(9)	-27.1 (6)	-27.1 (6)	2.744(7)
WTBAC	Bu^t	acetone (1:1)	89.1(6)	-26.9(5)	-26.9(5)	2.752(5)
WCL	Cl		97.9(5)	-6.8(4)	-6.8(4)	3.502 (5)
			89(1)	-15(1)	-15(1)	3.327 (5)
1[3]	Bu^t	butyronitrile (1:1)	88.4(6)	-28.5(7)	-28.5(7)	2.729(5)
2[3]	Cl	cyclohexanone (1:2)	89.0(9)	-22.4(8)	-28.1(8)	2.697(7)
3[3]	Cl	cyclopentanol (1:2)	90.8(9)	-25.2(8)	-27.1(9)	2.698(6)
4[3]	Br	DMF (1:2)	92(2)	-1(2)	-3(2)	
5[2]	H	DMF (1:2)	93(1)	-18(1)	-19(1)	2.773(9)
6[2]	H	cyclohexanone (1:2)	92(2)	--24(2)	-19(1)	2.76(1)
7[2]	H	di-*n*-propylamine (1:1)	93(2)	-19(2)	-13(2)	2.93(1)
8[2]	H	acetonitrile (1:1)	90.9(5)	-23.5(5)	-21.8(5)	2.826(4)
9[4]	H	diethyl ether (1:1)	93.2(4)	-30.0(4)	-19.2(4)	2.727(3)
10[5]‡	H	(S)-butanol (1:2)	90(1)	-24(1)	-19(1)	2.685(8)
11[5]†	H	(R)-butanol (1:2)	90(2)	-28(2)	-22(2)	2.67(2)
12[5]†	H	butanol (1:2)	89(1)	-22(1)	-24(1)	2.682(8)
13[5]	H	(S)-butanol (1:2)	91(1)	-24.2(9)	-17.9(9)	2.709(7)
14[5]	H	(R)-butanol (1:2)	91(1)	-23(1)	-20(1)	2.70(1)
15[5]	H	butanol (1:2)	89.8(9)	-25.9(9)	-19.9(9)	2.682(8)
16[5]†	H		95.6(9)	-16(1)	-8(1)	3.886(7)

‡ Unless otherwise indicated racemic mixtures of the host compounds were used
† (S)-enantiomer of host

There exists a correlation between the O···O distance, observed in the crystal structures and the three torsion angles, discussed above. This can be seen in Fig 7.1a) to c). The outlier, marked (a), was excluded from the regression analyses, since it represents the α-phase of (S)-$C_{38}H_{26}O_2$ and all the other structures are of inclusion compounds. The correlation coefficients (R^2) from the regression analyses are summarised in Table 7.2.

Table 7.2. Correlation coefficients from the regression analyses of Figs 7.1a)-c) and 7.2.

	R^2
O···O *vs.* τ_1	0.71
O···O *vs.* τ_2	0.91
O···O *vs.* τ_3	0.75
(τ_2 and τ_3) *vs.* τ_1	0.60

For crystal structures with an O···O distance greater than 3Å a much wider range of torsion angles exists, whereas the host compounds, locked into conformation by the intramolecular hydrogen bond, are restricted to a much smaller range of τ_1 to τ_3. This is also illustrated in Fig 7.2., in which τ_2 and τ_3 are plotted *vs.* τ_1. Block A represents inclusion compounds where the O···O distances are less than 3Å. The host compounds are clearly restricted to a much narrower range of the three torsion angles in order to permit the intramolecular hydrogen bonding. A correlation exists between torsion angles (τ_2 and τ_3) *vs.* τ_1.

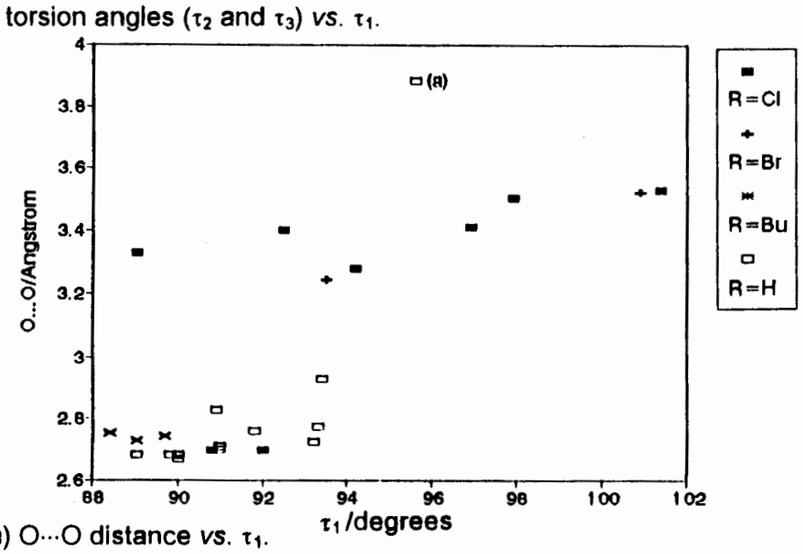

Fig 7.1 a) O···O distance *vs.* τ_1.

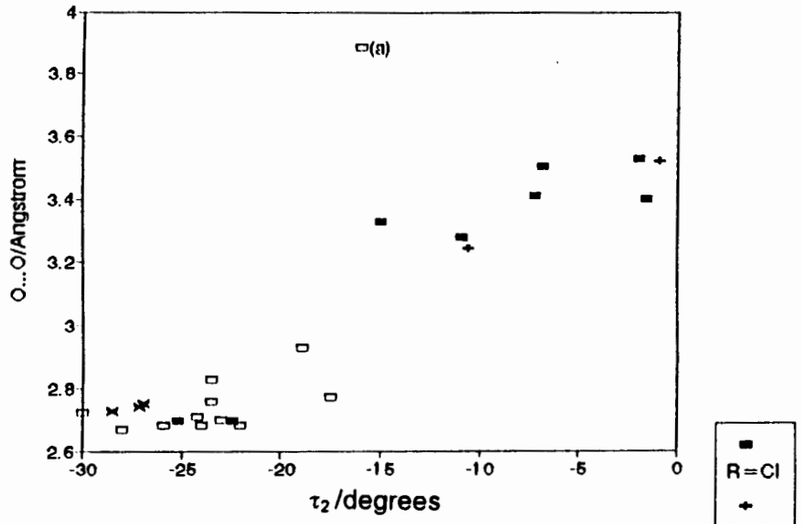

Fig 7.1 b) O···O distance *vs.* τ_2.

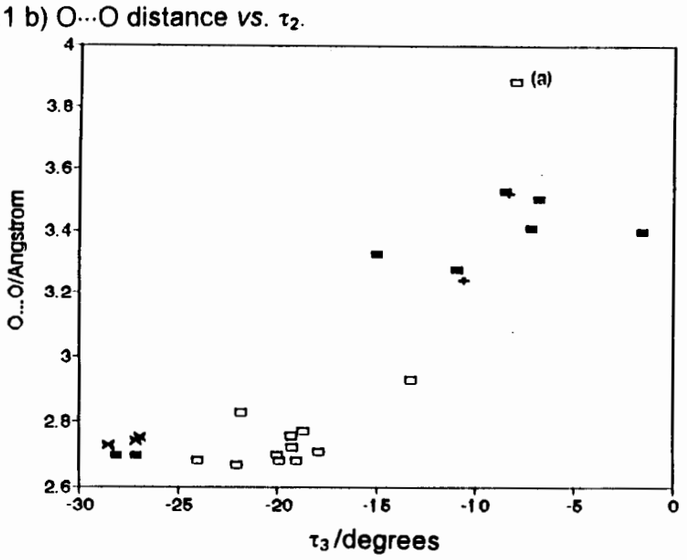

Fig 7.1. c) O···O distance *vs.* τ_3.

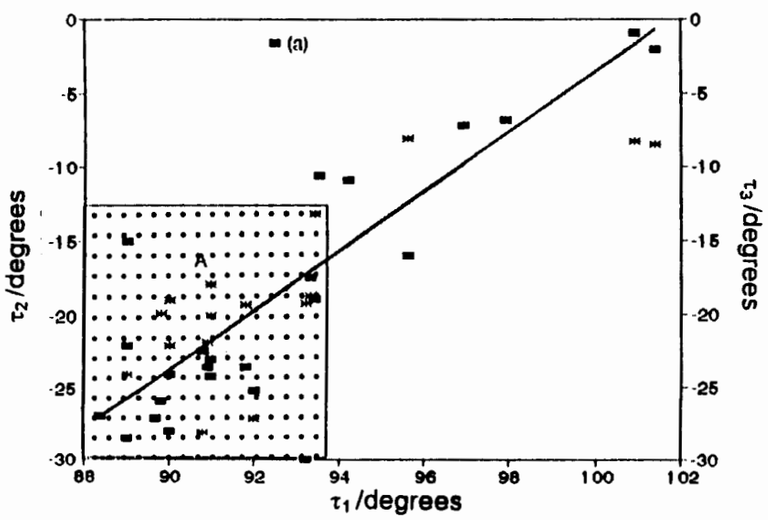

Fig 7.2. (τ_2 and τ_3) *vs.* τ_1.

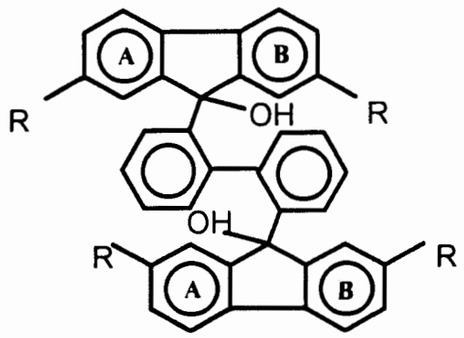

Scheme 3

The fluorenyl moiety was reported to be planar in the structures of other inclusion compounds[2,3,4,5], where the host was $C_{38}H_{26}O_2$. In this study it was found that the fluorenyl moiety can deviate significantly from planarity. The angle between the least-squares planes through the two benzene rings C(1AA)-C(1A)-C(2A)-C(3A)-C(4A)-C(4AA) [Plane **A**] and C(5AA)-C(5A)-C(6A)-C(7A)-C(8A)-C(8AA) [Plane **B**] (see Scheme 3), obtained in the current study, are summarised in Table 7.3.

Table 7.3. Angles describing the deviation from planarity of the fluorenyl moiety in hosts in Class **A**.

Compound	R	Space group	Angle/°
W17DIA	Cl	$P\bar{1}$	2.2(5) 1.0(1)
W17DB	Br	$P\bar{1}$	2.8(6) 1.5(1)
WTB14D	Bu^t	*C*2/*c*	13.9(3)
W17	Cl	*C*2/*c*	6.0(3)
WB3DA	Br	*C*2/*c*	6.3(3)
W13DT	Cl	*C*2/*c*	5.9(3)
WC17AC	Cl	*C*2/*c*	3.9(3)
WTBAC	Bu^t	*C*2/*c*	13.6(3)
WCL	Cl	*P*2/*n*	7.1(2) 5.4(2)

In the structures of **W17DIA** and **W17DB** the fluorenyl moiety approximates planarity with the angle between the planes varying from 1.0(1)° to 2.8(6)°. In the case of the other inclusion compounds studied the fluorenyl moiety is bent, so that the halogen atoms are pointing away from the biphenyl (see Fig 7.3.). This results in the angle between the least-squares planes **A** and **B** for **W17**, **WB3D** and **W13DT** being

approximately 6°. This is larger than the 4° angle observed in **WC17AC**, which displays the same host packing motif. This angle is much larger in structures containing the p-*tert*-butyl substituted host molecule. In both **WTBAC** and **WTB14D** this angle was approximately 14°, resulting in the *tert*-butyl groups pointing away from the central biphenyl moiety as shown in Fig 7.4.

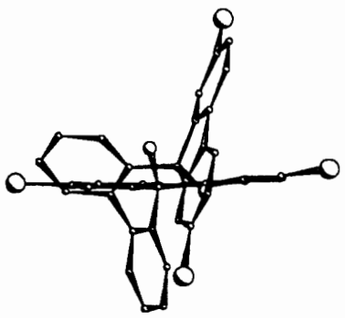

Fig 7.3. Host from **W17**, showing angle between the l.s. planes **A** and **B**.

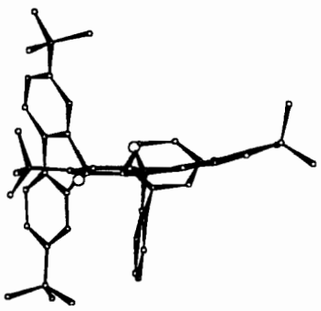

Fig 7.4. Host from **WTB14D**, showing angle between the l.s. planes **A** and **B**.

The variation from planarity of the aromatic rings in all the structures never exceeded 0.01Å. The different bond types observed in the host compound are indicated in Scheme 4, and the bond length ranges observed in each structure are summarised in Tables 7.4. - 7.6.

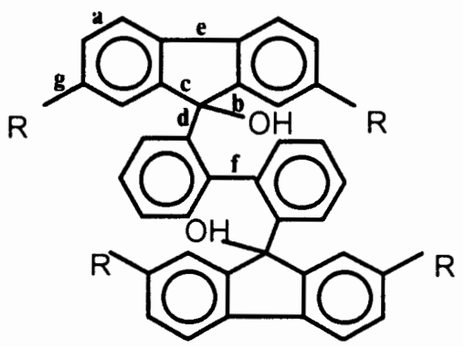

Scheme 4

Table 7.4. Bond length ranges observed for host **A1**.

Compound		W17DIA/Å	W17/Å	W13DT/Å	WCL/Å	WC17AC/Å
a=$C_{ar} \cong C_{ar}$	min	1.361(9)	1.358(7)	1.366(6)	1.361(4)	1.361(5)
	max	1.409(9)	1.400(7)	1.401(6)	1.403(5)	1.406(5)
b=C_{sp^3} - O	min	1.415(7)	1.440(5)	1.439(5)	1.426(4)	1.426(4)
	max	1.426(6)			1.428(4)	
c=C_{ar} - C_{sp^3}	min	1.533(7)	1.537(5)	1.529(6)	1.516(4)	1.536(5)
	max	1.538(8)	1.540(6)	1.535(5)	1.540(4)	1.546(5)
d= C_{sp^3} - C_{ar}	min	1.525(8)	1.552(6)	1.535(6)	1.546(4)	1.515(5)
	max	1.532(7)				
e= C_{ar} - C_{ar}	min	1.469(8)	1.479(6)	1.469(6)	1.464(5)	1.458(5)
	max	1.488(9)			1.465(4)	
f= C_{ar} - C_{ar}		1.495(7)	1.515(8)	1.526(8)	1.509(6)	1.515(7)
g=C_{ar}-Cl	min	1.731(7)	1.757(5)	1.732(5)	1.741(3)	1.737(4)
	max	1.756(7)	1.762(5)	1.747(5)	1.750(4)	1.746(4)

Table 7.5. Bond length ranges observed for host **A2**.

Compound	W17DB/Å	WB3DA/Å
a=$C_{ar} \cong C_{ar}$	1.356(6) - 1.39(1)	1.358(7) - 1.412(6)
b=C_{sp^3} - O	1.408(8) - 1.437(8)	1.422(5)
c=C_{ar} - C_{sp^3}	1.499(9) - 1.526(9)	1.525(6) - 1.538(6)
d= C_{sp^3} - C_{ar}	1.502(9) - 1.526(9)	1.537(6)
e= C_{ar} - C_{ar}	1.45(1)	1.486(6)
f= C_{ar} - C_{ar}	1.499(9)	1.509(8)
g=C_{ar}-Br	1.888(7) - 1.904(7)	1.900(5) - 1.901(5)

Table 7.6. Bond length ranges observed for host **A3**.

Compound	WTB14D/Å	WTBAC/Å
a=$C_{ar} \cong C_{ar}$	1.36(1) - 1.408(7)	1.363(3) - 1.398(5)
b=C_{sp^3} - O	1.424(6)	1.419(4)
c=C_{ar} - C_{sp^3}	1.532(7) - 1.541(7)	1.515(5) - 1.538(4)
d= C_{sp^3} - C_{ar}	1.535(7)	1.551(5)
e= C_{ar} - C_{ar}	1.459(7)	1.471(5)
f= C_{ar} - C_{ar}	1.50(1)	1.505(7)
g=C_{ar}- C_{sp^3}	1.525(8) - 1.531(8)	1.527(5) - 1.545(6)

All bond lengths and angles observed in these structures are comparable with known values[6].

The crystal structures of hosts **A1** and **A2** with the same guests were found to be isomorphous, i.e. **W17DIA** and **W17DB**, which crystallised in the space group $P\bar{1}$, as well as **W17** and **WB3DA**, crystallising in *C*2/*c*.

Host Polymorphism

The host compound $C_{38}H_{22}O_2Cl_4$ (**A1**) exists in three different polymorphic phases, α_1, α_2 and α_3. The α_1-phase was obtained by desolvation of the inclusion compound **W17DIA**. **W17DIA** crystallises in the space group $P\bar{1}$. In Chapter 4 it was shown that **W17DIA** is desolvated partially to form a stable intermediate 1:1 inclusion compound. Complete desolvation of **W17DIA** yields the α_1-phase of the host compound, with a melting point substantially higher than that observed for the α_2-phase (see Table 7.7). **W17**, **W13DT** and **WC17AC** all crystallised in the space group *C*2/*c*, with host:guest ratios of 1:2. All three compounds are isostructural, and yielded the α_2-phase of the host compound, upon desolvation. The third polymorphic phase (α_3) was obtained by recrystallisation of host A1 from 1,3,5-trimethylbenzene. The single crystal structure of this polymorph was discussed in Chapter 6. The X-ray powder diffraction patterns of the three different polymorphic forms of the host are compared in Fig 7.5. From these traces it is clear that the three phases differ substantially. Over a period of a few weeks, the α_1-phase converts to the α_2-phase, suggesting that the former is metastable.

Similar behaviour was observed for $C_{38}H_{22}O_2Br_4$, (**A2**) with **W17DB** yielding the high melting α_1-phase. Upon desolvation of **WB3DA** the host compound decomposed partially and the existence of the α_2-phase could therefore not be confirmed. The partially decomposed host compound melted in a single endotherm, at a much lower temperature than the α_1-phase.

Host **A3** formed isostructural inclusion compounds with 1,4-dioxane and acetone (**WTB14D** and **WTBAC**), which yielded the same host α-phase upon desolvation of the respective inclusion compounds.

The enthalpy change of melting varied between 41 and 58 kJ.mol^{-1} for the various hosts, with no apparent difference between different hosts or polymorphs of the same host, as can be seen in Table 7.7.

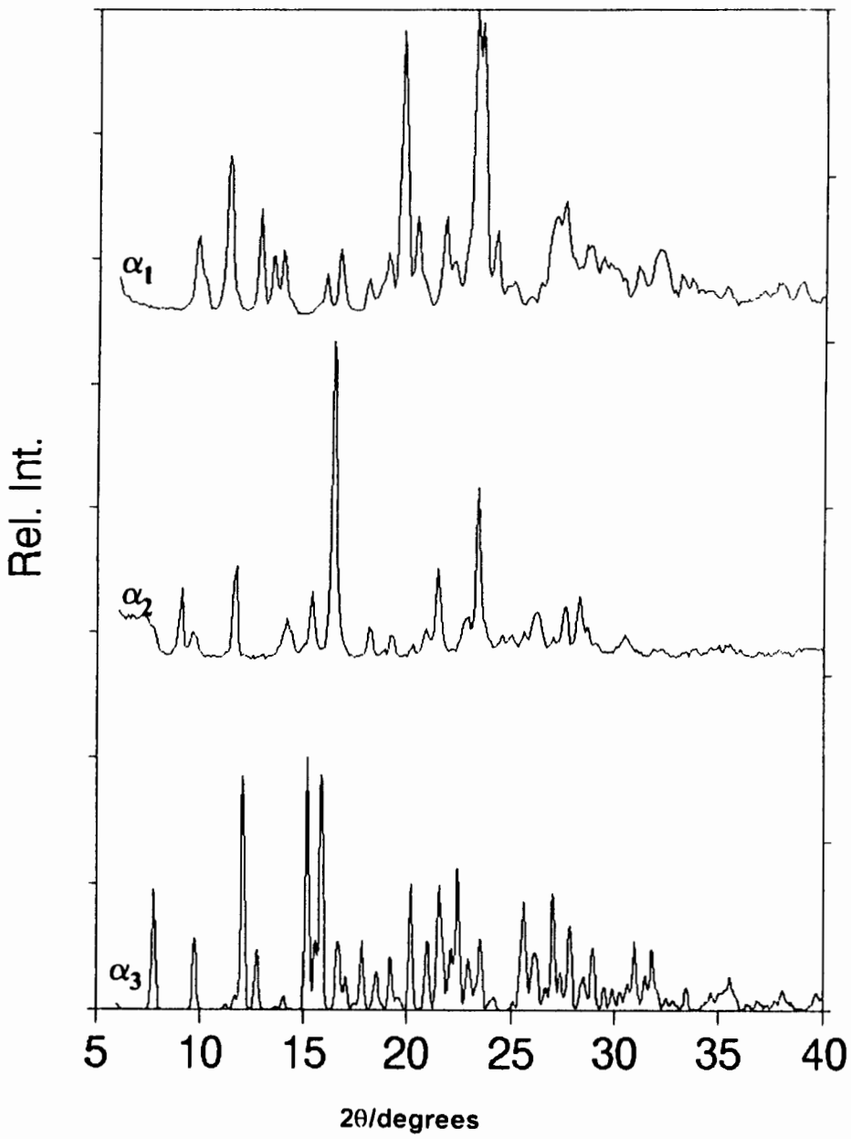

Fig 7.5. X-ray powder diffraction patterns for the α_1-, α_2- and α_3-phases of host **A1**.

Table 7.7. Thermal analytical results for the different polymorphic phases of hosts in Class **A**.

Compound	R	Polymorph	Melting point/°C	ΔH/kJ.mol^{-1}
Host A1				
W17DIA	Cl	α_1	355	48(5)
W17	Cl	α_2	340	45(2)
W13DT	Cl	α_2	340	49(1)
WC17AC	Cl	α_2	340	58(6)
WCL	Cl	α_3	336	-
Host A2				
W17DB	Br	α_1	380	46(5)
W3DBA	Br	α_2	357	41(4)
Host A3				
WTB14D	p-*tert*-butyl	α_1	334	51(1)
WTBAC	p-*tert*-butyl	α_1	334	47(5)

Kinetics of Desolvation

The kinetics of desolvation was investigated for seven of the inclusion compounds studied in this class. The desolvation kinetics of **W13DT** and **WB3DA** were investigated using a constant heating rate of 20°C.min^{-1}, whereas the kinetics of the rest of the compounds were studied using isothermal thermogravimetry, over the temperature ranges indicated in Table 7.8. The compensation effect[7], discussed in Chapter 1, occurs in a group of related reactions, for which the influence of changes in A on reaction rate is accompanied by a change in E_a:

$$ln\, A = B\, E_a + C$$

where B and C are constants. Since desolvation of the inclusion compounds of hosts in Class **A** occurred over a wide range of temperatures (40-160°C), $ln\, A$ had to be corrected in order to investigate such a relationship between the Arrhenius parameters obtained in this study. Galwey[8] defined a mean reciprocal temperature (T_M) as the mean of the minimum (T_{min}) and maximum (T_{max}) temperatures at which the reaction kinetics were investigated, so that $T_M^{-1} = 0.5(T_{max}^{-1} + T_{min}^{-1})$. He has shown

that one can assume that the rate constant k=1h^{-1} at T_M. Hence a corrected value of $ln\ A$ can be calculated from:

$$lnA_{T_M}=E_a/RT_M + lnk.$$

It is clear from a plot of lnA_{T_M} vs. E_a, shown in Fig 7.6., that a linear relationship, and hence a compensation effect, exists between the Arrhenius parameters for desolvation of the inclusion compounds of hosts in class **A**, obtained from isothermal TG.

Compound	Method	Kinetic model	T-range/°C	E_a/kJmol^{-1}	$ln\ A$	$ln\ A_{T_M}$
W17DIA	Isothermal	F1	60-88	35(3)	4.32	-8.176
		F1	100-125	111(9)	22.6	-8.153
W17	Isothermal	R2	60-72	128(15)	35.81	-8.143
W13DT	B-D[#]	R2	-	122(2)	44.13	-
WB3DA	B-D	F1	-	136(2)	38.98	-
WC17AC	Isothermal	D3	40-65	58.4(5)	11.11	-8.167
WTB14D	Isothermal	F1	148-160	151(6)	35.05	-8.146
WTBAC	Isothermal	F1	125-145	140.0(2)	34.86	-8.147

Compensation behaviour was also observed for the inclusion compounds of hosts in class **B** (see Chapter 8), and those discussed in this chapter.

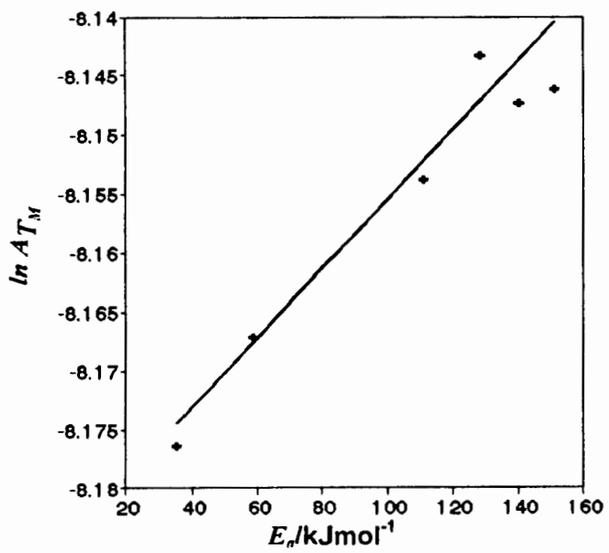

Fig 7.6. Compensation behaviour for inclusion compounds of hosts in Class **A**.

[#] Method described by Borchardt and Daniels see ref. 9

1 Cambridge Structural Database and Cambridge Structural Database System, Version 5.11 (April 1996), Cambridge Crystallographic Data Centre, University Chemical Laboratory, Cambridge, England.

2 L.J. Barbour, S.A. Bourne, M.R. Caira, L.R. Nassimbeni, E. Weber, K. Skobridis and A. Wierig, *Supramol. Chem.*, **1**, 1993, 331.

3 I. Csöregh, E. Weber, L.R. Nassimbeni, O. Gallardo, N. Dörpinghaus, A. Ertan and S.A. Bourne, *J. Chem. Soc., Perkin Trans. 2*, 1993, 1775.

4 M.R. Caira, L.R. Nassimbeni, N. Winder, E. Weber and A. Wierig, *Supramol. Chem.*, **4**, 1994, 135.

5 N. Winder, *Structure and Thermodynamics of Inclusion Compounds of a Diol Host*, M.Sc. Thesis, University of Cape Town, 1995.

6 F.H. Allen, O. Kennard, D.G. Watson, L. Brammer, A.G. Orpen, R. Taylor, *J. Chem Soc. Perkin Trans. 2*, 1987, S1-S19.

7 J. Zsako, Cs. Varhelyi and K. Szilagyi, *J. Therm. Anal.*, **7**, 1975, 41.

8 A.K. Galwey, *Thermochim. Acta*, **242**, 1994, 259.

9 H.J. Borchardt and F. Daniels, *J. Am. Chem. Soc.*, **79**, 1957, 41.

CHAPTER 8 INCLUSION COMPOUNDS CLASS B

In this chapter inclusion compounds of hosts belonging to Class **B** will be discussed. The general host structure is shown in Scheme 1. Three host molecules were investigated where R=phenyl, *p-tert*-butylphenyl and α-naphthyl. The compound with R=phenyl (DDDA) was first synthesised by Toda[1]. Diol host compounds based on the substituted *trans*-9,10-dihydroxy-9,10-dihydroanthracene moiety form a variety of inclusion compounds with a number of guest molecules[2,3,4,5]

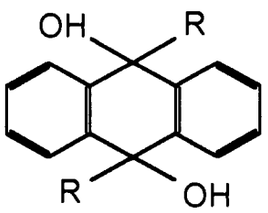

Scheme 1

These hosts readily form inclusion compounds and were considered as model compounds in the study of guest uptake and release. The inclusion compounds of the host (R=phenyl and R=α-naphthyl) with 1,3-dioxolane and the host with R=*p-tert*-butylphenyl with methanol are discussed in this chapter in terms of thermal analysis, crystal and molecular structure and kinetics. The host with R=phenyl was chosen as a model compound to illustrate the use of the quartz micro balance (described in Chapter 3) in the study of guest uptake.

The kinetics of desolvation of the benzene inclusion compounds of two hosts in this class (R= *p-tert*-butyl and R= α-naphthyl) were studied.

DP13D

$C_{26}H_{20}O_2 \cdot (C_3H_6O_2)$

Guest:1,3-dioxolane

Space group: $P\bar{1}$

a=8.253(2)Å α=108.58(6)°

b=8.433(9)Å β=93.60(5)°

c=9.032(7)Å γ=102.95(5)°

Volume = 574.5(7) $Å^3$

Z=1

Tables containing complete crystal and refinement data appear at the end of this chapter.

Thermal analysis

The TG, DTG and DSC traces for **DP13D** are shown in Fig 8.1. A single mass loss step of 17.5% confirmed a host:guest ratio of 1:1 (calc. 16.9%). This corresponds to a diffuse endotherm, with an onset temperature of 110°C, in the DSC trace.

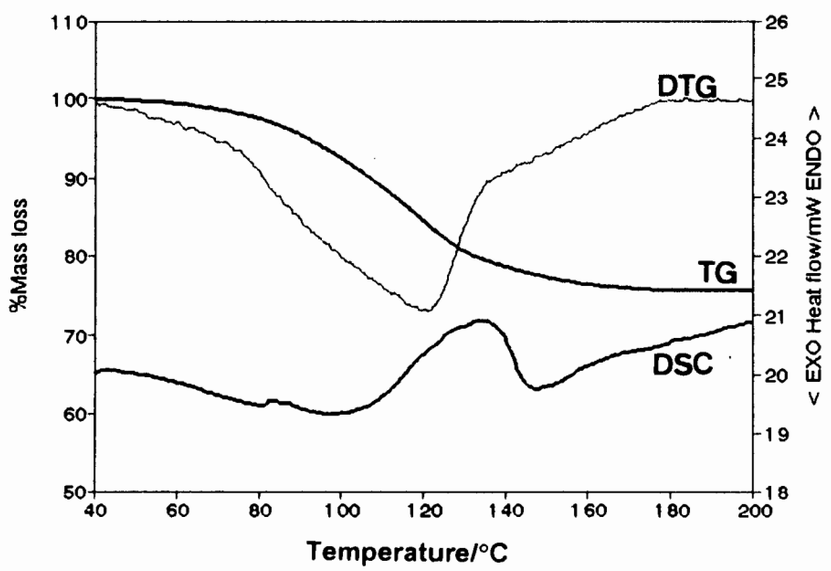

Fig 8.1. TG/DTG and DSC traces of **DP13D**.

Crystal structure

Preliminary photography indicated that the inclusion compound belongs to the triclinic crystal system. The space group $P\bar{1}$ was chosen based on the mean $|E^2-1|$ values obtained from direct methods. The space group choice was vindicated by the successful refinement of the structure.

Solution and Refinement

Direct methods yielded the positions of all the host non-hydrogen atoms. The host conformation, with numbering scheme used, is shown in Fig 8.2. The guest molecule was located in the difference electron density map, upon subsequent refinement. Because there is one host and one guest molecule per unit cell, symmetry requires that both be located at centres of inversion. Thus the host was placed with its molecular centre at the centre of symmetry at Wyckoff position *e*, while the dioxolane guest was disordered and treated as two molecules with site occupancies of 0.5, about the centre of inversion at Wyckoff position *a*. The guest disorder is depicted in Fig 8.3. The O atoms on the dioxolane molecule were placed as follows: O(1G) was placed in the position of the strongest peak in the electron density map. There was not much difference in intensity between the peaks representing O(3G) and C(4G). Both peaks were originally placed as C atoms and allowed to refine. The temperature factor for peak C(3G) was much higher than those of the other C atoms in the guest, and it was changed to an O atom, whose temperature factor refined to a satisfactory value. Both O(1G) and O(3G) were also located within hydrogen bonding distance from the hydroxyl O atom on the host, and could therefore confidently be placed as O atoms. All the host non-hydrogen atoms, as well as O(1G) were treated anisotropically. The remaining guest non-hydrogen atoms were treated isotropically. The hydroxyl hydrogen atoms were located in the difference electron density maps and refined with bond length constraints and individual temperature factors. The rest of the host hydrogen atoms were placed with geometric constraints and refined with common isotropic temperature factors for similar hydrogens. The guest hydrogen atoms were omitted from the final model. A residual electron density of $0.74 e Å^{-3}$ was observed in the

region of the guest, but could not be modelled. Th
R_1=0.0813.

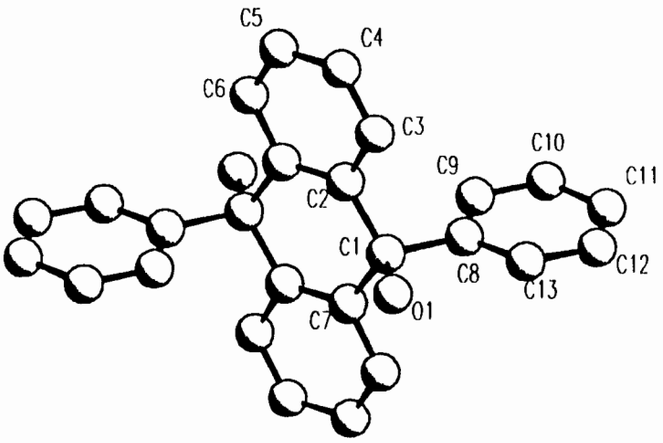

Fig 8.2. View of the host in **DP13D**, showing conformation and numbering.

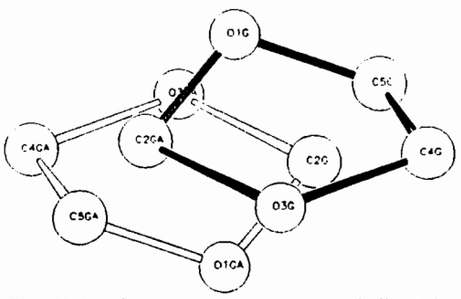

Fig 8.3. Guest disorder modelled in **DP13D**. The two disordered molecules are related by a centre of symmetry and were each placed with a site occupancy of 0.5.

Molecular structure

The molecular structure of **DP13D** is shown in Fig 8.4.

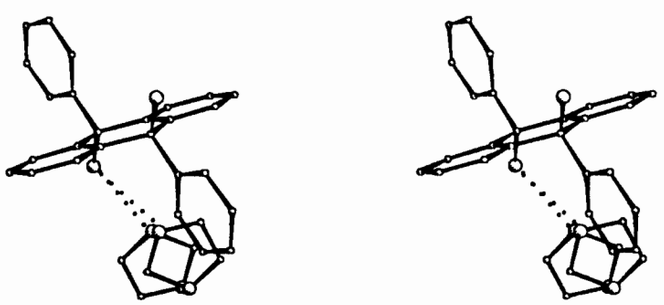

Fig 8.4. A stereoscopic view of the molecular structure of **DP13D**.

The structure is stabilised by O-H···O hydrogen bonds with d(O(1)···O(1G))=2.88(2)Å and d(O(1)···O(3G))=2.82(2)Å. This results in an infinite ribbon of hydrogen bonding running through the structure parallel to [100]. The disordered guest molecules are hydrogen bonded to the host as can be seen in the crystal packing diagram, viewed down [010] as shown in Fig 8.5. The crystal packing viewed down [001] is shown in Fig 8.6. The guest molecules are located in cavities as shown in Fig 8.7. where the host is represented by the hatched areas and the guest is represented with van der Waals radii.

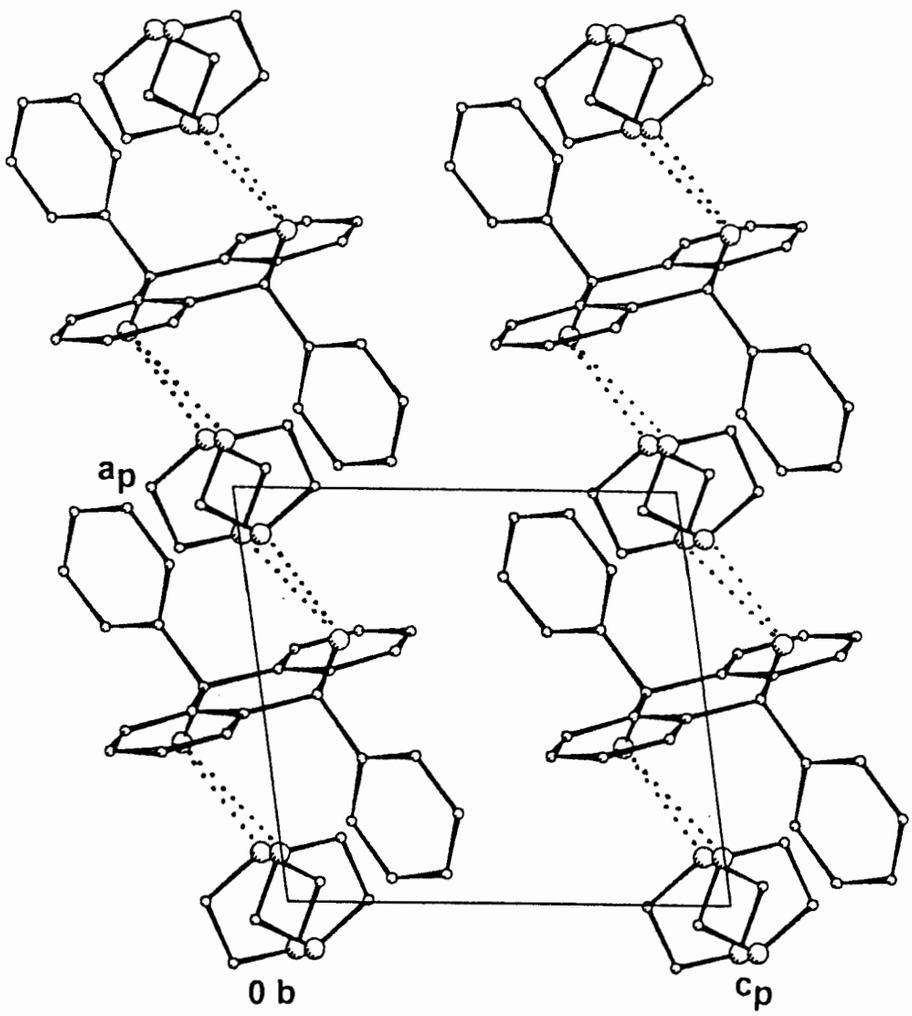

Fig 8.5. The crystal packing in **DP13D** as viewed down [010].

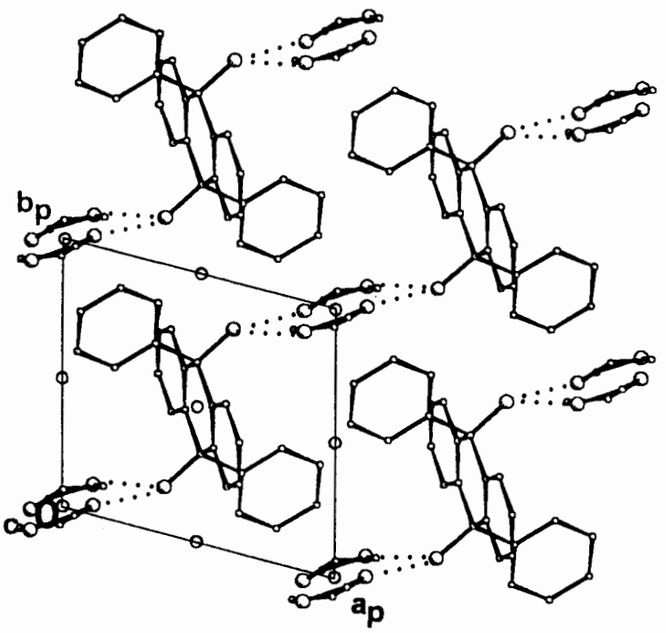

Fig 8.6. The crystal packing in DP13D as viewed down [001].

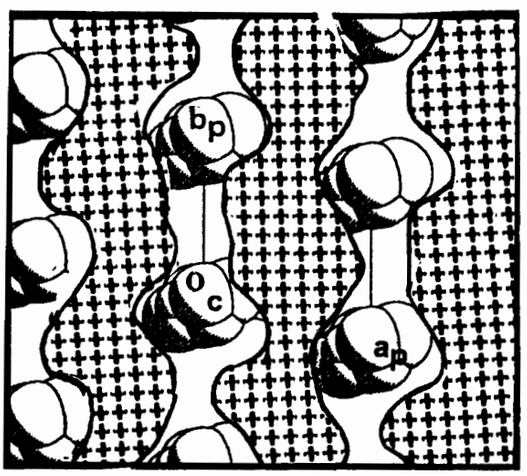

Fig 8.7. The host is represented by the hatched areas and the guest is represented with van der Waals radii.

Kinetics

The kinetics of decomposition was monitored using isothermal TG. A series of mass loss *vs.* time curves were obtained at 5°C intervals over a temperature range of 55-80°C. All the extent of reaction, α, *vs.* time curves were deceleratory and found to follow the contracting area[6] (R2) mechanism:

$1-(1-\alpha)^{1/2}=k_{obs}t$.

X-ray powder diffraction

The decomposition reaction

$Host{\cdot}dioxolane_{(s,\beta)} \rightarrow Host_{(s,\alpha)} + dioxolane_{(g)}$

is accompanied by a phase change in the crystal structure. The solvated, β-form is transformed to the non-porous α -phase, as can be seen in the X-ray powder diffraction patterns shown in Fig 8.8.

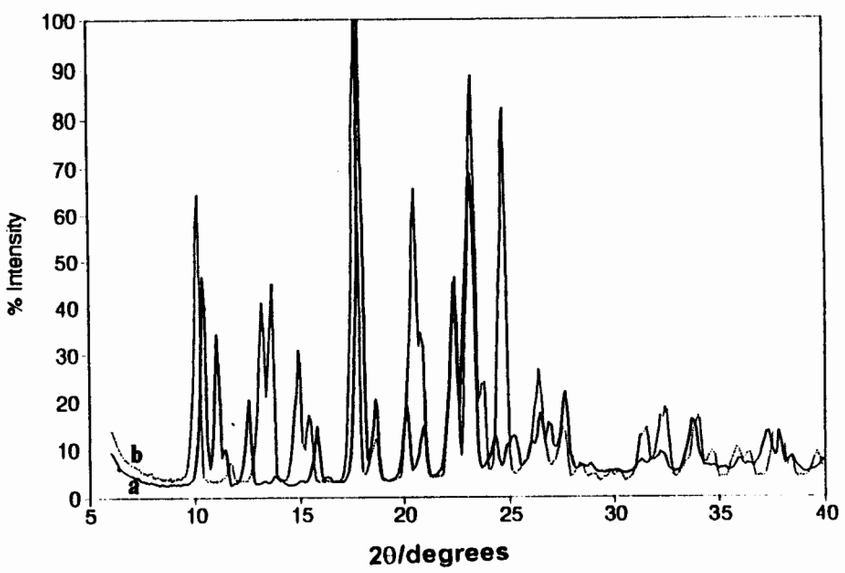

Fig 8.8. X-ray powder diffraction patterns for a) DP13D and b) the desolvated α-phase of the host compound.

The kinetics of desolvation could therefore be followed by measuring the changes in the X-ray powder diffraction patterns, which were recorded at room temperature (25°C), at selected time intervals over a period of 10 days, with a half-life of 60 hours. A 2θ-range of 9-18° was scanned, at 0.05° steps and 1second counts. Over this 2θ region the appearance and disappearance of a few peaks could be monitored. In Fig 8.9. the appearance of two peaks is visible in the 2θ-range 12.7-14.1°. The extent of the desolvation reaction (α) can be calculated from the relative peak areas:

$$\alpha = \frac{a_t}{A}$$

where a_t is the peak area at any time t and A is the peak area when the reaction has reached completion. The peak areas were determined by integration. Various kinetic models were tested for linearity on these α-time data. In Fig 8.10. a plot of $f(\alpha)$ *vs.* time for the R2 mechanism is shown. It is clear from this plot that the desolvation of **DP13D**, measured as a function of the change in crystal structure also follows the R2 mechanism, proposed for the isothermal mass loss reactions. This point was included in the Arrhenius plot of ln k_{obs} *vs.* $1/T$ (shown in Fig 8.11.) which yields a value of 78(2) kJ mol^{-1} for the activation energy of the decomposition reaction.

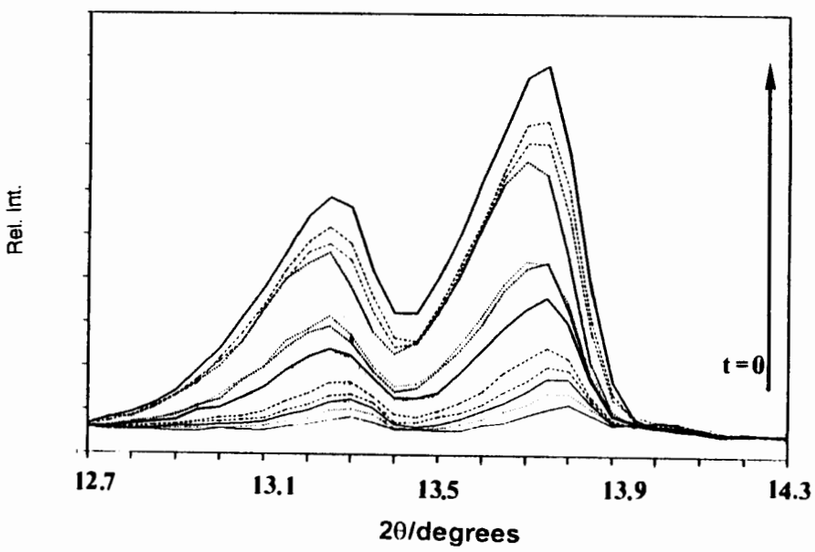

Fig 8.9. The appearance of two peaks in the 2θ-range 12.7-14.1°.

It is gratifying to note that the kinetic curve obtained by the X-ray powder diffraction method follows the same mechanism as the decay curves analysed by TG. What is more, the rate constant thus measured fits in sensibly with those obtained at the higher temperatures by TG, and yields a very good Arrhenius plot (see Fig 8.11.).

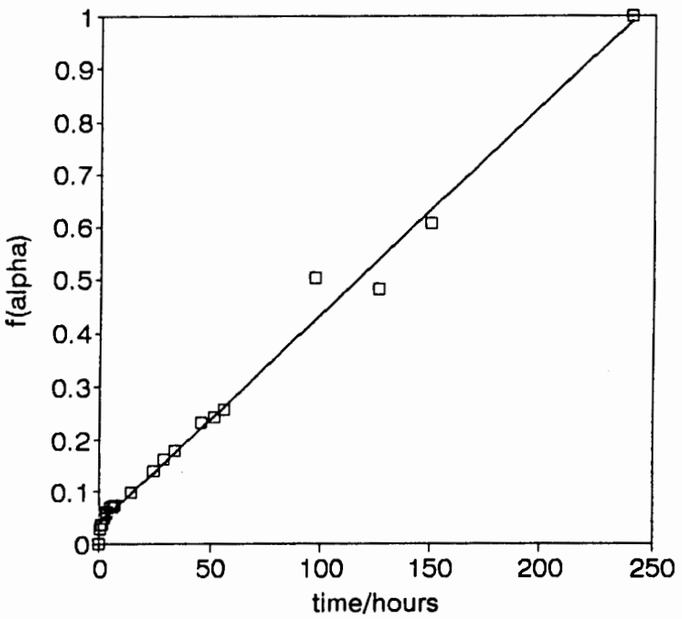

Fig 8.10. *f(α) vs.* time for **DP13D**, obtained from XRD.

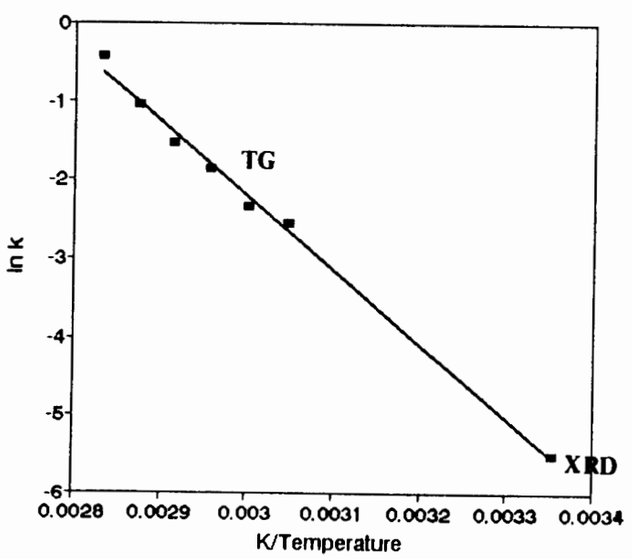

Fig 8.11. Arrhenius plot for the desolvation of **DP13D**.

Sorption studies

We have also studied the enclathration reaction, by exposing the non-porous α-phase of the host compound to the dioxolane vapour and measuring the mass gain with time, at various temperatures and vapour pressures of dioxolane. This was carried out on a Quartz Micro Balance (QMB) described in Chapter 3. The QMB was developed to be able to do sorption studies on small samples. As pointed out in Chapter 3, this apparatus is inherently less accurate than the levitating balance, designed by Barbour *et al.*[7] The levitating balance requires the use of a minimum of 400mg of sample and we were therefore constrained to the use of the QMB, due to a lack of sample. The α-time curves at various temperatures, for the injection of a fixed volume of 1,3-dioxolane are shown in Fig 8.12. An excess of guest was injected (typically ten times more than stoichiometric amounts) to ensure that the partial pressure of guest does not decrease with increased extent of reaction. The guest absorption reactions reached completion within a few minutes, since such small host samples were used (typically 500μg). The observed rate of absorption, for a given number of moles of guest vapour, decreases with an increase in temperature.

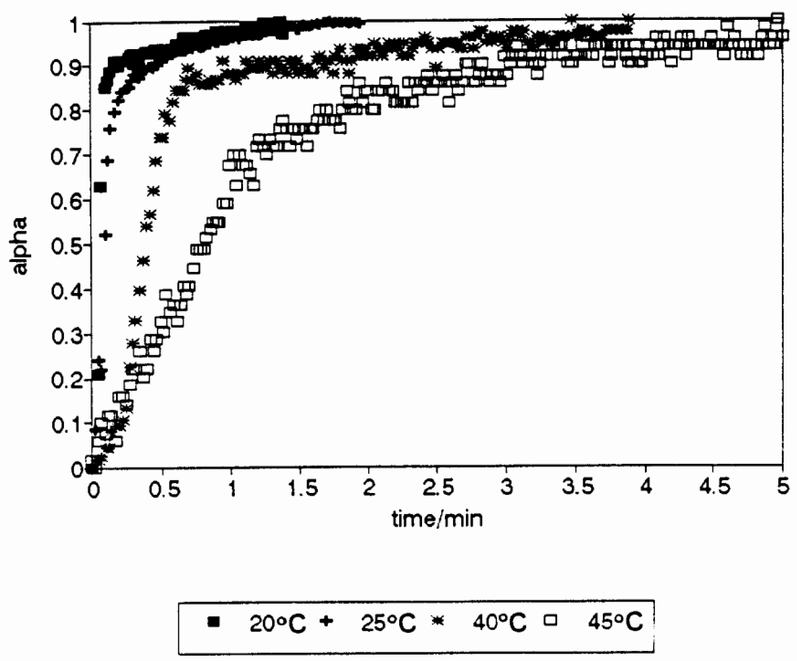

Fig 8.12. α *vs.* time curves for the addition of 118mmHg of 1,3-dioxolane.

This phenomenon was first observed by Barbour, Caira and Nassimbeni[8] for the reaction of this host with acetone vapour. They proposed an empirical rate law:

$$\ln(1-\alpha) = k_f \frac{(P-P_o)}{P_o} t$$

where $k_{obs} = k_f \frac{(P-P_o)}{P_o}$, k_f is the rate constant for the (forward) inclusion reaction and P_o is a threshold pressure, below which the absorption reaction will not take place. The α-time curves at 40°C, and at various vapour pressures of the dioxolane guest are shown in Fig 8.13. They fit the Prout-Tompkins mechanism for sigmoidal curves:$ln[\alpha/(1-\alpha)]=k_{obs}t$.

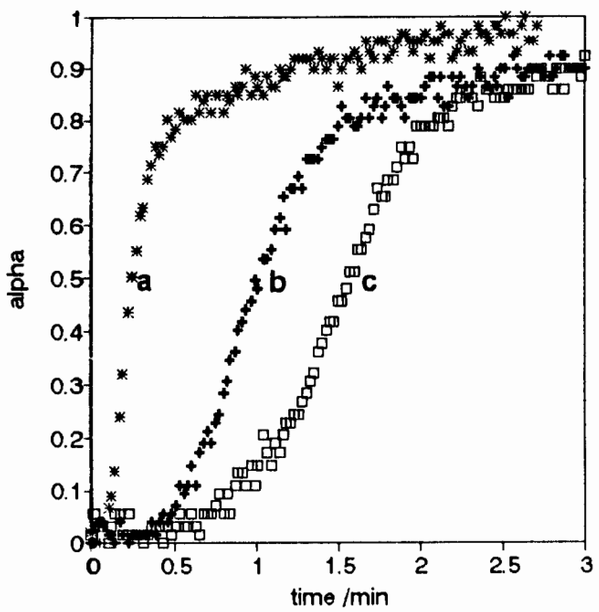

Fig 8.13. α *vs.* time curves obtained at 40°C and (a) 120 mmHg, (b) 97 mmHg and (c) 82 mmHg of 1,3-dioxolane.

From a plot of k_{obs} *vs.* the pressure of the guest , yielding a straight line, for each temperature, the threshold pressure, P_0 and the rate constant, k_f can be obtained. In Fig 8.14. these curves are shown for three different temperatures, 30,35 and 40° C and the information obtained is summarised in Table 8.1. Unfortunately it was not possible to evaluate k_f for the reaction at 45°C , since the reaction only took place over a limited pressure range and the α *vs.* time curves could only successfully be evaluated at two different vapour pressures of 1,3-dioxolane.

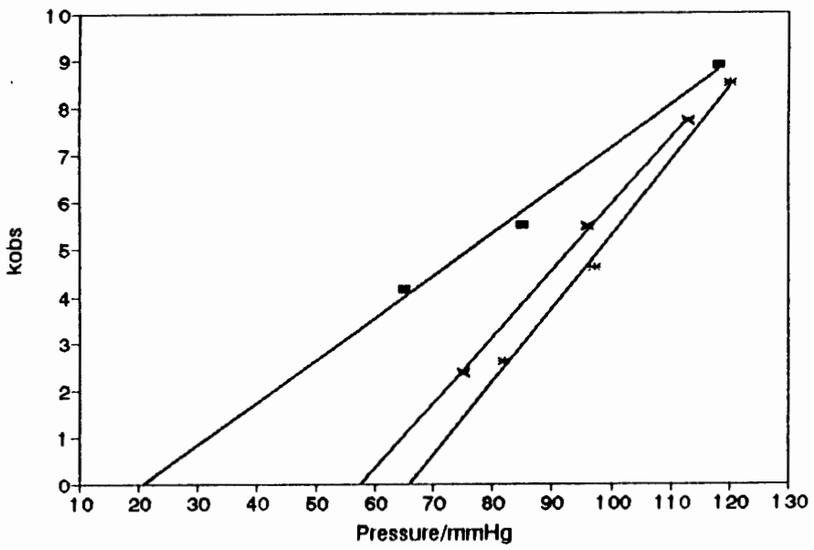

Fig 8.14. A plot of k_{obs} *vs.* pP(1,3-dioxolane).

Table 8.1.

Temperature/°C	P_o/mmHg	k_f (from slope)	k_f (from intercept)
30	21	1.9(1)	1.9(4)
35	58	8.1(2)	8.1(1)
40	66	10.6(2)	10.4(3)

The results summarised in Table 8.1. confirm the existence of a threshold pressure, P_o, below which the absorption reaction does not take place. This has also been confirmed experimentally. The reactions show Arrhenius behaviour, with respect to the rate of the forward reaction. A plot of $ln\ k_f$ *vs.* $1/T$ approximated linearity and an activation energy of 140(50) kJ.mol^{-1} was obtained. From this result, it seems that the activation energy of sorption is nearly double that of desorption. It would be presumptuous to make any more statements about the activation energy for the sorption study, since a limited number of data points were available, and the accumulated error incurred in this method was very large.

DN13D

$C_{34}H_{24}O_2 \cdot 2(C_3H_6O_2)$

Guest:1,3-dioxolane

Space group: $P2_1/n$

a=8.743(2)Å

b=14.623(5)Å β=91.25(2)°

c=12.321(2)Å

Volume =1574.5(7)Å^3

Z=2

Tables containing complete crystal and refinement data appear at the end of this chapter.

Thermal Analysis

The TG/DTG and DSC traces for the desolvation of **DN13D** are shown in Fig 8.15. A host:guest ratio of 1:2 was confirmed by thermal analysis (calc. 24.2%, obs. 23.8%). The TG trace shows two overlapping mass loss steps. This is also clearly visible in the DSC trace, two endotherms, with onset temperatures of 60°C and 100°C, correspond to the desolvation reaction. This behaviour is probably due to the formation of a more dense product layer (in this case the non-porous α-phase of the host compound), resulting in a diffusion barrier to the escape of the gaseous desolvation product.

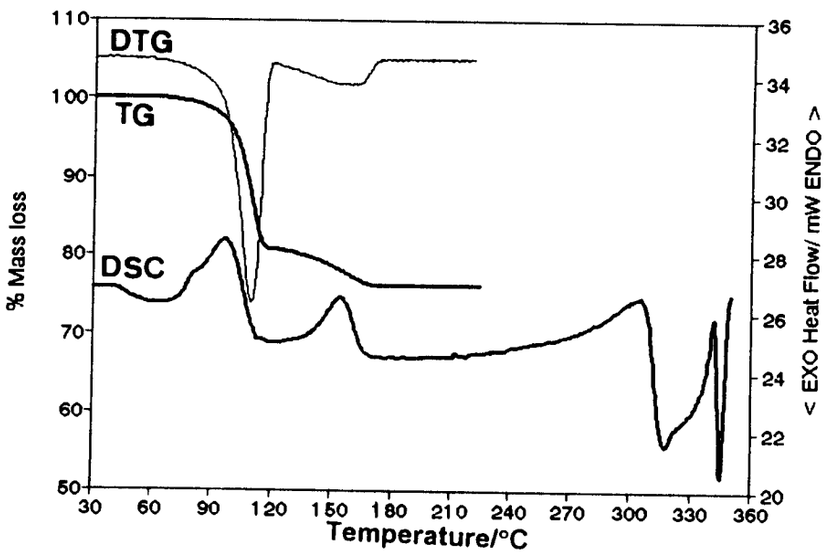

Fig 8.15. TG/DTG and DSC traces for the desolvation of **DN13D**.

Crystal Structure

Solution and Refinement

Direct methods yielded the positions of all the host non-hydrogen atoms. The unit cell contains two host molecules (Z=2). The host was located at a centre of inversion, at Wyckoff position *d*. The guest molecule was located at a general position in the difference electron density map, upon subsequent refinement. The O atoms on the dioxolane molecule were placed as follows: O(1G) was placed in the position of the strongest peak in the electron density map. There was not much difference in electron density between the peaks representing C(3G) and O(4G). Both peaks were originally placed as C atoms and allowed to refine. The temperature factor for peak C(4G) was much higher than those of the other C atoms in the guest, and it was reassigned as an O atom, whose temperature factor refined to a satisfactory value. All the host non-hydrogen atoms, as well as O(1G) were treated anisotropically. The remaining guest non-hydrogen atoms were treated isotropically. The hydroxyl hydrogen atoms were not located, and were omitted from the final model. The rest of the host hydrogen atoms were placed with geometric constraints and refined with common isotropic temperature factors for similar hydrogens. The guest hydrogen atoms were omitted from the final model. A residual electron density of 0.89eÅ^{-3} was observed in the region of the guest, but could not be modelled. The structure refined to R_1=0.1030.

The host conformation, with numbering scheme used, is shown in Fig 8.16.

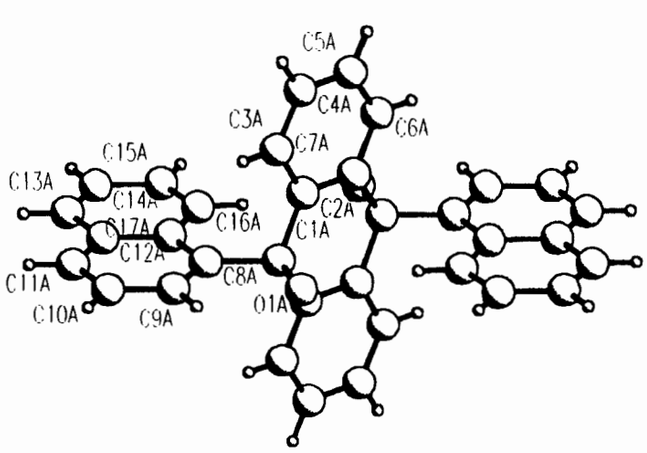

Fig 8.16. Host conformation in **DN13D**.

The host:guest ratio of 1:2 requires the dioxolane guest to be located in a general position. The guest disorder modelled in **DN13D** is depicted in Fig 8.17. The structure is stabilised by a O-H···O hydrogen bond with d(O1···O1G)= 2.808(6)Å. The difference electron density map revealed a strong peak close to O(4G). It was therefore modelled as disordered over the two positions, O(4G) and O(4GA). The site occupancy factors for these two positions were linked and allowed to refine. The final site occupancies refined to 0.5 each. The bond lengths were:

C(3G)-O(4G)	1.31(2)Å
C(3G)-O(4GA)	1.46(2)Å
O(4G)-C(5G)	1.53(2)Å
O(4GA)-C(5G)	1.38(2)Å

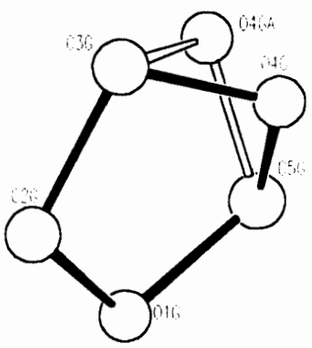

Fig 8.17. Guest disorder as modelled in **DN13D**.

Molecular Structure

The molecular structure of **DN13D** is shown in Fig 8.18. The model of guest disorder was omitted for clarity. Each guest molecule is bonded to the host hydroxyl group, via one hydrogen bond. This is indicated in Fig 8.19., which shows a projection of the crystal structure down [001]. The 1,3-dioxolane guest molecules are located in channels running parallel to [100], with centres at (0,0,½) and (½,½,0). This is shown in Fig 8.20., where the host is represented by the hatched area, and the guest is represented with van der Waals radii.

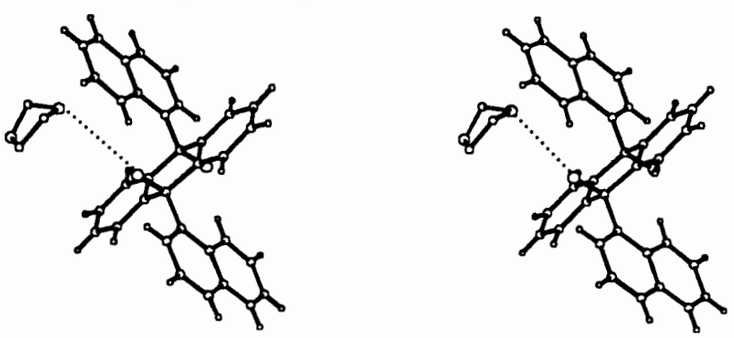

Fig 8.18. Stereoscopic view of the molecular structure of **DN13D**.

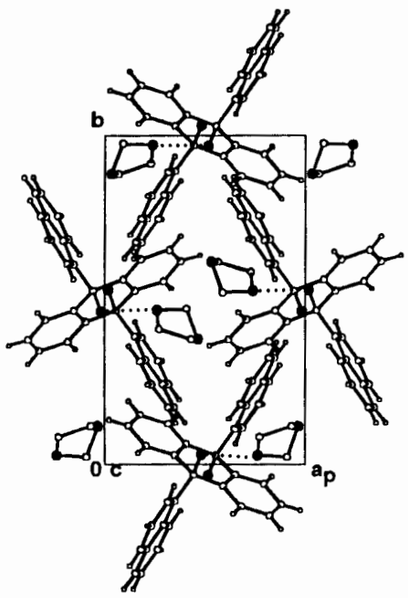

Fig 8.19. Crystal packing of DN13D as viewed down [001].

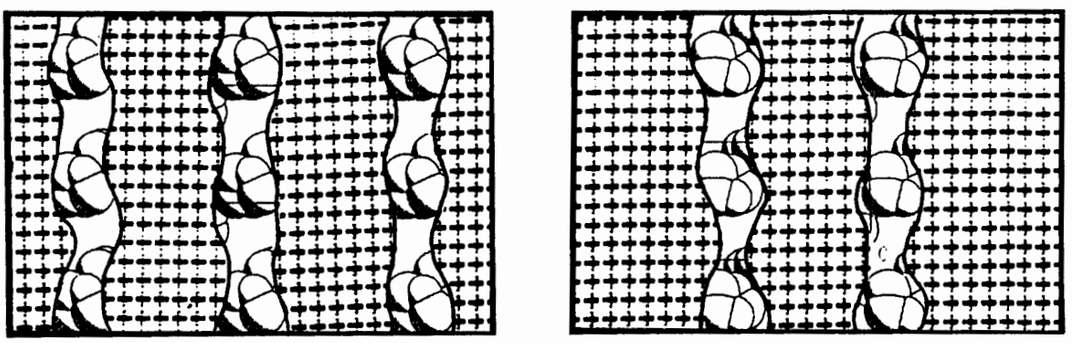

Fig 8.20. A projection of the crystal structure of DN13D, viewed down [010]. The hatched area represents a cross-section of the host molecules cut at a) y=0 and b) y=½. The guest molecules are represented with van der Waals radii.

Kinetics

A series of isothermal TG curves were collected at 5°C intervals, over a temperature range of 55-75°C. It was not possible to separate the two mass loss steps which were observed in the programmed temperature TG experiment. The reaction did not reach completion below 70°C. Thus the converted α *vs.* time curves were investigated in the α-range 0.05-0.50. These α *vs.* time curves are gently curved as seen in Fig 8.21. Attempts to fit different models to these curves resulted in a best fit by the zero order kinetic model, which requires linear decay. Often approximately linear α *vs.* time curves are obtained when the reaction is done at too high a temperature, and the real rate law is observed when the experiment is repeated at a lower temperature. The reaction was investigated at lower temperatures (as low as room temperature), but it still exhibited a linear region, although the desorption reaction did not reach completion. Increasing the temperature tended to speed the reaction up, but also resulted in a linear first part. We therefore decided to analyse the available isothermal data according to an apparent zero order reaction mechanism. An Arrhenius plot was obtained, see Fig 8.22. The resultant activation energy of 50(10)kJ.mol^{-1} is relatively low. A zero order kinetic model would imply that there is no barrier to the loss of the guest, and for this α-range the guest loss process approximates evaporation.

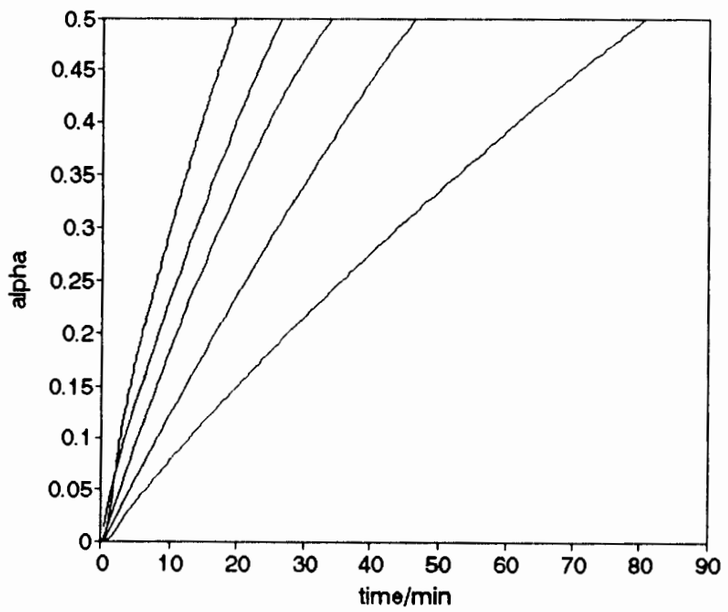

Fig 8.21 α *vs.* time curves obtained for the desolvation of **DN13D**.

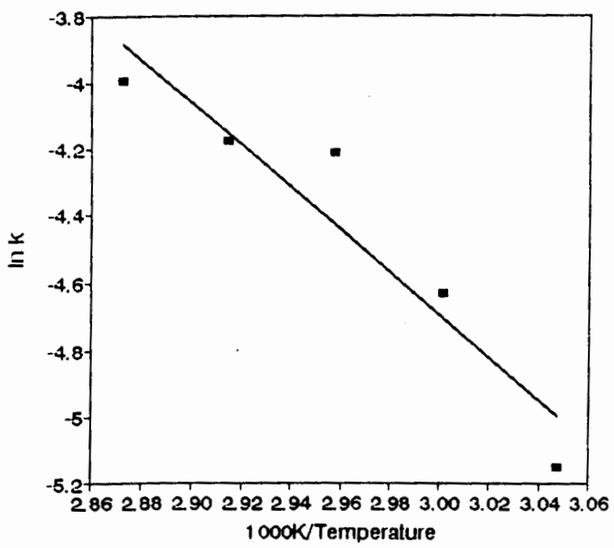

Fig 8.22 Arrhenius plot for the desolvation of DN13D.

X-Ray Powder Diffraction

The guest loss reaction is accompanied by a phase transformation. The inclusion compound is transformed to the non-porous α-phase of the host, upon desorption. This can be seen in Fig 8.23 where the calculated X-ray powder diffraction pattern for DN13D is compared with the powder pattern of the desolvated host compound, obtained experimentally. The crystal structure of the α-phase of the host compound is not known, since it has not yet been possible to grow single crystals of the host alone from any of the solvents used.

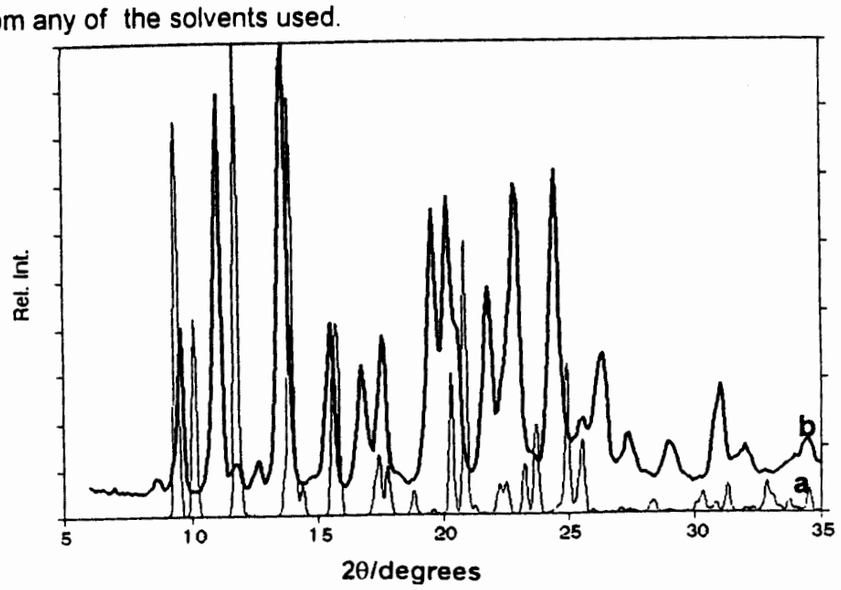

Fig 8.23. X-ray powder diffraction patterns for a) DN13D and b) the desolvated α-phase of the host compound.

DTBM

$C_{34}H_{38}O_2 \cdot (CH_3OH)$

Guest:Methanol

Space group: $P\bar{1}$

a=10.036(3)Å α= 69.86(2)°

b=12.174(2)Å β=70.20(2)°

c=13.294(4)Å γ=79.09(2)°

Volume= 1430.0(6) $Å^3$

Z=2

Tables containing complete crystal and refinement data appear at the end of this chapter.

Thermal Analysis

The TG and DSC traces for the desolvation of DTBM are shown in Fig 8.24. A single mass loss step observed in the TG experiment established a host:guest ratio of 1:1 (calc. 6.3 % obs. 7.3%). This corresponds to an endotherm with an onset temperature of 60°C in the DSC trace. Guest loss is accompanied by the shattering of the crystals (see hot stage microscopy below). The shape of the guest loss endotherm is possibly due to this shattering. A sharp endotherm at 270°C corresponds to the melt of the host, which is accompanied by sublimation.

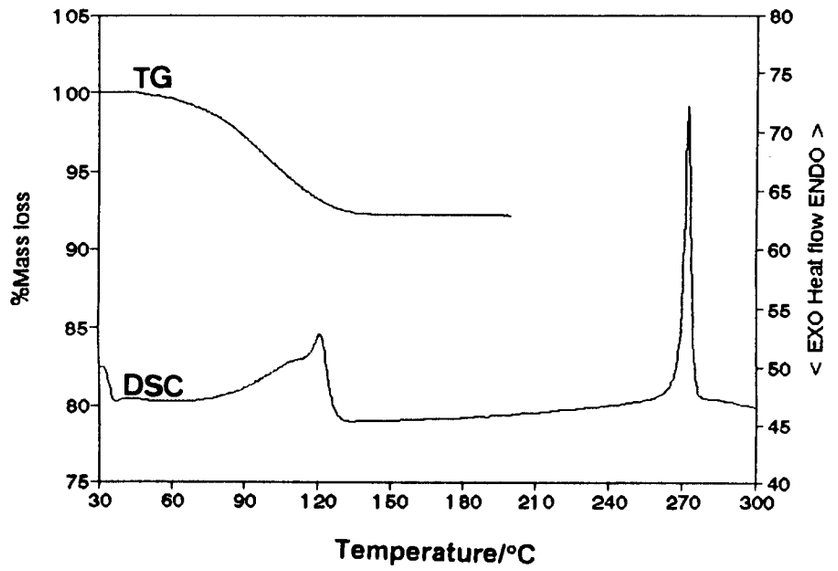

Fig 8.24 TG and DSC traces for the desolvation of DTBM.

Hot Stage Microscopy

A series of photographs, depicting the changes occurring in DTBM upon heating are shown in Colour Plate 8.1.

Colour Plate 8.1.

a) Crystals of DTBM at room temperature.

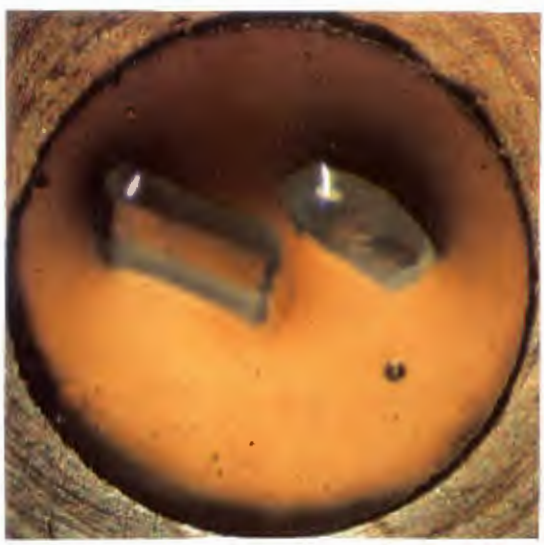

b) At 60°C the crystals became slightly opaque.

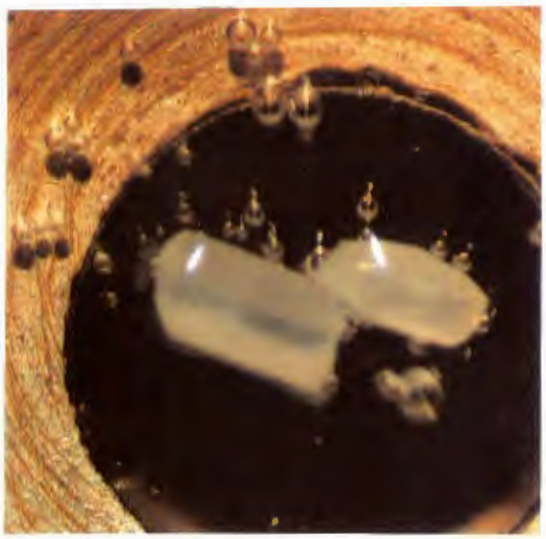

c) At 65°C the guest loss reaction commenced.

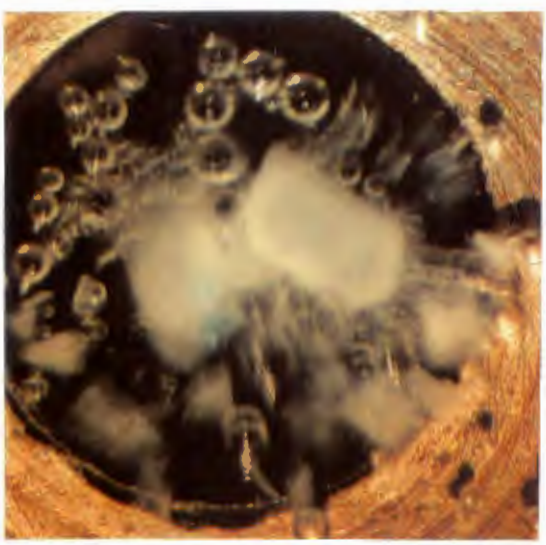

d) After 2min at 65°C the crystals shattered.

Crystal Structure

Preliminary X-ray photography was employed to determine the unit cell parameters and crystal system. Compound **DTBM** was found to belong to the triclinic crystal system, therefore the possible space groups are *P*1 and $P\bar{1}$. The centrosymmetric space group $P\bar{1}$ was chosen, based on the mean $|E^2-1|$ values for the zonal and general reflections. The space group choice was vindicated by the successful refinement of the structure.

Solution and Refinement

Direct methods yielded the positions of all the host non-hydrogen atoms in the asymmetric unit. Two crystallographically independent half host molecules were placed in the unit cell (Z=2). Both molecules were located at centres of inversion. Host molecule A was located at Wyckoff position *e* , and molecule B at Wyckoff position *d*. The non-hydrogen atoms in the guest molecule were subsequently located in the difference electron density maps. All non-hydrogen atoms were refined anisotropically. A residual electron density of $0.227eÅ^{-3}$ was observed in the region of the guest. The host hydroxyl hydrogen atoms were located in the difference electron density map and refined with bond length constraints and individual temperature factors. The rest of the host hydrogen atoms were placed with geometric constraints and refined with a common isotropic temperature factor for similar groups. The methyl hydrogen atoms on the guest were placed in idealised positions and allowed to refine, with a common temperature factor. The guest hydroxyl hydrogen atom was not located and was omitted from the final model. The structure refined successfully to R_1=0.0482.

The conformations of the two crystallographically independent host molecules, with atomic numbering schemes, are shown in Fig 8.25. An intermolecular hydrogen bond exists between the two host molecules with O(1A)···O(1B) = 2.823(2)Å.

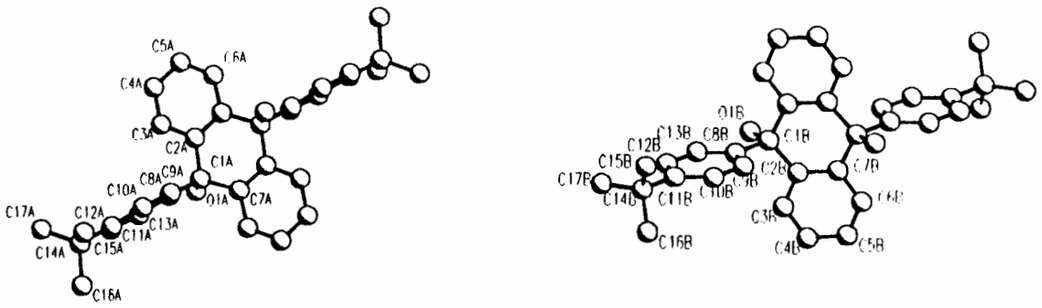

Fig 8.25. Conformations of the two crystallographically independent host molecules A and B.

The host:guest ratio of 1:1 requires that one guest molecule should be situated in a general position in the unit cell. The methanol guest is hydrogen bonded to host molecule A with O(1A)···O(1G)= 2.821(3)Å.

Molecular Structure

The molecular structure of **DTBM** is shown in Fig 8.26.

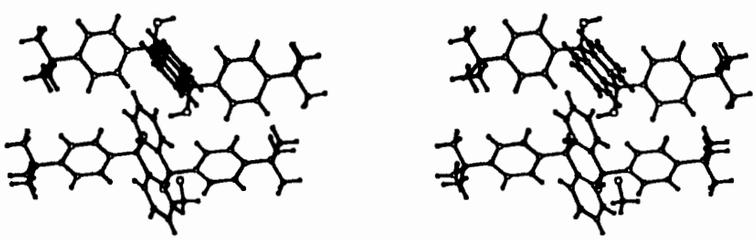

Fig 8.26. Stereoscopic view of the molecular structure of **DTBM**.

A projection of the crystal packing viewed along [001] is shown in Fig 8.27. The hydrogen bonding scheme is indicated with dotted lines. The host molecules are linked by an infinite chain of hydrogen bonds connecting alternating layers of crystallographically independent host molecules, stacked along [010], as can be seen in Fig 8.28. Hydrogen bonds from the O(1A) molecules link the host framework with the methanol guest molecules. The guests are situated in channels running parallel to [010] as shown in Fig 8.29., where the hatched area represents the host and the guest molecules are represented with van der Waals radii.

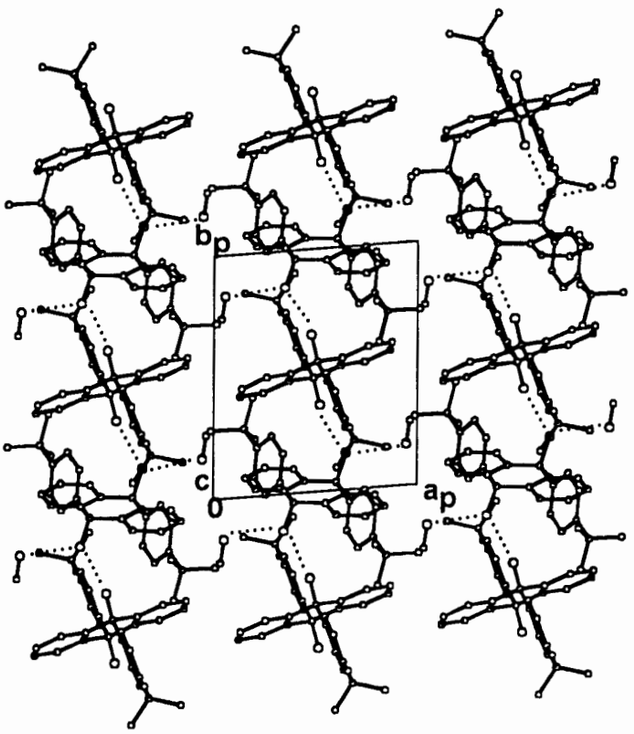

Fig 8.27. Crystal packing in **DTBM** as viewed down [001].

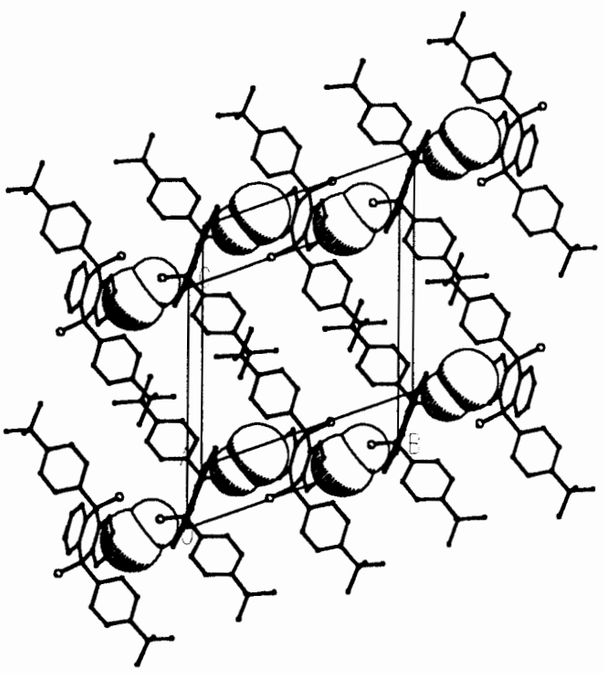

Fig 8.28. Crystal packing in **DTBM**. The guest molecules are represented with van der Waals radii. H-atoms were omitted for clarity.

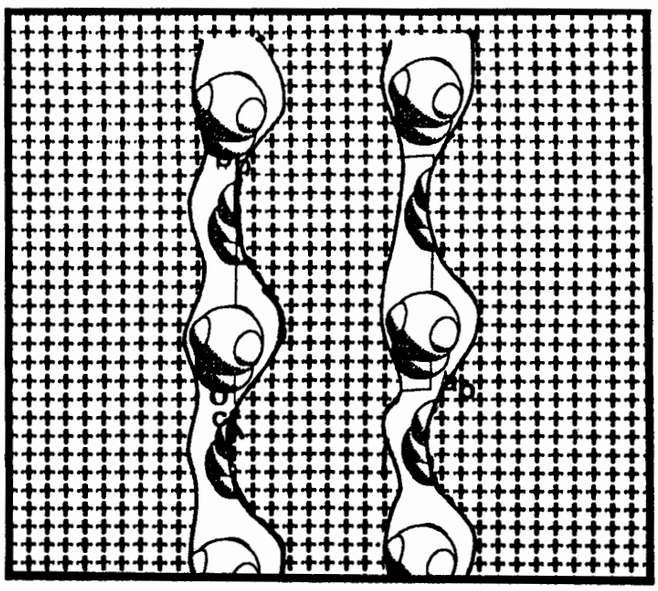

Fig 8.29. A projection of the crystal structure of **DTBM**, viewed down [001]. The hatched area represents a cross-section of the host molecules cut at z=0.

Kinetics

A series of isothermal TG experiments were carried out on **DTBM** at 5°C intervals over a temperature range of 40-65°C. The resultant α *vs.* time curves were deceleratory. Upon testing of a variety of deceleratory kinetic models for linearity, the F1 reaction mechanism was found to fit the data over a wide α-range (0.05-0.95). The Arrhenius plot for this reaction is shown in Fig 8.30. and it yielded an activation energy of 81(8)kJ.mol^{-1}.

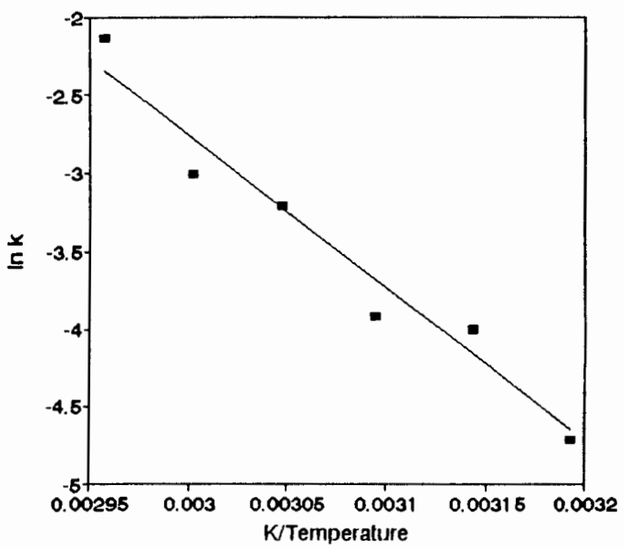

Fig 8.30. Arrhenius plot for the desolvation of **DTBM**.

X-Ray Powder Diffraction

In Fig 8.31. the calculated X-ray powder diffraction pattern for DTBM is compared with that obtained experimentally after desolvation. It is clear that the inclusion compound undergoes a phase change to form the non-porous α-phase. The crystal structure of the α-phase is not known, since it has not yet been possible to grow single crystals which did not include the solvent from which it has been grown.

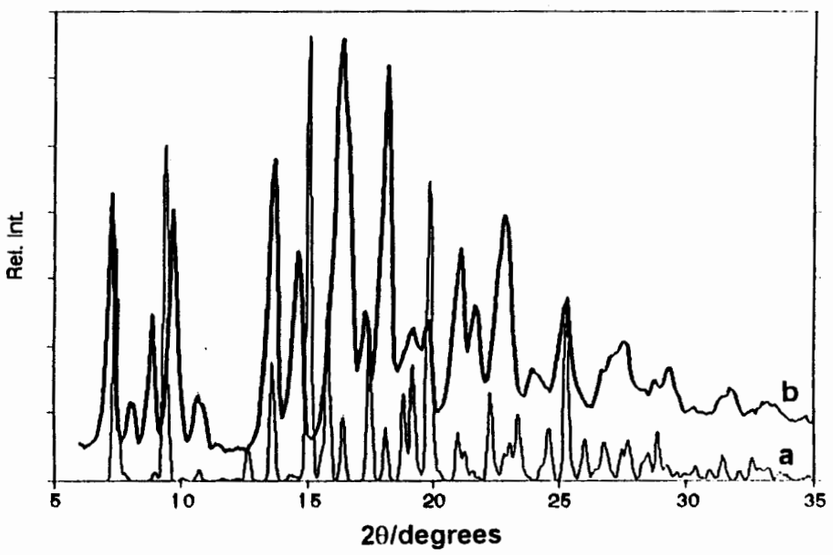

Fig 8.31. X-ray powder diffraction patterns for a) DTBM and b) the desolvated α-phase of the host compound.

DBBz and DNBz

The benzene inclusion compounds of *trans*-9,10-dihydroxy-9,10-di-p-*tert*-butylphenyl-9,10-dihydroanthracene (**DBBz**) and *trans*-9,10-dihydroxy-9,10-di-α-naphthyl-9,10-dihydroanthracene (**DNBz**) were previously prepared and their crystal structures elucidated by Barbour[9]. The main conclusions arrived at by Barbour and published in his PhD thesis, are reproduced here in order to discuss the kinetics in terms of the crystal structure. The kinetic decomposition study, however, was carried out as part of the present work. The crystal structure and refinement parameters for **DBBz** and **DNBz** are summarised in Table 8.2.

TG yielded a host:guest ratio of 1:3, for **DBBz**. It crystallises in the space group $P2_1/c$ with Z=2. The host molecule and two of the six benzene guest molecules were found to be located at centres of inversion. A projection of the structure, viewed along [100] is shown in Fig. 8.32. The guest molecules are situated in cross-linked channels running along [011] and [01 $\bar{1}$] in the (100) plane. This is illustrated in Fig. 8.33, in which the hatched area represents space occupied by the host, while the guest molecules are represented with van der Waals radii.

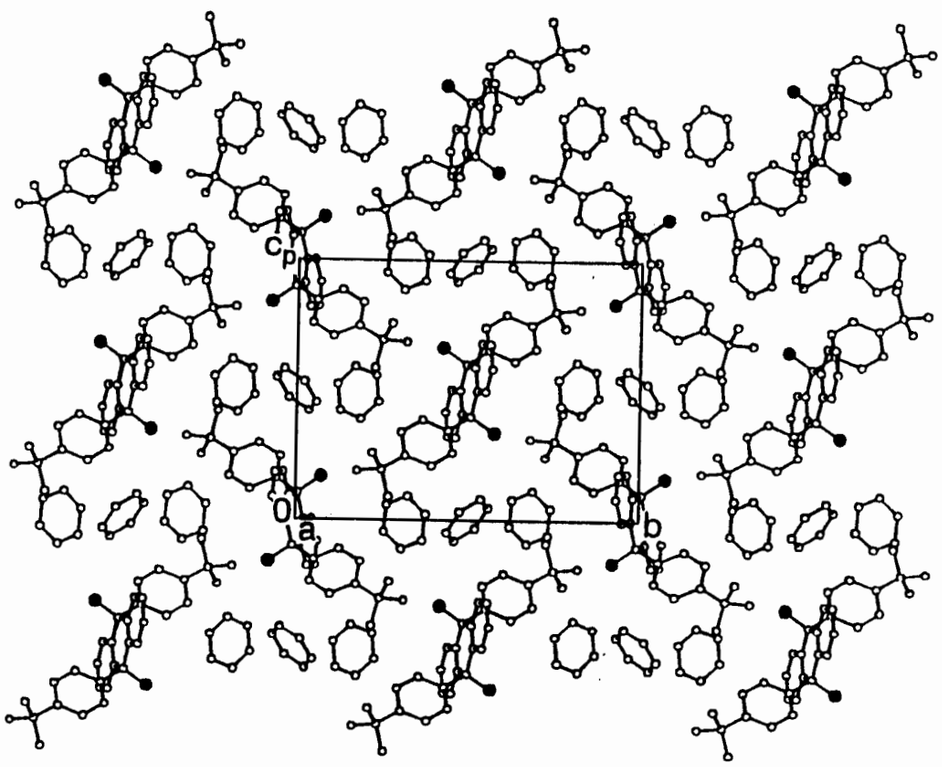

Fig 8.32. A projection of the crystal structure of **DBBz** viewed along [100].

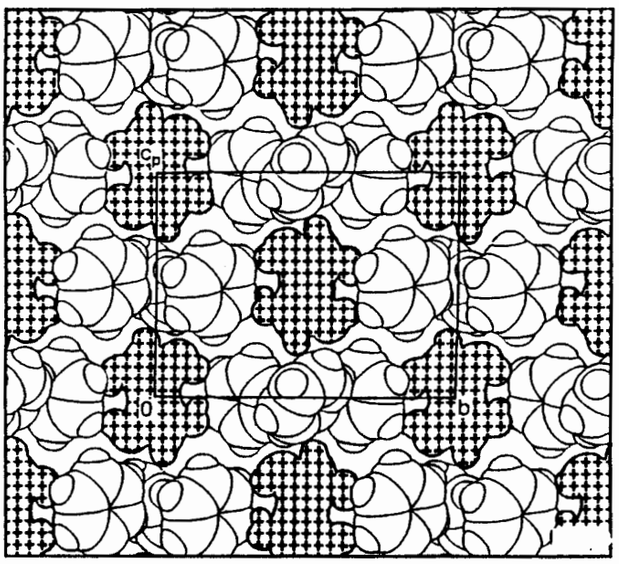

Fig 8.33. A cut through the unit cell of **DBBz** at x=1. The hatched area represents space occupied by the host, while the guest molecules are represented with van der Waals radii.

For **DNBz**, which crystallises in the space group $P\ \bar{1}$ with Z=1, both host and guest molecules again lie at centres of inversion. A projection of the structure viewed along [001] shows the benzene guests to be located in cavities, centred on Wyckoff position *g*, as shown in Fig 8.34.

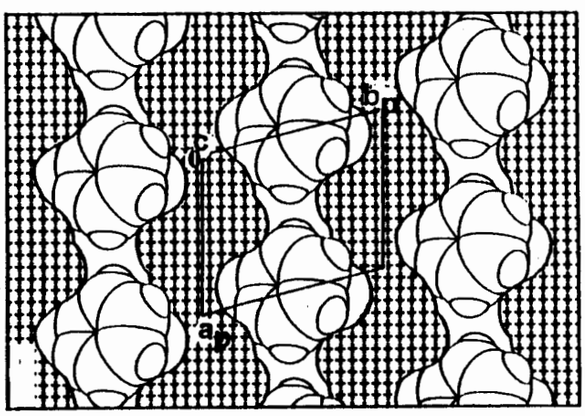

Fig 8.34. A projection of the structure of **DNBz** viewed along [001] showing the benzene guests located in cavities.

Table 8.2. Crystal structure and refinement parameters for **DBBz** and **DNBz**, taken from ref. 9.

CRYSTAL DATA		
Compound	**DBBz**	**DNBz**
Molecular formula	$C_{34}H_{36}O_2 \cdot 3(C_6H_6)$	$C_{34}H_{24}O_2 \cdot C_6H_6$
M_r	711.00	542.68
Space group	$P2_1/c$	$P\bar{1}$
Z	2	1
a (Å)	8.970(4)	7.254(2)
b (Å)	17.128(2)	9.003(3)
c (Å)	13.275(2)	11.882(3)
α (°)	90	108.13(2)
β (°)	90.26(2)	97.40(2)
γ (°)	90	101.29(2)
Volume (Å^3)	2040(1)	708.0(3)
D_m (gcm^{-3})	1.15(1)	1.27(1)
D_c (gcm^{-3})	1.157	1.273
μ (Mo K_α) (cm^{-1})	0.64	0.72
F(000)	764	286
DATA COLLECTION PARAMETERS		
Crystal dimensions (mm)	0.44×0.41×0.34	0.22×0.22×0.31
θ range scanned (°)	1-25	1-25
Range of indices h,k,l	±10,20,15	±8,±10,14
Total exposure time (hrs)	26.0	18.1
Overall intensity variation (%)	-14.3	-0.2
Scan width, x in (x + 1.05tanθ)°	0.85	0.85
# Unique reflections collected	2883	2186
# Observed reflections with $I_{rel} > 2\sigma I_{rel}$	2040	1771
FINAL REFINEMENT PARAMETERS		
Number of variables	264	196
R	0.097	0.050
R_w	0.108	0.064
g in $w = (\sigma^2(F_0) + g(F_0)^2)^{-1}$	0.0027	0.05
Max. shift/e.s.d.	0.158	0.015
Avg. shift/e.s.d.	0.013	0.002
Max., min. heights in difference Fourier (eÅ^{-3})	0.36, -0.34	0.20, -0.27

Kinetics

A series of mass loss *vs.* time curves were obtained for the isothermal desolvation of **DBBz**. The data were reduced to fractional reaction (α) *vs.* time curves. An example of an α *vs.* time curve obtained is shown in Fig 8.35. and it is clearly deceleratory. Various appropriate kinetic models were fitted to the data. The first order (F1) reaction mechanism fitted this reaction over an α-range of 0.1 to 0.9. The semilogarithmic plot of $ln\ k$ *vs.* $1/T$ is shown in Fig 8.36., which yields an activation energy of 87(2) kJ.mol^{-1}. We repeated the kinetic analysis, using rising temperature TG results, obtained at a constant heating rate of 20°C.min^{-1}. The rising temperature thermogram was converted to an α *vs.* time curve. The data were analysed according to the method of Borchardt and Daniels[10] discussed in detail in Chapter 4. If the reaction mechanism is F1, as observed for the isothermal kinetics then: $k=d\alpha/dT/(1-\alpha)^{-1}$. A linear plot of $ln\ k$ *vs.* $1/T$ was obtained over an α-range of 0 to 0.58. The slope of this curve was used to calculate E_a. An activation energy of 89(4) kJ.mol^{-1} was obtained. This corresponds well with that obtained from the isothermal experiments.

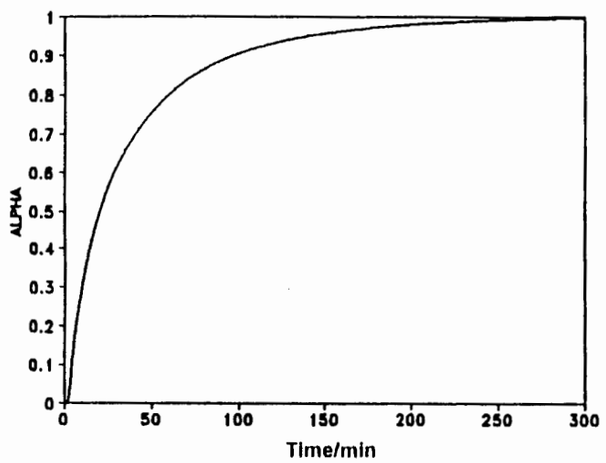

Fig 8.35. α *vs.* time curve for the desolvation of **DBBz**.

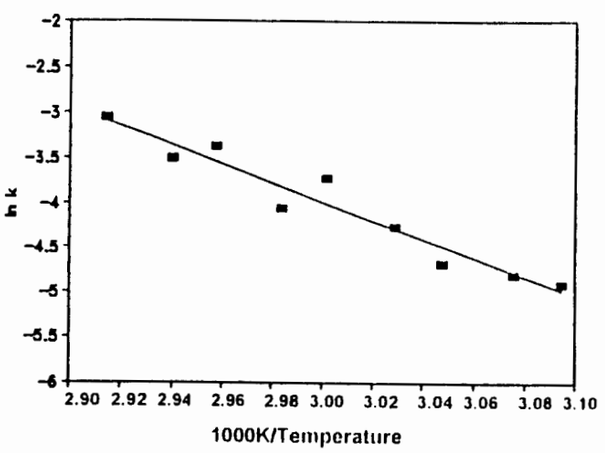

Fig 8.36. Arrhenius plot for the desolvation of **DBBz**.

An example of the α *vs.* time curves, obtained from a series of isothermal TG experiments carried out on **DNBz** over a temperature range of 70-85°C can be seen in Fig 8.37. Slight irregularities were observed in the first part of the curve as the isothermal temperatures were approached. These sections were ignored in the kinetic analysis, since they occurred over a very small time period. The curves were of truncated sigmoidal shape. They did not possess a significant induction period, but clearly consisted of an acceleratory and deceleratory section. Sigmoidal kinetic models were fitted to the data and were best described by the Prout-Tompkins kinetic model. An activation energy of 116 (4) $kJ.mol^{-1}$ was obtained for this reaction over an α-range of 0.05 to 0.95. A curve of *ln k vs. 1/T* is shown in Fig 8.38.

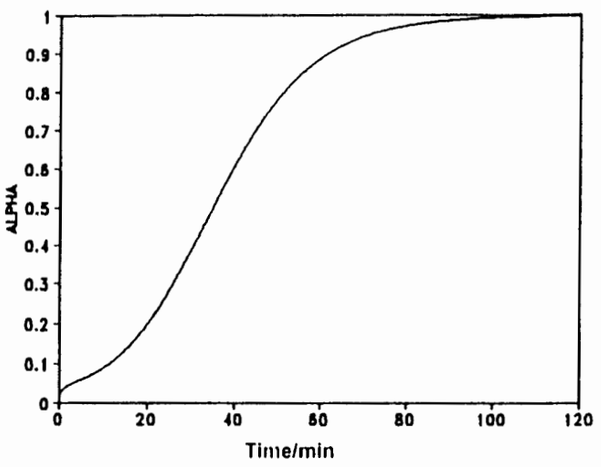

Fig 8.37. α *vs.* time curve for the desolvation of **DNBz**.

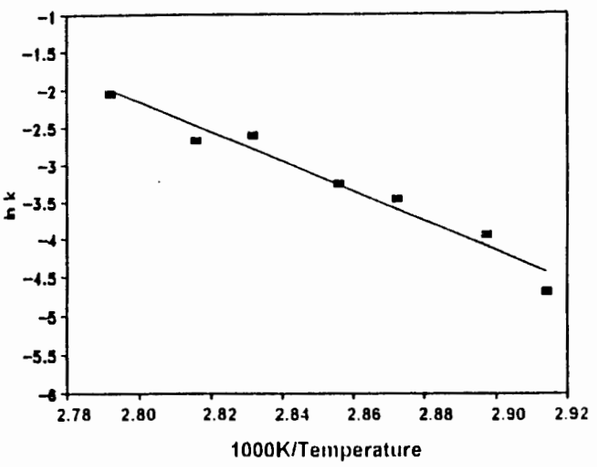

Fig 8.38. Arrhenius plot for the desolvation of **DNBz**.

X-Ray Powder Diffraction

X-ray powder diffraction data were collected for the inclusion compounds as well as the desolvation products in each case. The powder patterns for the host-guest inclusion compounds and their desolvation products are shown in Fig 8.39. and 8.40. for **DBBz** and **DNBz** respectively. Each compound desolvates to form a non-porous α-phase. It is clear from the diffraction patterns that desolvation is accompanied by a phase change in each case.

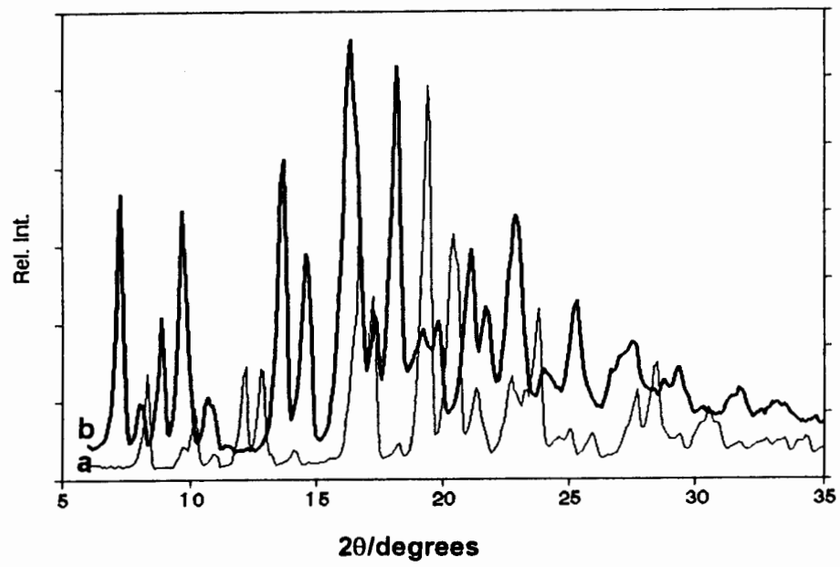

Fig 8.39. X-ray powder diffraction patterns for a) **DBBz** and b) the desolvated α-phase of the host compound.

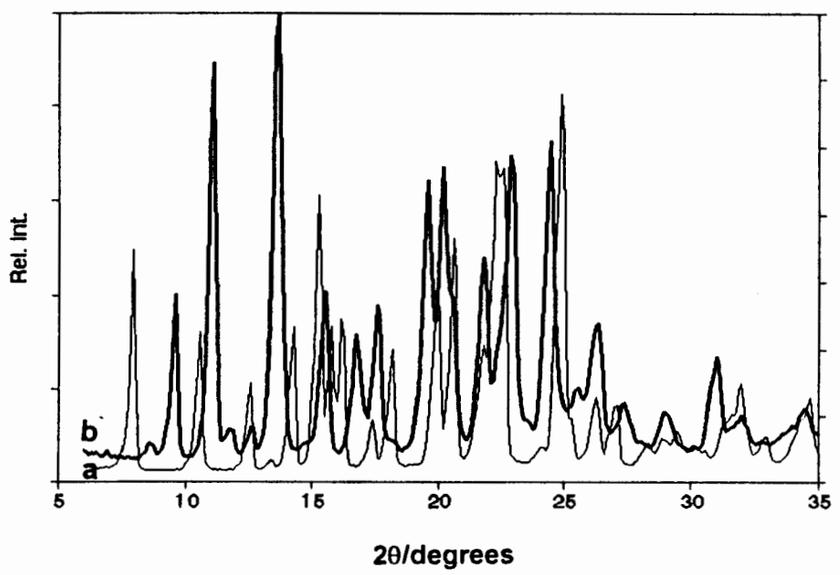

Fig 8.40. X-ray powder diffraction patterns for a) **DNBz** and b) the desolvated α-phase of the host compound.

Host Conformations

All three of the host compounds whose crystal structures have been elucidated in this chapter share the common tricyclic "template" with its *trans*-9,10-dihydroxy functional groups. The main difference in host conformation is the size and shape of the aromatic substituents in the 9,10-positions. These substituents mainly influence the crystal packing and have not been found to participate in direct coordination with the guest molecules. In all three structures the host molecules were located on a centre of symmetry. The 9,10-dihydroanthracenes were tested for planarity. The host molecules in **DP13D** and **DTBM** both yielded least-squares planes through atoms C(1), C(2), C(7), C(2'), C(7') and C(1') with the RMS deviation from the plane, d < 0.03Å. Schubert[11] has suggested that a value of d $\geq$ 0.03Å indicates significant deviation from planarity, based on the technique of Duax and Norton[12]. In **DN13D**, C(1A) was found to deviate significantly from the plane. It is clear from Fig 8. 41. that the deviation from planarity of the central ring results in a chair puckering, so that the host still occupies a site of $\bar{1}$ symmetry in the unit cell.

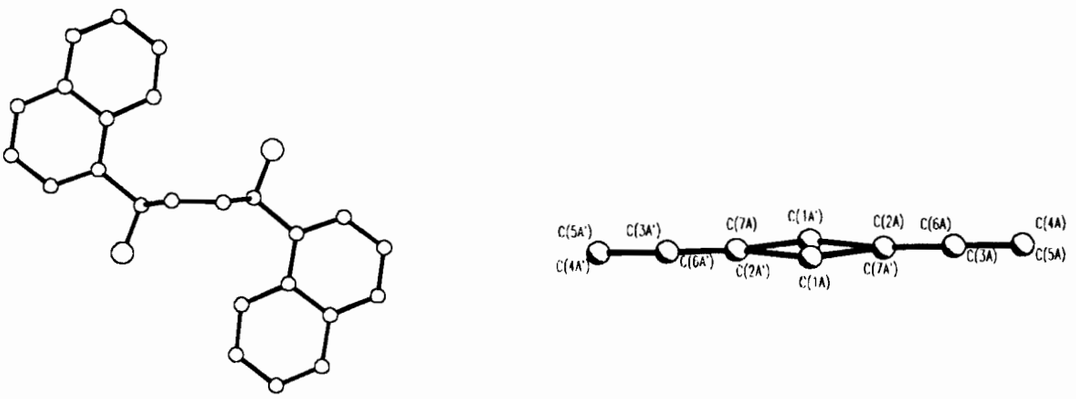

Fig 8.41. The chair conformation observed in the central ring of the anthracene moiety of the host in **DN13D**.

A search of the Cambridge Structural Database[13] revealed that twenty two structures involving the host DDDA (R=Ph) have been elucidated. A further eight structures involving the substituted host compounds were elucidated by Barbour[9]. In all such structures[2,3,5,14,15,16] the central 9,10-dihydroanthracenes were either found to be planar, or when significant deviations from planarity occurred, the "chairing" of the central ring was observed. One structure (with R=*p*-tolyl) discussed

by Barbour[9] showed a "boat-like" puckering of the central ring. The host molecules with R=*p-tert*-butylphenyl and α-naphthyl[9] were always located on centres of symmetry, requiring either the chair or planar conformation .

The different bond types observed in the host compounds are indicated in a general Scheme 2, and the bond length ranges observed in each structure are summarised in Table 8.3.

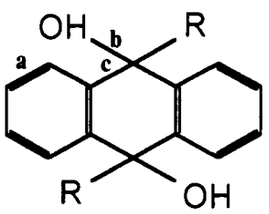

Scheme 2

Table 8.3. Bond length ranges observed for **DP13D**, **DN13D** and **DTBM**.

Compound	**DP13D/Å**	**DN13D/Å**	**DTBM/Å**
a=$C_{ar} \cong C_{ar}$	1.361(5) - 1.405(3)	1.361(7) - 1.435(6)	1.362(4) - 1.399(3)
b=C_{sp^3} - O	1.440(3)	1.432(5)	1.442(3)
c=C_{ar} - C_{sp^3}	1.516(3) - 1.527(3)	1.522(6) - 1.541(6)	1.515(3) - 1.538(3)
d= C_{sp^3} - C_{sp^3}			1.515(4) - 1.528(4)

All bond lengths and angles observed in the structures are comparable with known values for similar structures[17].

Discussion

In all cases desolvation is accompanied by the collapse of the host crystalline phase to the non-porous α-phase. The mechanism for the desolvation reaction, of **DP13D** although determined by completely different analytical techniques, was consistently found to be R2, and this held over a wide temperature range, 25°C to 80°C, yielding a satisfactory Arrhenius plot. The guest absorption follows a different mechanism from the desolvation reaction. The existence of a threshold pressure, below which guest uptake does not take place, was first observed for the reaction of this host with acetone. This has now also been confirmed for the uptake of dioxolane from the vapour.

DN13D desolvates according to an apparent zero order reaction mechanism over an α-range of 0.05-0.50.

The crystal structure of **DTBM** is such that the guest molecules are located in channels, with no physical barriers to the escape of the gaseous desolvation products. The guests are hydrogen bonded to the host. The guest loss reaction takes place in a single deceleratory step and the F1 reaction mechanism fits the data best.

A typical sigmoidal curve can be divided into an induction period, an acceleratory stage and a deceleratory stage. The α *vs.* time curves for the desolvation of **DNBz** lack the induction period and they can be described as truncated sigmoidal curves. The initial rate of reaction is slow and can probably be ascribed to the fact that the gaseous desolvation product cannot easily escape without disruption of the crystal structure, since the guest is captured in cavities in the host framework. The rate of reaction increases until a point of inflection is reached after which the curves become deceleratory. The channel structure of **DBBz** on the other hand would imply that the gaseous decomposition product can easily escape and does not impair the rate of the reaction. The desolvation is deceleratory and follows the F1 mechanism. The ease with which the gaseous product can escape during desolvation of **DBBz** probably explains why the activation energy for this reaction is much less than that of the desolvation of **DNBz**.

The Arrhenius parameters obtained for the desolvation of inclusion compounds of hosts in class **B** are summarised in Table 8.4. The compensation effect[18], discussed in Chapter 1, occurs in a group of related reactions, for which the influence of changes in A on reaction rate is accompanied by a change in E_a:

$\ln A = BE_a + C$

where B and C are constants. Corrected values of $\ln A$ ($\ln A_{T_M}$) were calculated, according to the method suggested by Galwey [19], discussed in Chapter 7.

$\ln A_{T_M} = E_a/RT_M + \ln k$, where $T_M^{-1} = 0.5(T_{max}^{-1} + T_{min}^{-1})$ and T_{max} and T_{min} are the maximum and minimum temperatures at which the kinetics of a specific inclusion compound were evaluated. Thus a comparison could be made between the Arrhenius parameters obtained for inclusion compounds of hosts in class **B** with those obtained in class **A**. It is evident from a plot of $\ln A_{T_M}$ *vs.* E_a, shown in Fig 8.42., that a linear relationship, and hence a compensation effect, exists between the Arrhenius parameters of the inclusion compounds of hosts in class **A** and **B**, obtained from isothermal TG.

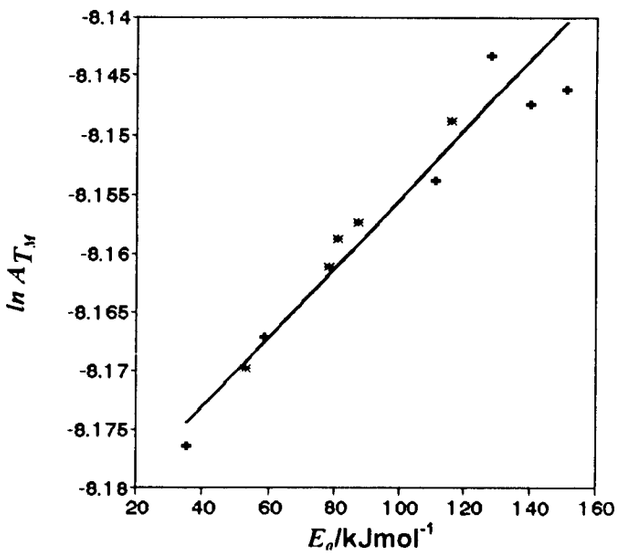

Fig 8.41. The compensation effect for + inclusion compounds formed by hosts in Class **A**; * inclusion compounds formed by hosts in Class **B**.

Table 8.4. Kinetic data for inclusion compounds of hosts in Class **B**.

Compound	**Method**	**Kinetic model**	**T-range/°C**	E_a/kJmol^{-1}	$ln\ A$	$ln\ A_{T_M}$
DP13D	Isothermal	R2	55-80	78.1(3)	21.87	-8.161
DN13D	Isothermal	zero order	55-75	53(10)	10.26	-8.169
DTBM	Isothermal	F1	40-65	81(8)	22.33	-8.159
DBBz	Isothermal	F1	50-70	87(8)	27.43	-8.157
DNBz	Isothermal	B1	70-85	116(4)	49.73	-8.132

Code	DP13D	DN13D	DTBM
Guest	1,3-dioxolane	1,3-dioxolane	methanol
Molecular formula	$C_{26}H_{20}O_2 \cdot (C_3H_6O_2)$	$C_{34}H_{24}O_2 \cdot 2(C_3H_6O_2)$	$C_{34}H_{38}O_2 \cdot (CH_3OH)$
M_r/g mol^{-1}	438.52	612.69	510.72
Temperature/K	294(2)	294(2)	294(2)
Crystal data			
Crystal system	Triclinic	Monoclinic	Triclinic
Space group	$P\bar{1}$	$P2_1/n$	$P\bar{1}$
a/Å	8.253(2)	8.743(2)	10.036(3)
b/Å	8.433(9)	14.623(5)	12.174(2)
c/Å	9.032(7)	12.321(2)	13.294(4)
α/°	108.58(6)	90.0	69.86(2)
β/°	93.60(5)	91.25(2)	70.20(2)
γ/°	102.95(5)	90.0	79.09(2)
Z	1	2	2
V/Å^3	574.5(7)	1574.9(7)	1430.0(6)
D_c/g cm^{-3}	1.264	1.292	1.187
μ(MoK_α) /cm^{-1}	0.83	0.86	0.73
F(000)	231	648	548
Data collection			
Crystal dimensions /mm	0.53 x 0.53 x 0.50	0.50 x 0.40 x 0.35	0.37 x 0.25 x 0.25
Range scanned θ/°	2.40 to 29.95	2.16 to 27.96	1.71 to 25.01
Range of indices *h,k,l*	-10,10; -11,11; 0,11	-11,11; 0,19; 0,16	-11,11; -13,14; 0,15
No. of reflections collected	3450	3959	5270
No. of unique reflections	3260	3793	5029
No. of reflections observed with $I_{rel}>2\sigma(I_{rel})$	2271	1739	2850
Final refinement			
No. of restraints	3	2	4
No. of parameters	158	200	376
R1 ($I_{rel}>2\sigma(I_{rel})$)	0.0813	0.1030	0.0482
wR2 ($I_{rel}>2\sigma(I_{rel})$)	0.2499	0.3153	0.1181
Extinction coefficient	0.11(3)	0.008(7)	-
Max. height in electron density map /eÅ^{-3}	0.743	0.888	0.227
Min. height in electron density map /eÅ^{-3}	-0.455	-0.481	-0.231

1 F. Toda, K. Tanaka, G. Ulibarri Danmas and M. C. Sanchez, *Chem. Lett.*, 1983, 1521.

2 D. R. Bond, L.R. Nassimbeni and F. Toda, *J. Incl. Phenom. Mol. Recog. Chem.*, **7**, 1989, 623.

3 D. R. Bond, L.R. Nassimbeni and F. Toda, *J. Cryst. Spectr. Res.*, 1989, **19**, 847.

4 M. R. Caira, L.R. Nassimbeni, W-D. Schubert and F. Toda, *Thermochim. Acta,* **206**, 1992, 265.

5 D. R. Bond, M.R. Caira, G.A. Harvey, L.R. Nassimbeni and F. Toda, *Acta Cryst.*, **B46**, 1990, 771.

6 M.E. Brown, *Introduction to Thermal Analysis*, Chapman and Hall, 1988, Chapter 13.

7 L.J. Barbour, K. Achleitner and J.R. Greene, *Thermochim. Acta*, **205**, 1992, 171.

8 L.J. Barbour, M.R. Caira, L.R. Nassimbeni, *J. Chem. Soc. Perkin Trans. 2*, 1993, 2321.

9 L.J. Barbour, *Clathration by Diol Hosts: Thermodynamics and Structure*, PhD Thesis, University of Cape Town, 1994.

10 H.J. Borchardt and F. Daniels, *J. Am. Chem. Soc.*, **79**, 1957, 41.

11 W.-D. Schubert, M.Sc. Thesis, University of Cape Town, 1991.

12 W.L. Duax and D.A. Norton (Eds.), *Atlas of Steroid Structure,* Vol. 1, Plenum Press, London, 1975.

13 Cambridge Structural Database and Cambridge Structural Database System, Version 5.11 (April 1996), Cambridge Crystallographic Data Centre, University Chemical Laboratory, Cambridge, England.

14 F. Toda, K. Tanaka, S. Nagamatsu and T.C.W. Mak, *Isr. J. Chem.*, **25**, 1985, 346.

15 F. Toda, K. Tanaka and T.C.W. Mak, *Tetrahedron Lett.*, **25**, 1984, 1359.

16 F. Toda, K. Tanaka and T.C.W. Mak, *J. Incl. Phenom.*, **3**, 1985, 225.

17 F.H. Allen, O. Kennard, D.G. Watson, L. Brammer, A.G. Orpen, R. Taylor, *J. Chem Soc. Perkin Trans. 2*, 1987, S1-S19.

18 J. Zsako, Cs. Varhelyi and K. Szilagyi, *J. Therm. Anal.*, **7**, 1975, 41.

19 A.K. Galwey, *Thermochim. Acta*, **242**, 1994, 259.

CHAPTER 9 INCLUSION COMPOUNDS OF HOSTS IN CLASS C.

In this chapter the thermal analysis and crystal structures of three inclusion compounds of 2,2'-bis(diphenylhydroxymethyl)-1,1'-biphenyl (**H**) will be discussed.

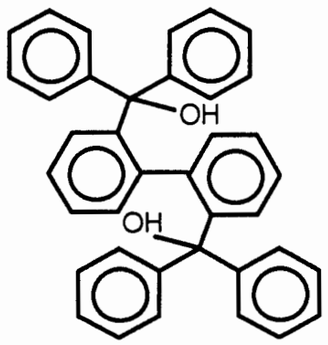

Scheme 1

This host is similar to the hosts in class **A**. The fluorenyl moiety has been replaced with two phenyl groups, which renders it conformationally more flexible than the hosts in class **A**. The host compound was dissolved in benzene, and formed a mixed inclusion compound, **TODBEN1**, which included water as well as benzene, resulting in the formation of **H**:H_2O: $\frac{1}{6}C_6H_6$. This structure was found to be highly symmetrical, belonging to the trigonal space group $R\bar{3}$. This structure is similar to that reported for the acetone inclusion compound of the same host [1]. Attempts to form inclusion compounds of *o*-xylene and *m*-xylene resulted in the formation of a hydrate, **TODOXLT**, with composition **H**:2$\frac{1}{6}H_2O$. The hydrate was also found to belong to the space group $R\bar{3}$, exhibiting a similar packing motif to **TODBEN1**. An inclusion compound with *p*-xylene, **TODPXLT**, was formed by rapid crystallisation from dry *p*-xylene. Slow crystallisation from *p*-xylene resulted in the formation of the hydrate. **TODPXLT** was found to belong to the monoclinic crystal system, crystallising in the space group $P2_1/n$. The crystals of **TODPXLT** could easily be distinguished visually from the hydrate crystals, which morphologically reflected the three-fold symmetry, as shown in Colour Plate 9.1. Attempts to force the *o*-xylene and *m*-xylene inclusion compound out of solution before formation of the hydrate, as in the case of *p*-xylene, failed.

Colour Plate 9.1

a) Crystals of **TODBEN1** at room temperature.

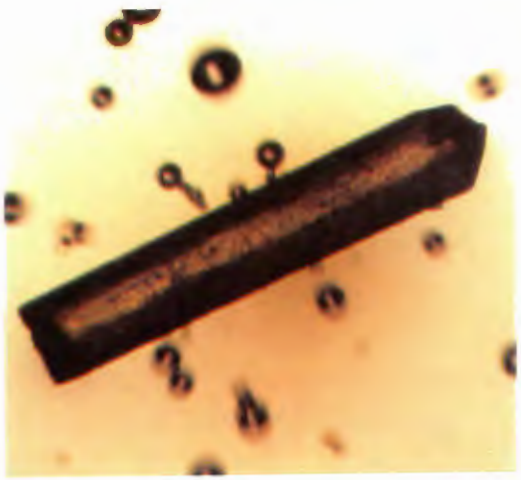

b) **TODBEN1** desolvates at 100°C.

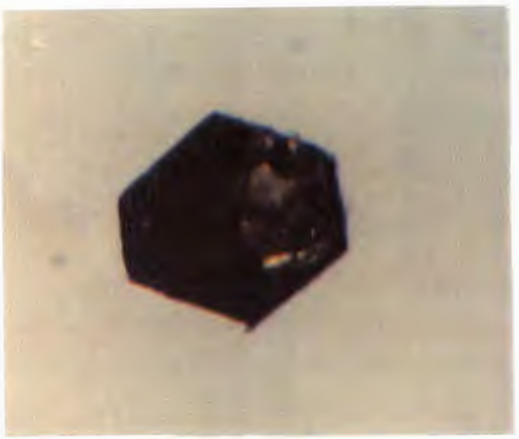

c) A cross-section through a crystal of **TODOXLT**, showing the three-fold symmetry.

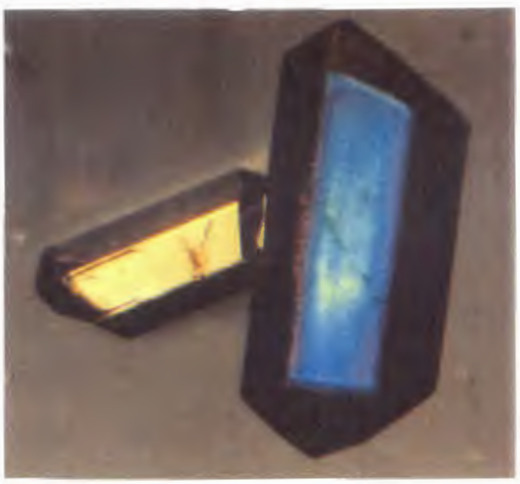

d) Crystals of **TODOXLT** viewed through polarised light.

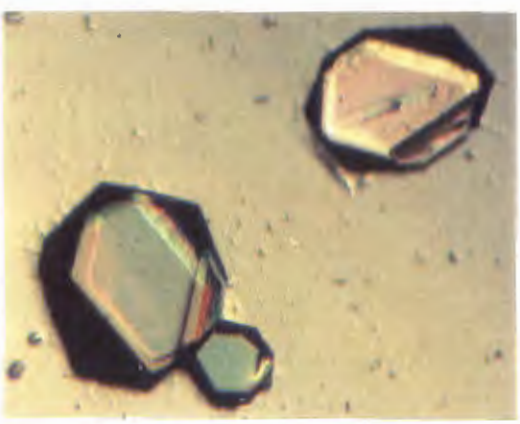

e) Crystals of **TODPXLT** are lozenge-shaped and could easily be distinguished from **TODOXLT**.

TODBEN1

$C_{38}H_{30}O_2 \cdot H_2O \cdot \frac{1}{6} C_6H_6$

Guest: H_2O: $\frac{1}{6} C_6H_6$

Space group: $R\bar{3}$

a=35.370(4)Å

c=12.570(8)Å

Volume=13619(9)Å^3

Z=18

Tables containing complete crystal and refinement data appear at the end of this chapter.

NMR

The ^{1}H NMR spectrum of the pure host compared with that of the inclusion compound confirms the presence of benzene and water in the latter, with single sharp resonances at 7.36 ppm and 1.56 ppm, assigned to benzene and H_2O respectively. Confirmation of the assignment of the 7.36 ppm resonance to benzene was obtained by addition of small quantities of benzene to a solution of the pure host. This resulted in a peak at 7.36 ppm growing proportionately in intensity. The relative resonance integrals obtained from the spectrum support formulation of the inclusion compound as **H**:H_2O: $\frac{1}{6} C_6H_6$ within experimental error.

Thermal Analysis

The TG and DSC traces for **TODBEN1** are shown in Fig 9.1. Desolvation occurred in a single mass loss step, corresponding to 6.8%. In the light of the NMR results this was attributed to the loss of 1 mole of water and $\frac{1}{6}$ of a mole of benzene for each mole of host (calc. 5.7%). The guest loss was observed as a single diffuse endotherm in the DSC trace, with an onset temperature of 90°C (peak A). A sharp endotherm at 250°C corresponds to the host melt (peak B). Repeated attempts under various conditions of differing heating rates and crystallite size did not yield separate endotherms for the loss of benzene and water.

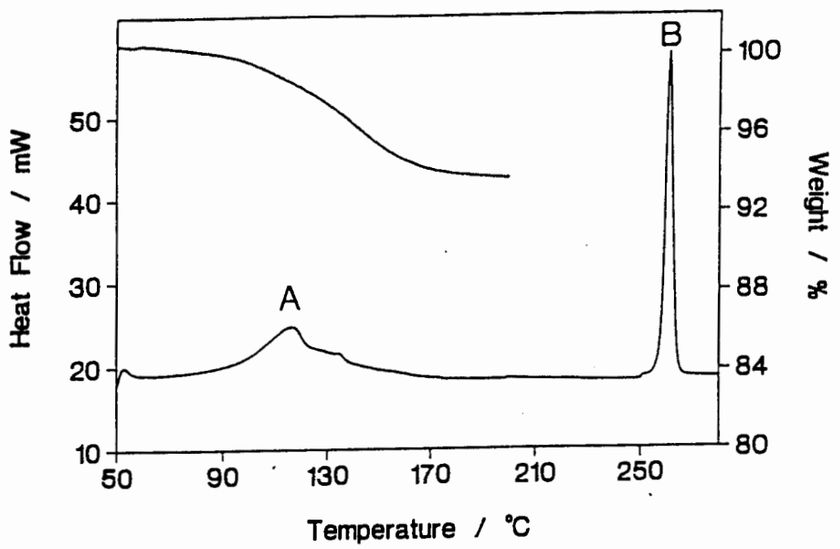

Fig 9.1. TG and DSC traces for TODBEN1.

Crystal Structure

Preliminary photography indicated that TODBEN1 and TODOXLT belong to the trigonal crystal system. The reflection conditions

hkil -h+k+l=3n

were observed which would imply that the space group is either *R*3 or *R* $\bar{3}$. Based on the mean $|E^2-1|$ values obtained from direct methods the centrosymmetric space group *R* $\bar{3}$ was chosen. The solutions of both structures were carried out using hexagonal axes. The choice of the centrosymmetric space group was vindicated by the successful final refinement of both structures. The data collection for TODOXLT was initially done at room temperature, but repeated at -50°C in order to obtain better defined peaks for the guest molecules. The structure based on the low temperature data is reported.

Solution and Refinement

Direct methods yielded the positions of all the host non-hydrogen atoms. The host molecule was located in a general position (Z=18). Upon subsequent refinement the difference electron density map yielded a water molecule, and in addition a single peak at a distance of 1.4Å from the origin at Wyckoff position *a*. The $\bar{3}$

symmetry multiplies this to a regular hexagon with interatomic distances which refined to 1.411(7)Å. This was interpreted as a benzene guest.

The structure was refined with anisotropic displacement parameters on the heavy atoms of the host and water molecules, but isotropically for the benzene molecule, since it exhibited a comparatively large temperature factor (U_{eq}=0.167(3)Å^2). Aromatic hydrogen atoms on the host were constrained and refined as a riding model and hydroxyl hydrogen atoms of the host were located in a difference electron density map and refined with a simple bond length constraint[2]. The hydrogen atoms of the water molecules were not located and were left out of the final model. The hydrogen atoms on the benzene molecule were placed in geometrically constrained positions and refined with temperature factors at 120% that of the preceding C atom. The structure refined to a final R_1 = 0.0498. A residual electron density of 0.419eÅ^{-3} was observed, but could not be modelled.

Fig 9.2. depicts the host conformation and indicates the numbering scheme used. The host molecule is stabilised by an intramolecular hydrogen bond, with d(O···O)=2.723(3)Å , which results in the torsion angle about the central biphenyl bond being 100°.

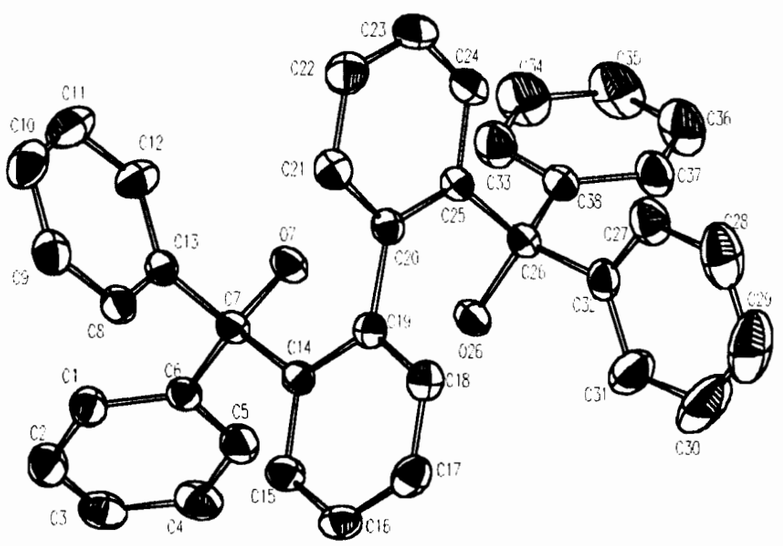

Fig 9.2. Host conformation and numbering scheme for **TODBEN1**.

The structure is further stabilised by intermolecular hydrogen bonds between the host hydroxyl groups and the water molecules, d(O(26)···O(1G)[i])=2.795(3)Å and d(O(7)···O(1G)[ii])=2.828(3)Å.

The host molecules are locked into a hexagonal array by a ring of 18 hydrogen bonds, in which the pattern ...O(7)···O(26)···O(1G)···O(7)... is repeated six times by symmetry; this is clearly visible in Fig 9.3. This hydrogen bonding pattern can be described using graph sets[3] as $R_{18}^{18}(36)$. This is similar to the packing arrangement of the inclusion compound of this host with acetone[1] in which the guest molecules are disordered. The benzene molecule fits deftly into the cavity formed by six phenyl rings, each from a different host molecule, in a $\bar{3}$ configuration, three above and three below the benzene molecule. Fig. 9.4. shows how the benzene molecule fits into the cavity created by the host-water hydrogen-bonded arrangement.

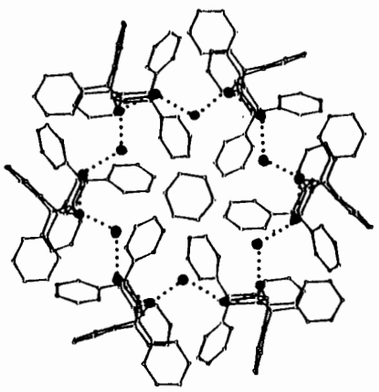

Fig 9.3. View of a section of the unit cell of **TODBEN1**, down [001].

Fig 9.4. Stereoscopic view of **TODBEN1**, showing how the benzene molecule fits into the cavity created by six host molecules.

[i] x, y, 1+z
[ii] x-y, x, 1-z

TODOXLT

$C_{38}H_{30}O_2 \cdot 2\ ⅙\ H_2O$

Guest:Water

Space group: R $\bar{3}$

a=35.123(2)Å

c=12.460(4)Å

Volume=13312(4) $Å^3$

Z=18

Tables containing complete crystal and refinement data appear at the end of this chapter

Thermal Analysis

The thermal analytical results for the dehydration of **TODOXLT** are shown in Fig 9.5. A TG mass loss of 7.1% (calc. 7.0%) confirms the 1:2⅙ host to guest stoichiometry for **TODOXLT**. The DSC trace shows that dehydration occurs as a diffuse endotherm with an onset temperature of 70°C.

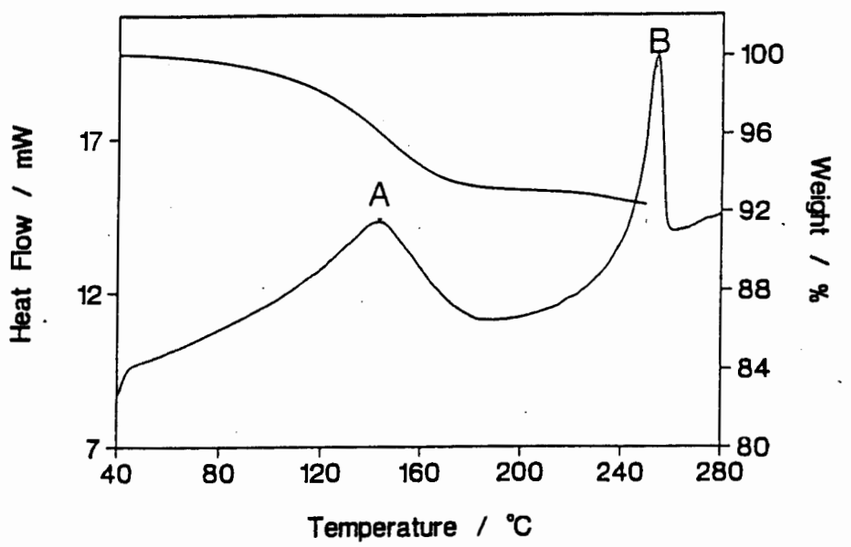

Fig 9.5. TG and DSC traces for **TODOXLT**.

Crystal Structure

Solution And Refinement

The crystal structure of **TODOXLT** was solved using the host heavy atom co-ordinates obtained from the structure solution of **TODBEN1** in isomorphous replacement, and the guest atoms were located in difference electron density maps. The electron density map yielded the positions of two water molecules (O(1G) and O(2G)) as well as a peak at (0,0,0.0386). Based on the TG results, this peak was interpreted as the O atom of a disordered water molecule with a site occupancy of 0.167. The structure was refined with anisotropic displacement parameters on the heavy atoms of the host molecule, O(1G) and O(2G), but O(3G) was refined isotropically. Aromatic hydrogen atoms were constrained and refined as a riding model and hydroxyl hydrogen atoms of the host, as well as the H-atoms on water molecule (1G), were located in a difference electron density map and refined with a simple bond length constraint[2]. The hydrogen atoms of the remaining water molecules were not located and were left out of the final model.

The conformation of the host is similar to that of **TODBEN1**. The host molecules are held together by a series of hydrogen bonds, involving bridging water molecules (O(1G)) and the hydroxyl moieties of the host. The $R_{18}^{18}(36)$ hydrogen bonding packing motif, observed in **TODBEN1**, is present, locking the host molecules into a hexagonal array by a ring of 18 hydrogen bonds, in which the pattern ...O(7)···O(26)··O(1G)···O(7)... is repeated six times by symmetry. As shown in Fig. 9.6. **TODOXLT** exhibits additional H-bonding. The pattern ...O(2G)···O(1G)···O(2G)... [with O(1G)···O(2G) = 2.799(3) and 2.868(3)Å alternately] is repeated six times by the $\bar{3}$ axis to yield a star-shaped H-bonded ring. This corresponds to graph set $R_{12}^{12}(24)$. There is also evidence for a weak H-bond between the O(2G) atoms related by the three fold axis and O(3G) (O(2G)···O(3G) = 3.043Å). Fig 9.7. shows a stereoscopic view of the water oxygen atoms in **TODOXLT** surrounded by six host molecules. The crystal packing observed in both **TODBEN1** and **TODOXLT** viewed down [001] is shown in Fig 9.8. The guest molecules, except for O(1G), were omitted for clarity.

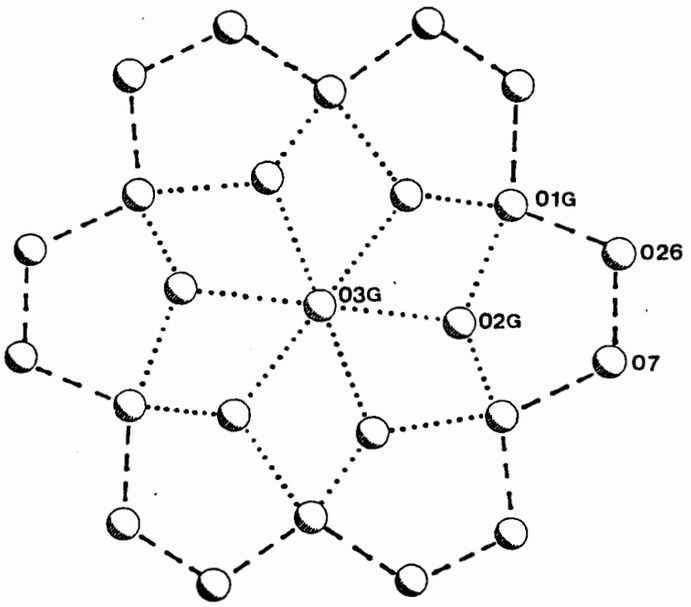

Fig 9.6. Hydrogen bonding (- - -) observed in both **TODBEN1** and **TODOXLT** and (···) observed only in **TODOXLT**.

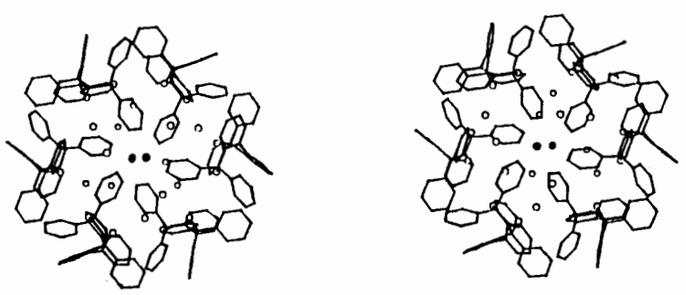

Fig 9.7. Stereoscopic view of a section of the unit cell of **TODOXLT**, showing the disordered water molecule (shaded), surrounded by six host molecules, generated by $\bar{3}$ symmetry.

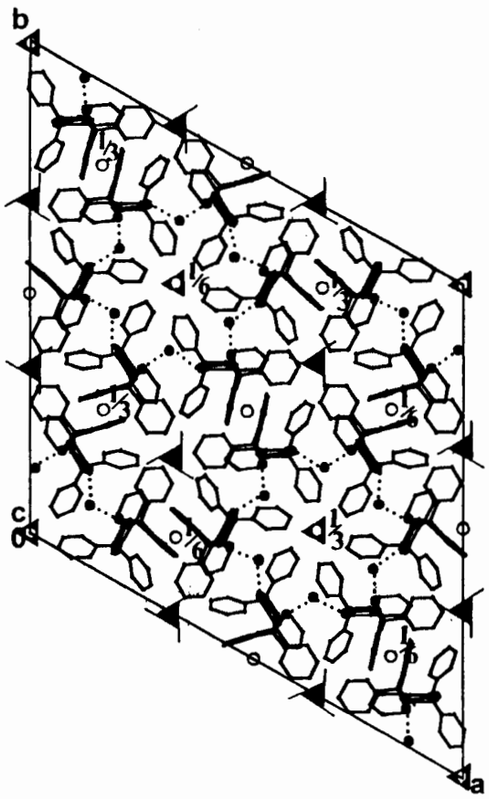

Fig 9.8. A projection down [001], showing the host packing observed in **TODOXLT**. O(2G) and O(3G) were omitted for clarity.

X-Ray Powder Diffraction

The X-ray powder diffraction patterns for **TODBEN1** and **TODOXLT** are identical, within experimental error. They both undergo a phase change to the non-porous α-phase upon desolvation. The powder diffraction patterns for **TODBEN1** before and after desolvation are shown in Fig 9.9.

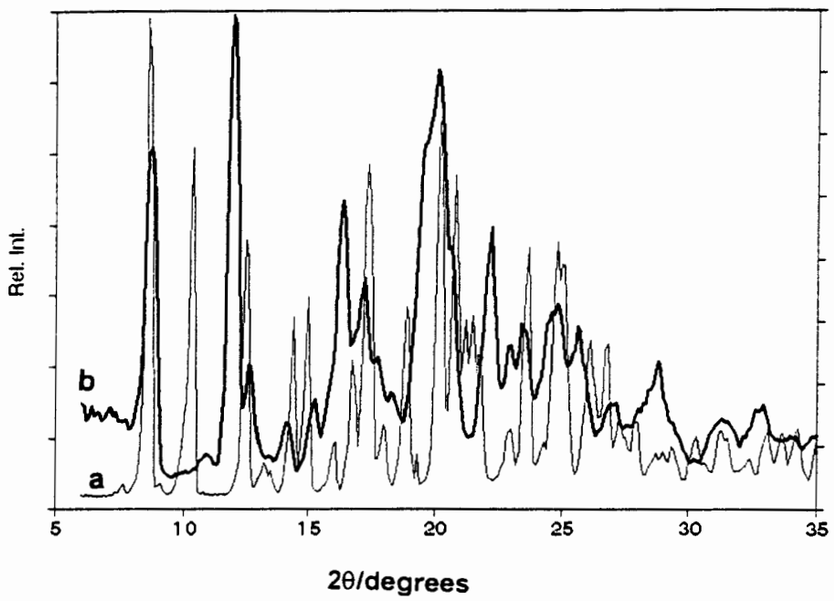

Fig 9.9. X-ray powder diffraction pattern for a) **TODBEN1** and b) the desolvated α-phase of the host.

TODPXLT

$C_{38}H_{30}O_2 \cdot ½C_8H_{10}$

Guest:*p*-xylene

Space group: $P2_1/n$

a=9.522(2)Å

b=21.020(3)Å β=105.75(2)°

c=16.145(3)Å

Volume=3110.0(9) $Å^3$

Z=4

Tables containing complete crystal and refinement data appear at the end of this chapter.

Thermal Analysis

The TG and DSC traces for TODPXLT are shown in Fig 9.10. Desolvation occurred in a single mass loss step of 9.1%. This corresponded to a host:guest ratio of 1:½ (calc. 9.3%). The guest loss was observed as a single endotherm in the DSC trace, with an onset temperature of 160°C. A sharp endotherm at 250°C corresponds to the host melt.

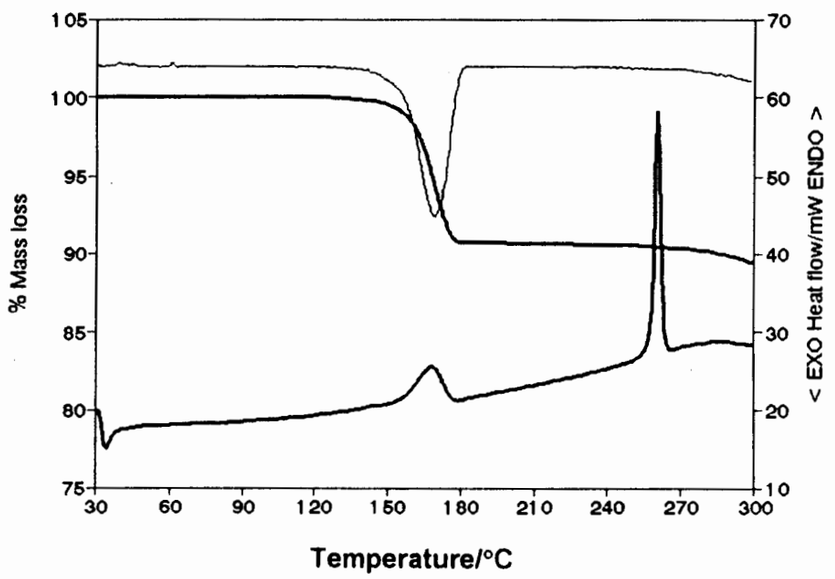

Fig 9.10. TG and DSC traces of TODPXLT.

Crystal Structure

Preliminary X-ray photography indicated that **TODPXLT** belongs to the monoclinic crystal system. The following reflection conditions were observed:

hkl none

h0l h+l=2n

0k0 k=2n

The structure was solved in the space group $P2_1/n$, based upon these reflection conditions. The guest could not be located from the data set collected at room temperature. The data collection was therefore repeated at -50°C, and the low temperature results are discussed below.

Solution And Refinement

Direct methods yielded the positions of all the host non-hydrogen atoms. Four host molecules comprised the unit cell (Z=4). The host was located in a general position. Upon subsequent refinement the difference electron density map yielded the positions of the guest non-hydrogen atoms. All the host non-hydrogen atoms were treated anisotropically. The guest non-hydrogen atoms were treated isotropically. The hydroxyl hydrogen atoms were located in the difference electron density maps and refined with bond length constraints and individual temperature factors[2]. The rest of the hydrogen atoms were placed with geometric constraints and refined with common isotropic temperature factors for similar hydrogens. A residual electron density of 0.54eÅ^{-3} was observed in the region of the guest, but could not be modelled. The structure refined successfully to a final R_1 = 0.0740.

The host is stabilised via an intramolecular hydrogen bond with d(O(7)···O(26))=2.775(5)Å, twisting the central biphenyl at right angles, with the torsion angle (C(14)-C(19)-C(20)-C(25)) = -102(1) °. The host conformation is shown in Fig 9.11. The host:guest ratio of 1:½ ,obtained from TG requires half a *p*-xylene molecule in the asymmetric unit. The guest molecule is located on a centre of symmetry at Wyckoff position *d*.

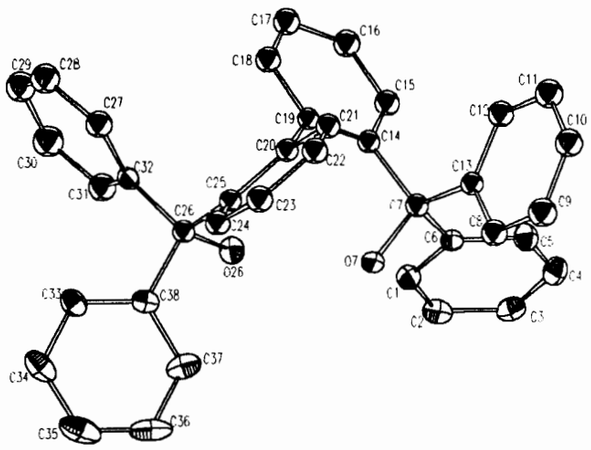

Fig 9.11. Host conformation in **TODPXLT**.

Molecular Structure

The molecular structure of **TODPXLT** is shown in Fig 9.12.

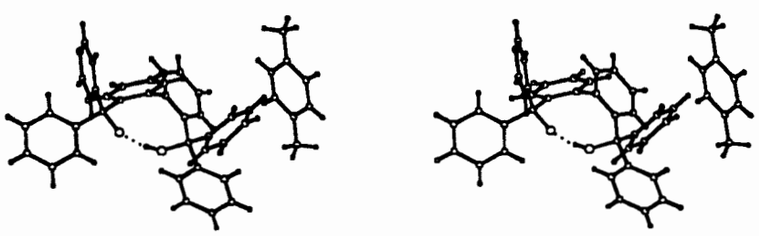

Fig 9.12. Stereoscopic view of the molecular structure of **TODPXLT**.

One guest molecule is surrounded by four host molecules, as illustrated in a stereoscopic view of the crystal packing down [100] in Fig 9.13. The crystal packing is stabilised by a number of aromatic edge to face interactions[4], listed in Table 9.1.

Table 9.1. Aromatic edge to face distances and angles as observed in **TODPXLT**.

Atom	**d(H···centre$_{guest}$)/Å**	**d(C···centre$_{guest}$)/Å**	**C-H···centre$_{guest}$/°**
C(11)	3.43(1)	3.95(1)	117.8(1)
C(12)	3.140(9)	3.81(1)	130.4(1)

Close contacts also exist between the methyl group on the *p*-xylene guest and the host aromatic groups, as indicated in Table 9.2.

Table 9.2. Intermolecular distances as observed in **TODPXLT**.

Atom	**d(H(1G1)···C)/Å**	**d(C(1G)···C)/Å**
C(16)	3.05(1)	3.99(1)
C(17)	3.09(9)	3.99(1)
Atom	**d(H(1G2)···C)/Å**	**d(C(1G)···C)/Å**
C(30)	2.98(1)	3.81(1)
C(31)	3.11(1)	3.85(1)

The crystal packing viewed down [010] can be seen in Fig 9.14, with the guest molecules indicated with van der Waals radii. The hydrogen atoms were omitted for clarity. In Fig 9.15. a view of the crystal packing is shown looking edge-on at the *p*-xylene molecule.

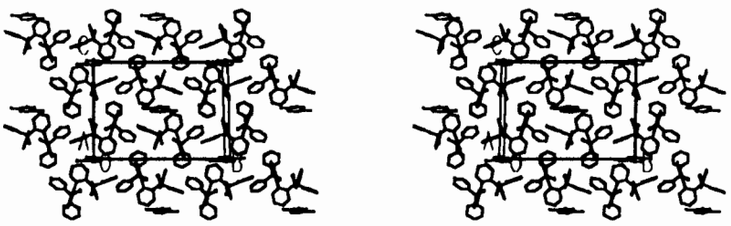

Fig 9.13. Crystal packing in **TODPXLT** as viewed down [100].

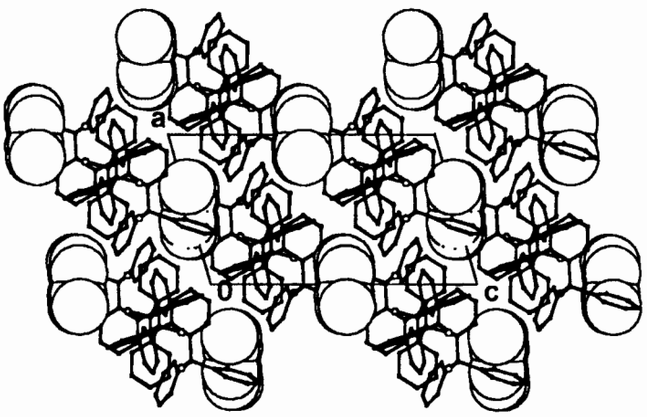

Fig 9.14. Crystal packing in **TODPXLT** as viewed down [010], showing the guest molecules with van der Waals radii. H-atoms were omitted for clarity.

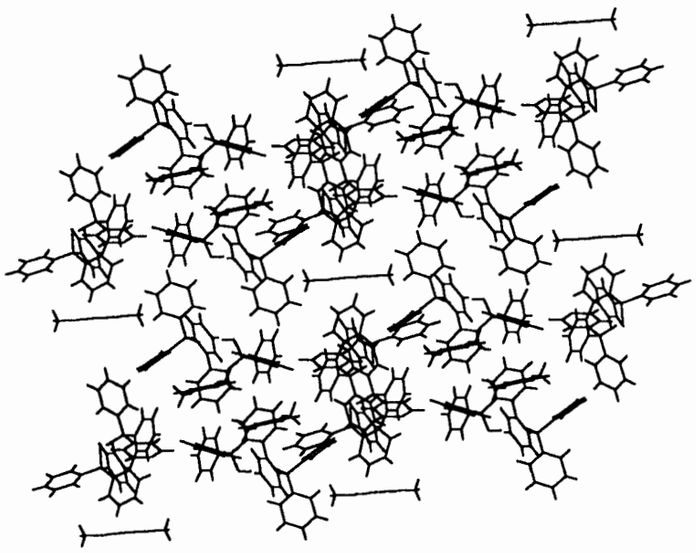

Fig 9.15. A view of the crystal packing in **TODPXLT** looking edge-on at the *p*-xylene molecule.

X-Ray Powder Diffraction

In Fig 9.16. the calculated X-ray powder diffraction pattern for **TODPXLT** is shown, compared with that measured for the desolvated α-phase of the host compound. It is clear that a phase change occurs upon desolvation, from the β-phase of the inclusion compound to the α-phase of the host compound.

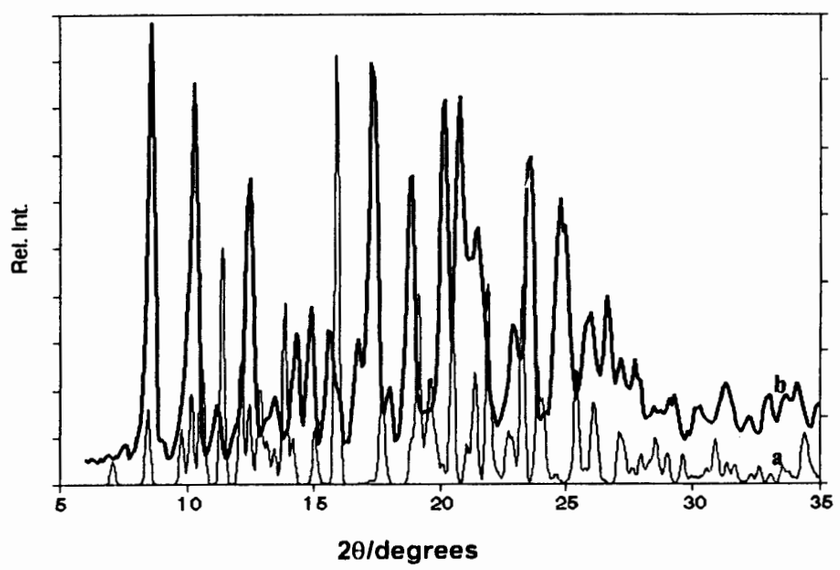

Fig 9.16. X-ray powder diffraction patterns for a) **TODPXLT**; b) the desolvated α-phase of the host compound.

Host Conformations

The host conformation can be described in terms of seven torsion angles, τ_1-τ_7, indicated in Table 9.3., based on the numbering scheme indicated in Scheme 2.

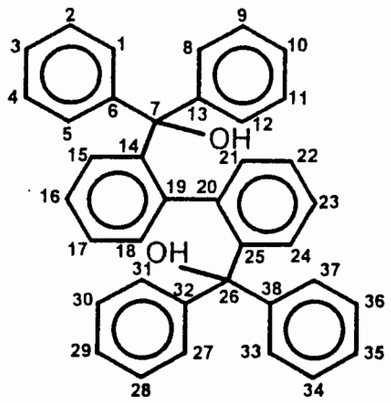

Scheme 2

The host conformations of **TODBEN1** and **TODOXLT** are identical. The host conformation of **TODPXLT** was remarkably similar to that of the other two structures, with the corresponding torsion angles differing by less than 10°. The structures are all centrosymmetric and we have chosen the enantiomers with τ_4 negative in each case for purposes of comparison.

Table 9.3. Selected torsion angles for the host compounds in **TODBEN1**, **TODOXLT** and **TODPXLT**.

Compound	**TODBEN1**	**TODOXLT**	**TODPXLT**
τ_1[O(7)-C(7)-C(14)-C(19)]°	43.9(3)	43.5(2)	37(1)
τ_2[C(6)-C(7)-C(14)-C(19)]°	160.4(2)	160.4(2)	152.2(7)
τ_3[C(13)-C(7)-C(14)-C(19)°	-74.5(3)	-75.4(2)	-81(1)
τ_4[C(14)-C(19)-C(20)-C(25)]°	-99.8(3)	-101(1)	-102(1)
τ_5[C(20)-C(25)-C(26)-O(26)]°	38.4(4)	35.3(3)	43(1)
τ_6[C(20)-C(25)-C(26)-C(32)]°	-80.4(3)	-83.3(2)	-74(1)
τ_7[C(20)-C(25)-C(26)-C(38)]°	153.9(3)	151.4(2)	160.5(8)

The deviation from planarity of the aromatic rings in all three structures never exceeded 0.01Å. The different bond types observed in the host compound are

indicated in Scheme 3, and the bond length ranges observed in each structure are summarised in Table 9.4.

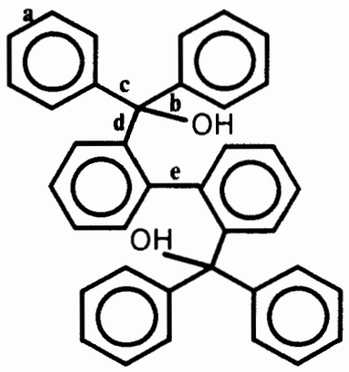

Scheme 3

Table 9.4. Ranges of bond length observed for the host compounds in **TODBEN1**, **TODOXLT** and **TODPXLT**.

Compound	**TODBEN1/Å**	**TODOXLT/Å**	**TODPXLT/Å**
a=$C_{ar} \cong C_{ar}$	1.356(4) - 1.406(4)	1.373(3) - 1.409(3)	1.369(7) - 1.408(6)
b=C_{sp^3} - O	1.445(3) - 1.449(3)	1.443(2) - 1.446(2)	1.449(5) - 1.453(5)
c=C_{ar} - C_{sp^3}	1.526(4) - 1.537(4)	1.529(3) - 1.538(3)	1.522(6) - 1.541(6)
d= C_{sp^3} - C_{ar}	1.529(4) - 1.532(4)	1.534(3) - 1.541(3)	1.532(6) - 1.544(6)
e= C_{ar} - C_{ar}	1.501(4)	1.506(3)	1.511(6)

All bond lengths and angles observed in the structures are comparable with known values for these bond types[5].

All three structures contain an intramolecular hydrogen bond, O(7)···O(26) locking the host into a 100° torsion angle about the biphenyl moiety. The intramolecular hydrogen bonding distances and angles observed in the three compounds are summarised in Table 9.5.

Table 9.5. Intramolecular H-bonding distances and angles for **TODBEN1, TODOXLT** and **TODPXLT**.

Compound	d[O(7)···O(26)]/Å	O(7)-H(7)···O(26)/°
TODBEN1	2.724(3)	171(5)
TODOXLT	2.712(2)	173(3)
TODPXLT	2.775(5)	169(8)

Discussion

TODBEN1 and **TODOXLT** exhibit the same host packing. The $R_{18}^{18}(36)$ hydrogen bonding motifs are also present in both inclusion compounds. The structures of **TODBEN1** and **TODOXLT** are stabilised by intermolecular hydrogen bonds between the host and guest water molecules. These hydrogen bonding distances are summarised in Table 9.6.

Table 9.6. Intermolecular H-bonding distances for **TODBEN1** and **TODOXLT**

O···O	Compound	Distance/Å	Symm. Code
O(26)···O(1G)[(1)]	**TODBEN1**	2.795(3)	[(1)] x, y, 1+z
O(7)···O(1G)[(2)]	**TODBEN1**	2.828(3)	[(2)] x-y, x, 1-z
O(26)···O(1G)[(1)]	**TODOXLT**	2.767(2)	[(1)] x, y, 1+z
O(7)···O(1G)[(2)]	**TODOXLT**	2.917(2)	[(2)] x-y, x, 1-z
O(1G)···O(2G)	**TODOXLT**	2.868(3)	
O(1G)···O(2G)[(3)]	**TODOXLT**	2.799(3)	[(3)] y, -x+y, -z
O(3G)···O(2G)[(4)]	**TODOXLT**	3.043(5)	[(4)] -x, -y, -z
O(3G)···O(2G)[(3)]	**TODOXLT**	3.043(5)	[(3)] y, -x+y, -z
O(3G)···O(2G)[(5)]	**TODOXLT**	3.043(5)	[(5)] x-y, x, -z

TODBEN1 is a typical example of double molecular recognition, where the host molecules are assembled via hydrogen bonding to water, resulting in a cavity which encompasses the benzene guest. This is a somewhat different structure from that found in the 6:1 cyclohexanedione:benzene inclusion compound, in which the benzene guest fits precisely into the hexagonal cavity formed by six host molecules which are interlinked by hydrogen bonds[6,7]. In the case of **TODOXLT** the same hydrogen-bonded assembly is observed, but the cavity is filled with another ring of hydrogen-bonded water molecules. The inclusion of both hydrophobic and hydrophilic guest molecules of suitable size has therefore been demonstrated in this assembly.

Although formation of the hydrate (**TODOXLT**) seems to be preferred, we managed to grow crystal of the *p*-xylene inclusion compound (**TODPXLT**). These crystals

were stable at room temperature. The crystal structure is stabilised by weak interactions between the aromatic groups on the host and the *p*-xylene guest. The host conformation observed in **TODPXLT** does not differ markedly from that of **TODBEN1** and **TODOXLT**.

Code	TODPXLT	TODOXLT	TODBEN1
Guest	*p*-xylene	water	water/benzene
Molecular formula	$C_{38}H_{30}O_2$. 1/2C_8H_{10}	$C_{38}H_{30}O_2$.2 1/6H_2O	$C_{38}H_{30}O_2$.H_2O.1/6C_6H_6
M_r/g mol^{-1}	571.70	557.65	549.69
Temperature/K	172(2)	172(2)	293(2)
Crystal data			
Crystal system	Monoclinic	Trigonal	Trigonal
Space group	$P2_1/n$	R $\bar{3}$	R $\bar{3}$
a/Å	9.522(2)	35.123(2)	35.370(4)
b/Å	21.020(3)		
c/Å	16.145(3)	12.460(4)	12.570(8)
β/°	105.75(2)		
Z	4	18	18
V/Å^3	3110.0(9)	13312(4)	13619(9)
D_C/g cm^{-3}	1.221	1.252	1.206
D_m/g cm^{-3}	1.19(4)	1.22(4)	1.20(4)
μ(MoK_α) /cm^{-1}	0.073	0.080	0.075
F(000)	1212	5322	5238
Data collection			
Crystal dimensions /mm	0.22 x 0.22 x 0.38	0.38 x 0.44 x 0.44	0.30 x 0.38 x 0.38
Range scanned θ/°	1.63 to 24.97	1.16 to 24.98	1.15 to 24.97
Range of indices *h,k,l*	-11,10; 0,24; 0,19	-41,0; 0,36; -14,14	-42,42; -42,42; 0,14
No. of reflections collected	5672	5480	16733
No. of unique reflections	5472	5199	5314
No. of reflections observed with $I_{rel}>2\sigma(I_{rel})$			
Final refinement			
No. of restraints	2	8	4
No. of parameters	262	397	384
R1 ($I_{rel}>2\sigma(I_{rel})$)	0.0740	0.0432	0.0498
wR2 ($I_{rel}>2\sigma(I_{rel})$)	0.1819	0.1104	0.1199
Max. height in electron density map /eÅ^{-3}	0.541	0.405	0.419
Min. height in electron density map /eÅ^{-3}	-0.344	-0.333	-0.241

1 F. Toda, A. Kai, R.Toyotaka, W-H. Yip and C.W. Mak, *Chem. Lett.*, 1989, 1921.

2 P. Schuster, G. Zundel and C. Sanderfy, *The Hydrogen Bond II, Structure and Spectroscopy*, North Holland Publishing Co., Amsterdam, 1976.

3 J. Bernstein, R.E. Davies, L. Shimoni and N.-L. Chang, *Angew. Chem. Int. Ed. Engl.*, **34**, 1995, 1555.

4 G.R. Desiraju, *Crystal Engineering The Design Of Organic Solids*, Elsevier, Amsterdam, 1989, 92.

5 F.H. Allen, O. Kennard, D.G. Watson, L. Brammer, A.G. Orpen, R. Taylor, *J. Chem. Soc. Perkin Trans. 2*, 1987, S1-S19.

6 M.C. Etter, Z. Urbanczyk-Lipkowska, D.A. Jahn and J.S Frye, *J. Am. Chem. Soc.*, **108**, 1986, 5871.

7 M.C. Etter, D.L. Parker, S.R. Ruberu, T.W. Panunto and D. Britton, *J. Incl. Phenom. Mol. Recogn. Chem.*, **8**, 1990, 395.

CHAPTER 10 CONCLUSION

This study dealt mainly with the structure-reactivity relationships of selected hydroxy host inclusion compounds. The literature reveals very few studies in which attempts have been made to correlate the kinetics of decomposition reactions with crystal structures[1]. The crystal structures of inclusion compounds from three different groups of host compounds were elucidated. The guest compounds under investigation were predominantly volatile solvents. This rendered the inclusion compounds fairly unstable in the atmosphere. The crystals had to be sealed in Lindemann capillaries in the presence of mother liquor to prevent the desolvation of the inclusion compound during the X-ray data collection. The guests were often found to be disordered. In all the crystal structures which were elucidated, the dominating components of guest disorder were modelled. However, often residual electron density in the region of the guest could not be modelled. In two cases, namely **TODPXLT** and **TODOXLT**, the data collections were carried out at -50°C, in an attempt to enhance refinement of the guests.

The host in Class **C** formed inclusion compounds with both hydrophobic and hydrophilic guests. **TODBEN1** is a typical example of double molecular recognition, where the host molecules are assembled via hydrogen bonding to water, resulting in a cavity which encompasses the benzene guest.

The inclusion compounds of hosts in Classes **A** and **B** with a wide variety of volatile guests (namely acetone, methanol, benzene, 1,3- and 1,4-dioxane, 1,3-dioxolane) were investigated. Hydrogen bonds exist between the host hydroxy groups and most of the guests compounds. The only exceptions were the benzene inclusion compounds, in which only van der Waals interactions were observed between the host and guest molecules. From the crystal structure solutions it was evident that the guest molecules in these structures were either located in channels (e.g. **W17DIA** and **W17**), constricted channels (e.g. **WTB14D** and **WTBAC**) or cavities (e.g. **DNBz**).

The kinetics of desorption of a variety of host-guest inclusion compounds were investigated in this study. The kinetic mechanisms proposed from TG experiments

deal only with the guest loss as rate determining step, since thermogravimetry measures only the mass loss and does not account for concomitant thermal events. Thus we cannot detail the mechanism of the phase change which has been shown to occur upon guest loss, in the crystal structure of the host. It is reassuring to find that data derived from TG and X-ray powder diffraction (see Chapter 8) obeyed the same rate law expression, and showed Arrhenius behaviour. This phenomenon could possibly be further investigated, by carrying out X-ray powder diffraction at elevated temperatures.

Attempts were made to study the formation of inclusion compounds, and a new system for studying these reactions has been designed. The QMB system developed in this study is still a prototype, but it was demonstrated in Chapter 8 that it can be used to study the kinetics of formation of an inclusion compound. This can be done, using extremely small amounts of material. This information is valuable for the application of inclusion compounds as chemical sensors.

The activation energies for desolvation, obtained in this study, ranged from 35 to 150 kJ.mol^{-1}. Galwey[2] surveyed over 400 decomposition reactions, including dehydrations and the decompositions of oxides, hydrides, azides, carbonates, permanganates and carboxylates. The activation energies obtained in the current study were compared with those reviewed by Galwey, in order to obtain an intuitive feel for the magnitudes of the activation energies of guest desolvation. A histogram of the percentage frequency of E_a for the current study, compared with the activation energies from Galwey's survey is shown in Fig 10.1. The current sample is small (only 12 desolvation reactions), but it is clear that the host-guest desolvation reactions show relatively low activation energies, compared with the decomposition of inorganic salts. This is not surprising, since guest desolvation does not require the breaking of covalent bonds, but at most the breaking of hydrogen bonds. Table 10.1. contains a summary of some of the features of guest desolvation observed in this study. The enthalpy changes due to guest loss ($\Delta H_{desolv.}$) for inclusion compounds with hosts in class **A**, ranged from 30 to 76 kJ.mol^{-1}. The values of $\Delta H_{desolv.}$ for inclusion compounds in class **B** varied widely, with the lowest enthalpy change observed being 17 kJ.mol^{-1} for the desolvation of **DP13D** and the highest 133 kJ.mol^{-1}, for the desolvation of **DBBz**. The changes in enthalpy observed for the desolvation reactions of the inclusion compounds are generally much lower than

the change of enthalpy for the dehydration of inorganic compounds. For example, $\Delta H_{dehydr.}$ for metal oxalates[3], where the water is removed from the coordination sphere, varies from 100 to 230 kJ.mol^{-1}.

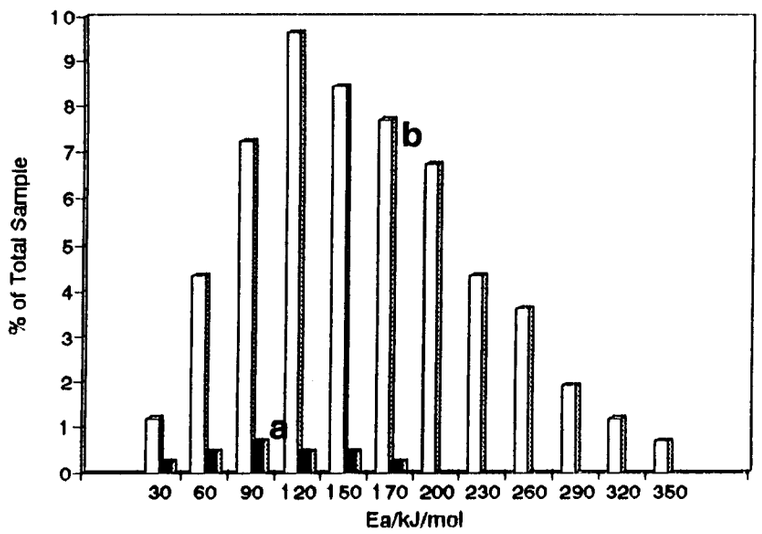

Fig 10.1. Percentage frequency distribution of activation energies for a) desolvation of inclusion compounds investigated in this study, b) decomposition of compounds surveyed in ref. 2.

A relatively high activation energy was obtained for the desolvation of the benzene inclusion compound, **DNBz** (116(4) kJ.mol^{-1}). This is the only inclusion compound in this study in which the guests were located in cavities. As stressed in the literature[1], and pointed out in Chapter 1, one has to be cautious when attempting to interpret the kinetic rate law followed by a reaction. The decomposition of **DNBz** was the only reaction in this study for which sigmoidal α-time curves were obtained. Deceleratory α-time curves were observed for all the other desolvation reactions. The first order reaction mechanism (F1) was observed for the majority of reactions (7/12), while the contracting area (R2) and three-dimensional diffusion (D3) mechanisms were also observed. The F1 reaction mechanism was predominantly observed for channel type structures (with the constricted channel structure of **WTB14D** being an exception). In these structures there is no physical barrier to the diffusion of guests out of the host framework. In cases where the same guests were included in a channel structure and constricted channel structure, higher E_a values were observed for the constricted channel structures, e.g. E_a (**WTBAC**) > E_a (**WC17AC**) and E_a(**WTB14D**) > E_a (**W17DIA**). A larger database of kinetic

parameters for the desolvation of different inclusion compounds will have to be built up in order to draw conclusive correlations between the types of packing, kinetic models and magnitudes of activation energies. A larger database of such parameters might even allow predictions to be made regarding the stability of new inclusion compounds.

Table 10.1. Selected information for the desolvation of the inclusion compounds dealt with in the current study.

Compound	T_{on} (DSC) /°C	T_b /°C	$\Delta H_{desolv.}$ /kJ.mol^{-1}	T-range /°C	E_a /kJmol^{-1}	Inclusion mode
W17DIA	66	101.1	76	50-70	34(3)	Channel
	114		34	100-125	111(9)	
	145					
W17DB	94	101.1	50	-	-	Channel
	154		30	-	-	
WTB14D	179	101.1	45	148-160	150(6)	Constricted channel
W17	143	74-75	55	60-72	130(9)	Channel
WB3DA	103	74-75	48	-	136(5)	Channel
W13DT	130	105-106	78	-	122(2)	Channel
WC17AC	80	56.5	56	40-65	58(3)	Channel
WTBAC	175	56.5	42	125-145	147(4)	Constricted channel
DP13D	110	74-75	17	55-80	78(2)	Channel
DN13D		74-75	48	55-75	50(10)	Constricted channel
			23			
DTBM	60	64.7	56	40-65	81(8)	Channel
DNBZ	98	80.1	42	70-85	116(4)	Cavity
DBBz	79	80.1	133	50-70	89(4)	Channel

The compensation effect[4] was discussed in Chapter 1. It occurs in a group of related reactions, if changes in A are accompanied by a change in E_a, according to the relation:

$$ln\, A = BE_a + C$$

where B and C are constants. Parameter C is related to the structure of, and defects in, the starting material. The value of B characterises the strength of the bond to be broken when gaseous products are formed. A decrease in B would imply an increase in the strength of the bond to be broken. It was shown in Chapters 7 and 8 that the Arrhenius parameters for all the reactions in this study exhibit the compensation effect. All the inclusion compounds under investigation comprised hydroxy hosts and volatile guests. In each case guest loss was accompanied by a rearrangement of the host crystalline network. The existence of the compensation effect confirms that the desolvation reactions were similar with respect to the types of bonds to be broken. A substantial database of kinetic parameters for host-guest desolvation reactions has to be established. It is conceivable that different types of host compounds would give rise to different sets of compensation behaviour. Hence parameters like B and C could potentially be used for comparison of the reactivities of different types of inclusion compounds.

1 C.H. Bamford and C.F.H. Tipper (eds), *Comprehensive Chemical Kinetics* (Vol 22), Elsevier, Amsterdam, 1980.

2 A.K. Galwey, *J. Therm. Anal.*, **41**, 1994, 267.

3 A. Coetzee, D.J. Eve and M.E. Brown, *J. Therm. Anal.*, **39**, 1993, 947.

4 J. Zsako, Cs. Varhelyi and K. Szilagyi, *J. Therm. Anal.*, **7**, 1975, 41.

APPENDIX A

The supplementary material for structures of compounds from Class **A** appear on this diskette. The material are divided into two files for each structure, with the code of the structure used as the filename. The files with the extension "tex", e.g. W17DIA.tex, contain:

- atomic coordinates and isotropic displacement parameters
- bond lengths and angles
- anisotropic displacement parameters
- hydrogen coordinates and isotropic displacement parameters

The calculated and observed structure factors are contained in files with the extension "sft", e.g. W17DIA.sft.

APPENDIX B

The supplementary material for structures of compounds from Class **B** and **C** appear on this diskette. The material are divided into two files for each structure, with the code of the structure used as the filename. The files with the extension "tex", e.g. DP13D.tex, contain:

- atomic coordinates and isotropic displacement parameters
- bond lengths and angles
- anisotropic displacement parameters
- hydrogen coordinates and isotropic displacement parameters

The calculated and observed structure factors are contained in files with the extension "sft", e.g. DP13D.sft.

All these files are text files and can be viewed in an editor, under any of the following operating systems:
DOS
WINDOWS 3.1
WINDOWS 95
OS/2
APPLE MAC
UNIX
VMS
Linux

HOST		GUEST	H:G	CODE
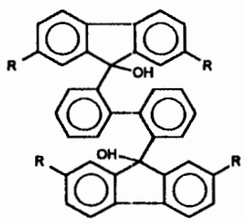	**A1**			
	R=Cl	1,4-dioxane	2:7	**W17DIA**
	R=Cl	1,3-dioxolane	1:2	**W17**
	R=Cl	1,3-dioxane	1:2	**W13DT**
	R=Cl	acetone	1:2	**WC17AC**
	R=Cl	-	-	**WCL**
	A2			
	R=Br	1,4-dioxane	2:7	**W17DB**
	R=Br	1,3-dioxolane	1:2	**WB3DA**
	A3			
	R=Bu^t	1,4-dioxane	1:1	**WTB14D**
	R=Bu^t	acetone	1:1	**WTBAC**
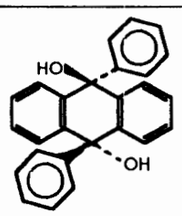	**B1**	1,3-dioxolane	1:1	**DP13D**
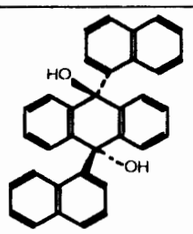	**B2**	1,3-dioxolane	1:2	**DN13D**
		benzene	1:1	**DNBz**
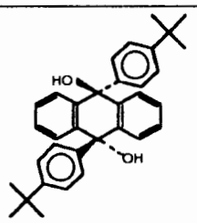	**B3**	methanol	1:1	**DTBM**
		benzene	1:3	**DBBz**
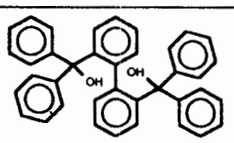	**C**	water:benzene	1:1:1/6	**TODBEN1**
		water	1:21/6	**TODOXLT**
		p-xylene	1:½	**TODPXLT**

HOST		GUEST	H:G	CODE
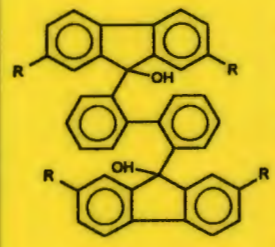	**A1**			
	R=Cl	1,4-dioxane	2:7	**W17DIA**
	R=Cl	1,3-dioxolane	1:2	**W17**
	R=Cl	1,3-dioxane	1:2	**W13DT**
	R=Cl	acetone	1:2	**WC17AC**
	R=Cl	-	-	**WCL**
	A2			
	R=Br	1,4-dioxane	2:7	**W17DB**
	R=Br	1,3-dioxolane	1:2	**WB3DA**
	A3			
	R=Bu^t	1,4-dioxane	1:1	**WTB14D**
	R=Bu^t	acetone	1:1	**WTBAC**
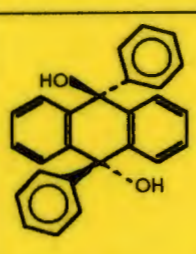	**B1**	1,3-dioxolane	1:1	**DP13D**
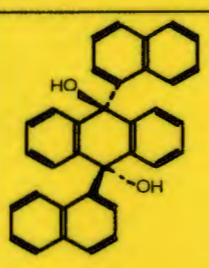	**B2**	1,3-dioxolane	1:2	**DN13D**
		benzene	1:1	**DNBz**
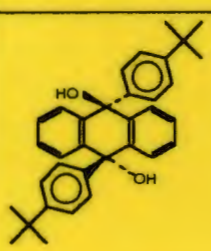	**B3**	methanol	1:1	**DTBM**
		benzene	1:3	**DBBz**
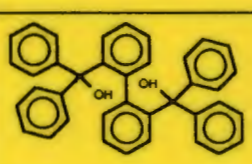	**C**	water:benzene	1:1:1/6	**TODBEN1**
		water	1:21/6	**TODOXLT**
		p-xylene	1:½	**TODPXLT**